Development of optically transparent alumina and spinel ceramics with fine microstructure

Annika Pille

▶ To cite this version:

Annika Pille. Development of optically transparent alumina and spinel ceramics with fine microstructure. Mechanics of materials [physics.class-ph]. Université Sorbonne Paris Cité, 2018. English. NNT : 2018USPCD026 . tel-02464071

HAL Id: tel-02464071
https://theses.hal.science/tel-02464071v1

Submitted on 2 Feb 2020

Université Paris 13
Institut Galilée
Mémoire de thèse présenté pour obtenir le grade de
DOCTEUR DE L'UNIVERSITÉ PARIS 13
SORBONNE PARIS CITÉ
Discipline : Science des Matériaux

Annika PILLE

"Development of optically transparent alumina and spinel ceramics with fine microstructure"

Soutenue le 19/12/2018

MEMBRES DU JURY

MME. MONOT-LAFFEZ Isabelle, Labo. GREMAN, Univ. de Tours, France	Rapporteuse
M. KHODAN Anatole, Académie des sciences de Russie, Moscou	Rapporteur
MME. MONNIER Judith, ICMPE-CNRS, France	Examinatrice
M. FELDBACH Eduard, Institut de physique, Université de Tartu, Estonie	Examinateur
M. VREL Dominique, LSPM-CNRS, Université Paris 13, France	Examinateur
M. SCHOENSTEIN Frédéric, LSPM-CNRS, Université Paris 13, France	Directeur de thèse
M. KANAEV Andrei, LSPM-CNRS, France	Directeur de thèse

Thèse préparée au Laboratoire des Sciences des Procédés et des Matériaux
LSPM-CNRS, UPR 3407, Université Paris 13, Sorbonne Paris Cité

Université Paris 13
Institut Galilée
Mémoire de thèse présenté pour obtenir le grade de
DOCTEUR DE L'UNIVERSITÉ PARIS 13
SORBONNE PARIS CITÉ
Discipline : Science des Matériaux

Annika PILLE

"Development of optically transparent alumina and spinel ceramics with fine microstructure"

Soutenance prévue le 19/12/2018

MEMBRES DU JURY

MME. MONOT-LAFFEZ Isabelle, Labo. GREMAN, Univ. de TOURS, France	Rapporteuse
M. KHODAN Anatole, Académie des sciences de Russie, Moscou	Rapporteur
MME. MONNIER Judith, ICMPE-CNRS, France	Examinatrice
M. FELDBACH Eduard, Institut de physique, Université de Tartu, Estonie	Examinateur
M. VREL Dominique, LSPM-CNRS, Université Paris 13, France	Examinateur
M. SCHOENSTEIN Frédéric, LSPM-CNRS, Université Paris 13, France	Directeur de thèse
M. KANAEV Andrei, LSPM-CNRS, France	Directeur de thèse

Thèse préparée au Laboratoire des Sciences des Procédés et des Matériaux
LSPM-CNRS, UPR 3407, Université Paris 13, Sorbonne Paris Cité

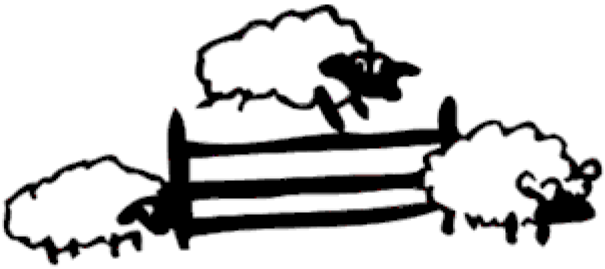

My last hurrah to academic science

Acknowledgements

This work has been carried out within the framework of the EUROfusion Consortium and French Research Federation for Fusion Studies and has received funding from the Euratom research and training program 2014–2018 under grant agreement No. 633053. The views and opinions expressed herein do not necessarily reflect those of the European Commission.

First of all, I would like to thank the members of the jury for taking the time to read and discuss my thesis just before the holidays.

Thank you to my supervisors, Andrei Kanaev and Frédéric Schoenstein for inviting me onto this topic and for their endless advice (you still owe me at least 10 hours for the times we started our meetings "in 5 minutes").

I thank my two interns, Ferhat and Hugo for their interest in the topic and the work included in this thesis.

A big thank you for their generous collaboration to Eduard Feldbach for luminescence measurements and analysis, Daniel Chateigner for XRD texture measurement and analysis, Benjamin Villeroy for SPS-help and advice. Thank you to Jean-Louis Vignes for his advice on ultraporous alumina. Thank you to the colleagues from LVTS for their help with transparency measurements and to the colleagues from LPL for their advice on transparency measurements and help with polishing.

Thank you to the kind people in the lab. Rachid, for making sure I have a place to live, teaching me about alumina and believing in order and organization in the lab. Khaled for always asking every student about the applications of their work and trying to include English to different lab events. Ovidiu for advice on polishing and SEM and the hours spent measuring the EBSD. Valérie for measuring almost 100 XRD patterns for me and my interns. David for the help with density measurements with the pycnometer. Azziz for carrying out the HIP treatments. Thank you to the generous Ouafa, Chrystel, Sandrine and Nathalie for their help with various documents and packages.

Thank you to Yann, Silvana and Noureddine for providing advice mixed with countless laughs and for their continuing critique on Fred's *verrry gud Anglish* (one day, guys, one day he'll be ready…maybe).

Thanks to other PhD/internship students and postdocs for good conversations and aid with random problems, with a special mention to the library crowd. Thank you to Sabrine who taught me to stick to my guns. Thank you to Anna for confirming that I am not going mad in a TV-sitcom.

My gratitude to the people that made me choose and stay in physics and science. My high school physics teacher Airi, who bravely stood in front of a class full of idiot teenagers and still got the point across. My first physics professor Kalev Tarkpea, who forced me to think. My Bachelor's supervisors Eduard and Eliko, who taught me everything one needs to know about how to science. My expanded Bachelor's course friends for showing me that physicists don't have to be dry and boring. My Master's supervisor Sven for his endless rants on how things are wrong.

Thank you to my family who let me escape to a foreign country with a weird language to do bizarre science stuff in a city with 10 times more people than in our whole country. And of course, thank you to my wonderful husband Joffrey who had to tolerate my academia rants and play WoW alone while I wrote this magnificent piece of work.

Table of contents

1 Introduction

1.1 Context and objective

This project deals with elaboration, more particularly sintering, as well as the study of the properties of optically transparent and luminescent ceramics. In 2016, transparent ceramics for commercial products celebrated their 50th birthday[1], yet until today, sapphire is still considered to have the most market potential[2,3]. The branch of polycrystalline transparent ceramics is expected to undergo rapid growth[3] in the coming years, due to their superior and unique features such as long term reliability, superior mechanical properties, environment friendliness, ease of manufacturing, performance at high-temperature environments and chemical durability.

Among a great deal of possible applications in medicine, space engineering, optoelectronics, applications for use in harsh environments such as future nuclear fusion facilities as optical windows are foreseen for polycrystalline transparent ceramics. More specifically for fine-grained materials, applications are anticipated in the field of detectors resistant to ionizing radiations as one of the top priorities of the EUROfusion consortium research program[4] started 4 years ago.

Durable optical materials are valuable in diagnostic systems for future fusion reactors, having to withstand neutron irradiation in the order of megaelectronvolts. On a microstructural level, the power of a material to resist irradiation depends[5] on how efficiently it can remove pairs of interstitial defects and vacancies, avoiding the movement of interstitials to the surface of the material and swelling. From here arises the importance of the presence of stoichiometric defects in the chosen materials. Bai et al[6] have shown the promising radiation resistance of nanomaterials, in which grain boundaries can capture interstitials and bombard them back into the lattice to destroy a vacancy a few nanometers from the grain boundary. Thus, the material "self-heals".

Hence, the challenge of this work is to find a balance between producing a transparent ceramic (normally demanding high sintering temperature and pressure), keeping in mind the optical applications, while also minimizing the grain size (normally calling for softer sintering conditions) to increase radiation resistance. Additionally, grain isotropy is important for uniform transparency and the intrinsic structural defects need to be characterized for radiation resistance applications. To achieve ceramics with homogeneous grain size distribution, the homogeneity of the precursor powder is of utmost importance and the effect of different morphologies will be tested.

1.2 Methods and means

Alumina and spinel were chosen as the materials to be studied, due to their known intrinsic defects[7,8] leading to characteristic luminescence and radiation resistance[9,10]. Other than the luminescence of F and F^+ centers in alumina, transitions within quasimolecules (three anions and two cations) have long been known[7] to cause intrinsic luminescence at 7.5 eV. The thermal quenching of this so-called A-band depends on the thermal treatment of the sample, being higher in the case of untreated nominally pure crystals (38 meV) and lower (27 meV) for samples annealed at 1900 K and low oxygen pressure 10^{-4} Pa. Thus, the thermal behavior of structural defects depends not only on the material, but also on the conditions it was acquired at. As an example of radiation resistance of spinel, amorphization due to irradiation by 400 keV Xe^{2+} ions has been shown[10] to occur at very high damage level of 25 displacements per atom (dpa).

The ceramics in this work will be sintered from ultra-porous aluminas (UPA) with a very high degree of purity and nano-sized crystallites along with various commercial powders for comparison purposes. UPAs will be developed using an original process patented[11,12] by members of the Inorganic Nanomaterials team of the Laboratory of Process and Materials Sciences (LSPM-CNRS).

The synthesized UPAs will then be consolidated by Spark Plasma Sintering (SPS), a technology located in Île-de-France as part of a consortium of laboratories, LSPM being a co-founder. The innovative SPS technique was chosen as the sintering method because of its high heating rates and short sintering times, allowing to obtain nanograined ceramics[13]. A fine structuring of our ceramics, and more particularly a high density of grain boundaries, should then allow the capture and recombination of induced charges[5,6], thus giving the ceramics resistance to ionizing radiation of high intensities. It is noted that existing monolithic compounds do not withstand this type of radiation well and fracture quickly.

To successfully produce transparent and fine-grained materials, two opposing sintering cycles were developed. A long (60-minute dwell) sintering cycle at relatively low temperature to obtain maximal density and a short (3-minute dwell) cycle at high temperature to maximally benefit from the rapid nature of SPS and obtain minimal grain growth during sintering.

The study of the optical properties of the elaborated ceramics will be carried out thanks to the characterization tools recently set up in the laboratory. Finally, an Estonian partner, the Institute of Physics of the University of Tartu, will be in charge of the study of the radiation resistance and luminescence of the elaborated materials, characterizing structural defects.

The originality of this work lies in using LSPM know-how of producing ultraporous alumina to obtain dense, transparent alumina-based ceramics with fine microstructure. Furthermore, it is rare to investigate microstructure, optical properties and structural defects through luminescence with their dependence on various synthesis and sintering parameters.

To the best of our knowledge, this is the first work to synthesize Al_2O_3-MgO mixture precursor powders via the impregnation and polyol methods to then be reactively sintered to spinel phase via spark plasma sintering.

1.3 Plan of the manuscript

Following the Introduction, Chapter 2 – State of the art – firstly summarizes the formation of alumina polymorphs and magnesium aluminate spinel and also gives details about their synthesis methods. Next, achieving transparency and radiation resistance in polycrystalline ceramics will be reviewed. The SPS technique is introduced with its benefits and drawbacks, along with some popular sintering treatments used in combination with SPS. Finally, an overview is given on the optical and luminescence properties of alumina and spinel, including some thermochemical and – physical properties.

Chapter 3 – Experimental techniques – summarizes the information about the synthesis, sintering and characterization techniques used in this work. An overview is given on the growth of UPA as well as polyol synthesis and impregnation method for doping. Along with sintering and characterization techniques, the polishing procedure is detailed.

Chapter 4 presents the results obtained by sintering six different alumina powders in various phases with assorted morphologies. Firstly, the powders are characterized, then the results on the obtained grain structure are demonstrated including a texturation study and hot isostatic pressing post-treatment. Lastly, the absorption and luminescence of consolidated materials is investigated. The final goal of this chapter is to determinate which source of alumina should be used in obtaining the spinel phase.

Chapter 5 presents the results of sintering a commercial spinel powder in comparison to two precursor powders for reactive SPS. Polyol synthesis and magnesium nitrate impregnation are examined in contrast to determine which doping method leads to a dense spinel ceramic with maximal possible transparency and minimal grain size. Doping with various concentrations of Ta_2O_5 as a grain growth inhibitor is investigated.

Finally, Chapter 6 concludes the results of the work and gives suggestions for future research directions.

2 State of the art

In this chapter, an overview will be given on the general knowledge and state of the art publications most relative to the current work. In chapter 2.1, the phase formations and properties of alumina and spinel are explained, along with the structural defects characteristic to both materials and important for radiation resistance. Chapter 2.2 focuses on the synthesis routes used to obtain alumina, magnesia and spinel precursor powders for sintering. The classical production methods and applications of transparent and fine-grained ceramics are summarized in chapter 2.3 along with the explanation of the self-healing process of radiation-induced defects in nanostructures. Chapter 2.4 addresses spark plasma sintering as the process chosen to consolidate the materials, giving an overview of the technique with its intrinsic problems and benefits. In chapter 2.5, the physical properties of alumina and spinel are summarized, including optical absorption-transparency, defect luminescence and some thermophysical and – chemical properties. Lastly, chapter 2.6 sets the goals of this project.

2.1 *Phase formations and properties of alumina and spinel*

Here, the phase transformations of alumina are discussed with the focus on the thermodynamically stable α–Al_2O_3 (corundum) phase. Additionally, the pseudo-binary Al_2O_3 – MgO system is discussed for the formation of the spinel phase. The standard crystallographic information is given for both of the phases along with the description of intrinsic crystallographic defects crucial for radiation resistance.

2.1.1 Alumina

The principal ore of alumina is bauxite, composed of a mixture of aluminum (oxy)hydroxide minerals (boehmite (γ-AlO(OH)), diaspore (α-AlO(OH) and gibbsite ($Al(OH)_3$)) with natural impurities of iron oxides, clays, and titanium oxides. Alumina produced from boehmite goes through the phase transformations shown in Figure 1 [14]. Aluminas heated at temperatures under 1100°C were considered to be amorphous and loosely described as "γ-alumina" in the 1920s, remaining ill-defined and complex[15] in comparison to the thermodynamically stable α-alumina. These materials were only known for their ability to change into crystalline α-Al_2O_3. In 1950, Stumpf *et al*[16] described the crystalline structure of the intermediate phases, expanding the list of crystalline phases of alumina to the following: **alpha (trigonal-hexagonal, $R\bar{3}C$, a=4.75 Å, c=12.98 Å)**[17,18], **gamma (cubic, $Fd\bar{3}m$:2, $a_\gamma \approx 7.9$ Å)**[18], **delta (tetragonal, $P4_1$, a= a_γ, c≈ $3a_\gamma$ //orthorhombic, $P2_12_12_1$, a≈ a_γ b ≈ $2a_\gamma$, c = $1.5a_\gamma$)**[18], eta, **theta (monoclinic, C2/m, a ≈ $1.5a_\gamma$, b = $a_\gamma\sqrt{2}/4$, c = $a_\gamma\sqrt{2}/2$)**[18], kappa, and chi. The phases in bold will be discussed in this thesis, the main focus being on the thermodynamically stable α–Al_2O_3 (corundum) phase.

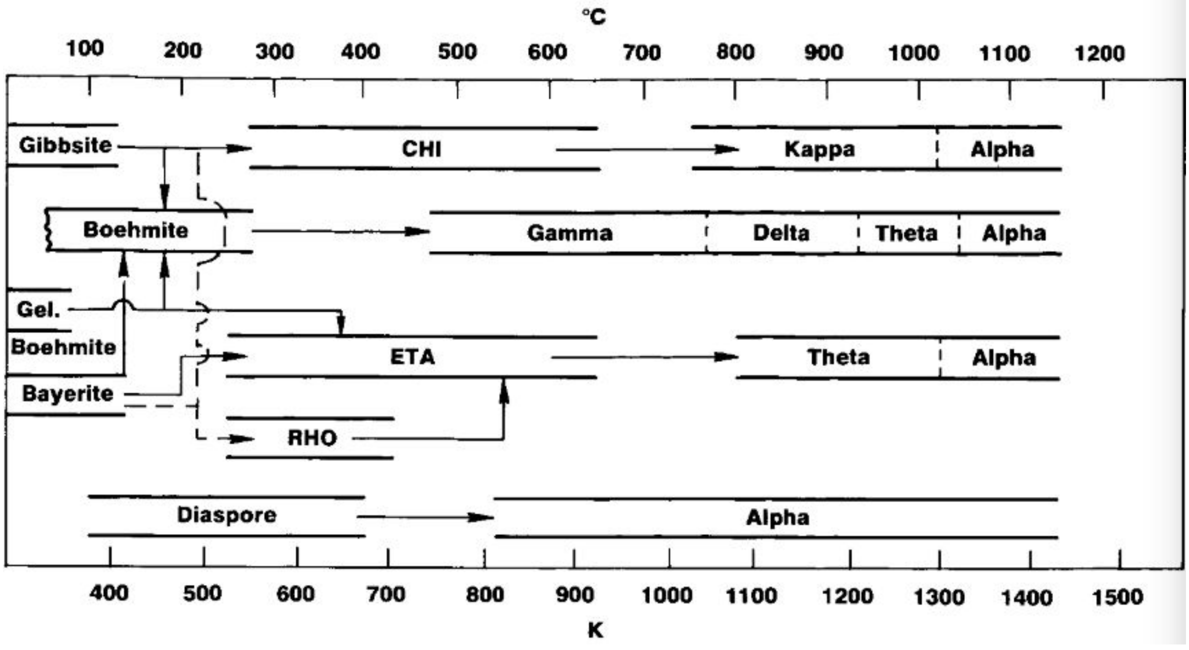

Figure 1. Alumina phase transfers [14].

Corundum has a trigonal symmetry with rhombohedral Bravais centering as listed above and has 6 formula units in the unit cell[19], see Figure 2. The structure of α–Al_2O_3 is often considered as a hexagonal hcp sublattice of oxygen anions, with 2/3 of the octahedral interstices filled with aluminum cations in an ordered array. This simplified model characterizes the general essence of the ion packing, while not reflecting the true trigonal symmetry of the crystal

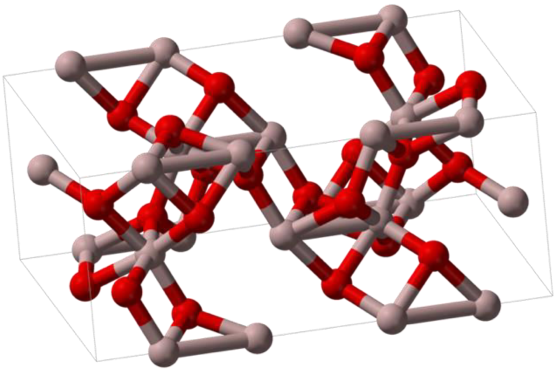

Figure 2. Corundum unit cell[19].

and thus being somewhat deceiving. One key difference of the trigonal symmetry is the nonequivalence of cation layer translations along the $[10\bar{1}0]$ and $[\bar{1}010]$ directions (using hexagonal indices)[18]. The theoretical XRD pattern of corundum[20,21] along with the Miller indices of the reflections is shown in Figure 3.

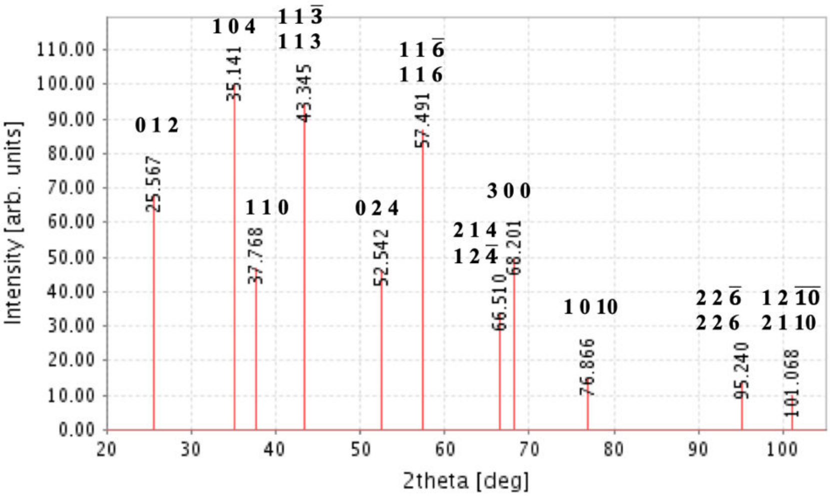

Figure 3. Theoretical XRD pattern of corundum. [20,21]

The most common point defects in corundum and ionic crystals in general include Schottky and Frenkel defects[22]. The first occurs when the cation and anion leave their respective lattice sites and thus create a vacancy pair, whilst maintaining the overall electrical neutrality of the crystal and reducing the density. In the case of Frenkel defects, an ion escapes its lattice site and becomes an interstitial.

2.1.2 Al_2O_3–MgO system and $MgAl_2O_4$ spinel

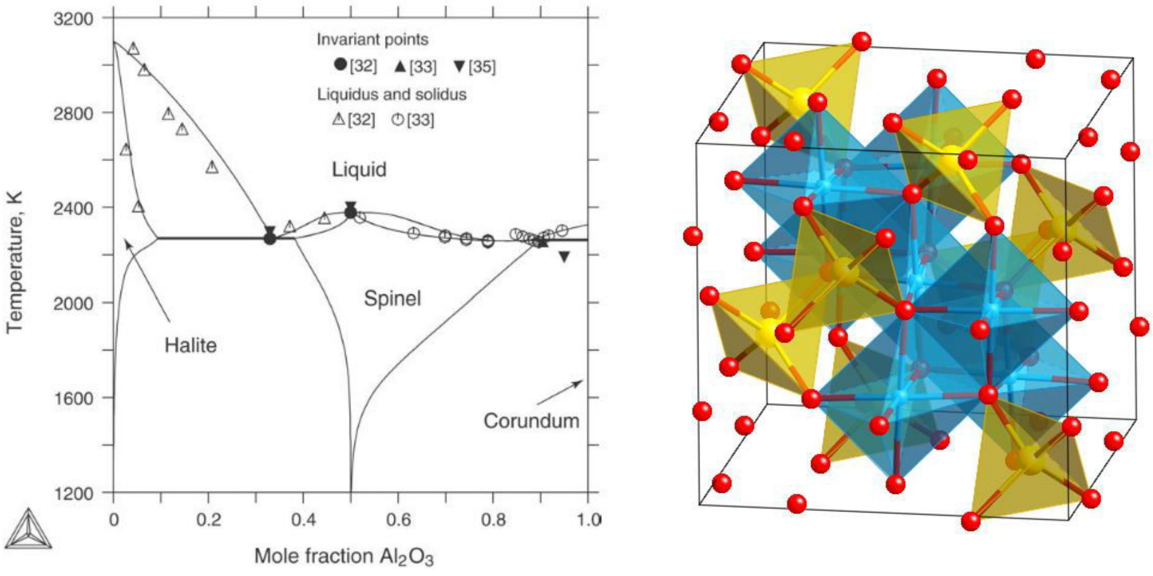

Figure 4. Phase diagram of the Al_2O_3-MgO system[23] *and $MgAl_2O_4$ crystal structure.*

As can be seen from Figure 4(left)[23], the only intermediate phase in the Al_2O_3–MgO system is magnesium aluminate spinel (MAS, $MgAl_2O_4$), requiring exact 50:50 mole fraction of alumina and periclase below 1400 K and benefiting from higher ratio of periclase/alumina at higher temperatures. The composition can be expressed as $MgO \cdot nAl_2O_3$, where $0.8 \leq n < 3.5$[24,25] and the only stable phase is $MgAl_2O_4$, n=1.

Nonetheless, the crystal structure of spinel (see Figure 4 (right)) is flexible when it comes to the cation sites. The unit cell of MAS consists of 8 formula units, has a cubic structure within the Fd3m space group with lattice parameter a=8.0898 Å. The Mg^{2+} cations normally occupying 1/8 of the tetrahedral positions can easily exchange places with the Al^{3+} cations occupying half

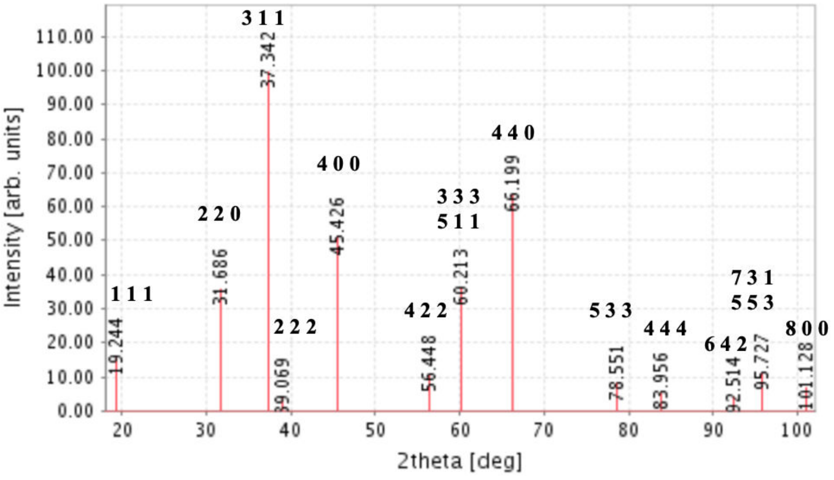

Figure 5. Theoretical XRD pattern of $MgAl_2O_4$. [32,33]

of the octahedral positions, creating an inversion (I=0…1) in the material and modifying the lattice parameter[26,27]. This cation flexibility makes the structure tolerant towards nuclear irradiation[28], see further discussion in chapter 2.3.2. Similarly, Mg^{2+} cations can be replaced by various other divalent cations (as an example, Yb^{2+}[29] and Co^{2+}[30]), making spinel an interesting material for doping and optoelectronic applications[31]. The classical diffractogram of $MgAl_2O_4$[32,33] is shown in Figure 5.

The Al_2O_3/MgO ratio X can be estimated using an empirical equation developed by Viertel and Seifert[34,35]: $X = \frac{8.6109 - a_0}{3a_0 - 23.7195}$, where a_0 is the lattice parameter of obtained spinel. It has been suggested that the non-stoichiometric spinel formation is controlled by oxygen vacancy diffusion arising from evaporation of MgO[36,37].

Furthermore, the spinel structure exists with many different cation combinations (for example, aluminum spinels MAl_2O_4, iron spinels MFe_2O_4, chromium spinels MCr_2O_4), of which iron spinels also have interesting magnetic properties[38], making the material group as a whole very intriguing. The inverse spinel structure is in additional limelight of research because of the possibility to "un-inverse" the structure by thermal annealing, however, color centers introduced into the structure are thermally stable even at 1000 K[39].

Different types of intrinsic defects can exist in the magnesium aluminate spinel structure: magnesium vacancy (V_{Mg}^{2-}), aluminum vacancy(V_{Al}^{3-}), oxygen vacancy(V_O^{2+}), aluminum interstitial ion (Al_i^{3+}), magnesium interstitial ion (Mg_i^{2+}), oxygen interstitial ion (O_i^{2-}), aluminum ion on magnesium lattice site (Al_{Mg}^{+}), magnesium ion on aluminum site (Mg_{Al}^{-}), the last two are also called antisite defects[40].

γ-Al_2O_3, having a crystal structure more complex than α–Al_2O_3, can be represented as defect spinel[41]: $(vacancies)_{2+2x}Al_{21+x}O_{32}$, x = 1/3.

2.2 Powder synthesis

In this chapter, the most popular routes for receiving alumina and magnesia nanoparticles will be described. The classical sol-gel and polyol synthesis methods will be introduced, along with the LSPM know-how on growing UPA monoliths and their doping.

2.2.1 Alumina: The classical sol-gel route

The first transparent aluminas were produced from transparent aluminum alkoxide gels. This method investigated and patented by Bulent E. Yoldas in 1970s[42,43] and is thus known as the Yoldas process. Aluminum alkoxides are very reactive and often require chelating agents to control the condensation rate and hydrolysis. During the Yoldas process, aluminum alkoxide (most commonly $Al(OBu)_3$) is hydrolyzed in a large excess of water (hydrolysis ratio R=100 – 200) at 80 – 100 °C, precipitating fibrous boehmite and later peptized with a mineral acid (HNO_3) to produce a stable particulate solid. Maximal 220 m^2/g surface area is obtained at optimized acid concentration of 0.07 moles of acid per 1 mole of hydrate[43]. Bayerite ($Al(OH)_3$) is obtained after ageing the amorphous precipitate through dissolution-recrystallization. Vigorous liberation of OR-groups from the amorphous phase by heating above 80°C causes the phase to convert to boehmite[44]. Lastly, gelation occurs by concentrating the sol by evaporation or boiling[45].

To obtain aluminum oxide, the gel must be pyrolyzed to 500°C. A critical electrolyte concentration exists to keep the gel intact, the sols that gel at less than about 4 g/100 ml concentration of equivalent oxide do not retain integrity during pyrolysis[43]. Both bayerite and boehmite conversions are inhibited by the presence of alcohols in the aging liquor.

Room temperature (20°C) water hydrolysis results in formation of amorphous monohydroxide with lower alumina content (82% vs 73%) and conversion to bayerite does not occur when the slurry is heated to 80°C[42]. In fact, it has been shown that heating at any stage of aging eliminates the capability of the amorphous hydroxide to convert to bayerite from that point on[42].

2.2.2 MgO: The polyol method

Polyols are alcohols containing multiple hydroxyl groups. Polyol method, also known as polyol process is a popular liquid route to synthesize metals, non-metal main-group-elements, metal chalcogenides and oxides [46]. It was first introduced by Fievet, Lagier and Figlarz in 1989[47] and has since become a classical tool for anyone working in the field of crystalline nanoparticle synthesis. The biggest benefits of the polyol process are combined water-like high solubility of common metal salts, high boiling temperature (depending on chosen polyol, from 200°C – 350°C), reducing properties for metal synthesis, good colloidal stabilization and a variety of polyols to choose from, ranging from low to high molecular weight. Ethylene glycol (EG, the simplest polyol), diethylene glycol (DEG), glycerol and butanediol are the most commonly used to prepare nanoparticles. Low-weight polyols (EG, DEG, butanediol, propanediol and glycerol) can be easily removed from the particle surfaces by washing with methanol, acetone and/or water or thermal treatment at 200°C – 320°C. The creation of metal, metal oxide or metal hydroxide in polyol can be driven by the concentration of water. The resulting particle size grows with the growing concentration of starting materials and water. The outcome of the polyol synthesis is a colloidally stable suspension of 1 – 200 nm particles, reaching 20 wt.%. Although the first report of polyol process included synthesizing metal particles, in 1994-5[48,49] the same authors reported synthesizing ZnO and CoO. Since polyols endure high synthesis temperatures, most crystalline oxide nanomaterials can be received directly from the synthesis without need for further thermal annealing. However, thermal annealing is necessary for producing MgO[50], because of its higher-than-polyol-boiling-point crystallization temperature. The polyol process is also a popular method to produce multinatry oxides, including iron and cobalt spinels. In this work we are interested in the synthesis of MgO with addition of Al_2O_3 as precursor in the polyol medium to receive respective aluminum spinels. Only one study of synthesizing γ-alumina particles via polyol process has been published[51]. Alumina produced via the method described in the next section will be used as a source of Al_2O_3 in this work. Finally, the spinel phase will be formed via reactive SPS.

2.2.3 Alumina monoliths and doping, co-sintering

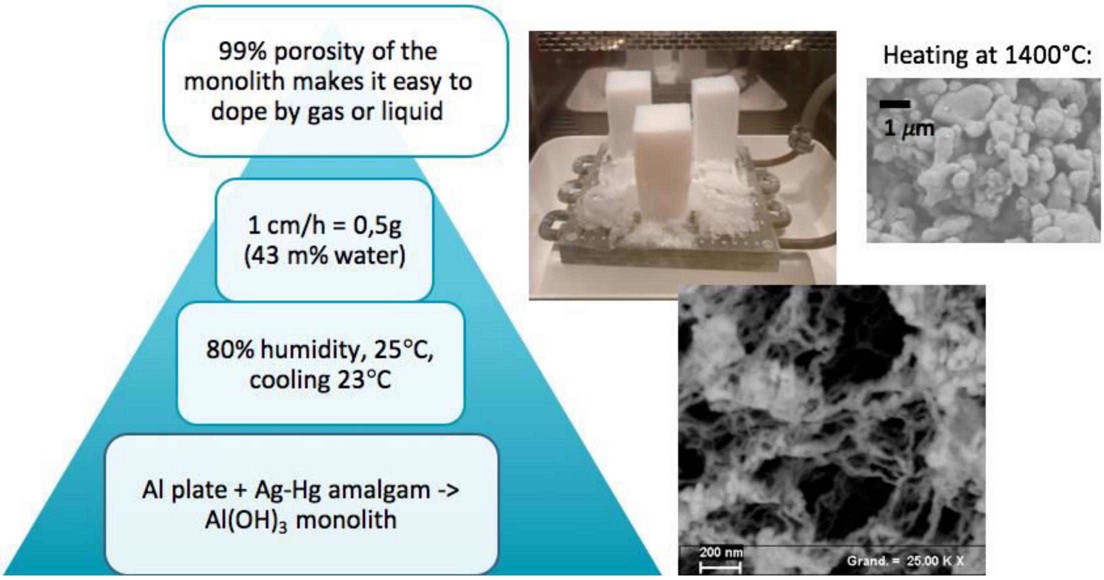

Figure 6. Alumina monolith growth process (left), the resulting monolith (middle) and alpha alumina received after heating at 1400°C for 4 h (top right).

The process of growing amorphous alumina monoliths via oxidation through liquid layer of mercury (see Figure 6) is patented and published in CEA-CNRS and LSPM-CNRS by Jean-Louis Vignes[11,12,52]. It starts from using a high purity laminated aluminum plate, depassivating the surface with 10% NaOH and then dipping the plate into a mixture of silver and mercury nitrates ($Ag(NO_3) – Hg(NO_3)$), where silver plays a reaction stabilizing role. The plate is then quickly washed, dried and placed into the climate chamber. Since oxidation of aluminum is an exothermic reaction, a cooling radiator is used inside the climate chamber. Resulting aluminum oxidation will produce about 1 cm (or 0.5 g per 25 cm^2) of amorphous $Al(OH)_3$ per hour, the reaction continues in a stable manner for 8 – 12 hours. The porosity of received monolith is > 98%. Depending on the final desired alumina phase, the monolith is annealed in air at temperatures ≥ 1000°C generally for 4h. It is important to note that the highly nanometric grain size (10 nm) and high surface area are maintained until the θ-Al_2O_3 phase that can be obtained at 1100°C. The grain size for the thermodynamically stable α–Al_2O_3 obtained at 1300°C varies from 150 to 250 nm[53,54]. A model describing the phase, morphology and elemental content variations depending on temperature has recently been presented[55].

One big advantage of highly porous alumina is the fact that it can be easily doped by an impregnation of vapors or liquids. For example, to receive silica-doped alumina, the monolith is placed in a closed container with trimethylethoxysilane/tetraethoxysilane (TMES/TEOS) liquid in a petri dish at the bottom of the container. The duration of the doping depends on the desired concentration of silica in the final product. After annealing at 600°C in air, TMES forms a monolayer of SiO_2 on the monolith and can introduce up to 6 wt% of SiO_2 onto the alumina fibers and $3Al_2O_3$-$2SiO_2$ mullite monoliths with 30 nm grain size can be obtained when using TEOS vapor and heating at 1200°C [53,54]. In a similar way, liquid colloid deposition method has been previously applied to impregnate ultraporous alumina monoliths with functional nanoparticles; in this method the nanoparticles (TiO_2) agglomeration state can be effectively controlled that permitted to attain an enhanced photocatalytic response of the material[56,57].

2.2.4 Spinel powder

Spinel has been a material of interest due to similar chemical and physical properties as corundum, with the benefit of cubic crystal structure and the homogeneity arising from it. One of the earlier papers by Singh and Sinha [58] on low-temperature synthesis of spinel describes a gelation-precipitation process of alumina and magnesia chlorides and sulfates in aqueous solutions in proper proportions to give 1:1 alumina-magnesia ratio upon calcining. This logic is very much similar to the process of doping UPA monoliths described by T. di Costanzo *et al*[53] and also most other spinel synthesis routes. Singh and Sinha observed the beginning of spinel formation at 600°C and completely converted spinel phase was obtained after firing at 1000°C for 1 hour, resulting in average particle size of 210 nm. However, for high theoretical densities (> 80%), firing at higher temperatures (≥1300°C) during longer periods (up to 3h) was necessary.

With a goal of lessening the formation of coarse agglomerates of powder during drying, leading to nonhomogeneous final product, Suarez *et al* [59] tested reverse-strike coprecipitation and oxides mixture sintering routes, starting from oxides, chlorides and nitrates to find the best parameters for obtaining transparent spinel. They obtained the best transparency (35% at 500 nm, porosity 0.06%) when using the chloride sol-gel process at 800°C, while spinel formation in the case of oxide mixture was observed at 1200°C. Both nitrate and chloride route resulted in 20 nm spinel particles, however, powders obtained via the nitrate route were more agglomerated. The biggest particles and agglomeration was observed in the case of oxide mixture which resulted in a cracked green body after pressing.

Thus, to synthesize fine spinel powders suitable for sintering transparent final products, one should start from alumina-magnesia salts, not already formed oxides.

Similarly, UPA can be used to produce nanometric MAl_2O_4 spinels, where M stands for Mg, Ni or Co[53,54]. In this case a liquid route is used, consisting of UPA absorbing aqueous solutions of divalent metal salts followed by calcination at low temperature (200 – 500°C). In the case of α–Al_2O_3 obtained from UPA, $Mg(NO_3)_2$ water solution can be used for doping. To obtain the necessary 1:1 molar ratio of Al_2O_3 and MgO, taking into account the maximum solubility of $Mg(NO_3)_2$, the doping has to be carried out in cycles[54]. MgO forms after annealing at 500°C, spinel appears at 900°C and the reaction is completed at 1200°C. Interestingly, even after a week-long annealing at 1000°C, all three phases are present in the sample, proving the necessity of higher temperature[54]. After treatment at 1200°C, the spinel sample keeps the same microstructure as that of the starting α-Al_2O_3. However, the transformation of each corundum grain into spinel produces aggregated spinel crystallites with a size around 100 nm. Moreover, the developing spinel crystallites after 4h annealing at 900°C are only 10 nm[53] in size, making this in between phase an interesting starting point for sintering. The results of the impregnation method will be presented in chapter 5.2.

2.3 Transparent and fine-grained ceramics: producing and applications

2016 marked 50 years since the first transparent ceramic-based commercial product[1], a sodium vapor-based street lamp envelope, reached the market.

Nowadays, transparent ceramics have a huge international market. Market research has estimated the market size to be valued at 179[3] – 246[2] million USD in 2015 with an expected growth rate 17.4[2]– 22.4%[3] from 2016 – 2022/2024. According to the market research,

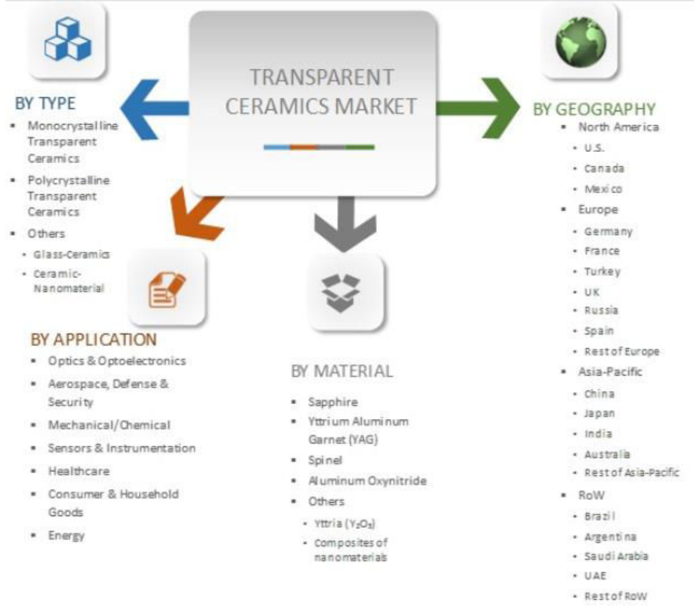

Figure 7. Transparent ceramics market segmentation. [2]

monocrystalline transparent dominated the market in 2015[3], mostly for dental applications. In addition, insulation materials for photovoltaic cells[3] are expected to boost the growth of the market. Moreover, polycrystalline transparent ceramics are expected to undergo a fast significant growth[3] due to their superior physical properties. A report[3] based on the data of 2013 – 2015 notes Saint-Gobain S. A., Schott A. G. and Surmet Corp. as the biggest companies on the market, making it hard for the newcomers to be successful. Another report from 2017 remarks how the transparent ceramics market is segmented by type, application and material (see Figure 7). Both reports still see sapphire as the main market potential.

2.3.1 Classical methods of producing high-transparency alumina and spinel

Although, from transparency standpoint, cubic crystal structure is preferred for being completely isotropic, transparent ceramics are possible beyond this limitation[60]. The most common examples of non-cubic transparent ceramics are tetrahedral ferroelectric lead/lanthanum zirconate titanates (PLZT)[61], orthorhombic mullite[62], and of course, hexagonal Al_2O_3[63]. Beyond specific ferroelectric properties, perhaps the most aspiration for near-future applications lies in alumina. It is hoped that polycrystalline alumina and/or spinel could replace sapphire in many optical applications[40], noticeably cutting the cost of these systems.

First ever transparent alumina was produced via a sol-gel technology that became known as the Yoldas process[42,43,64]. The US patent granted in 1982[64] describes the method to produce ‘finely divided high purity alumina doped with a small predetermined percentage of magnesia’. The patent then describes what now is known to be the classic sol-gel route: forming a mixed clear solution of aluminum alkoxide and water/alkoxide soluble magnesium salt with a substantial excess of water to completely hydrolyze the alkoxide; adding acid to peptize the resulting slurry and allowing the formed milky slurry to become fully peptized to form a clear sol. To obtain fine powder, the slurry is either formed into a gel, dried and mechanically reduced or spray drying is used. The fine powder then goes through calcination at 900 °C to form δ-Al_2O_3. The original US patent granted in 1973[42] describes the same process without the addition of magnesia, resulting in a ‘transparent, activated, nonparticulate alumina with total porosity of about 63% with unique pore morphology and size distribution, being thermally stable up to 1200°C.

This description of unique pore morphology and stability up to high temperatures is very similar to the resulting product from a process of producing ultraporous ultrapure monolithic alumina developed in LSPM in 1990s[11,12]. In this work we are focusing on adding to this previous know-how of raw material production with suitable sintering parameters.

In the case of spinel ceramics, first reports of producing powders suitable for sintering dense polycrystalline ceramics come from various soft solution chemistry routes from the late 1960s – early 1970s[65], starting from a stoichiometric mixture of aluminum hydroxide and magnesium hydroxide, the compact after sintering at 1600°C for 6h had relative density of 96%. The biggest progress in the American side on transparent spinel was made in Coors Ceramics around 1970, initially for transparent armor by Donald W. Roy. Don Roy later became the face of transparent spinel in America, working with numerous companies[66]. The first company to manufacture highly transparent and durable ceramics in Europe is CeramTec GmbH. The company got their start in Marktredwitz, Germany in 1903, where it originally produced porcelain[67]. One of the biggest advanced ceramics R&D competences in Europe is Fraunhofer IKTS that was founded in 1992[68].

The biggest concern with the classical methods of obtaining transparent polycrystalline ceramics is the rapid grain growth due to high sintering temperatures and/or long dwell times. For this reason, we are focusing on using Spark Plasma Sintering (SPS), which is a process made popular because of its rapid heating and short dwell times.

2.3.2 Radiation resistance and fine microstructure

One of the biggest challenges of the humankind in the near future will be sufficient power production. One of the most promising massive energy sources is nuclear fusion which comes with the problem of finding materials to last in such an extreme environment. Alumina and spinel ceramics have long been investigated as suitable materials for fusion applications due to their mechanical strength, chemical inertness and intrinsic radiation resistance[69]. The benefits of fine-grained polycrystalline ceramics and why they are good candidates for use in extreme environments will be discussed below.

A classical approach to achieving irradiation resistance in various materials is grain boundary engineering (GBE)[70] which is mostly carried out by thermomechanical processing. GBE has been shown to improve the strength, creep strength, and resistance to stress corrosion cracking and oxidation of austenitic stainless steels and Ni-base alloys and is less popular for other structural materials of nuclear reactors[71].

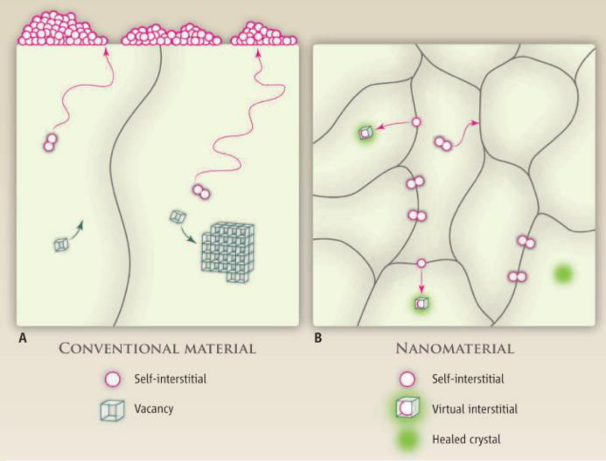

Figure 8. Interstitial defects caused by irradiation in (A) conventional material and (B) nanostructured material. [5]

It has been shown that grain boundaries and interfaces can serve as an effective anchor point for radiation-induced point defects (creation of interstitial sites and vacancies). It has been proposed that in the case of nanostructured ceramics, recombination of defects such as Frenkel pairs at grain boundaries[6,72,73] could increase resistance to irradiation. The idea of heightened radiation resistance in nano-grained materials arises in the case of polycrystalline ceramics with intrinsic stoichiometric defects. If the grain size is small enough (≤ 100 nm) so-called 'self-healing' can take place in these systems[5,6,72,73] (see Figure 8). Self-healing emanates from the collection of intrinsic defects of the material near the grain boundaries and the capability of the newly radiation-formed defects to recombine with them. This only works if the new defect is able to move to the intrinsic defect, from here arises the demand for high defect mobility and small grain size. With a small enough grain size, the newly formed defects get trapped at grain boundaries. Virtual interstitials re-emitted from grain boundaries then recombine with vacancies, resulting in a healed crystal. In a conventional material with big grain size, irradiation-induced interstitials move to the surface of the material, resulting in swelling and finally cracking. There are few publications presenting work on the radiation resistance of semiconducting or insulating nanocrystalline compounds for which the same phenomena have been demonstrated [74–76]. The atomistic diffusion mechanisms leading to the formation of these defects are therefore not yet well interpreted.

Based on the results obtained for conventional materials (structure with micrometric grains), several criteria must be taken into account to guide the choice of the compound to be studied. First, it must be an ionic compound[77]. Additionally, it has been experimentally shown[78] that crystal lattices with stoichiometric defects exhibit better radiation resistance. The vacancies lead to the formation of a lattice of unoccupied sites in which the recombination processes of Frenkel pairs can occur, as is the case, for example, for $MgAl_2O_4$, a compound well known for its radiation resistance properties, where only 8 sites out of 64 possible are occupied by the Mg^{2+} ion and 16 out of 32 possible sites are occupied by Al^{3+}. The third criterion to take into account is the size of the crystalline lattice of the considered structure. Indeed, the Frenkel pairs created inside a large lattice move less easily out of it, resulting in an increasing probability for the occurrence of recombinations.

Defect mobility in the material and grain boundary mobility are known to change depending on the grain size. Theoretical and experimental studies have shown that in the case of spinel, cation disorder (antisite defects) plays a crucial role in controlling defect mobility and radiation tolerance. The most remarkable example of spinel's natural radiation tolerance is the fact that the stable crystal structure has been shown to contain up to 30% concentration of antisite defects[39], thus containing a great deal of traps for electrons and holes, allowing to, as necessary for irradiation resistance, trap equal amounts of positively and negatively charged defects.

The main synthesis parameters for obtaining optically transparent nanostructured ceramics have recently been identified by Maglia *et al*[13]. According to this work, another point must be taken into consideration when choosing the material, it seems easier to obtain optically transparent ceramics when they have an isotropic crystalline lattice. Moreover, doping (for example with rare earths) of the initial chemical composition of these optically transparent ceramics makes them even more attractive and allows to consider their application as luminescent materials in extreme environments. The ability to boost the chemical composition of the chosen phase should therefore also be one of the criteria to be considered. Finally, the study of grain boundary formation processes and their influence on the physical properties of the material under consideration should guide the choice of design parameters.

UPAs developed in LSPM perfectly meet all these criteria. That's why we chose to focus our study on these compounds. To our knowledge, of all the methods implemented for the production of alumina (the best known are the Bayer process and the sol-gel process developed by Sasol Ltd.), our UPA preparation process is currently the only one leading to the monolithic growth of the aluminas. This makes it possible to obtain a compound of very high purity. Preliminary measurements on our samples showed exceptionally low absorption losses in the UV spectral range greater than 280 nm.

The most talked about additional benefits of fine microstructure in the case of polycrystalline ceramics are heightened mechanical properties (high hardness[79], superplasticity[80,81], extremely low/high thermal conductivity[82]). For example, a study[83] on the dependence of Vickers microhardness on the grain size of alumina found that grain sizes < 1 µm result in 3-4 HV1/GPa gain in microhardness compared to ceramics with grain sizes > 2 µm.

Tang et al[84] have reported that for inverse spinel $MgIn_2O_4$ (I=1), irradiation with 5 dpa (displacements per atom, equal to irradiation dose 2 x 10^{17} He/cm^2) 200 keV He ions only resulted in some exchange in cation positions, going from a fully inverse structure to a “random” (I=2/3) structure. In contrast, when irradiating with 4 dpa (equal to irradiation dose 1 x 10^{16} Ne/cm^2) 400 keV Ne ions, the inverse spinel transformed into a disordered rocksalt structure with an amorphous layer covering the surface. The authors chose to work on $MgIn_2O_4$ due to the fact that the X-ray atomic form factor differences between Mg and In allow for more conclusive identification of irradiation-induced phases than in $MgAl_2O_4$.

In this work we use a molecular hydrogen beam irradiation to get the first impressions on the effect of irradiation on the produced ceramics.

2.4 Spark Plasma sintering (SPS)

Spark Plasma Sintering is a sintering technique, where heating happens through Joule effect, allowing rapid heating rate. The combined actions of pressure and temperature then make it possible to perform sintering at much lower temperatures and with much shorter dwell times (of the order of 5 min) than during conventional sintering. This has the consequence of minimizing the effects of grain size growth by diffusion of matter, while allowing to obtain compounds with high relative densities (close to 100%). The SPS is therefore a suitable technique for obtaining ceramics with controlled grain sizes. Previous work on metals[85] and ceramics[38] has shown that it is possible to sinter powders and obtain bulk-type compounds with relative densities in the order of 99% and controlled structuring (grain sizes close to those of the initial particles) and therefore a high density of grain boundaries. In this work, we will focus on performing a parameterized study of the sintering steps (pressure, heating rate, dwell time, dwell temperature) in order to obtain dense massive ceramics with controlled grain sizes. Additionally, we explore the use of LiF and Ta_2O_5 as, respectively, sintering aid and grain growth inhibitor.

2.4.1 Overview of the technique

The application of external electric current to aid sintering was initiated in General Electric Co in 1933 by Taylor, who incorporated the idea of resistance sintering during the hot pressing of cemented carbides and in the case of other hard metals[86]. In addition to continuous current, some researchers also investigated a single discharge method, where the powders were densified by a single discharge generated from a capacitor bank. In all the early methods developed, electrically conductive powders are heated by Joule heating generated by an electric current.

Spark Plasma Sintering (SPS) is a technology developed in Japan by K. Inoue, described in two patents from 1966[87,88]. Since then, SPS has been widely used in Japan at an industrial scale. In 1990 Sumitomo Heavy Industries Ltd. (Japan), developed the first commercially operated plasma activated sintering (PAS) and spark plasma sintering (SPS) machines with punches and dies made from electrically conductive graphite[89]. One of the most important features of these machines was that high density was also achieved in insulating materials. This was the beginning of the spark plasma sintering technique used nowadays. In other countries, the tendency is still to investigate it at a laboratory level, even though some industrial applications are now in the air.

Hence, SPS is a relatively new and fast sintering technique utilizing pulsed direct current (0 – 1000 A) to heat the sample in a graphite die with pressure applied via uniaxial force. The sintering takes place under low atmospheric pressure (10 – 30 Pa) or in inert gas (Ar, N). Direct heating of the graphite die makes it possible to use rapid heating and cooling rates and thus the SPS process enhances densification over grain growth. Subsequently, this technique is widely used for producing nano-grained ceramic materials[90–92].

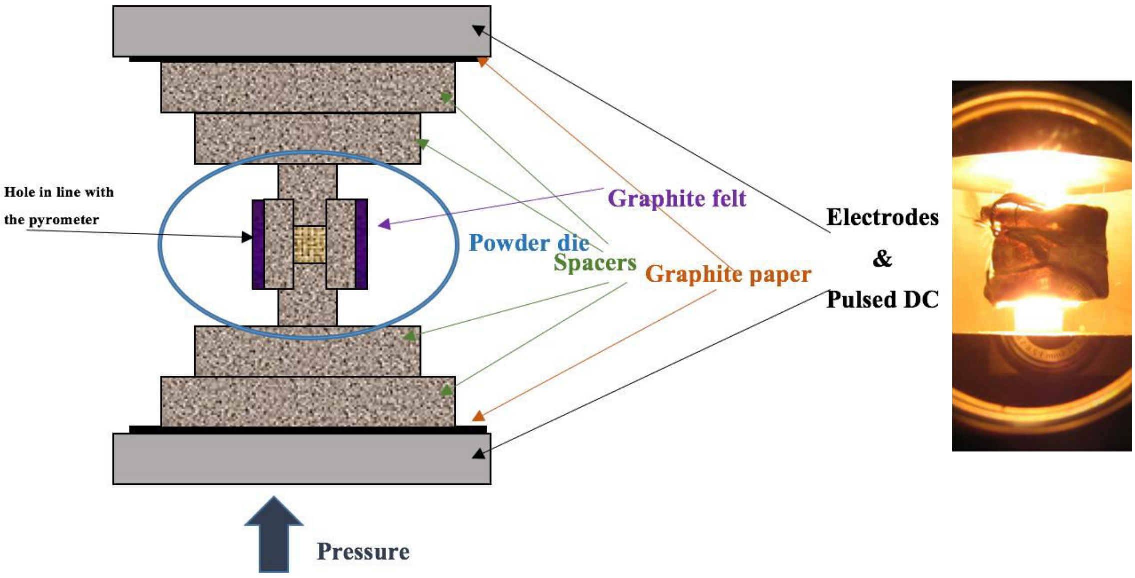

Figure 9. Scheme of sample positioning in the SPS chamber and an optical photo taken during sintering.

Sample placement into the SPS machine is described in Figure 9. Direct current with 3.4 ms on:off pulses (generally 12 pulses on to 2 pulses off) is forced through the setup of spacers and powder die, while applying pressure. The pyrometer can be positioned horizontally 90° from the pressure axis or along the vertical pressure axis, depending on the setup. Graphite paper is used to assure electrical contact between the spacers and electrodes as also between the powder die parts. Graphite felt is used to cover the powder die in case of high temperature sintering (>1000°C) to suppress heat and irradiation escaping the die. In addition to the sample chamber, the SPS systems generally also include programming panels for temperature and pressure, depending on the make and model.

Despite evidences of unusual phenomena occurring during sintering process using pulsed current, most of the knowledge is still empirical. To enhance SPS potentialities as well as efficiency, theoretical investigations are needed.

Depending on whether or not the powder to be sintered is conductive, different heating mechanisms take place[93,94]. Anselmi-Tamburini *et al*[93] have calculated the current distribution for Al_2O_3 and Cu at room temperature, see Figure 10. It can be seen that in case of a conductive material like copper, the current flows through the powder to be sintered and heats it. This is known as Joule heating. Contrarily, in the case of an insulating material like alumina, the current mostly flows through the graphite die, with some disputable percolation and/or breakthrough currents going through the actual powder. Thus, the heating is much more indirect in case of electrically insulating materials and generally no Joule heating through the powder is observed. However, in both cases the biggest current density is noticed on the little plungers of the die. The authors have provided further temperature distribution calculations which conclude that in the beginning (9 s) of the heating cycle, the plungers act as heat sources from top and bottom of the sample, but later (150 s) the temperature distribution in the die becomes uniform.

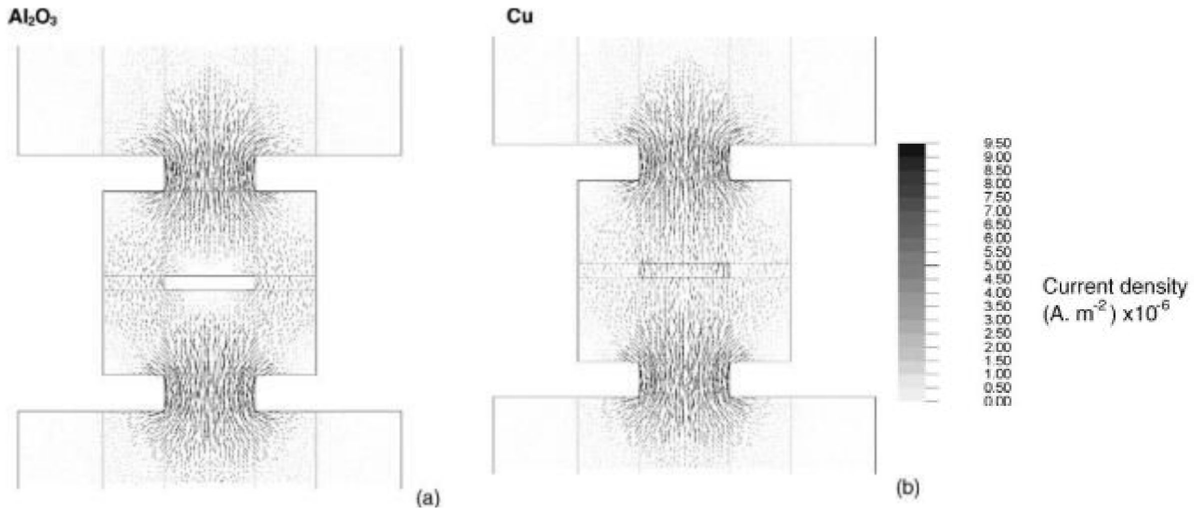

Figure 10. Simulations of SPS current distribution for Al_2O_3 and Cu.

2.4.2 Sintering and grain growth

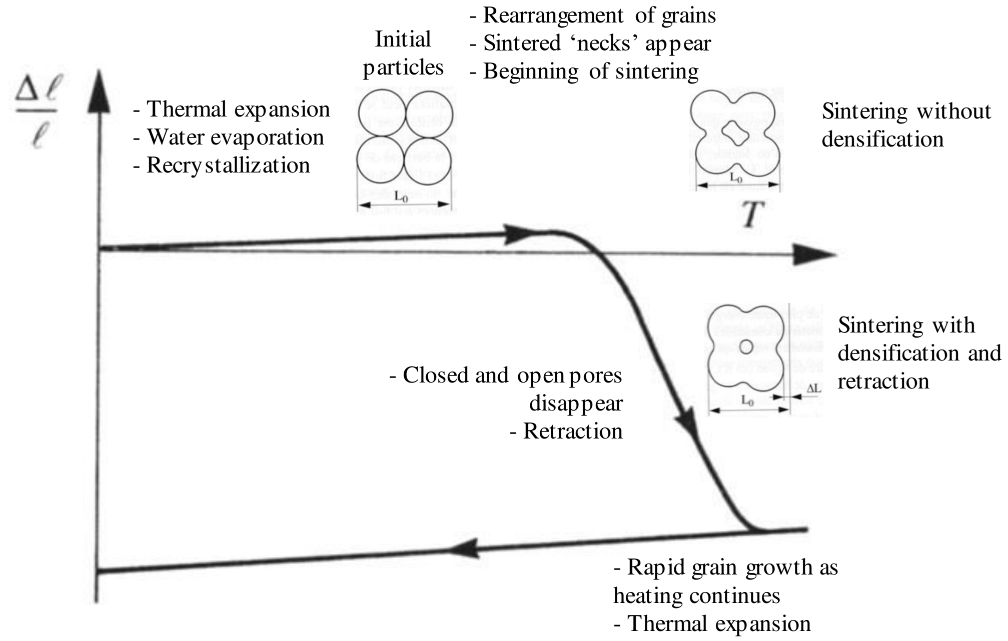

Figure 11. Stages of sintering. [95]

Figure 11 characterizes the different stages of sintering[95]. In the beginning, the particles are freely packed with characteristic dimensions. As the heating starts, thermal expansion, water evaporation and recrystallization take place. Under continuous heating, the initial step of sintering rearranges the grains and sintered connections ('necks') appear at the contact points of particles. The neck formation[96] is driven by the energy gradient arising from the different curvatures of the particles and the neck. The dominant mass-transport mechanism during this phase is surface diffusion. The sintering has begun but no dimensional changes have yet taken place and porosity is equal to the initial value.

During the intermediate stage of sintering, adjacent necks begin to trespass each other, giving rise to densification and grain growth, also closing off interconnected pore channels and thus isolating porosity. The sources of pore channel closure are neck growth and creation of new contact points. In this stage, bulk transport mechanisms (grain boundary diffusion and volume diffusion) control the sintering process[97].

The final stage of sintering begins as most of the pores are closed and is much slower (in case of classical sintering) than the previous stages. Pores break away from the grain boundaries and as the grains grow, pores take a spherical form. Pores are only able to shrink if solids are transported into them and there is an escape route for the gas to reach the surface. Smaller pores are eliminated, but larger pores can grow, this is known as Ostwald ripening[98]. If gas pressure exists in larger pores with no escape route, the pores will grow and the density can lower. Ostwald ripening is accompanied by non-uniformity in grain size[98] or even bimodal grain size distribution[99].

The grain boundary is a 2D defect in the crystal structure and so it is associated with a certain amount of energy. This results in thermodynamic driving force[100] for the total area of boundary to be reduced. In comparison to phase transformations, the energy available to drive grain growth is very low and so it tends to occur at much slower rates and is easily slowed by the presence of second phase particles or solute atoms in the structure.

Crystallite grain growth mostly occurs at high temperature when recrystallization and defect recovery are complete and the only way to reduce the internal energy of the material is via reducing the total area of grain boundaries. Ideal grain growth[101] is a special case of normal grain growth where boundary motion is only driven by the local curvature of the grain boundary, not by grain boundary mobility or energy. In this case additional contributions to the driving force (temperature gradients, elastic strains) are neglected.

When all grains grow at roughly the same rate, it is considered normal (continuous) grain growth. In the opposite case we observe abnormal (discontinuous) grain growth[102]. The latter exhibits a subset of grains growing at an elevated rate at the expense of their neighbors and generally results in a microstructure dominated by a few very large grains.

From observing polished samples under an optical microscope, general grain growth rules have been proposed in metallurgy[101]:

1. Grain growth occurs by the movement of grain boundaries, not by merging through contact.
2. Grain boundary movement is discontinuous; the direction of the motion can change suddenly.
3. One grain may grow into another grain whilst being consumed from the other side.
4. The rate of consumption often increases when the grain is nearly consumed.
5. A curved grain boundary typically migrates towards its center of curvature.
6. When grain boundaries in a single phase meet at angles other than 120°, the grain included by the more acute angle will be consumed so that the angles approach 120°[103].

In the case of SPS, we have also have to take into account the effect of current, electric field and uniaxially applied pressure on the densification and grain growth processes. A very thorough review of grain growth during SPS and flash sintering was recently published by Chaim et al[104]. They discuss that in the case where densification is aided by external pressure and electric current, enhanced diffusion mechanisms take place mainly at the (nano)particle surfaces. Additional electric field effects that may arise during SPS are generation of point defects, dielectric breakdown, plasma and spark formation, local surface softening and/or melting. These effects also drive sintering stages, giving rise to particle coarsening and hierarchical grain growth, which can be exaggerated by the presence of gas or liquid. Even so, if the SPS process parameters are optimized, fully dense nanocrystalline ceramics can be obtained.

One key to avoiding excessive grain growth during SPS lies in green body preparation, like discussed by Ghanizadeh *et al*[83]. The authors found that while directly sintering as-received 50 nm alumina powder resulted in large grain sizes (~6.25 µm), powders molded into green bodies via slip-casting, thus having higher density and no air bubbles, could be SPSed to full density with an average grain size of 0.32 µm after 20 min at 1200°C. Even so, the grains still showed somewhat bimodal size distribution, with grains smaller than 100 nm and larger than 400 nm visible in the presented SEM micrographs.

Additionally, certain compounds introduced in small quantities as a secondary phase inside the material being sintered can either act as aids to grain growth or as inhibitors. The most popular sintering aid in use for ceramics is LiF, which can also have a positive role in lessening carbon contamination during sintering (see chapter 2.4.4) and Ta_2O_5 can be used as a grain growth inhibitor.

LiF is a very popular sintering aid for sintering spinel by hot pressing[105]. It is believed that LiF, having a much lower melting temperature than spinel (~850°C[106]), will liquefy in the beginning of the sintering process, lubricating the particles and aiding in creating more contact points for sintering. However, the LiF must be removed from the material before final consolidation or it will result in white precipitates[105].

It is interesting to note that in the classical hot press spinel sintering scheme, two different dwell temperatures exist, first dwell at 950°C is supposed to help homogenize the distribution of LiF and the second hold at 1200°C is meant to help LiF escape the material. Experimental results have proved that LiF will be completely eliminated at 1400°C[105]. The authors further hypothesized that liquid (but not yet vaporized) LiF preferentially reacts with Al_2O_3, forming

$LiAlO_2$ and leaving more refractive opaque white MgO-rich areas behind. White spot formation due to LiF addition was not a problem in the case of hot pressing alumina-rich ($MgO \cdot 1.5 Al_2O_3$) spinel at 1600°C, when the LiF concentration was kept to 0.25 wt%[107].

The biggest drawback of using LiF as a sintering aid is significant grain growth[108]. An investigation of LiF doping of spinel for SPS have found that while the grain size of the final ceramic yielded from LiF-doped powder is ten times bigger, the transparency is also higher[99].

Ta_2O_5 has long been known to block the grain growth of materials, as an early example, Suchomel *et al*[109] investigated Ta_2O_5 doping in Eu_2O_3 in 1975. They fired the pure and Ta_2O_5 doped (3 at%) Eu_2O_3 at 1900°C in vacuum for 1h, decreasing the grain size from 440 μm to 10 μm. They found that Ta inhibits the grain growth by solute segregation at grain boundaries and that dopant concentrations as low as 0.75 at % hinder grain growth, showing a very small amount of secondary phase formation. A study from 1988[110] compared MgO and Ta_2O_5 as grain growth inhibitors in ultrapure alumina. The authors confirm that both dopants improve the sintering of alumina ceramics but through different mechanisms. While Ta_2O_5 acts by a solid solution mechanism, MgO acts mainly by concentrating on grain boundaries and retarding the grain growth. They found that the optimal Ta_2O_5 concentration is about 0.75 wt% and to obtain fully dense nanoceramics, Ta_2O_5-MgO co-doping is the most effective.

2.4.3 SPS of transparent ceramics

As published by Krell *et al*[60], optically transparent compact ceramics fight against some inherent physical issues. First of these issues arises from point defects in the crystal lattice, be it impurities or oxygen vacancies. These point defects are known to absorb light in various portions of the spectrum. The authors also discuss the difference of in-line and diffuse transmission[111] brought out by scattering. Scattering can be due to slight differences in the refractive index (*n*) throughout the material or arise from non-cubic (and so non-isotropic) crystal structure. The best way to keep this birefringence to a minimum is to minimize the grain size. In addition, all ceramics are optically inhomogeneous because of the inevitable resistant porosity. In addition to the fraction of resistant porosity, pore size also plays key role in transparency in the visible range. Depending on the wavelength of incident light, the size of the remaining pores should be smaller than λ/n~300 nm for maximal transparency in the visible range. Evidently, all different types of extinction losses increase with thickness, so the more inhomogeneous is the material, the thinner it needs to be to retain transparency. Here it is important to define transparency and translucency. A material is transparent when it exhibits high in-line transmission and translucent, if the transparency depends on the distance from the viewed object[111].

Despite these inherent challenges, SPS of alumina and other transparent ceramics is a popular research topic from the 1990s[112], as it is an effective and inexpensive process for obtaining high-density alumina with a controlled microstructure. The benefit of SPS is the relatively short processing time, since the heating is done via direct current under high pressure. This process has shown great success in yielding high-transparency ceramics, including those based on birefringent materials like alumina.

2.4.3.1 SPS of alumina

Using the SPS and HIP processes to sinter Al_2O_3 has allowed researchers to lower the standard 1700°C[31] sintering temperature of alumina in hydrogen to 1200 – 1300°C, while obtaining densities $\geq$ 99,95% and grain sizes smaller than a micron[113].

To start with a contrasting example, transparent Al_2O_3 has been sintered at 1150 or 1300 °C under a pressure of 80 or 90 MPa, with a heating rate of 8 or 170 °C/min and a dwell time 20 min or 5 min[114,115], using a very similar precursor powder (high-purity Al_2O_3 TM-DAR powder from Taimei Chemical Co., with particle size of 150 or 200 nm used for the two sintering conditions described, respectively). On the other hand, Morita *et al*[116] have shown that a heating rate above 50 °C/min is detrimental to the transparency of the material, at least for spinel structures. The influence of different sintering cycles on a chosen powder precursor has been investigated frequently, while less attention has been given to detailed analyses of differences between the products of different precursor powders exposed to an identical sintering process.

The sintering of transition aluminas rather than α-Al_2O_3 has not been thoroughly examined due to their thermal instability and the inevitable volume change involved in reaching the thermodynamically stable α-Al_2O_3 phase. However, it has been shown that both boehmite and γ-Al_2O_3 have strong sintering capacities[117], specifically when using explosive pressing to form the green bodies. γ-Al_2O_3 has been sintered[118] to full density α-Al_2O_3 with an average grain size of 300 nm at 1400°C without holding time with an applied pressure of 100 MPa, when using attrition milling to reduce agglomeration in the starting powder. Pure dense α-Al_2O_3 has been fabricated by the cold isostatic pressing and sintering of mixtures of seeded boehmite and fine α-Al_2O_3 (~70%)[119]. Samples with 0.2 μm and 0.3 μm alumina achieved densities greater than 95% when sintered at 1300 °C and 1400 °C, respectively, proving that boehmite can be used as a substitute for the relatively expensive ultrafine α-alumina powders. Seeding γ-Al_2O_3 powder with α-Al_2O_3 before sintering has been shown to decrease the optimal sintering temperature by 200-300 °C[120]. In our team's previous research, sintering locally synthesized γ-alumina at 1550 °C for 20 min at 80 MPa resulted in a translucent and dense α-Al_2O_3[121].

Prakasam *et al*[122] carried out an extensive study to determine the best sintering conditions for obtaining transparent alumina ceramics with a small grain size from a commercial α-Al_2O_3 powder with 100 – 150 nm particle size. They varied the sintering temperature from 1150°C to 1400°C and the dwell time from 3 min to 120 min. Different variations in pressure application and heating/cooling rate were tested. Relative densities of all received ceramics were >97%, the highest density (99.8%) with the smallest grain size (0.1 μm) was acquired at 1150°C during a 120-minute dwell at 100 MPa. Interestingly, the sample obtained during half the previous dwell time (60 min) had four times bigger average grain size (0.4 μm), while the density was only very slightly lower (99.7%). Both samples yielded transmission of 63% at 640 nm.

To suppress the grain growth of alumina, different impurity inclusions have been tested. Maybe one of the most interesting examples is classical sintering research done by Bodišová *et al*[123], where they doped alumina (TM-DAR, 150 nm) with magnesia, zirconia and yttria, additionally investigating the effect of a two-step sintering process. The two-step sintering process consisted of heating up to (dwell time zero) a higher temperature (1400°C or 1475°C), followed by a long dwell (8h or 24h) at a lower temperature (1150 – 1300°C). All sintered samples had final relative density > 99% and grain sizes between 0.49 μm and 1.43 μm. Complete grain growth elimination was accomplished by two-step sintering and simultaneous doping with 500 ppm MgO (density 99.7%, grain size 0.5 μm). See more detailed discussion of grain growth during sintering in Chapter 2.4.2.

While far from being the most popular choice of sintering for transparent ceramics on an industrial level, SPS of nanosized α-alumina powders is quite well-researched. Due to differences in set-ups (die sizes, temperature measurement technique, choice of conductive layer between the powder and the die, etc.) it is difficult to make any definitive conclusions, leaving first-hand local experience to have the greatest value. There is room for developments in investigations of sintering precursor powders of different phases via identical cycles to understand the effect of phase and morphology. The possibility of utilizing less expensive low-temperature polymorphs of alumina to obtain translucent ceramics with controlled microstructure is of great industrial interest.

2.4.3.2 SPS of spinel

Research on the SPS process of spinel has been popular since the patenting of general principles of producing transparent ceramics by Shen *et al*[124] in 2006. Three years later Wang and Zhao[125] suggested a two-step pressure profile to obtain 51% transparency at 550 nm in spinel produced without any sintering aids at 1300°C with a dwell time as short as 3 min and grain size up to 700 nm. The two-step pressure application consisted of a preloaded pressure P_1 that was raised during one minute to 100 MPa upon reaching 1250°C and kept constant until the end. They have found that even 20 MPa preloaded pressure resulted in the discoloration of the sample center, thus suggesting the use of as low P_1 as possible. However, the authors do not discuss the chosen pressure application rate or why it was kept constant throughout cooling. When applying high pressure from the beginning of the sintering cycle, one "shaves" some carbon contamination from the graphite die/paper into the powder, which will then be sintered along with the powder. On the other hand, using minimal pressure in the beginning of the cycle and a milder pressure application rate helps to minimize this effect. For further information on carbon contamination during SPS, see chapter 2.4.4.

Morita *et al*[116] obtained similar results, achieving 47% transparency and keeping the grain size down to 450 nm. Krell *et al*[126] have shown that grain sizes as small as 270 nm are achievable for transparent spinels, starting from 55 nm powder and hot isostatic pressing (HIP) at temperatures lower than 1300°C. Contrastingly, optical homogeneity without any sintering aids was only received in the case of 120 nm powder.

As in the case of alumina, very different sintering approaches have given similar good results on increasing the transparency and lowering the grain size of resultant ceramics. Commonly, "SPSed" spinel bodies sintered for maximal transparency have grain sizes > 10 µm[116,127], especially when using sintering aids such as LiF. Frage *et al*[127] have shown that when sintering pure spinel with average particle size of 0.78 µm, the densification starts at 950°C and continues until pressure application at 1220°C, after which further temperature increase does not result in additional densification.

Both, low (10°C/min)[116,127] and high heating rates (≥ 100°C/min)[116,125] have successfully been used, with high heating rates being slightly more popular, taking full advantage of the possibilities of SPS processing[128]. Morita *et al*[129] have shown that temperatures higher than 1300°C become detrimental for transparency due to precipitation of second phases and coalescence of residual pores raised by rapid grain growth. They successfully sintered a fully dense transparent spinel at 1300°C with a 20-minute dwell.

In general, it is found that the resultant ceramic grain size is inversely proportional to the heating rate, i.e. the higher the heating rate, the smaller the resulting grain size[128]. Extreme pressure (4 GPa) has been used to lower the sintering temperature of transparent spinel to 600°C, keeping the grain size as low as 40 nm[130]. A drawback of using such extreme pressures is the possible unsuitability for industrial production[125].

In conclusion, when choosing SPS parameters for spinel, in addition to heating rate, dwell temperature, dwell duration and applied pressure; pressure application rate should also be taken into account due to possible discoloration effects. Due to intrinsic high concentration of oxygen vacancies in the spinel lattice and standardly used vacuum environment, it is not uncommon to obtain a completely black sample, that can be easily re-oxygenated by a simple annealing in air.

2.4.4 Carbon contamination

One of the drawbacks of SPS is an unavoidable contamination of the final product by carbon when the whole die system holding the powder to be sintered is made of graphite. However, the exact degree and cause for this contamination remains a topic open for discussion. Definite contamination takes place at the sample surface, which is in direct contact with graphite paper, nevertheless, this contamination is eliminated during the grinding and polishing of resultant pellets. Additional carbon contamination can arise from steps taken before sintering, for example residual organics present in the powder or drying/calcining the powder in CO-rich atmosphere.

A work published in January 2018[131] investigated the effect of carbon contamination in sintering alumina ceramics' sinterability and carbon diffusion in purposefully contaminated samples. When testing different sintering atmospheres (low vacuum, nitrogen, argon), the authors concluded that the biggest drawback arises in nitrogen atmosphere as formation of aluminum nitride takes place. Sintering in vacuum environment wasn't ideal either as it increases carbon diffusivity and leads to discoloration in the whole volume of the sample. Additionally, samples sintered in vacuum or nitrogen environment were covered by a porous surface layer. However, the thickness of the affected layer was only 15 µm and showed no additional phase upon XRD analysis, making it unimportant after grinding and polishing. Finally, densification suppression was observed in only some spots when alumina was sintered in argon atmosphere, where the diffusion of carbon was the slowest, making it the most beneficial sintering atmosphere.

Carbon contamination in spinel has been thoroughly investigated via Raman, EPR- and IR-spectroscopy[132–134]. They found that a small amount of excess impurity carbon compounds can be detrimental for contamination, namely the trace CO_3 in the starting powder was transformed into glassy carbon during sintering at any chosen temperature when using heating rates ≤ 10°C/min[133]. In the case of heating rates ≥ 50°C/min, a supplementary contamination arose from the evaporation and diffusion of carbon from carbon papers and graphite dies surrounding the sintered powder into the open pore channels of the sintered powder. This encapsulated carbon then gets stuck in the pores and sinters to glassy carbon along grain boundaries[134]. As the deformation rate of the powder increased with the higher heating rate, the creation of color centers formed by dislocation also increased. This effect can be lessened by using lower sintering temperature in the case of higher heating rates to bleach oxygen vacancies[133]. The authors also found that for slow heating rates the carbon contamination only takes place in 300 µm thick surface layer, therefore being much less problematic. In the case of heating rate as high as 100°C/min, the highest concentration of carbon contamination is still observed in surface layers, however, the contamination spreads throughout the whole volume of the sample with 3 mm thickness. The formed carbon phases can be, at least in some cases, annealed thermally in air, but they will transform into high-pressure CO and CO_2 gas[132] and leave behind porous channels along grain boundaries. This shows that removing the carbon contamination from the whole volume of the sample is difficult.

A solution to eliminate carbon contamination totally lies in exchanging the graphite paper insulation by a transition metal (Mo[135] or Pt[136]) foil. The results of using Mo foil have been impressive, leading to almost 40% gain in transparency at 300 nm[135]. Interestingly, using Mo foil instead of graphite paper also increased the final ceramic's grain size from 16 µm to 260 µm, showing that sintering parameters should be adjusted if obtaining small-grained materials is of interest. The drawback is the high cost of these materials and the complexity of removing the thin foils without breaking after sintering.

Another solution lies in using LiF as a sintering additive (0,5 - 2 wt%). LiF has been investigated in multiple transparent ceramics, here we bring yttria[137], yttrium aluminum garnet (YAG)[138] and spinel[139] as examples. LiF is most commonly used as a sintering aid during traditional hot pressing[105] to increase the sinterability of the material. The drawback of using LiF as a tool to clean carbon contamination is significant grain growth[140]. It is believed that LiF, having a much lower melting temperature (~850°C[106]) than traditional transparent ceramics, acts as a lubricant and allows better particle packing. It is also proposed that LiF etches and removes impurities from the surface of particles to be sintered, thus improving diffusion. LiF is an important additive from the standpoint of carbon contamination as some researchers suggest that LiF reacts with the carbon from the sintering environment[141,142], forming volatile $(CF)_n$ gases and acting as a cleanser, leaving behind residual Li. This residual Li can be problematic and form secondary phases with the main material, as was the case for YAG, where Li_2SO_4, YF_3 and Y_2S_3 as well as H_2O didn't evaporate completely and thus got trapped inside the material[138]. A study on LiF-doped spinel powder has shown the effectiveness of carbon contamination cleansing through the formation of gaseous C-F phases[139]. The excess Li increased the amount of oxygen vacancies present in the lattice, improving the mass transport but coarsening the grains and therefore lessening the mechanical properties.

In conclusion, while the porous surface layer and mild carbon diffusion in vacuum poses no great problem to samples to be polished later, it would be more beneficial to use argon atmosphere to avoid the contamination completely. In alignment with our strides of sintering materials with intrinsic defects, it would be interesting to see the difference in the luminescence of samples sintered in vacuum and argon, especially in the case of spinel. While carbon contamination is a slight drawback of using graphite dies, they are also essential for our goal of stoichiometric defects, as carbon acts as a reducer and thus leads to the creation of oxygen vacancies.

2.4.5 Routes to transparent fine-grained alumina from TM-DAR

Although it is generally accepted that starting powder morphology plays a huge role in the sintered ceramics properties, there are no thorough investigations published on this topic. The most popular alumina powder used in publications from all over the world is TM-DAR-powder produced by Taimei Chemicals Co. Ltd., Tokyo, Japan. The powder family has an average particle size of 100 – 200 nm measured by SEM[143]. Countless authors use this powder as a starting material for sintering fine-grained dense ceramics and investigating doping effects [114,144–154]. Thus, it is a good reference material to bring to light different routes to obtain transparent fine-grained alumina. Best results of 9 selected studies have been summarized in Table 1.

A quick observation at the optimized parameters by different authors confirms that there are multiple ways to sinter alumina to transparency (or at least high density). Chosen sintering temperatures vary from 800 – 1300°C, pressures from 80 MPa to 7.7 GPa while the resulting grain sizes are between 0.15 and 0.8 μm and transparencies vary from 20% to 73%. Furthermore, it is clear that both, high and low heating rates can effectively be used to obtain dense ceramics.

One of the most interesting conclusions was made by Krell et al[79], they found that it's easier to obtain the closest ratio of powder particle size to sintered particle size when starting from particles sized 100 – 200 nm rather than finer nanoparticles.

Table 1. Various results obtained from sintering TM-DAR powder.

Starting powder and particle size	Sintering temperature Heating rate and dwell time	Sintered ceramic grain size (μm)	Sintering pressure (MPa)	Sintered ceramic porosity (%)	Sintered ceramic transparency	Notes/comments	Article reference
TM-DAR 140 nm	1200°C 5 min/1100°C 60 min	0.5/0.5	100	1.5/0.2			[150] A5/A6
TM-DAR 150 – 200 nm	1300°C N/A 2h	0.41	HIP?	<0.05		Fluidized bed granulation, pressureless sintering + HIP	[79] Fig. 4.
TM-DAR 150 nm	1150°C 20 min 25°C/min to 1000°C; 8°C/min to 1150°C	0.27	80	0.03	47% at 640 nm sphere	Post-annealing in SPS at 1000°C for 10 min Thermally etched at 1050°C for 1 h	[114]
TM-DAR 150 nm	1250°C 2°C/min 20 min	0.8	80	0.03	72% at 650 nm sphere	Post-annealing in SPS at 1000°C for 10 min	[146]
TM-DAR 200 nm	1150°C 100°C/min 60 min	0.47	80 at dwell	0.14	20% at 645 nm in-line		[153]

TM-DAR 100 nm	800°C N/A 30 min	0.15	7700	0	71% at 640 nm in-line	Belt, vacuum furnace Sample preparation process carried out at < 1 ppm humidity	[149]
TM-DAR 102 nm	SPS at 1200°C 100°C/min 10 min HIP at 1230°C, 3h	0.24	SPS 80, HIP 198	0	73% at 633 nm	SPS + removing carbon 10h@800°C+ HIP Doped with 0.3 wt% zirconia and spinel	[155]
TM-DAR 200 nm	1000°C 10°C/min 10 min	0.2	500	<0.05	64% at 645 nm	Special WC-graphite sintering die, sample Ø 5 mm	[143]
Super TM-DAR 130 nm	1000°C 10°C/min 20 min	0.15-0.25	400	0	64% at 645 nm	Special CFC-graphite sintering die, sample Ø 10 mm, annealed at 900°C, 30 min	[156]

2.4.6 Pre- and post-sintering treatments

Occasionally, to reap the benefits of multiple sintering processes, pre- or post-sintering treatments are used. Here we will shortly discuss some more popular sintering routes used in combination with SPS.

Sometimes pre-pressed green bodies are briefly sintered via classical pressureless sintering to make sure they are not as fragile to fall apart[79] before being introduced to the SPS die or other sintering setup. This type of pre-sintering is of course carried out at a temperature low enough to not cause any grain growth.

The most used post-SPS thermal treatment for further densification is hot isostatic pressing (HIP). Whereas during SPS the sample is consolidated in one direction under low atmospheric pressure, HIP takes place in a heated homogenous high-pressure environment (usually argon at around 200 MPa[157]), aiding in the final stage of sintering and pore closure. While SPS provides direct and rapid heating, heating during HIP is usually slower (200 – 400 °C/h) and the dwell time is longer (1 – 3h being common[157,158]). It has been suggested that HIP post-treatment is suitable for materials with small grains as intergrain pores can be eliminated, but not intragrain pores common to materials gone through Ostwald ripening[159].

Additionally, annealing in air at a temperature at least 100°C lower[160] than the original sintering temperature is popular to remove any residual stresses and lattice defects (mostly oxygen vacancies[35,161]) discoloring the sample. However, this treatment normally does not remove excess carbon in the volume of the sample due to the formation of CO/CO_2 bubbles[134].

2.5 Physical properties of alumina and spinel

In this chapter, the optical and luminescence properties of alumina and spinel are presented along with some thermochemical and physical characteristics.

2.5.1 Scattering, transparency and translucency

Firstly, it is important to define the difference between a transparent and a translucent material, polycrystalline birefringent alumina is used as an example. The difference between the two as well as the path of light through a polycrystalline material are shown in Figure 12[111]. In the case of translucent alumina (Figure 12 A and A'), the diffuse transmission of light is high but the in-line transmission is low. These types of ceramics mostly have big grain sizes (20 µm in the case of A), scattering light at grain boundaries and pores (Figure 12 C), thus changing its direction inside the material. Polycrystalline alumina with smaller grain size (0.5 µm in the case of B) can be considered transparent, as most of the light travels through them without changing its path (Figure 12 B'). The proposed[162] reason for this seemingly illogical effect of larger-grained materials being less transparent lies in the fact that even the densest large-grained samples contain so many pores that every light beam hits at least one pore. In the case of small-grained materials, the pores are also smaller, so much so that many light beams

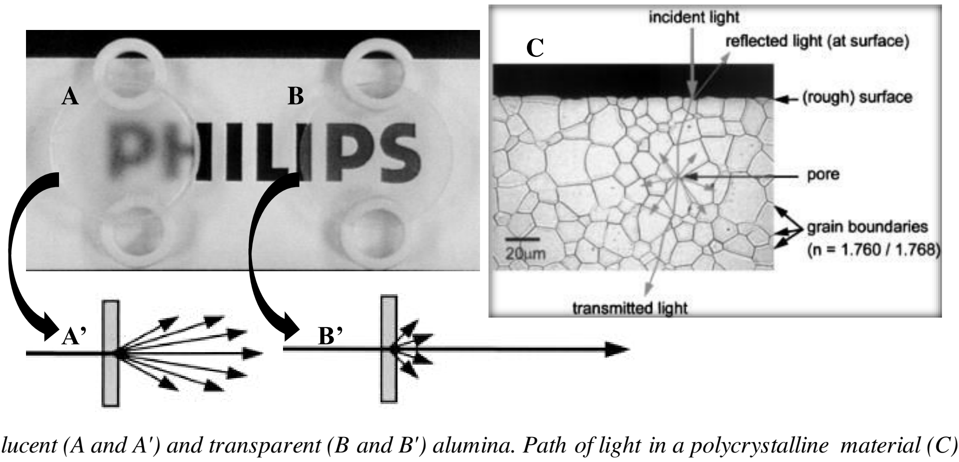

Figure 12. Translucent (A and A') and transparent (B and B') alumina. Path of light in a polycrystalline material (C). [111]

are able to pass through the material without hitting any pores. However, calculations[111] based on Mie theory have shown that even porosities as small as 0.1% are enough to deteriorate the transparency.

Alumina and spinel can both be manufactured to be transparent in the range of 0.2 – 6.5 µm[40,163]. The maximal theoretical transmittance values are those of the single crystals, about 85% for both, spinel[164] and alumina (sapphire)[165], see Figure 13.

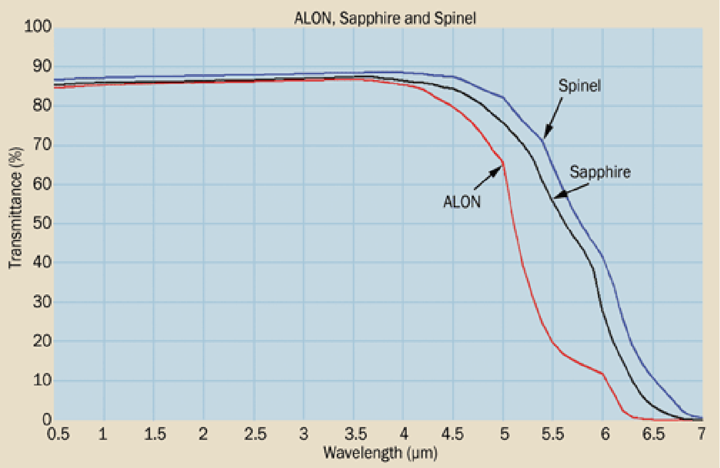

Figure 13. Transmittance of 2 mm thick sapphire, spinel and ALON. [165]

2.5.2 UV-Vis-NIR absorption and luminescence

Even though optical absorption measurements (see examples in Figure 14) are not particularly interesting in the case of alumina, irradiation effects on it have been researched[166,167]. It has been confirmed[168] that the F centers have an optical absorption

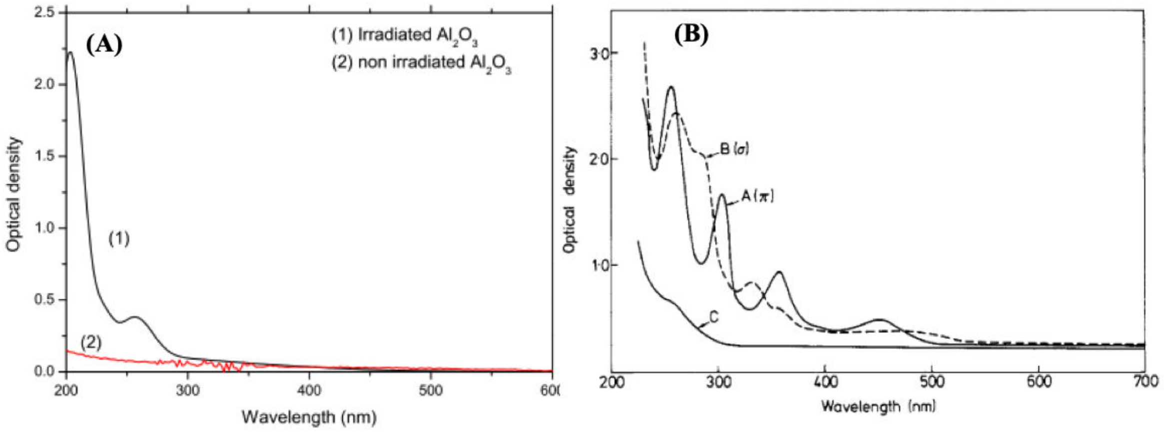

Figure 14. (A) Optical absorption spectra of alumina before and after irradiation with fast neurons to a dose of 4.4 x 10^{16} *cm*$^{-2}$ [166]*; (B) proton irradiated* [10$\bar{1}$0] *α-*Al_2O_3 *to a dose of 3 x* 10^{18} *cm*$^{-2}$ *absorption spectrums for curve A: E* ∥ [0001]*, curve B: E* ⊥ [0001]*, curve C: virgin crystal*[167].

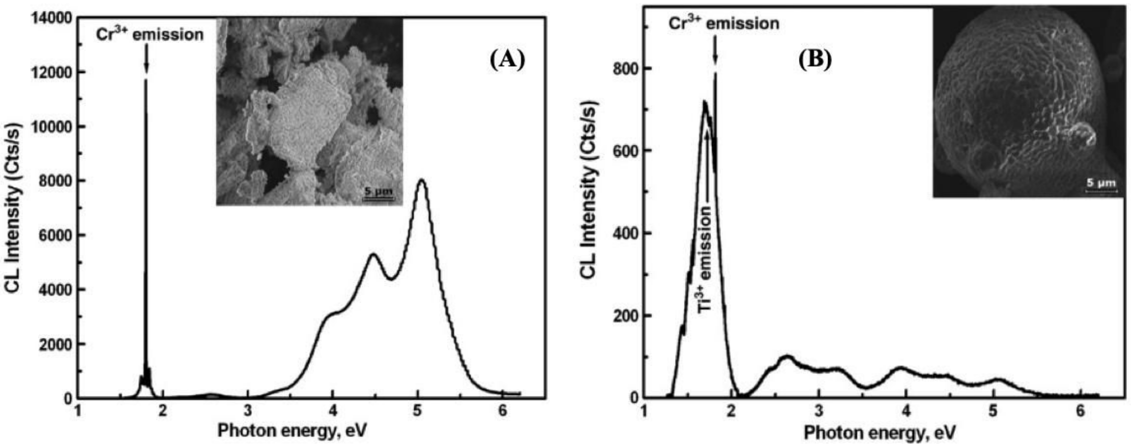

Figure 15. Cathodoluminescence spectra of corundum obtained from (A) gibbsite and (B) boehmite. [170]

band at 6.0 eV (≈ 207 nm, and luminescence band at 3.0 eV≈413 nm), at the same time, F$^+$ are linked to several symmetry-split absorption bands between 6 and 4 eV (6.3 eV≈197 nm, 5.4 eV≈230 nm, 4.8 eV≈258 nm, 4.1 eV≈302 nm; and luminescence band at 3.8 eV≈326 nm)[168]. F$^+$ and F centers, also called color centers, are anionic (in our materials oxygen) vacancies in the crystal lattice with respectively one or two trapped electrons[169], which composite absorption (V^{2-}, V^-, V_{OH}^-) can be observed at 3.0 eV (≈413 nm).

Studies[168] have found that in the case of $MgAl_2O_4$ exposed to high temperatures in strongly reducing atmospheres, an additional defect, an electron trapped at an antisite Mg ($F_{Mg} = Mg_{Al}^{2+} + e^-$), is formed. These centers form because it is energetically favorable[168] for an anion vacancy to be located near a cation with a lower charge and bigger ionic size. The absorption properties for this complex center are similar to that of F+ center, with lower symmetry and optical transitions shifted to higher energies.

Luminescence of Al_2O_3 has been studied to compare the effect of sintering boehmite versus gibbsite[170], see Figure 15. The authors found that the main luminescence bands are located at ~5.03 eV(interband transitions), ~4.42 eV(related to excitation density), ~3.91 eV (F+-center) and ~2.42 eV (interstitial Al_i^+), the main difference between the boehmite- and gibbsite-received ceramics being the intensities of interstitial and F center bands.

Lushchik *et al*[171] have previously investigated the cathodoluminescence (CL) of complex oxides, their results on α–Al_2O_3 and $MgAl_2O_4$ are presented in Figure 16 (A). They observed an intense emission at 5.8 eV which is either connected to self-trapped excitons or electron-hole recombination at intrinsic defects of spinel.

Radioluminescence (RL) of single crystals (Sc-Ver, Sc-Czo) and translucent/transparent polycrystalline (Cer-Trl, Cer-Trp) spinel was studied by Gritsyna et al[172] to explain radiation-induced electronic processes, see Figure 16 (B). They concluded that recombination of free electrons with holes captured at antisite defects results in RL at about 4.8 eV and the weak emission at 3.7 eV could be related to F^+ centers in spinel or in microphases of Al_2O_3.

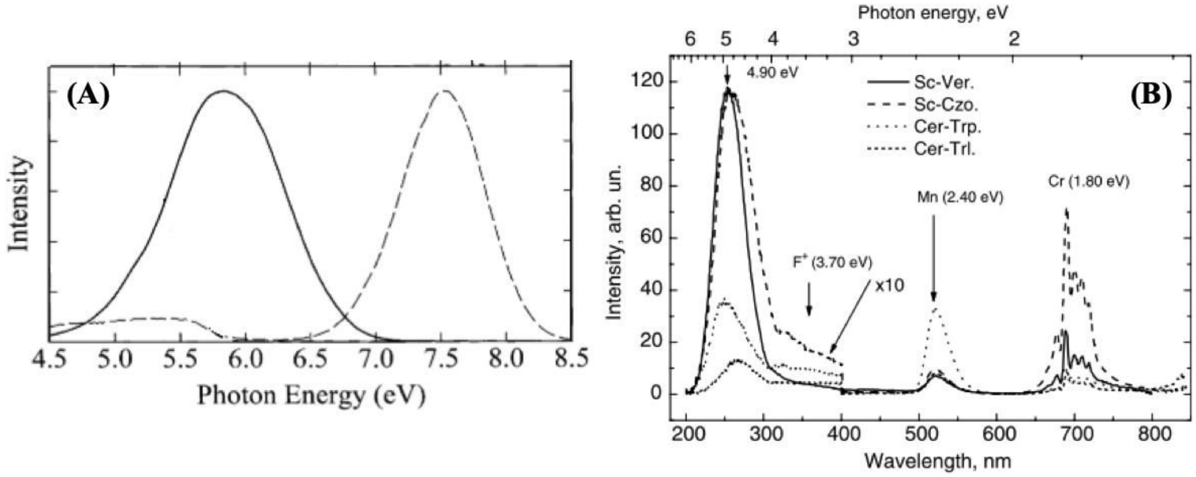

Figure 16. (A) cathodoluminescence of Al_2O_3*(dashed line) and* $MgAl_2O_4$*(full line) at 9K*[171]*; (B) radioluminescence of* $MgAl_2O_4$*.*

A study of time- and energy-resolved photoluminescence properties of γ, θ and α ultraporous alumina at has been carried out at cryogenic temperatures[173]. The photoluminescence of self-trapped excitons associated with singlet free exciton excitation were observed in α, θ, and γ polymorphs. A red shift of the fundamental absorption onset from 9.36 eV (α) to 7.60 eV (θ) and 6.85 eV (γ) was observed. These results are in agreement with a theoretical study[174], which predicted band gap narrowing in the order of α>θ>γ, and a decrease of the density of structural defects on order γ>θ>α.

2.5.3 Physical and chemical characteristics

Property	Alumina	Spinel
Density (g/cm^3)	3.987 [148]	3.58 [40]
Melting point (°C)	2044 [175]	2135 [40]
Enthalpy of formation (kJ/mol)	- 1680 [176]	- 2300 [177]
Dielectric constant	9.8 [178]	8.2 [40]
Resistivity (Ω cm)	>10^{14} [178]	>10^{14} [40]
Thermal conductivity (W/mK)	35 [178]	24.7 at RT[40]
Hardness (kg/mm^2)	1500 [179]	1400 [179]
Fracture toughness (MPa$\sqrt{m}$)	4 [178]	1.5 [40]
Elastic modulus (GPa)	375 [178]	273 [40]
Refractive index at 490 nm	1.775 [180]	1.736 [40]
Refractive index at 660 nm	1.765 [180]	1.724 [40]
Refractive index at 2 μm	1.737 [180]	1.702 [40]

2.6 Goals of the present study

The goals of this study can be divided into three steps for both chosen materials: 1) obtaining fully dense ceramics, 2) obtaining transparent ceramics, 3) diminishing the grain size of transparent ceramics. Additionally, focus will be put on correlating precursor powder morphology and phase to the final properties of sintered ceramics.

Firstly, we will sinter six different alumina powders of various phases and morphologies to see their effect on the final density and microstructure after sintering via identical cycles. To surely obtain transparency, a temperature slightly higher than commonly reported SPS dwell temperatures, 1450°C, is chosen based on previous experience of sintering γ-Al_2O_3. To improve the sinterability of low-temperature alumina polymorphs and obtain denser ceramics, LiF as a sintering aid will be tested. To minimize the grain size, sintering at pressures as high as 285 MPa will be tested. Texturation analysis is carried out to see if this pressure is sufficient to create any preferred orientation in the sintered material.

In the case of reactive sintering of spinel, we will compare the impregnation and polyol method for obtaining MgO to see which gives us consolidated ceramics with awaited properties. To inhibit the grain growth of spinel, doping the precursor powders with 0.5 and 1 wt% of Ta_2O_5 will be carried out. A commercial big-particle spinel powder will be used as a sintering reference.

To obtain information on the structural defects present in sintered ceramics, luminescence analysis will be carried out on selected samples. Proton irradiation with a dose of 10^{17} p/cm^2 along with luminescence analysis will be used as a model to estimate the effect of irradiation.

Finally, the benefits and drawbacks of used sintering conditions will be analyzed and we should know which sintering conditions should be applied to which precursor powders so that the resulting material is transparent and fine-grained.

3 Experimental techniques

In this chapter, a brief overview of synthesis and characterization techniques will be given.

3.1 Alumina monolith growth in climate chamber

The growth of alumina monoliths in this work was carried out according to the patent[11] and article[52] published in CEA-CNRS and LSPM-CNRS. However, there is a new, more stable climate chamber (Weiss GmbH environmental engineering simulation systems, WK3-180) in use for the process.

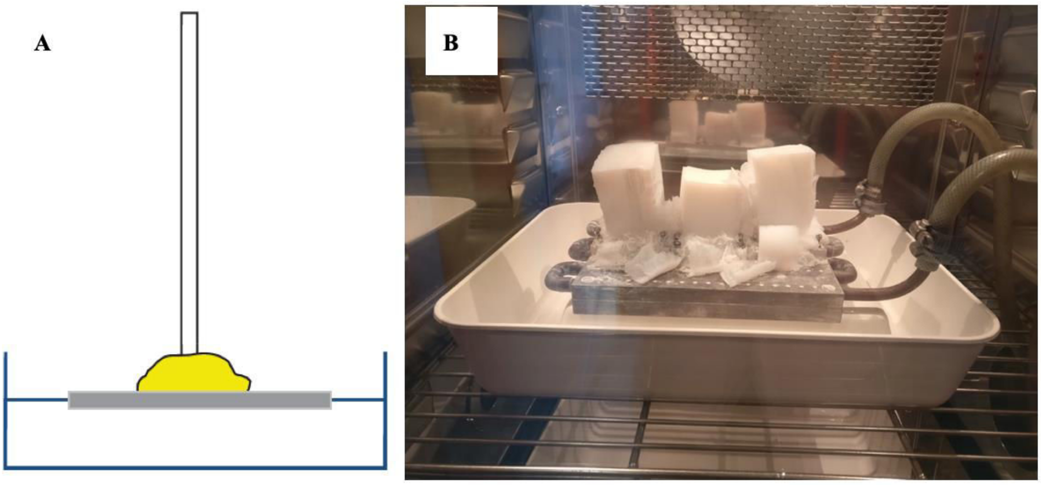

Figure 17. A: Glass stick-adhesive putty-aluminum plate setup; B: Alumina monolith growth in progress in the climate chamber.

Firstly, the climate chamber is set up, verifying sufficient deionized water level and environmental parameters (T=25°C, P_{H2O}=80%). The chamber is then turned on as it takes 10 – 15 minutes to reach desired conditions. At the same time, the cryostat and water flow for the cooling system at 23°C is turned on. The cooling radiator is kept 2°C lower than the set chamber temperature to further aid the cooling of aluminum plates oxidizing via an exothermic reaction.

In the meantime, the preparation of the aluminum plates for oxidation takes place in a fume hood. Firstly, 1 mm thick 99.999% purity laminated aluminum plates (5 x 5 cm, Goodfellow) are cleaned with acetone to remove any organic contamination from the surface. As the oxidation reaction of aluminum is exothermic, it is important to treat only a single side, in order to effectively remove heat by the other. For this reason, the aluminum plate is fixed to a glass tube by adhesive putty Patafix® (see Figure 17 A), helping to positon the aluminum plate exactly parallel to the level of treatment solution. The adhesive exhibits good adhesion with the aluminum and glass, and can be easily peeled off without leaving adhesive on the plate.

The surface to be treated is firstly taken into contact with 10% sodium hydroxide solution for two minutes to dissolve the passive alumina layer that protects the metal (depassivation). Gas bubbles are observed on the plate; this corresponds to the release of hydrogen gas formed by the oxidation reaction of aluminum metal by the hydroxide ions.

$$Al_2O_{3\,(s)} + 2\,HO^- \rightarrow 2\,AlO_2^- + H_2O \qquad (1)$$

$$2\,Al_{(s)} + HO^- + 2\,H_2O \rightarrow 2\,AlO_2^- + 3\,H_2 \qquad (2)$$

After rinsing the treated surface with distilled water (without drying), the latter is next contacted with the amalgamation solution which is formed by mixture of equal volumes of a silver nitrate ($2 \cdot 10^{-2}$ mol/L in 2 mol/L nitric acid) and mercury nitrate solutions (10^{-1} mol/L in 2 mol/L nitric acid). The amalgamation is carried out in an acidic medium to prevent the precipitation of mercury oxide. The duration of this treatment is 3 minutes, during which mercury and silver deposition on the perimeter of the plate is then observed.

$$2\,Al_{(s)} + 3Hg^{2+} \rightarrow 2\,Al^{3+} + 3\,Hg_{(s)} \qquad (3)$$

$$Al_{(s)} + 3Ag^{+} \rightarrow Al^{3+} + 3\,Ag_{(s)} \qquad (4)$$

After amalgamation, the plate is rinsed with water, then dried. Rinsing the passivated surface with distilled water will react with aluminum in developing a non-passivating alumina layer. It must be quickly attached to the radiator, because the oxidation reaction starts immediately after drying. The monolith begins grow perpendicularly to the surface of the plate (see Figure 17 B).

$$Al_{(s)} + 3\,H_2O \rightarrow Al(OH)_{3\,(s)} + 3/2\,H_{2\,(g)} \qquad (5)$$

The growth rate of the ultraporous aluminum hydroxide monolith in the described conditions is about 1 cm/h, which is equal to 0.5 g. Generally, 2 – 3 aluminum plates are prepared during the same experiment, allowing us to yield 12 g of $Al(OH)_3$ per 8-hour experiment, resulting in about 7 g of α-Al_2O_3 after calcination.

3.2 Polyol synthesis of MgO

The choice of precursors and concentrations was based on reference [50]. Firstly, 0.1 mol of alpha-Al_2O_3 was dispersed in 250 ml of EG. The solution was then subjected to ultrasonic treatment at an amplitude of 30% for 5 min to break any big agglomerates of alumina. Then, 0.1 mol of magnesium acetate ($(CH_3COO)_2Mg{\bullet}4H_2O$) and 0.03 mol of PVP (poly) were added to the mixture. The blend was then heated under constant stirring at 197°C for 2h (see set-up in Figure 18).

The received mixture was centrifuged and washed multiple times with ethanol and water to remove physisorbed PVP and EG. The MgO precursor was then left to dry at 80°C for 2h in air. A sample of this powder was kept for characterization. The MgO precursor was then calcined at 600°C for 2h in air to form stable MgO in the presence of Al_2O_3. This modified polyol synthesis yielded 1 g of MgO after calcination and a total of 3.5 g of oxide powder.

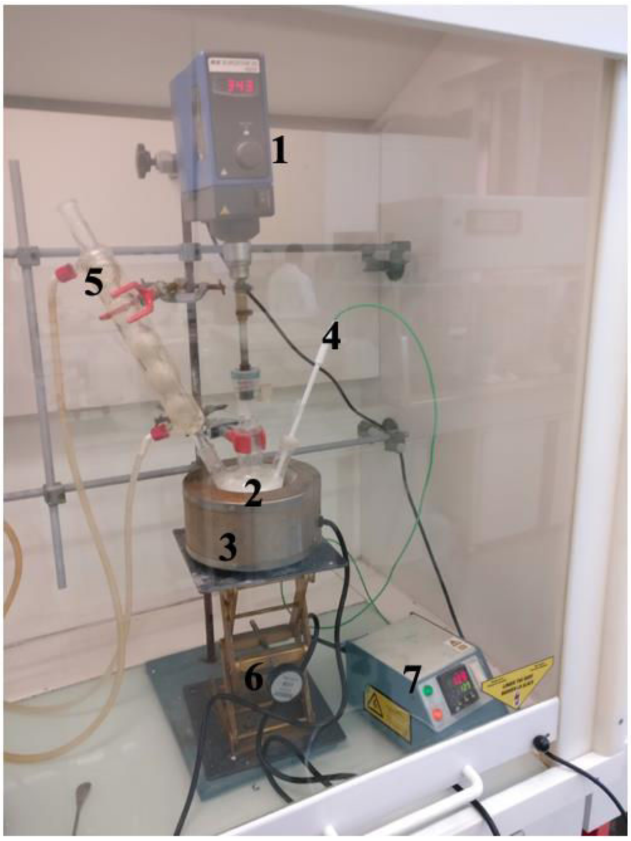

1 – mechanical stirrer,

2 – round-bottom flask (500 ml),

3 – flask heater,

4 – thermocouple type K,

5 – condenser (with water),

6 – platform,

7 – thermostat

Figure 18. Polyol synthesis in progress in the fume hood.

3.3 Doping alumina with MgO via impregnation

The synthesis of $MgAl_2O_4$ via doping in cycles with $Mg(NO_3)_2$ water solution was first mentioned in the PhD thesis of T. di Costanzo in 2001[54]. In this work, they used Mg precursor's water solution with concentration 3.0 mol/L, while in this work we used the maximum water solubility concentration, 1.5 mol/L. We started with 2 g of well-ground alpha-

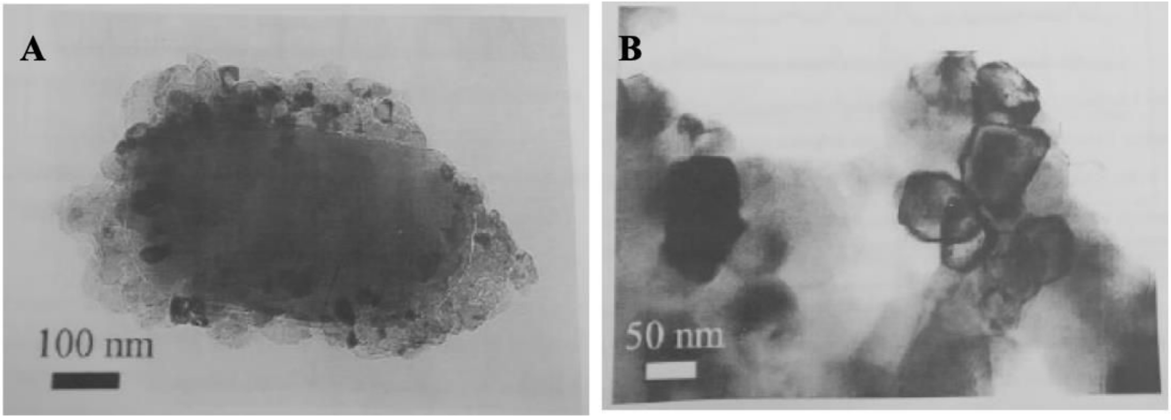

Figure 19. A: A big alpha-alumina crystallite covered by forming small magnesia crystallites after calcination at 800°C for 4h. B: Spinel crystallites formed after 7 days at 1000°C.[54]

Al_2O_3 powder received by calcining the monolith and added a fixed volume (1.55 ml) of nitrate solution to receive a paste with viscosity similar to toothpaste. This viscosity was chosen to avoid the loss of Mg-precursor due to excess liquid while having a homogeneous distribution of the precursor. After adding the liquid Mg-precursor to the alumina powder and mixing well, the paste was calcined at 500°C for 30 min in air to evaporate the liquid and form MgO. To achieve stoichiometric 1:1 ratio of Al_2O_3 and MgO inherent to $MgAl_2O_4$ spinel, 9 doping cycles were necessary, making the duration of the whole process to be 5 days.

This doping method was chosen to compare to the classical polyol synthesis because the reported first results from the PhD thesis[54] showed two interesting trends. Firstly, conventional pressureless sintering is not efficient in transferring the whole volume of the sample to spinel phase. It was shown that even after a whole week of sintering at 1000 °C, the XRD patterns still include peaks characteristic to all three crystallographic phases. Secondly, TEM investigation of the sintered powder showed that 250 – 300 nm alumina crystallites formed spinel with crystallites measuring 50 – 100 nm in size (see Figure 19).

3.4 Spark plasma sintering

The main sintering method used in this work is spark plasma sintering (SPS). Dr. Sinter LAB Series SPS-515S (Fuji Electronic Industrial, Japan) SPS system located in CNRS-ICMPE (Thiais, France) was employed with dies sized 15 mm in diameter. This system allows us to use sintering temperatures up to 2000°C, pressing force up to 50 kN (~292 MPa for a ⌀ 15 mm sample) while measuring the displacement and its' ratio during the sintering process. We used two types of sample dies, depending on the applied pressure: standard graphite mold was used for pressures up to 100 MPa (quality 2334 Mersen) and graphite composite mold (quality CX31V Toyo Tenso) was used for higher pressures. The molds were loaded with 1.2 – 2 g of powder, depending on powder density. After sintering, the received pellets had a thickness of about 3 mm. Since used sintering temperatures were > 1000°C, the sample die was wrapped in carbon felt to suppress heat radiation from the sample.

In our experiments, the pulse pattern of the SPS system was kept at the recommended standard 12:2 (on-off, pulse duration 3.4 ms). Sintering was carried out in primary vacuum of 20 – 60 Pa. Temperature was measured by an optical pyrometer (CHINO IR-AH) focused on an area of the sample die not covered by carbon felt (see prepared sample positioned in the sintering chamber in Figure 20). It is known from previous set-up calibration tests that the optical pyrometer will read the temperature to be about 50°C higher than the thermocouple. In this work we present all values as programmed into and read from the sintering system, this difference will be taken into account when comparing to results of other authors.

Figure 20. SPS sample ready to be sintered.

The system is composed of 3 columns (see Figure 21): I – sample chamber with mounted pyrometer and gas valves; II – temperature programming and displacement, current, voltage vacuum reading; and III – pressure programming and data visualization.

Figure 21. SPS system and sample placement, sample at high temperature.

3.5 Hot isostatic pressing

Hot isostatic pressing (HIP) was used in this work as a post-SPS densification method. The benefit of using HIP in addition to SPS is its isostatic pressure application via gas, allowing to help densify the samples in directions other than uniaxial SPS and close small intergrain pores.

The HIP (Nova Swiss, see Figure 22) used in this work allows us to use pressure from 0.5 – 400 MPa, temperature up to 1450°C, maximum heating rate 15°C/min, cooling rate 50°C/min and dwell time 1 – 3 hours. We used argon as the pressurizing gas with pressure application rate 25 MPa/min and target pressure of 200 MPa, heating rate 15°C/min and the temperature dwell was set at 1250°C during 3 h.

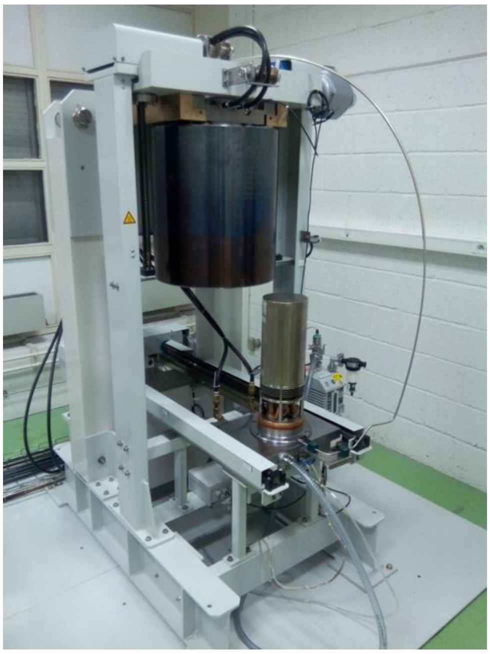

Figure 22. HIP in LSPM.

3.6 Polishing sintered ceramics

Polishing hard ceramic materials demands proper equipment and good procedure, using classical sandpapers is out of the question.

We used polishing discs and diamond liquids provided by Struers S.A.S (France) and diamond pastes provided by Escil (France). Using a ready-made diamond polishing solution or diamond paste with a polishing solution (Struers DP-Blue) for lubrication is up to user's choice.

The protocol used for grinding and polishing one side of the ceramic:

1. Struers MD Piano 220; 300 rpm; 15 min
2. Struers MD Piano 1200; 150 rpm; 15 min
3. Struers MD Plan 9 µm + 9 µm diamond liquid/10 µm diamond paste; 150 rpm; 30 min
4. Struers MD Dac 3 µm + 3 µm diamond liquid/paste ; 150 rpm; 30 min
5. Struers MD Nap 1 µm + 1 µm diamond liquid/paste; 150 rpm; 30 min
6. Struers MD Chem + ¼ µm diamond paste; 150 rpm; 30 min

It should be noted that the duration of grinding steps 1-2 depends heavily on desired final thickness of the sample.

3.7 X-ray diffraction and pattern analysis with Maud

X-ray diffraction provides information on the crystallographic structure of the material, following Bragg's law: $2d \sin\theta = n\lambda$; where d is the inter-plane distance of atoms, θ is the scattering angle, n is the integer representing the order of the diffraction peak and λ is the X-ray wavelength. More practically however, Rietveld refinement[181], developed by Hugo Rietveld in late 60s, is used to determine various phase parameters from measured XRD patterns. The Rietveld method uses least squares approach to refine a theoretical line's properties (setup details, background, crystalline phase percentages, lattice parameters, crystallite sizes, residual stresses, etc) until it matches the experimental profile. Nowadays, this refinement is carried out via a computer program, we have chosen the MAUD (Maud, Materials Analysis Using Diffraction) developed by Luca Lutterotti and co-authors[182]. To identify the phases present in the materials, the full profile search match using the Crystallography Open Database (COD)[183], also developed by Lutterotti, was used. The following COD[184] phase files were used for Rietveld refinements via Maud: alpha-alumina (#1000032, corundum, Al_2O_3); periclase (#9006485, MgO); spinel (#9007116, $MgAl_2O_4$).

X-ray diffraction pattern measurements were carried out on INEL (France) EQUINOX 1000[185] diffractometer (see Figure 23) with Cu K_α irradiation, acquisition in real time over 110° 2θ (omega was kept at 6°). Although this benchtop diffractometer allows us to see the diffractogram in some seconds, our measurements were collected during minimum of 2 hours to improve the signal to noise ratio. Sample preparation for powders and sintered ceramics was the following: the powders were set into a small cuvette and mixed with ethanol to form a paste, the ceramic pellets were fixed on the sample holder.

Figure 23. INEL EQUINOX 1000 diffractometer. [185]

3.8 X-ray texture analysis

Texture, coherent domain sizes and shapes, microstrains, and structural variations were also investigated by XRD. Below is the description of the process and analysis carried in collaboration with Daniel Chateigner and Yassine El Mendili at Normandie Université, CRISMAT-ENSICAEN, IUT-Caen, Université de Caen Normandie (Caen, France).

We used a four-circle diffractometer setup equipped with a Curved Position Sensitive detector (S120 by INEL SA, France), using the monochromatized CuK_α average radiation[186]. Data were analyzed within the combined analysis formalism[187] implemented in the MAUD software[188]. This methodology allows the quantitative texture determination of the samples, using a cyclic Rietveld refinement of a series of X-ray patterns measured at different sample orientations. It is then possible to determine other sample features like structure, residual stresses, crystallite size and microdistortions, phases, ... We measured 2θ patterns using a regular 5° × 5° grid in tilt and azimuth angles (χ and ϕ respectively) with $0° \leq \chi \leq 55°$ and $0° \leq \phi \leq 355°$. It resulted in 864 diagrams, each one exhibiting more than 4000 measured points. We used an incident angle of the X-ray beam on the sample plane of $\omega = 20°$, approximately centered on the main Bragg peaks range for the phases of concerns, to reduce, on an average, the blind areas on these peaks [187].

During refinements, the used unit-cell definition of corundum is the $R\bar{3}c{:}H$ space group, Crystallography Open Database n° 1000017[184]. Crystallite sizes, shapes, and microstrains were refined within the Rietveld cycles using the Popa description[189]. We estimate that our X-ray Combined Analysis setup probed several millions of crystallites. The instrument contributions (χ and ϕ broadenings, peak shapes, zero-shifts, line shapes, etc.) were calibrated using the 660b LaB6 powder standard from National Institute of Standards and Technology. A counting time of 4 min for each sample orientation was used.

3.9 Scanning electronic microscopy (SEM)

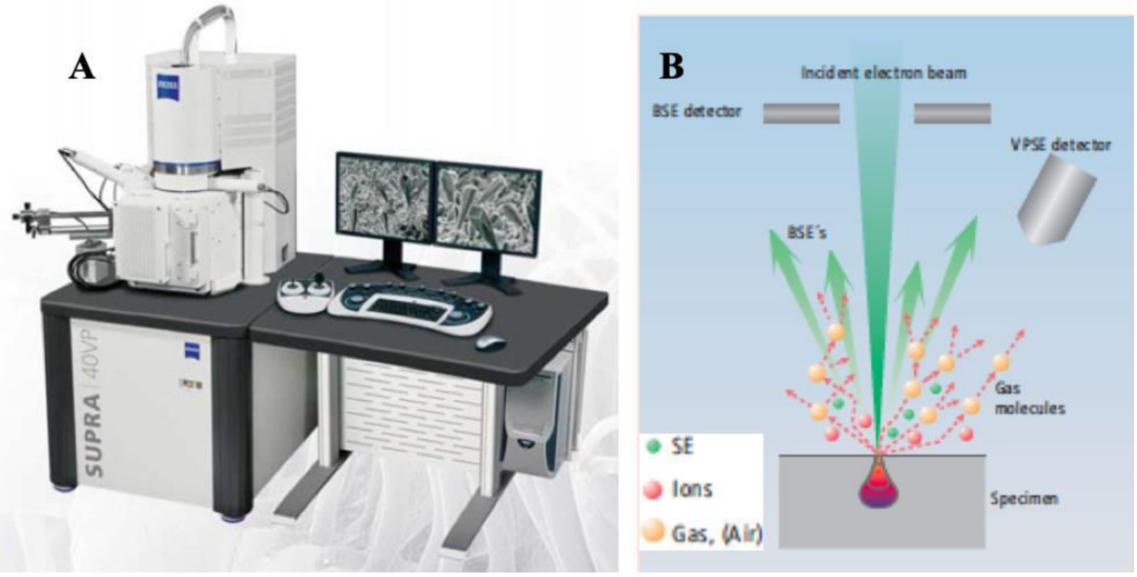

Figure 24. A: Zeiss Gemini Supra 40 VP FE-SEM. B: Detection of electrons in the SEM. [190]

In this work, Zeiss Gemini SUPRA 40VP (2007) SEM[190] (see Figure 24 A) was used to obtain secondary electron (SE) images of precursor powders and backscattered electron (BSE) images of consolidated ceramics, as well as to collect electron backscattering diffraction (EBSD) data. The interactions of the primary electron beam with the specimen are shown in

Figure 24 B along with the position of the SE and BSE detectors. The benefit of this set-up is the possibility to measure samples in low vacuum (4 – 30 Pa), allowing to avoid covering translucent samples by carbon or platinum. Energy-dispersive X-ray spectroscopy (EDX) analyses were carried out on Leica S440 SEM.

SE imaging was chosen to characterize the precursor powders because it gives the best topographical and morphological information[191]. Brightness of a point on the surface depends on the height of the respective sample point, a phenomenon known as edge effect, allowing more electrons to escape from higher points of the sample. The imaging was carried out at relatively low acceleration voltages of 3 – 5 kV, with the working distance between 4 and 7 mm.

BSE imaging was chosen to characterize the consolidated ceramics due to their high energy and elastic scattering from the specimen atoms. Since lighter elements backscatter electrons less strongly than heavy elements (higher atomic number = higher brightness), this detection provides information on the atomic weight as well as morphology[191,192]. The contrast of different local crystalline directions in a polycrystalline material arise from the BSE measurements due to either diffraction or channeling phenomena[191]. To achieve high enough contrast to differentiate crystalline grains, these measurements were carried out at 15 – 20 kV, with the working distances between 4 and 6 mm.

In the case of EBSD measurements, the sample is tilted for the diffracted electrons to create a pattern. Analogically to characterization by XRD, the Bragg's law applies to BSEs, diffracting the incident electron beam, and resulting in a diagram obtained by reflection[191,193]. The drawback of this method is a long data collection and indexing time.

EDX measurements are based on ionizing the atoms of the specimen by the primary electron beam, generating holes in the core shells followed by electrons from outer shells filling these holes, thus emitting X-ray fluorescence lines.

In any type of SEM imaging of insulating materials, one should be aware of charging effects.

3.10 Gas pycnometry

Micromeritics AccuPyc II 1340 pycnometer (see Figure 25[194]) equipped with a 10 cm^3 sample cell was used for all density measurements. The challenge in measuring density lies in accurate determination of the sample volume, the pycnometer uses inert gas displacement (in our set-up He) to do so.

Figure 25. Measuring density with the Micromeritics pycnometer. [194]

A sample with known weight is enclosed to the instrument chamber and sample cell with a known volume, then a known volume of gas is guided to the sample chamber (step one, opening valve a) and expanded into a second precision chamber as equilibrium is reached (step 2 and 3, opening valve b). Equilibrium will also be reached in comparison to the second chamber (step 4). The pressures measured while filling the sample chamber and later emptying it into the second chamber are then used to calculate the volume of the sample's solid phase, which is then divided by the given sample mass (step 5). Finally, the pressure is vented off to atmosphere via valve c (step 6).

3.11 Transparency measurements

Discussing transmittance of polycrystalline ceramics includes the real in-line transmission combined with the diffuse transmission. While the latter is normally measured using an integrating sphere, measuring real in-line transmission requires a distance of 60 to 100 cm between the sample and detector to minimize the collection of diffuse scattered light.

Absorption of light in a material is characterized by the Beer-Lambert-Bouguer law: $A = a_\lambda \cdot b \cdot c$, where a_λ is the absorptivity coefficient, b is the path length and c the analyte concentration. Practically, the transmittance (T) of a solid sample is normally measured by a

UV-Vis spectrophotometer and the absorption coefficient α is calculated using the following relation: $\alpha = \frac{\ln\frac{100}{\%T}}{d}$, where d is the thickness of the sample.

The transmittance of the samples was measured using a SAFAS UVmc1 spectrophotometer (SAFAS, Monaco) by placing a 5 mm pinhole before the sample and positioning the sample about 1 cm from the detector. The pinhole was used to help narrow down the measurement area. Alternatively, to study the absorption of spinel ceramics, PerkinElmer Lambda 35 spectrometer was used in collaboration with Moustapha Zaghrioui at IUT of Blois. This change was made due to better sensitivity.

3.12 Cathodoluminescence measurements and proton bombarding

Cathodoluminescence (CL) measurements were carried in collaboration with Eduard Feldbach at the Institute of Physics, University of Tartu (Tartu, Estonia). The CL setup[195] is equipped with a vacuum cryostat (5–400 K) and two monochromators covering spectral range from NIR (~1700 nm) to VUV (~110 nm). An ARC SpectraPro 2300i monochromator with various gratings and detectors or a self-made vacuum double monochromator with a Hamamatsu photomultiplier R6836 can be used. Both, steady and pulse (10 ns, 5 kHz) mode can be used for the electron gun (Kimball Physics EGG-3101). Luminescence kinetics (decay curves) can be detected by the Becker&Hickl MSA-300. To avoid surface charging under electron beam excitation, 3-nm Pt films were deposited on all samples.

Proton bombarding was chosen to investigate the effects of irradiation on the material. KIIA 500 kV ion implanter at the University of Helsinki was utilized in collaboration with Eduard Feldbach and Jyrki Räisänen. The chosen samples were irradiated by a 200 keV molecular hydrogen beam, corresponding to 100 keV protons. The molecular beam was chosen to shorten the irradiation time due to higher beam flux. 10^{17} protons/cm^2 was chosen as the goal fluence, corresponding to about 0.5 dpa and achievable in about 8h.

4 Alumina ceramics

The goal of this first part of the PhD project is to assess the suitability of various alumina precursor powders to produce dense, translucent and fine-structured ceramics. Additional focus is put on the differences emerging from the morphology and phase of said precursors to determine which would be most suitable as a base material to later obtain spinel phase by addition of magnesia.

To characterize the differences between the chosen precursor powders, each powder is sintered by a long (93 min) cycle with slow heating rate and a short (38 min) cycle with a high heating rate, followed by modifications in pressure and temperature for chosen precursors. During sintering, along with the temperature, the pressure and the displacement, the displacement ratio, the applied voltage, the applied current and the vacuum are registered to obtain the maximal information on the sample conditions at each moment.

This type of precursor powder comparison is of high importance since it opposes and adds to the almost standard way of SPS research of choosing one precursor powder and optimizing the sintering cycle, thus giving more details about the commonly known importance of precursor powder morphology and particle size.

In this chapter, results on sintering alumina ceramics will be presented. Firstly, the six different precursor powders for sintering are introduced and their morphology and crystalline phase characterized by SEM and XRD. Next, the sintering cycles carried out on these powders are described in detail. The overview of the results begins with a summarizing the sintering conditions and properties of resulting condensed ceramics in Table 2. The resulting crystallographic phase of the samples is presented next followed by a detailed description and discussion of the resulting morphology and grain size of each sample. Next, the transmittance of translucent samples is briefly discussed trailed by XRD and EBSD texturation studies and HIP post-densification tests. Finally, the absorption and luminescence of characteristic samples are investigated and the chapter is concluded by a summary of alumina ceramics.

4.1 Characterization of powders

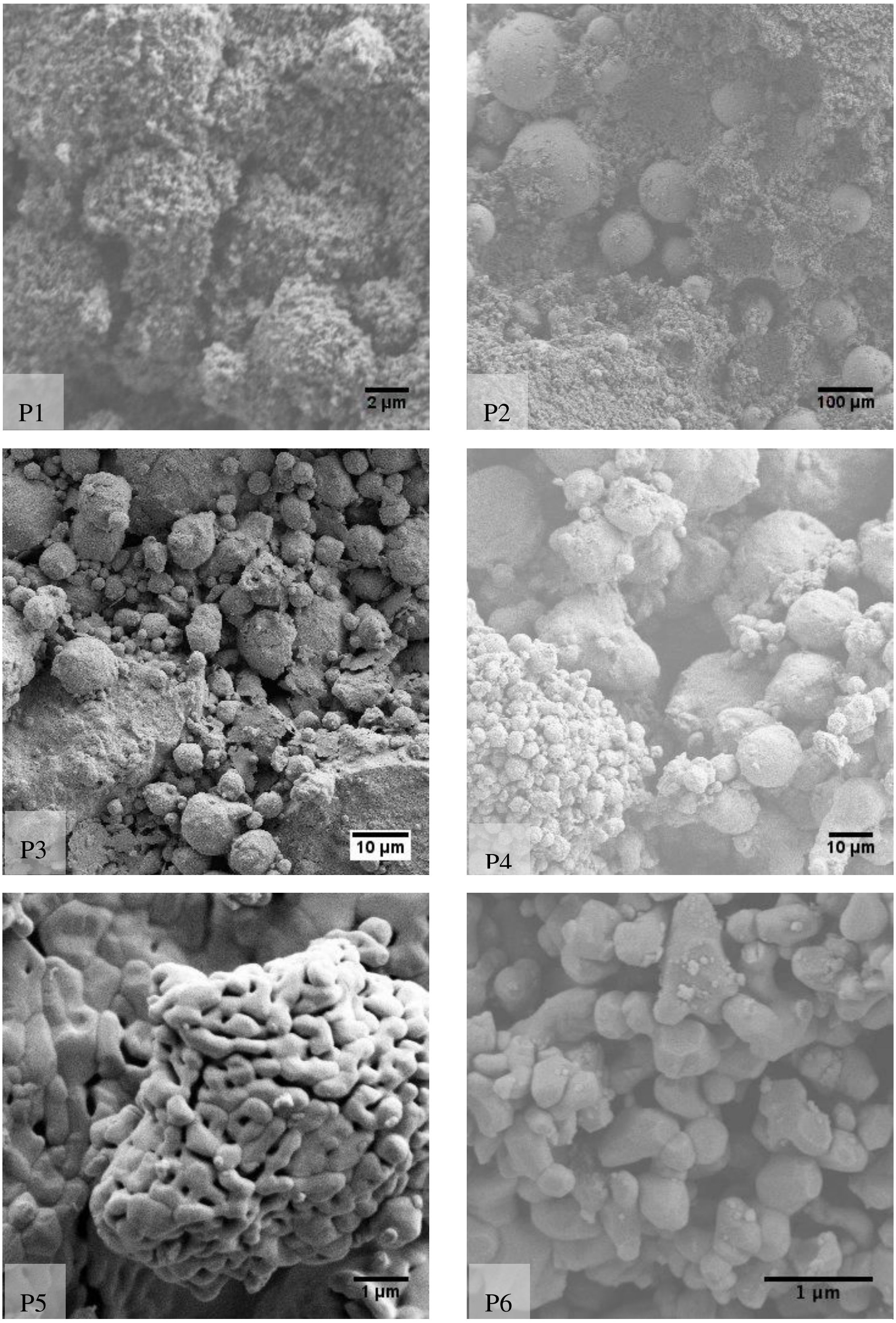

Figure 26. SEM micrographs of alumina powders used for sintering.

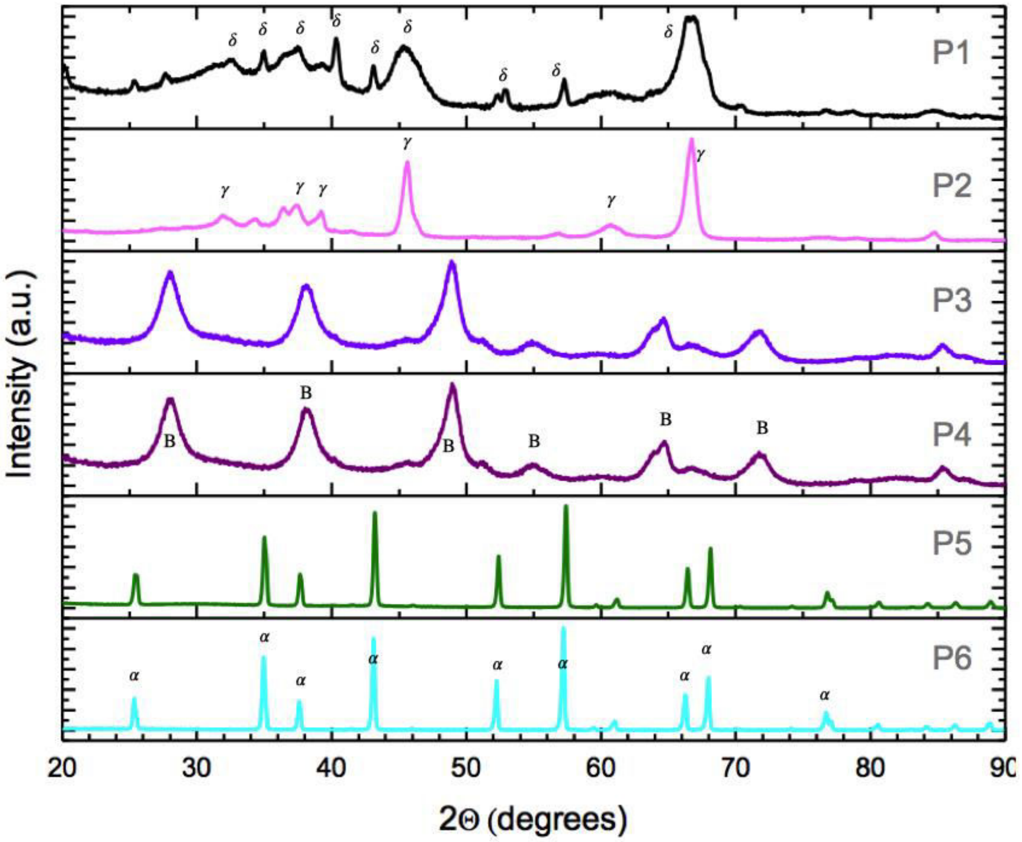

Figure 27. Characteristic XRD patterns of alumina powders. α, γ and δ denote the respective alumina polymorphs and B denotes boehmite phase.

In this work, six different Al_2O_3 powders were used for sintering. The morphology of the powders is shown in Figure 26 and Figure 27 shows the XRD patterns. The suppliers provided us with the following information for each powder: P1 powder (70% δ-Al_2O_3 30% γ-Al_2O_3, crystallite size 40-50 nm, Alfa Aesar), P2 powder (γ-Al_2O_3, TEM crystallite size 50 nm, Sigma Aldrich), P3 powder (boehmite, Sasol GmbH), P4 powder (Sasol GmbH boehmite exposed to 30-minute ultrasonic (US) deagglomeration in acetone at 40% amplitude), P5 powder (Sasol GmbH boehmite calcined to α-Al_2O_3 via a 4-hour heat treatment at 1400°C). P6 is ultraporous alumina - UPA - elaborated by an original patented process [11,52] at the LSPM CNRS laboratory and calcined to α-Al_2O_3 via a 4-hour treatment at 1400°C.

The SEM micrograph of P1 shows a loosely agglomerated fine-grained powder consisting of micrometric particle clumps while simultaneously demonstrating crystallites smaller than 10 nm. The XRD pattern shows peaks corresponding to both, γ- and δ- Al_2O_3, thus confirming the information of the supplier. P2 consists of clumps of fine nanometric crystallites in combination with clearly formed spherical particles in the size of 45 – 150 μm and the XRD shows the presence of mostly γ-Al_2O_3 with a couple of peaks hinting to a remaining low concentration of

δ-Al_2O_3. P3 and P4 are both of boehmite phase, the SEM and XRD analysis shows no significant difference before (P3) and after (P4) the US treatment. In both cases, big clumps of powder aggregates are visible in addition to clearly formed almost spherical smaller particles. Judging by the SEM micrograph of P4, the US treatment seems to have deagglomerated a big clump of powder into finer particles of 1 – 10 µm (see bottom left of the micrograph). The SEM micrograph of P5 shows that the calcination of boehmite at high temperature to obtain pure α-Al_2O_3 results in hard sintered porous particles of 2 – 8 µm consisting of crystallites in the size of about 0.5 µm. Contrary to the almost identical XRD patterns of P5 and P6, the SEM micrograph of UPA calcined to α-Al_2O_3 phase (P6) shows a fine morphology, consisting of somewhat interconnected slightly elongated crystallites of 0.2 – 0.8 µm in size. The general morphology of the powder remains monolithic. It should also be noted that whereas the crystallites of P5 are firmly sintered together, the crystallites of P6 are connected by a couple of sintered necks.

Powders P1 and P6 have the most homogenous morphology out of the investigated powders.

4.2 Sintering and resulting microstructure

The sintering conditions used in this work were designed taking into account the team's previous experience in sintering UPA in gamma phase[121]. Two types of sintering cycles, long and short (see Figure 28), were carried out at 1450°C with pressures varying from 80 MPa to 285 MPa. In the beginning of each sintering cycle, an additional 10-minute dwell at 600°C was carried out to evaporate any water absorbed into the powders. All cooling rates were kept constant at 100°C/min.

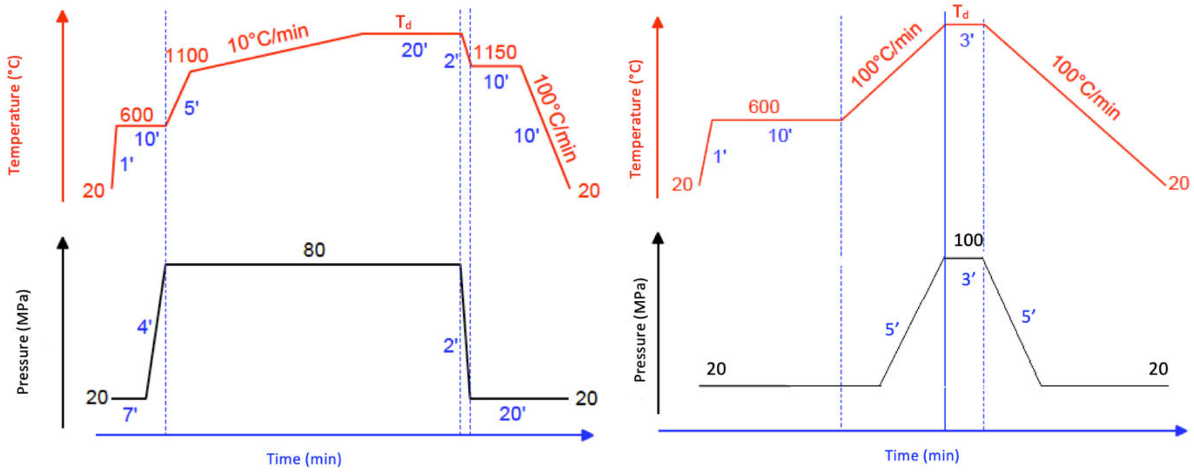

Figure 28. Long (left) and short (right) sintering cycles.

In the case of long sintering cycles designed to obtain maximum density, the sample was heated with a rate of 100°C/min until 1100°C and heating rate 10°C/min was employed to reach the dwell temperature. The pressure was applied (about 15 MPa/min) at the end of 600°C dwell and kept constant throughout heating and main dwell. An additional 10-minute dwell at 1150°C was carried out after releasing the pressure (about 30 MPa/min) to allow the sample to free from constraints/stresses brought on by high pressure. Generally, 80 MPa was used as sintering pressure for the long cycle, additionally the effect of 200 MPa was tested.

For short sintering cycles designed to make use of the high heating power of SPS and hinder the grain growth, the heating rate was kept constant at 100°C/min and the temperature dwell was kept at 3 minutes. The pressure dwell matched the 3-minute temperature dwell, applying and releasing rate was kept constant at about 20 MPa/min. Generally, 100 MPa was used as sintering pressure for the short cycle, additionally, the maximum 50 kN≈285 MPa was tested.

Due to high chosen sintering temperature (1350°C – 1450°C), all sintered ceramics were monophasic alpha alumina (see Figure 29 and Figure 30). For samples A1 – A8, the ceramics' cell parameters were calculated using Rietveld refinement via MAUD to see the variations due to sintering and difference in starting powder, since the variations were not very significant at maximum 0.0098 Å for *a* and 0.0316 Å for *c*, thus the cell parameters of the rest of the samples were not evaluated. All sintering conditions and results are summarized in Table 2. Our evaluations of α-Al_2O_3 ceramics' cell parameters are slightly smaller than standard hexagonal unit cell's parameters (a_H=4.759 Å, c_H=12.991 Å [196]) most likely due to 80-285 MPa pressure used during sintering, even though α-Al_2O_3 is known to be only 9% compressible at 300 kbar [197].

Table 2. Sintering conditions and properties of resulting consolidated aluminas.

Sample	Sintering cycle	Density (%)	Lattice parameters (Å)	Grain size (µm)	Transmittance at 650 nm (%)	Powder/ comments
A1	Long, 1450°C 80 MPa	95.8(1)	$a = 4.7583(3)$ $c = 12.996(2)$	3.3(1)	-	P1
A2		98.0(3)	$a = 4.7548(1)$ $c = 12.9859(5)$	4.9(2)	7.8	P2
A3		94.7(1)	$a = 4.7515(1)$ $c = 12.9806(4)$	24(1)	-	P4
A4		94.2(7)	$a = 4.7575(1)$ $c = 12.9936(5)$	7.5(3)	-	P3
A5		94.1(3)	$a = 4.7509(1)$ $c = 12.9774(4)$	6.3(2)	-	P5
A6		98.4(7)	$a = 4.7613(7)$ $c = 13.009(3)$	16(1)	7.5	P6
A7	Long, 1450°C 200 MPa	97.4(2)	$a = 4.7546(1)$ $c = 12.9877(6)$	12.3(6)	-	P6
A8	Short, 1450°C 285 MPa	96.6(1)	$a = 4.7535(2)$ $c = 12.98708$	1.3(1)	21.3	P6
A9	Short, 1450°C 285 MPa	98.6(1)		23.8(8)	35.5*/3.0**	P6 Pre-pressing at 4t
A10	Short, 1350°C 100 MPa	89.3(1)		-	-	P3
A11	Short, 1350°C 100 MPa	97.5(1)		-	-	P5
A12	Short, 1450°C 100 MPa	*98.9(8)*		11.7(4)	-	P3 + 1 wt% LiF
A13	Short, 1450°C 100 MPa	-		-	-	P5 + 1 wt% LiF
A14	Long, 1450°C 200 MPa	99.4(3)		6.5(3)	-	P3
A15	Short, 1450°C 100 MPa	97.4(2)		2.9(1)	-	P6
A16	Short, 1450°C 100 MPa	97.4(4)		7.0(2)	-	P5
A17	Short, 1450°C 100 MPa	92.8(1)		5.4(4)	-	P2
A18	Short, 1450°C 100 MPa	96.3(1)		8.7(2)	-	P1
A19	Short, 1450°C 285 MPa	95.5(1)		2.3(1)	-	P2

* *Measured by Jasco V770 (in-line)*

** *Measured by Agilent Cary 5000 (with an integrating sphere)*

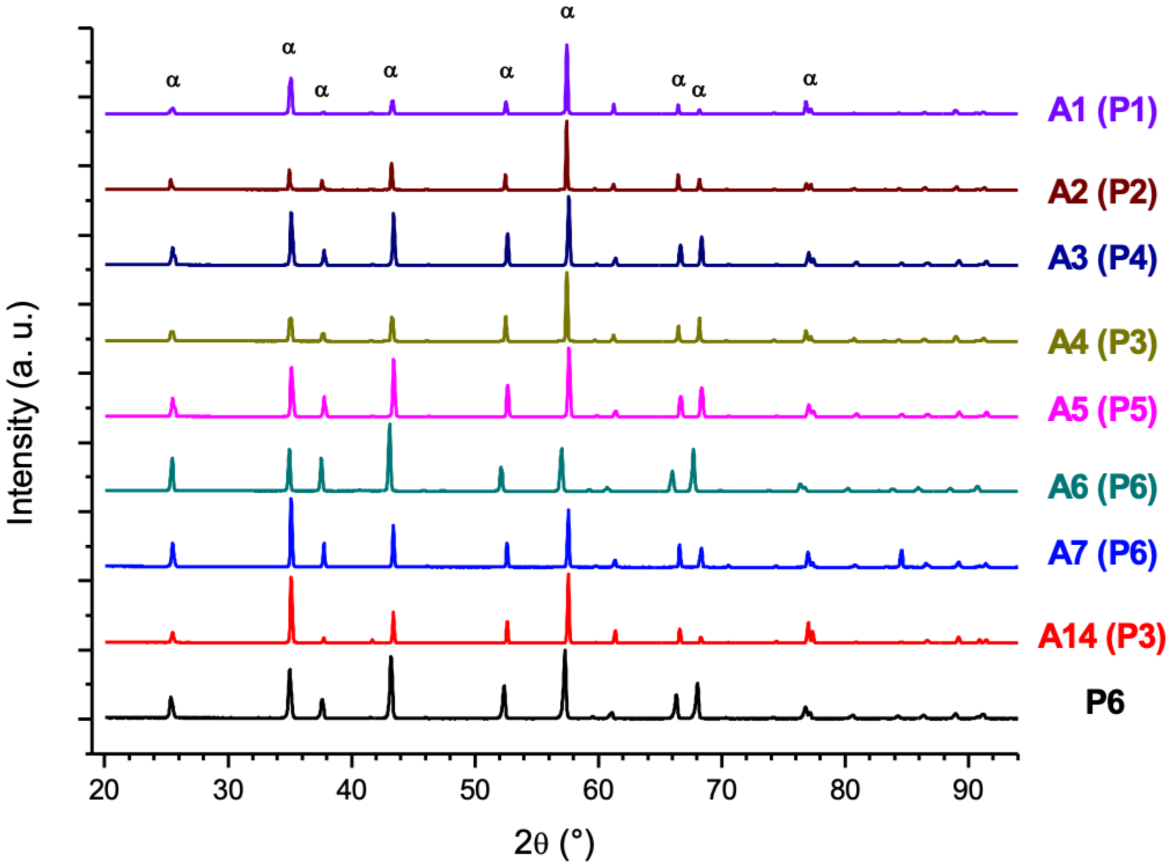

Figure 29. XRD patterns of alumina sintered via the long cycle.

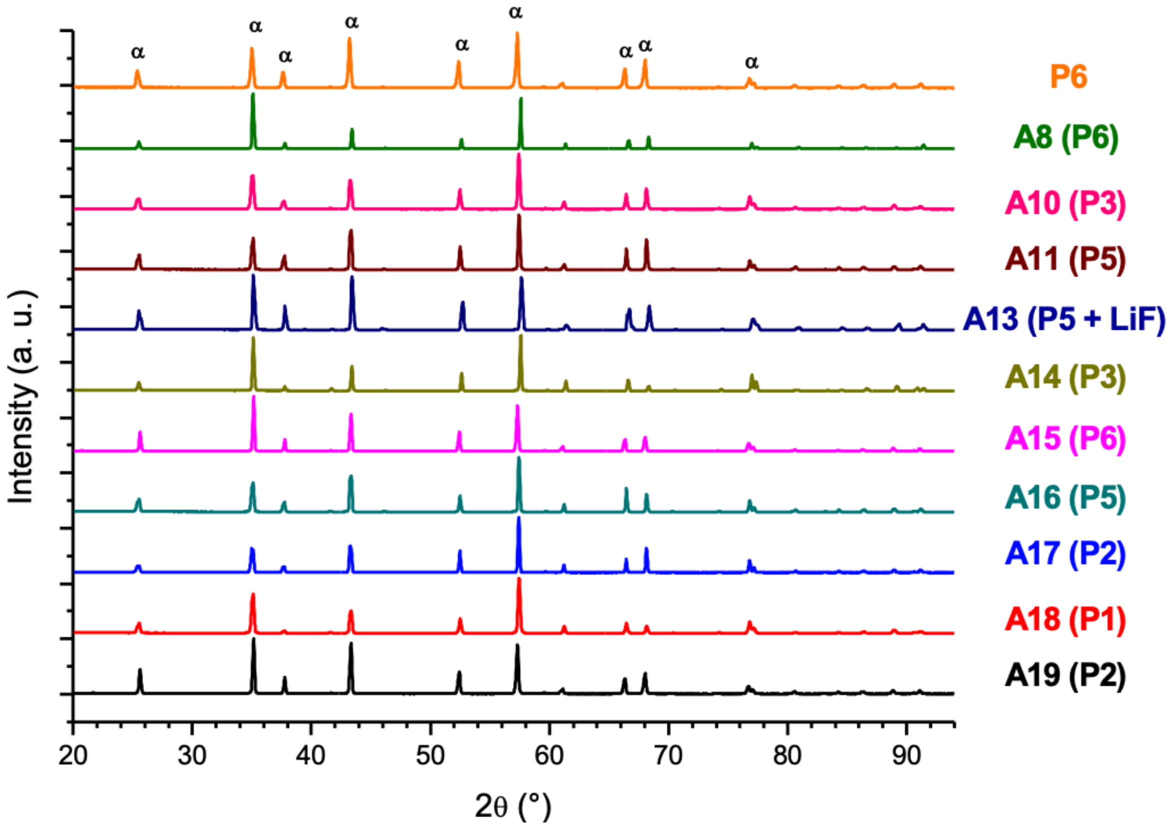

Figure 30. XRD patterns of alumina sintered via the short cycle.

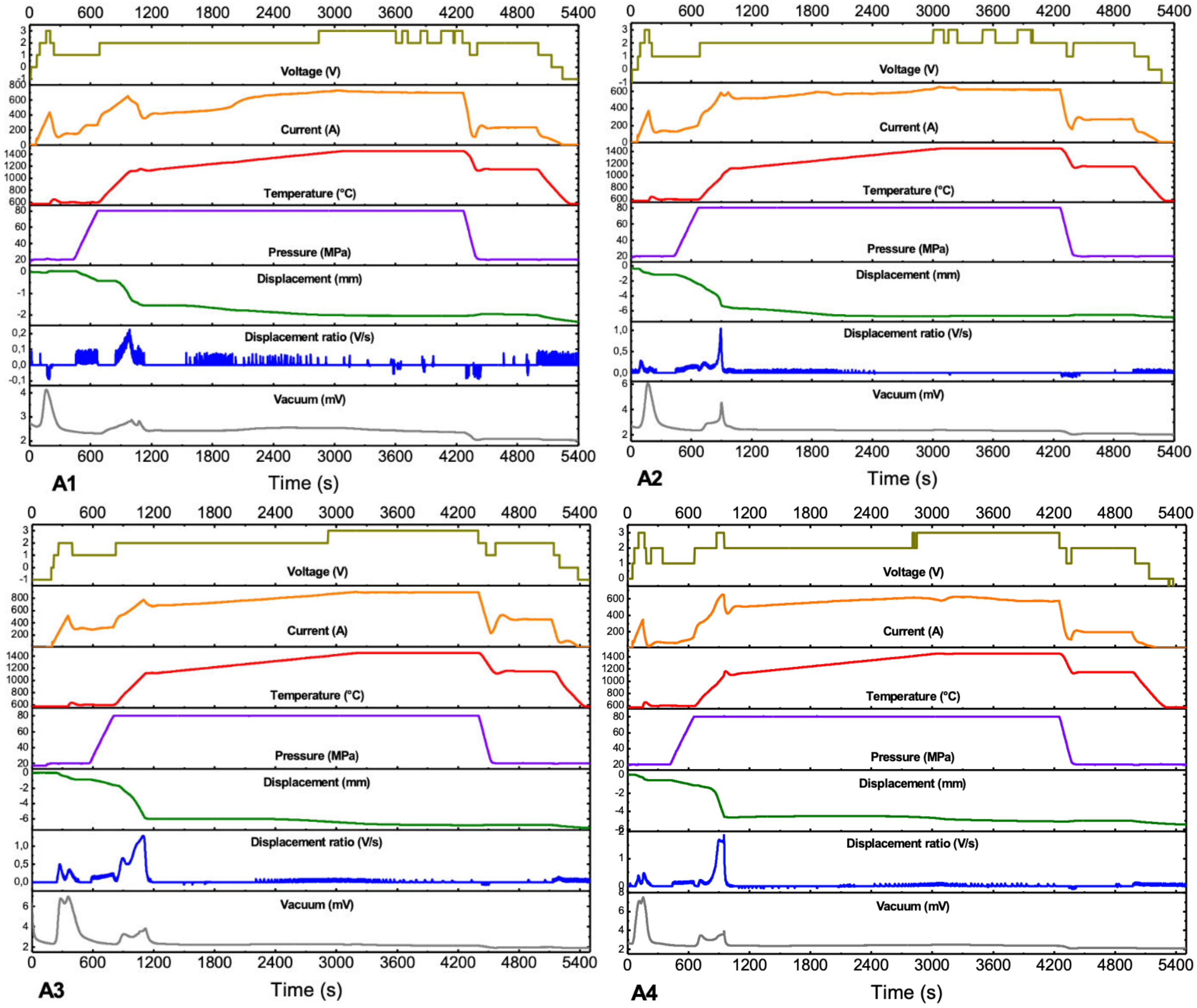

Figure 31. SPS sintering data of A1 - A4.

The data collected during the sintering of A1 – A4 is presented in Figure 31. It can be seen that the curve of applied current is directly linked to the measured temperature, as the heating source in SPS is direct current.

The displacement of the samples takes place in two steps, the first bigger change in sample position is observed as we start increasing the uniaxial pressure (at 660 s) and the second as we change the heating rate from 100°C/min to 10°C/min at 1100°C (at 960 s). Plotting the displacement ratio gives us an opportunity to quickly identify the moments where fast densification takes place. In the case of A2 and A3 we can clearly differentiate the densification due to pressure application and due to change in heating rate. For A4, the last two are not very well separated in time.

The peaks in vacuum data inform us that there is gas leaving the sample, allowing to predict possibly dangerous die explosions and providing information about water and additive evaporation from the sample. For samples A1 – A4, a peak in the vacuum value can be observed in the very beginning of the sintering cycle, when heating from room temperature to 600°C, and double peaks similar to those presented in displacement ratio are observed when raising the pressure and changing the heating rate.

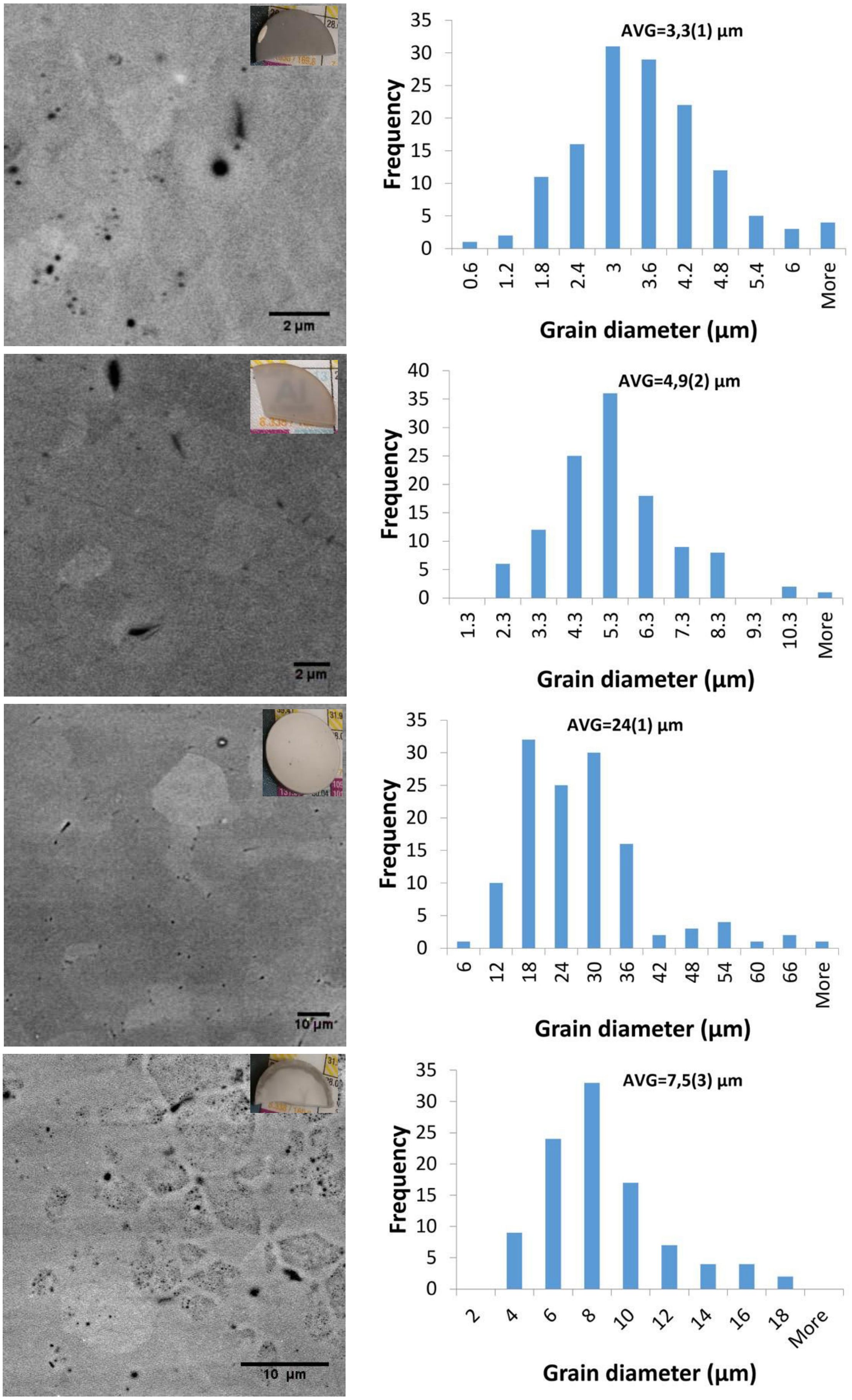

Figure 32. SEM micrographs of A1-A4 (top to bottom) with the grain size distributions and optical images.

Figure 32 shows the morphology and grain size distribution of samples A1 – A4 with their optical photos. Sample A1, sintered via the long SPS cycle at 1450°C is of relatively low density (95.8%) and rather small, developing grain size (3.3 μm). A2 has a higher density and is translucent (see Figure 32), even though the only difference between the starting powders is the 70% δ-Al_2O_3 composition in A1 compared to the pure γ-Al_2O_3 phase of A2 powder.

Since sintering γ-Al_2O_3 via SPS is not very common, our best source of comparison is the work carried out in LSPM[121] on the SPS of 10 nm γ-Al_2O_3 obtained from UPA by calcining it at 1050°C. The average grain size of A2 is 4.9 μm, which is much bigger than the 2 μm average grain size in the case of a sample sintered at identical conditions in the previous work[121]. The previously achieved full density is in the same range as the density achieved here for A2. The previously obtained ceramic from 10 nm γ-Al_2O_3 via the same sintering cycle showed no optical transparency, whereas A2 is translucent (see chapter **Error! Reference source not found.**). Additionally, it has been found[120] that seeding γ-Al_2O_3 with α-Al_2O_3 is necessary to produce dense ceramics via cold isostatic pressing (280 MPa, 30 min) followed by conventional sintering. The authors concluded that the inclusion of 1.5 wt% α-Al_2O_3 seeds provides a lot of nuclei for the formation of α-Al_2O_3 and thus diminishes the vermicular growth during the phase transformation, allowing to obtain full density ceramics at 1400°C during 100 minutes, characterized by a grain size of 1.5 μm.

Boehmite powders for samples A3 and A4 are set apart by a simple 30-minute US treatment in acetone. Although this leads to a small morphology difference in the SEM images, the ceramic sintered from US-treated boehmite has 3 times bigger (24 μm) average grain size and slightly higher final density, proving US-treatment a useful tool for increasing powders' sinterability via deagglomeration of powder clumps and increasing reactivity. Like in the case of γ-Al_2O_3, boehmite SPS has not been a topic of interest, but has been used for sintering dense alumina ceramics with added α-Al_2O_3 seeds by Kwon and Messing[119]. The authors found that a mixture of 36 wt% boehmite and 64% 0.2 μm α-Al_2O_3 sinter at nearly identical temperature with nearly identical shrinkage as the fine alumina alone, proving boehmite useful as a filler for expensive fine alumina.

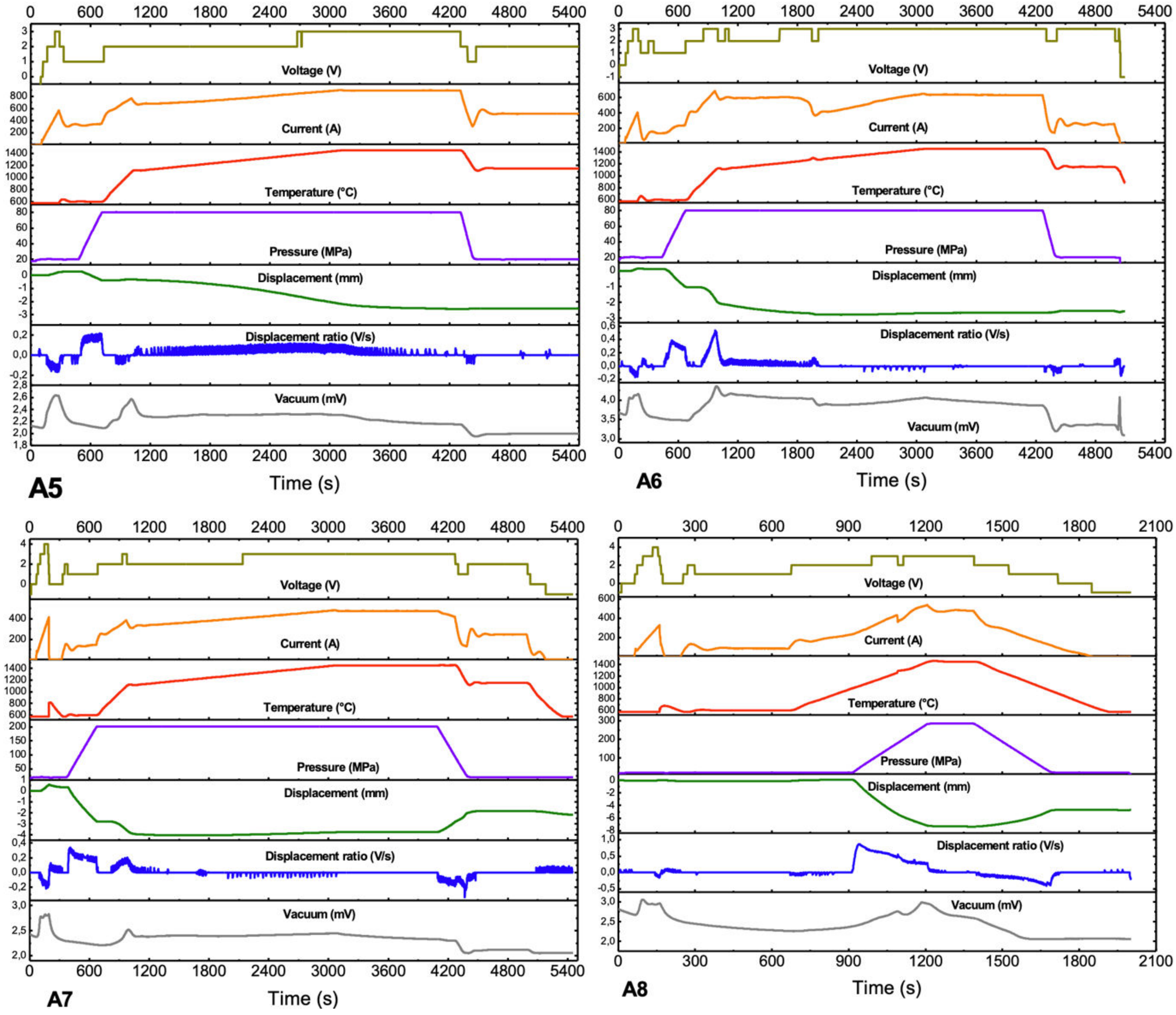

Figure 33. SPS data for samples A5 - A8.

The profiles of the SPS data collected for samples A5 – A8 are presented in Figure 33. A5 and A6 were sintered via the long cycle at 80 MPa and 1450°C, the pressure was raised to 200 MPa for A7 and A8 was sintered via the short cycle at 285 MPa and 1450°C. While the profiles of the current, displacement, its ratio and vacuum of A5 – A7 are similar to the ones presented for A1 – A4, in the case of A8 sintered by the short cycle we can no longer differentiate between the densification due to pressure application and densification due to raise in temperature.

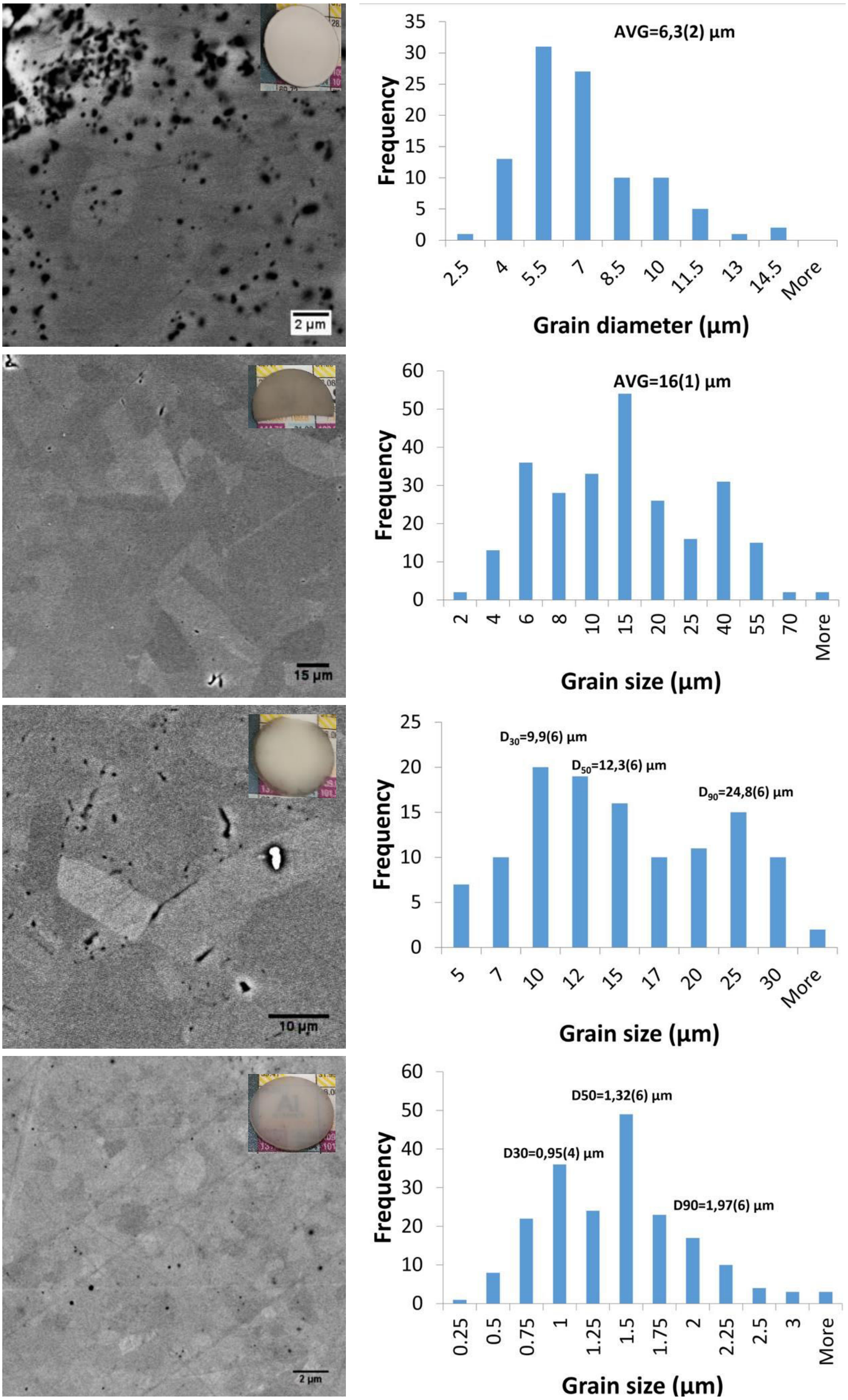

Figure 34. SEM micrographs of A5-A8 (top to bottom) with the grain size distributions.

A5-A8 (see SEM micrographs in Figure 34) were all sintered from α-Al_2O_3 powders, A5 from calcined boehmite and the rest from calcined UPA. A5 was chosen as a comparison, since α-Al_2O_3 crystallites from UPA have an elongated rectangular shape (crystallite length 250-300 nm, see [198]), remnant of the initial nanofibrous monolith. Unfortunately, the density of boehmite-received α-Al_2O_3 after sintering is only 94.1%, this is most likely due to the big agglomerate size of boehmite before calcination, creating hard sintered particles during calcination and needing more extreme sintering conditions for final densification via SPS. A6 on the other hand has high density (98.4%) and transparency (see section 3.2), interestingly accompanied by morphology of big long crystallite grains (average length 16 μm). To try and repress the lengthening of the crystallites, A7 and A8 were sintered under higher pressure, which is known to aid suppressing grain growth[143]. In the case of A7, we left the temperature cycle identical and just changed the applied pressure from 80 MPa to 200 MPa. To further investigate the power of high pressure, a short, 3-minute dwell sintering cycle at 282 MPa (maximum for our setup) was applied to A8. Interestingly, while the density of A7 is higher than that of A8, one can notice multiple elongated pores in the SEM image of A7, hinting to different pore size distribution of the two samples. This is in line with the optical opacity of A7 and translucency of A8, since optical absorption arises mostly from pores in the size range of the wavelength. Holding at high pressure for a long time (60 min) is thus counterproductive, leading to exaggerated grain growth and creation of closed pores characteristic to Ostwald ripening. Furthermore, the grain morphology of A8 is not elongated, proving the grain growth suppression abilities of higher pressure.

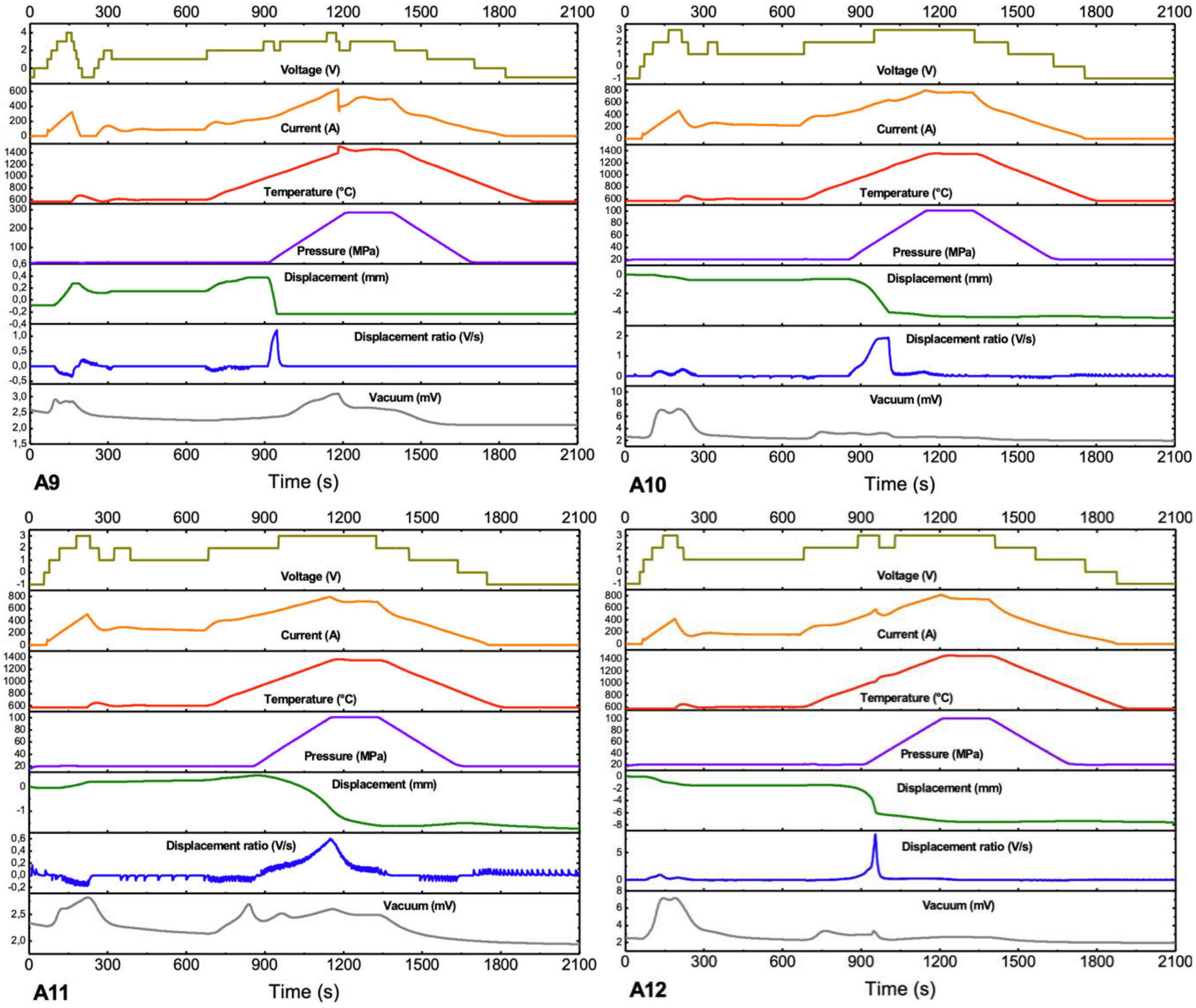

Figure 35. SPS data of A9 - A12.

Figure 35 shows the SPS data of samples A9 – A12, all sintered via the short cycle, A9 and A12 at 1450°C, A10 and A11 at 1350°C. The two pairs of samples demonstrate clearly different densification characterized by a narrow peak in densification ratio in the case of A9 and A12 signifying rapid densification at the moment pressure was applied, while the densification of A10 and A11 is slower. In the case of A9, the rapid densification can be explained by higher applied pressure (285 MPa), while for A12 the reason was most likely the added LiF. Additionally, comparing the displacement and the displacement ratio of A8 (P6, short, 285 MPa) and A9 (P6, short, 285 MPa + pre-pressing), it can be seen that re-expansion after pressure release only takes place in the case of A8.

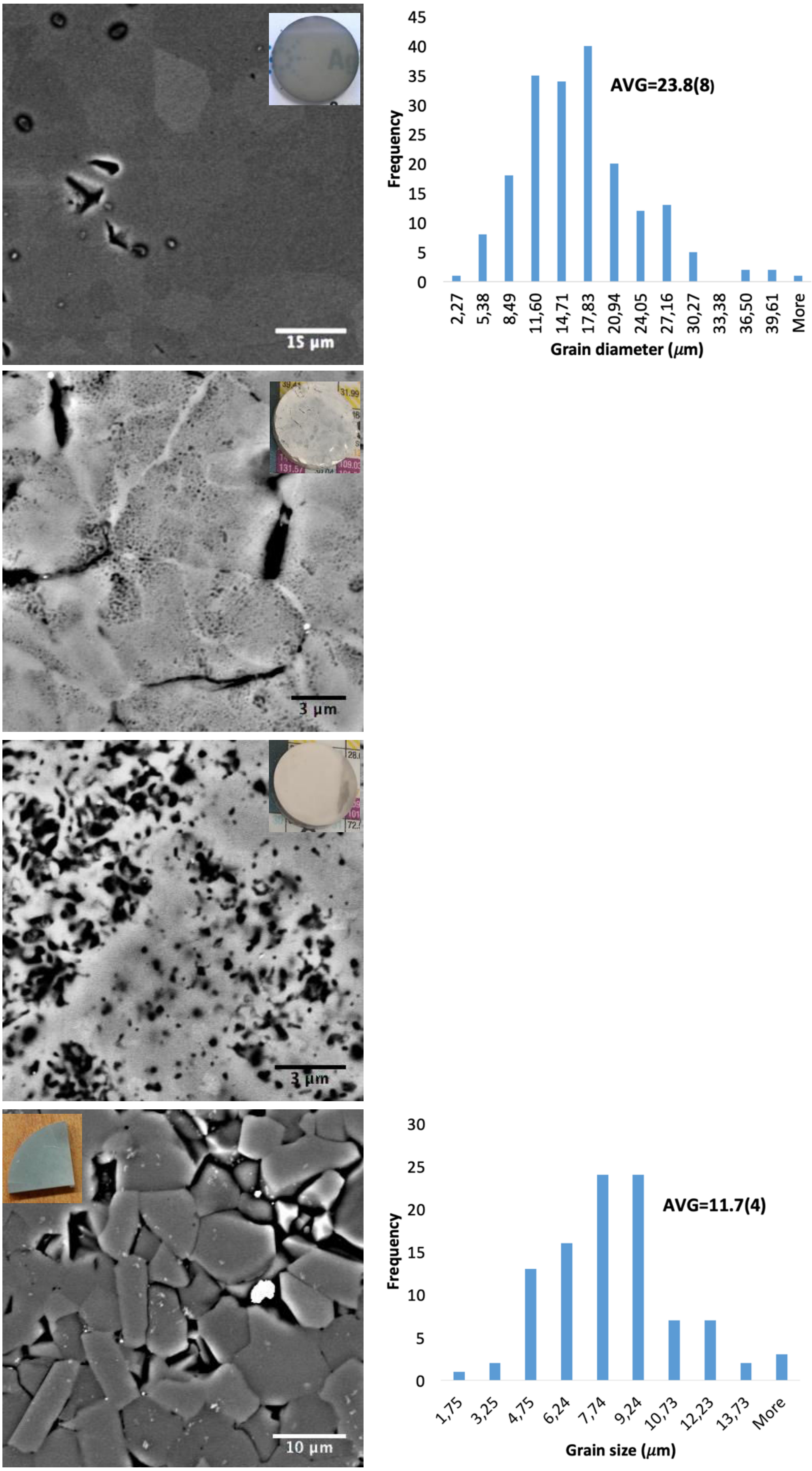

Figure 36. Morphology and grain size distribution of A9 - A12.

Figure 36 showcases the morphology and grain size distributions of A9 – A12. Sample A9 was sintered at identical conditions to A8, only differentiating factor being pre-pressing the powder in a stainless steel die at 4t to obtain the green body. This pre-pressing lead to a slightly denser sample with the grain size 18 times bigger than the directly sintered sample due to the increase in contact surface of the particles and thus resulted in exaggerated grain growth. This suggests that pre-pressing could be a useful tool to obtain denser green bodies and so soften sintering conditions. A10 and A11 were sintered via the short cycle at 1350°C, because this temperature has previously been shown as a maximal temperature to avoid excessive grain growth in alpha alumina[199,200]. Unfortunately, for our boehmite and alpha alumina powders this temperature was not sufficient to successfully carry out recrystallization of the powder into fully consolidated powder.

In the case of A10 (boehmite), big cracks have formed most likely due to the volume change accompanying the phase transfers and the final density reached only 89.3%. A11 (alpha alumina from boehmite) is much denser at 97.5% but a huge network of smaller pores can be observed via SEM. Wang *et al*[200] successfully used a very similar sintering tactic to fabricate AlF_3 doped alumina. However, even their seemingly opaque pure alumina showed about 10% transmission (at 600 nm, collected over 65°), while alumina doped with 0.5 wt% AlF_3 showed the worst transmission, <5% at 600 nm. To increase the sinterability, A12 was sintered from the boehmite powder doped with 1 wt% of LiF and the standard temperature of 1450°C, the slightly bimodal porous morphology will be compared with A13 sintered from α-Al_2O_3 in the next section.

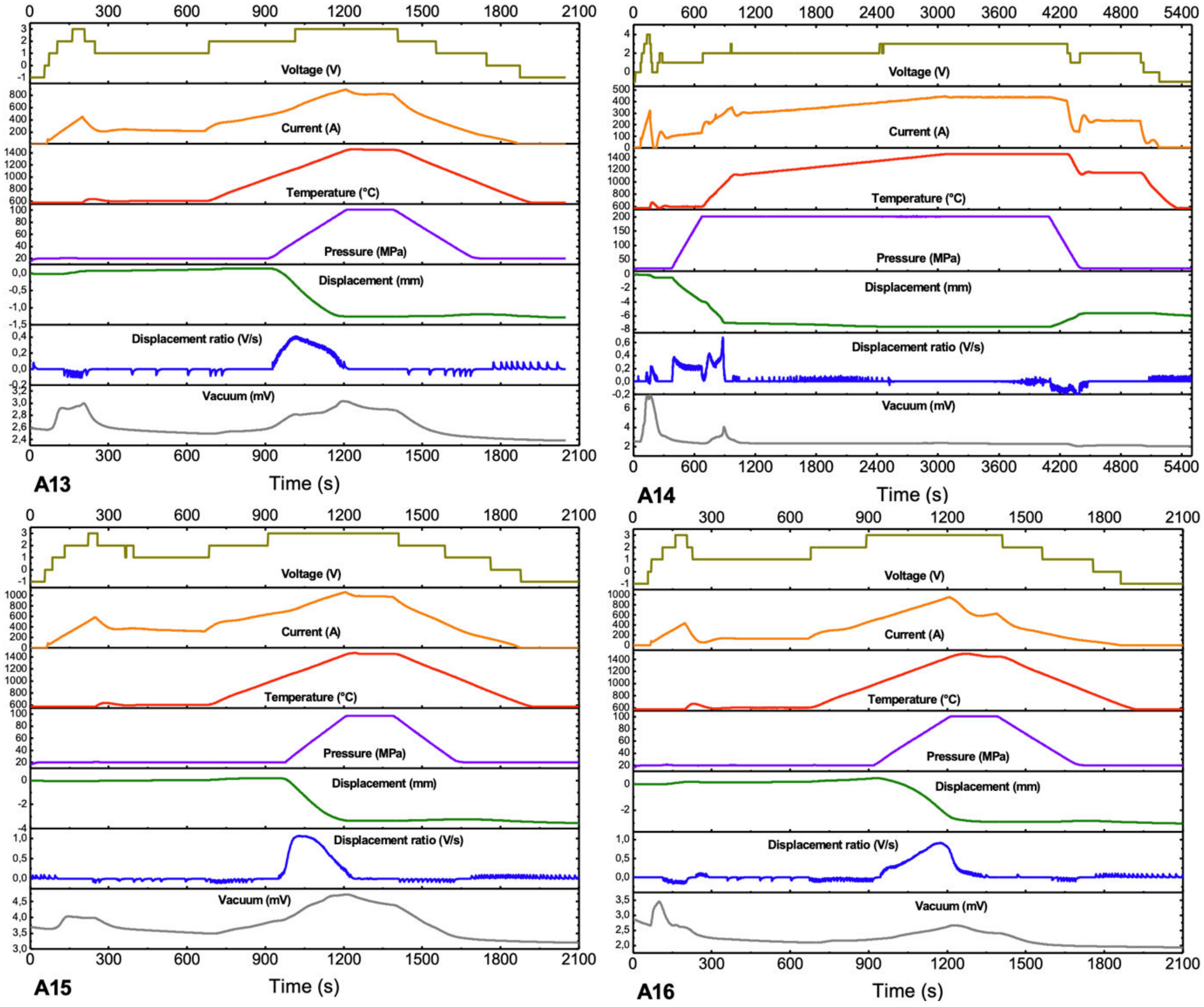

Figure 37. SPS data of samples A13 - A16.

The SPS data of samples A13 – A16 is presented in Figure 37. Compared to A12, the effect of LiF evaporation is more clearly visible during the temperature dwell of A13. Additionally, the majority of densification happens at the moment of pressure application in the case of A12 but lasts into the dwell for A13. The greater densification at pressure application can be explained by the lower density of the boehmite powder compared to α-Al_2O_3. The profiles of A14 follow those previously seen in the case of long sintering cycles and the compacting effect of higher pressure (200 MPa) is evidenced by big displacement and re-expansion after pressure release. Samples A15 (P6) and A16 (P5) are both sintered from α-Al_2O_3 and have identical densities. However, it can be seen from the displacement ratio profiles that in the case of A16, the majority of the densification takes place upon reaching the dwell pressure and temperature, whereas for A15, the densification is practically finished by this point. This can be explained by the more homogeneous particle size and morphology of P6.

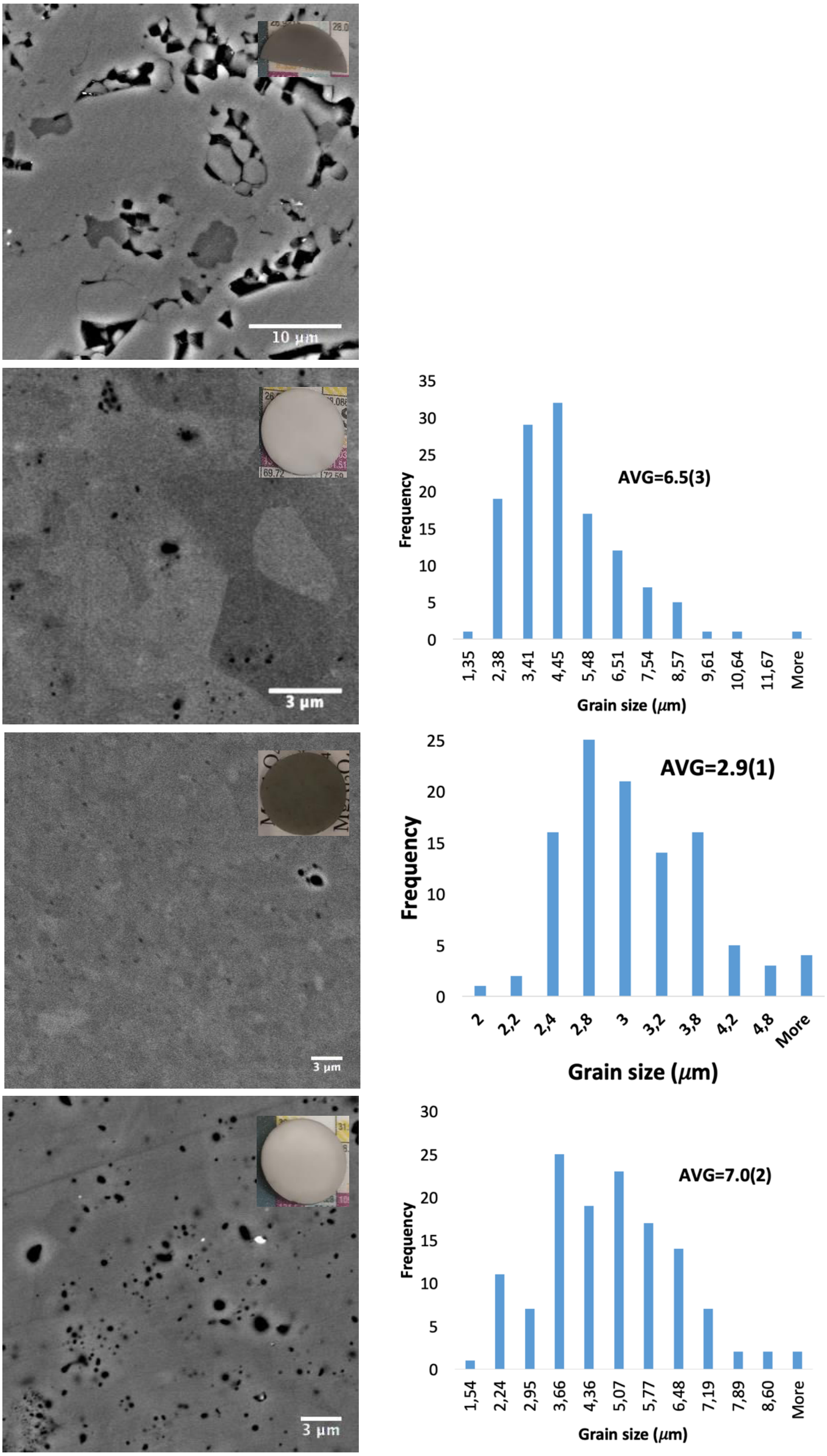

Figure 38. Morphology and grain size distribution of A13 - A16.

While A12 was sintered from the boehmite powder doped with 1 wt% of LiF, A13 (see Figure 38) was sintered from the boehmite powder calcined to alpha phase via the same short cycle at 1450°C. The hardness of these samples was so low that after only 5 minutes of grinding, the sample lost a lot of thickness, making an exact estimation of density difficult. Comparing the microstructures of A12 and A13, it is clear that A12 shows developing elongated grains alongside small grains, thus heading toward bimodal grain size distribution, while A13 shows the formation of first small grains along with darker islands on the BSE micrograph, hinting to the presence of a second phase. Thus, it seems that doping with LiF has a more beneficial effect on the sinterability when added to boehmite. Keeping in mind the applications of materials studied in this work, further research into LiF was stopped due to the greatly lowered hardness of the samples.

A14 was sintered via the long high-pressure cycle to compare the sinterability of alpha-alumina (UPA, A7) and boehmite. While the density of A14 is higher (99.4%) than A7's (97.4%) and grain size almost two times smaller (6.5 vs 12.3 μm), the optical quality of the sample is worse. This is most likely due to pore and dislocation creations related to the multiple phase transfers from boehmite to corundum and the less uniform morphology of boehmite, being more resistant to Ostwald ripening under high pressure. A15 was sintered via the short cycle in the hopes of obtaining a translucent sample like in the case of the same powder sintered via the long cycle (A6), while inhibiting the rapid grain growth. However, the gray appearance and relatively low final density of the sample leads us to believe that the dwell time was cut too short to achieve this goal. A16 was sintered from pure boehmite-derived α-Al_2O_3 (P5) to compare with LiF-doped A13 (P5 + LiF) and A15 derived from α-UPA (P6). Compared to A13, A16 has more developed grains and higher density, identical to that of A15 at 97.4%. The grain size of A15 is 2.9 μm, while that of A16 reaches 7.0 μm, proving the importance of small and homogeneous particle size of the precursor powder to inhibit excessive grain growth. Additionally, the amount of bigger, about 1.5 μm pores is higher in the case of A16, while A15 mostly shows pores sized about 0.5 μm, explaining the difference in the optical quality of the samples.

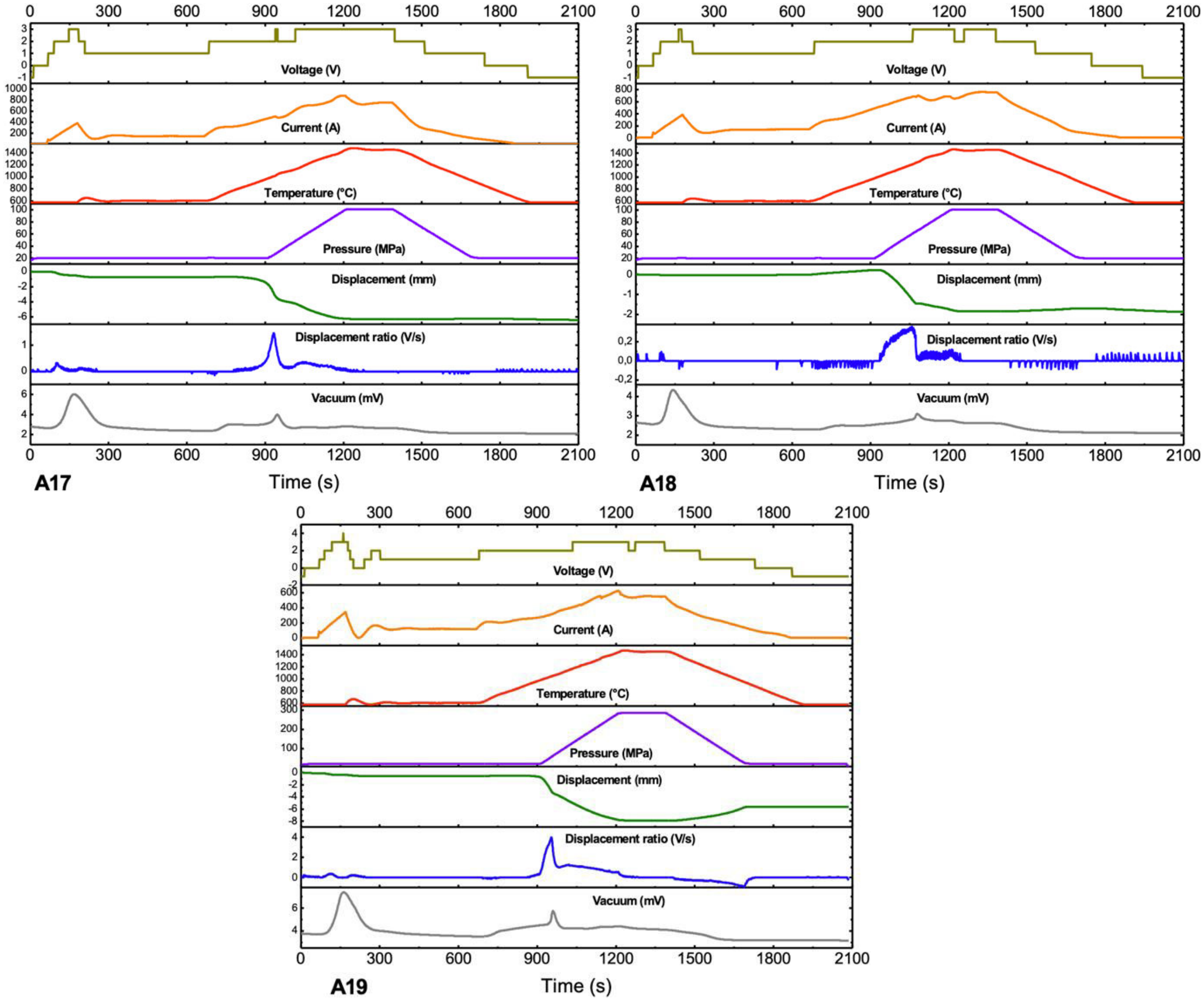

Figure 39. SPS data of samples A17 - A19.

Figure 39 showcases the SPS data profiles for samples A17 – A19, all in line with data shown for previous samples. Comparing the effect of the short (A17) and long cycle (A2) on P2, the densifications due to pressure and temperature are inversed. For A2, the first densification due to pressure application is much smaller than the second densification due to the change in heating rate. In the case of A17, the densification due to pressure application is greater, followed by a second densification due to raise in temperature until about 1200°C, which is known to be the temperature for the transition into α-Al_2O_3 phase. This point of phase transfer is not identifiable for A2. An analogical pair of samples are A18 (short) and A1 (long), sintered from a mixture of delta and gamma phases. Once again, the phase transfer into α-Al_2O_3 can be estimated from the displacement ratio profile of A18 to take place at around 1200°C. A19 was sintered via the short high-pressure cycle like A8, showing greater displacement due to the phase transfer from γ-Al_2O_3 to α-Al_2O_3.

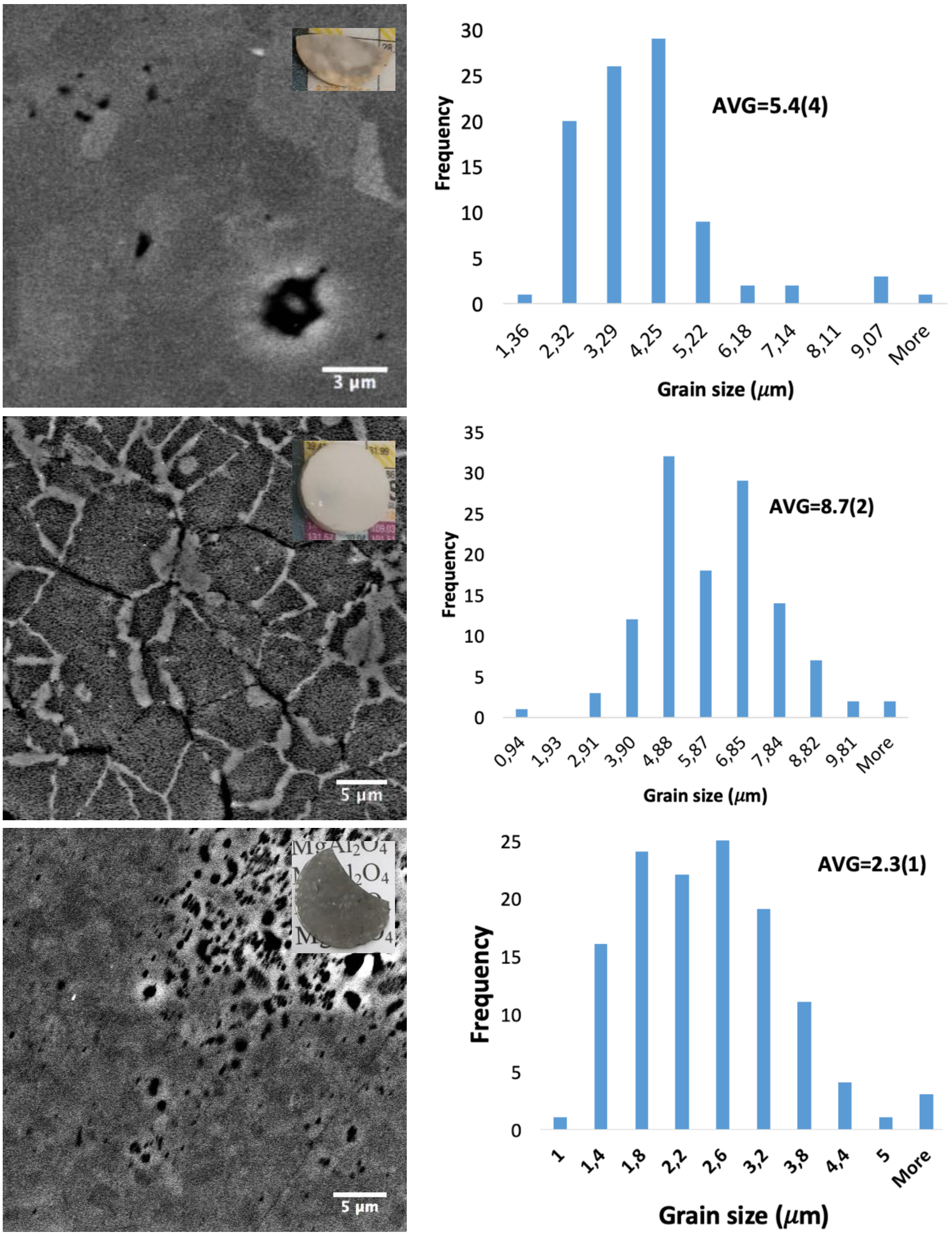

Figure 40. Morphology and grain size distributions of A17 - A19.

Short cycle counterparts were also sintered to A1 (A18) and A2 (A17, see Figure 40). The unexpected discoloration of A17 might be due to the presence of local high currents/temperatures. Both of these samples are opaque with respective densities of 96.3% and 92.8%. This result is somewhat surprising, taking into account that A2 is denser than A1, leading us to believe that the mixed delta/gamma-alumina phase densifies faster than the pure gamma-alumina in the beginning of the cycle (or during the short cycle) but then densification slows down. A19 was sintered via the short high-pressure cycle to obtain as good optical quality as A2 while keeping the grain size small. However, the optical image and SEM micrograph reveal a high concentration of pores in the material, hinting to exaggerated grain and pore growth characteristic to Ostwald ripening brought on by too high sintering temperature. This is confirmed by a low final density of 95.5%. However, the high sintering pressure allowed us to decrease the grain size of A19 to 2.3 µm compared to the 4.9 µm of A2.

In conclusion, the highest condensed ceramic density (96.3%) when starting from a delta-gamma alumina precursor (P1) was achieved via the short cycle at 1450°C (A18) with characteristic by grain size of 8.7 µm. In the case of P2 (pure gamma alumina), the highest density (98.0 %) was reached via the long cycle at 1450°C (A2), exhibiting grain size of 4.9 µm and transmittance of 7.8% at 650 nm. In the case of boehmite powder (P3), the most successful sintering cycle was the long cycle at 1450°C and 200 MPa (A14), allowing us to obtain a relative density of 99.4% and grain size of 6.5 µm. However, despite the high relative density, A14 is white in appearance, most probably due to the presence of big, micrometric pores in the material. Ultrasonification of the boehmite powder (P4) lead us to obtain slightly higher density sample (A3) than untreated boehmite with 3.2 times bigger grain size of 24 µm. In the case of α-Al_2O_3 obtained from the boehmite powder (P5), we obtained the best results via the short cycles at 100 MPa, proving the need of higher pressure to further densify crystallites already sintered together during the calcination. For α-Al_2O_3 obtained from UPA (P6), the highest density (98.6%) was reached via the short cycle at 1450°C and 285 MPa with pre-pressing (A9). However, the grain size of A9 was 18 times bigger than that of A8 obtained by the same cycle with no pre-treatment, which showed 2% lower density and similar transparency.

4.3 Optical transmission

Samples with enough transparency for optical measurements were A2 obtained from γ-Al_2O_3 precursor via the long cycle at 1450°C, A6 obtained from the UPA-derived α-Al_2O_3 via the long cycle at 1450°C, and A8 obtained from the same precursor via the short cycle at 1450°C and 285 MPa. The transmission spectra of these samples are presented in Figure 41. The transparency of the samples decreases in the following order: A8 > A2 > A6. However, it should be noted that the thickness of the sample is 0.8 mm in the case of A2 and A8, but 1.1 mm in the case of A6. The consequences of this factor unveil when discussing the absorption coefficients in chapter 4.6.

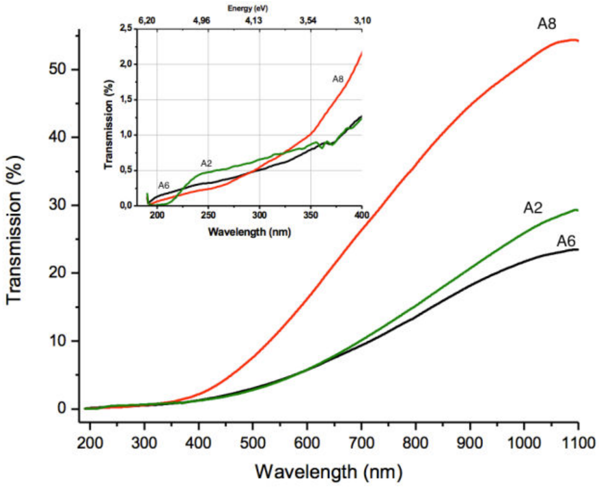

Figure 41. Transmission of translucent samples A2, A6 and A8.

The best result for an alumina ceramic with high transparency but fine microstructure (1.3 μm) was obtained by using UPA α-Al_2O_3 powder with a short sintering cycle at 284 MPa (A8). Similarly, raising the pressure to 500 MPa allowed Grasso et al [143] lower the sintering temperature to 950-1000°C and almost totally suppress grain growth.

4.4 Texturation studies

Two types of crystallographic texturation studies were carried out in this work to understand the effect of SPS to any preferential crystallographic orientation. Firstly, electron backscattering diffraction (EBSD) mapping on one translucent sample (A2) was carried out in LSPM. Secondly, XRD quantitative texture analysis was carried out on another translucent sample (A9) in CRISMAT-ENSICAEN by D. Chateigner. The drawback of both of these investigations is their extended length, thus we wished to establish if any specific texturation arises from SPS and if it should be a topic of further research.

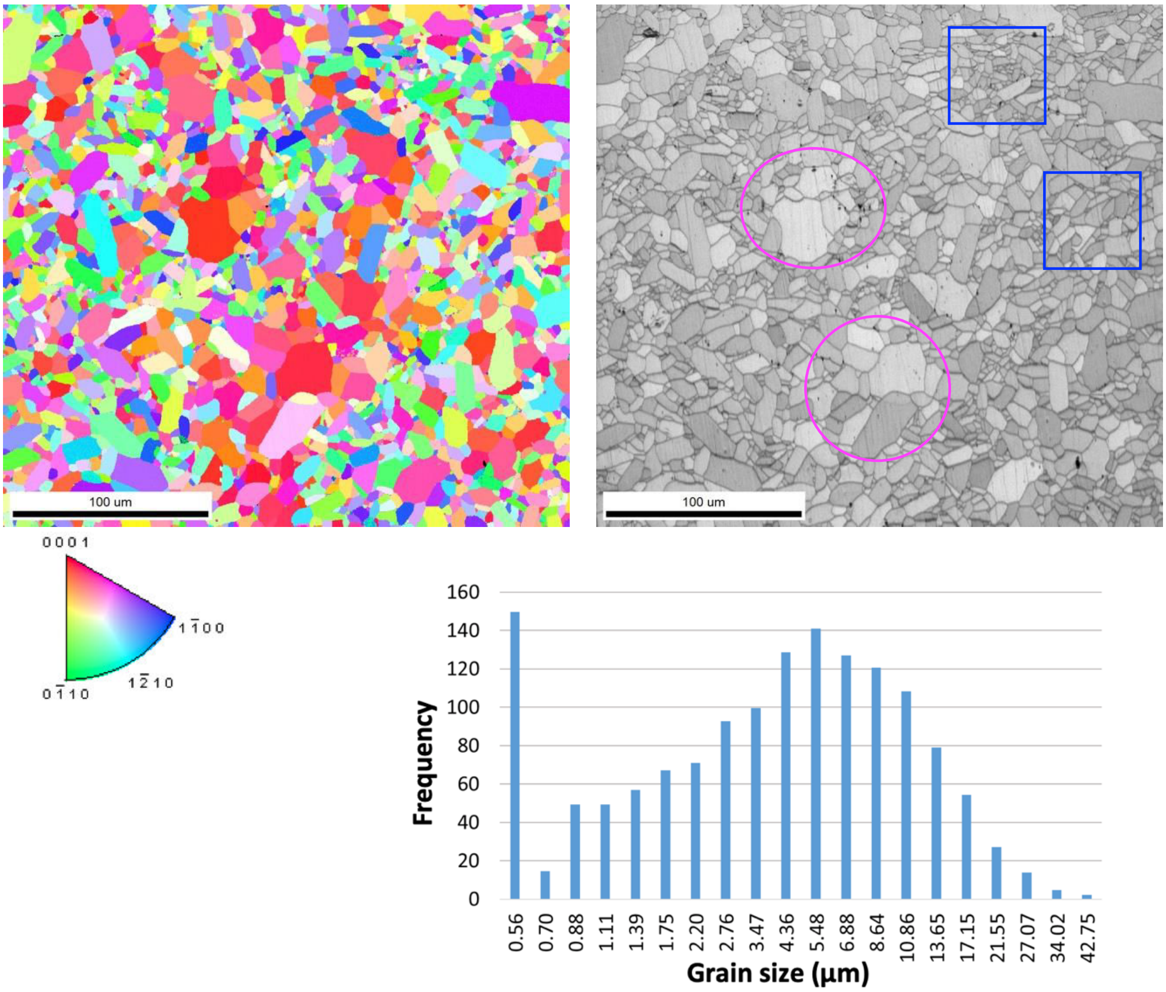

Figure 42. EBSD cartography of A2 and surface-averaged grain size from EBSD analysis.

Figure 42 shows the results of EBSD mapping of A2 carried out to confirm the validity of measuring the ceramics' grain sizes from SEM images and investigate the potential preferential orientation of the grains. EBSD analysis shows no preferential orientation of crystallites, meaning no strong texturation is created during the SPS process. The average grain size obtained from SEM micrographs (4.9(2) µm) is in agreement with the average grain size of ~6 µm from EBSD analysis, taking into account the presence of grains with size >10 µm that were not visible in the SEM micrographs. Similarly, grains smaller than 500 nm are difficult to measure due to low contrast (see the grain boundaries overlapped to the SEM images on the right side of Figure 42). The somewhat scattered bigger grains (compare the areas surrounded by ovals and rectangles in the SE image) are most likely due to so-called 'hot spots' formation during SPS, where the current distribution localizes into a small area, creating local higher temperatures and even melting [201,202]. In comparing the crystallite orientation map with the SE image overlapped with the detected grain boundaries, we can conclude that the produced ceramic consists of monocrystalline grains, which are preferable for obtaining good optical properties.

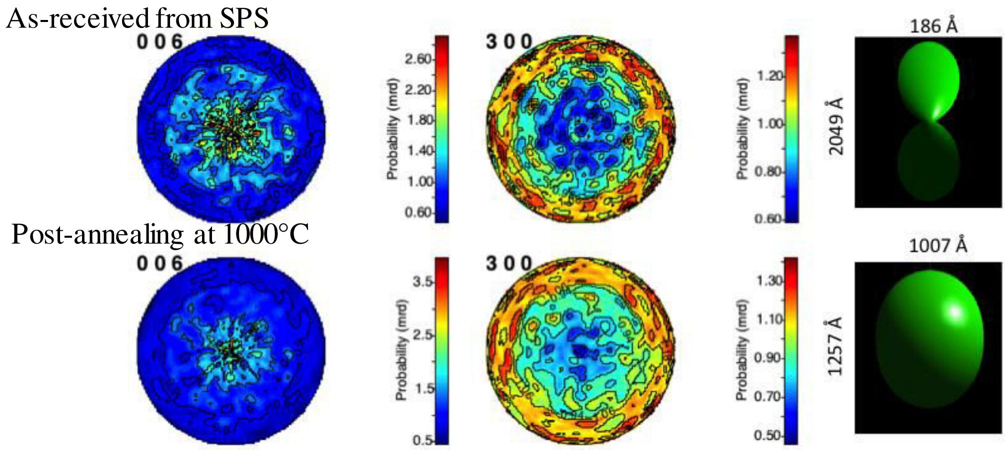

Figure 43.Quantitative texture analysis: {006} (left) and {300} (middle) pole figures and anisotropic mean crystallite shape (right, correct scale relative to each other) (right) for non-annealed(top) and annealed sample (bottom) obtained after OD refinement (linear density scale, equal area projection)

To go even further, XRD texturation study was carried out on A9 before and after annealing at 1000°C during 1h (heating and cooling rates 5°C/min) to relax strains. The texturation study was carried out with the help of a four-circle diffractometer equipped with a curved position sensitive detector, using the monochromatized CuK_{α} average radiation. 2Θ diagrams using a regular 5° × 5° grid in tilt and azimuth angles (χ and ϕ respectively) with $0° \leq \chi \leq 55°$ and $0° \leq \phi \leq 355°$ were measured, resulting in 864 diagrams, each one exhibiting nearly 4000 measured points. The sample reference frame is given by the SPS direction of pressure, PSPS, which corresponds to the centers of the pole figures (Z). We could not detect any residual strains within our experimental resolution, that is, the residual stresses, if existing, are estimated lower than 10 MPa.

The pole figures for the {006} and {300} crystallographic directions of corundum (see Figure 43) are showing the preferred orientation stabilized in the two samples. Both samples

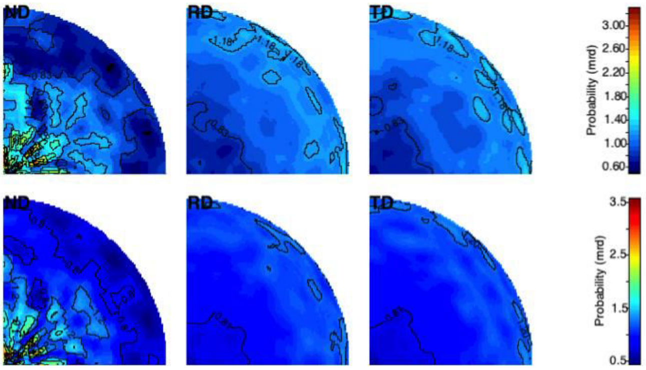

Figure 44. Inverse pole figures for the main sample directions r (ND), x (RD) and y (TD).

exhibit fiber texture with fiber axis corresponding to the mean c axis of the crystalline structure. The maxima of the OD (orientation distributions) are of 23.6 multiples of a random distribution (m.r.d.) for non-annealed and 29.1 m.r.d. annealed sample. The maxima in the {006} pole figures are of 2.9 m.r.d. and 3.9 m.r.d., respectively. After annealing, the averaged crystallite shape grows slightly, becoming rounder. The overall texture index and fraction of texture components were determined from the inverse pole figures in Figure 44, which are plotted for the main sample directions r (ND), x (RD) and y (TD). The overall texture strength index F^2 of 1.32 and 1.50 m.r.d.^{2}, respectively, point toward a relatively moderate texture strength. Only one component of texture exists, counting for the whole volume, which can be compared favorably with the textures observed in corundum ceramics elaborated by other techniques[203]. The refinement converges to unit-cell parameters and atomic positions close to the usual values, with no significant variation between the two samples (see Table 3).

Table 3. Refined parameters for the as-received A9 and after annealing at 1000°C.

Sample	OD min (m.r.d.)	OD max (m.r.d.)	F^2 (m.r.d.)	Cell parameters (Å)	Atomic position
RT	0	23.6	1.32	a=4.77105(5) c=13.0476(2)	zAl=0.35223(3) xO=0.69762(5)
1000°C	0	29.1	1.50	a=4.78335(6) c=13.0571(2)	zAl=0.35222(2) xO=0.69768(5)

In conclusion, the XRD texture analysis shows mild texturation with aligned crystalline structure c-axis and the pressure axis of SPS. Upon annealing, the texturation increases slightly due to possible growth in the number of accumulated defects attempting to release energy, reinforcing the texture. Additionally, the mean crystallite size grows slightly and the shape of the crystallite becomes rounder upon annealing.

Overall, according to these two case studies, the SPS does not create significant texturation in the resulting ceramics. However, EBSD is a useful tool for obtaining the grain size distribution of materials with grains smaller than a micron.

4.5 HIP post-densification

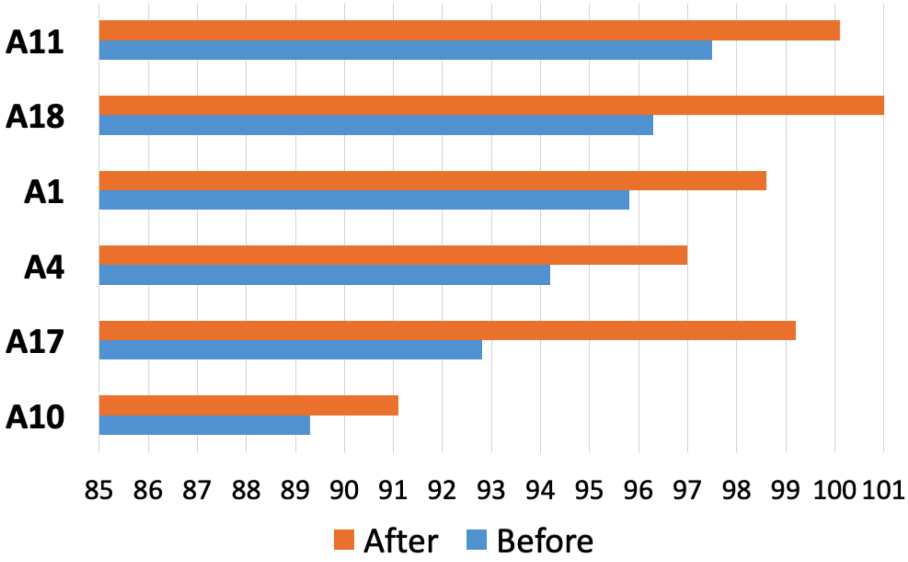

Figure 45. Alumina sample relative densities before and after HIP.

HIP post-densification was carried out on samples A1, A4, A10, A11, A17 and A18 in the hopes of improving their density and optical quality. These samples obtained from low-temperature alumina polymorph precursors were chosen to test the post-densification power of HIP.

The HIP dwell was set to 1250°C during 3 hours at argon pressure of 200 MPa. This temperature was chosen to limit any further grain growth, as it is 100°C lower than the lowest sintering temperature[160]. The changes in density are shown in Figure 45. Two samples obtained full density, A18 starting from 96.3% and A11 starting from 97.5%. A10 did not reap great benefits from HIP, as it's starting density was low (89.3%) and only further densification by 1.8% was achieved.

Optical observation showed no difference in the samples before and after HIP. The SEM micrographs of all samples before and after post-densification are shown in Figure 46. No significant change in microstructure or upon visual observation can be detected for any of the samples.

Thus, HIP is a good tool for densification, but it did not encourage microstructural changes in our samples at a temperature 200°C lower than the SPS temperature at double the pressure.

An interesting perspective is brought up by authors who believe that the most economical and effective way of combining SPS with HIP is to carry out short SPS at slightly lower temperature than the second step HIP (10 min at 1200°C SPS + 3h at 1230°C HIP[155]).

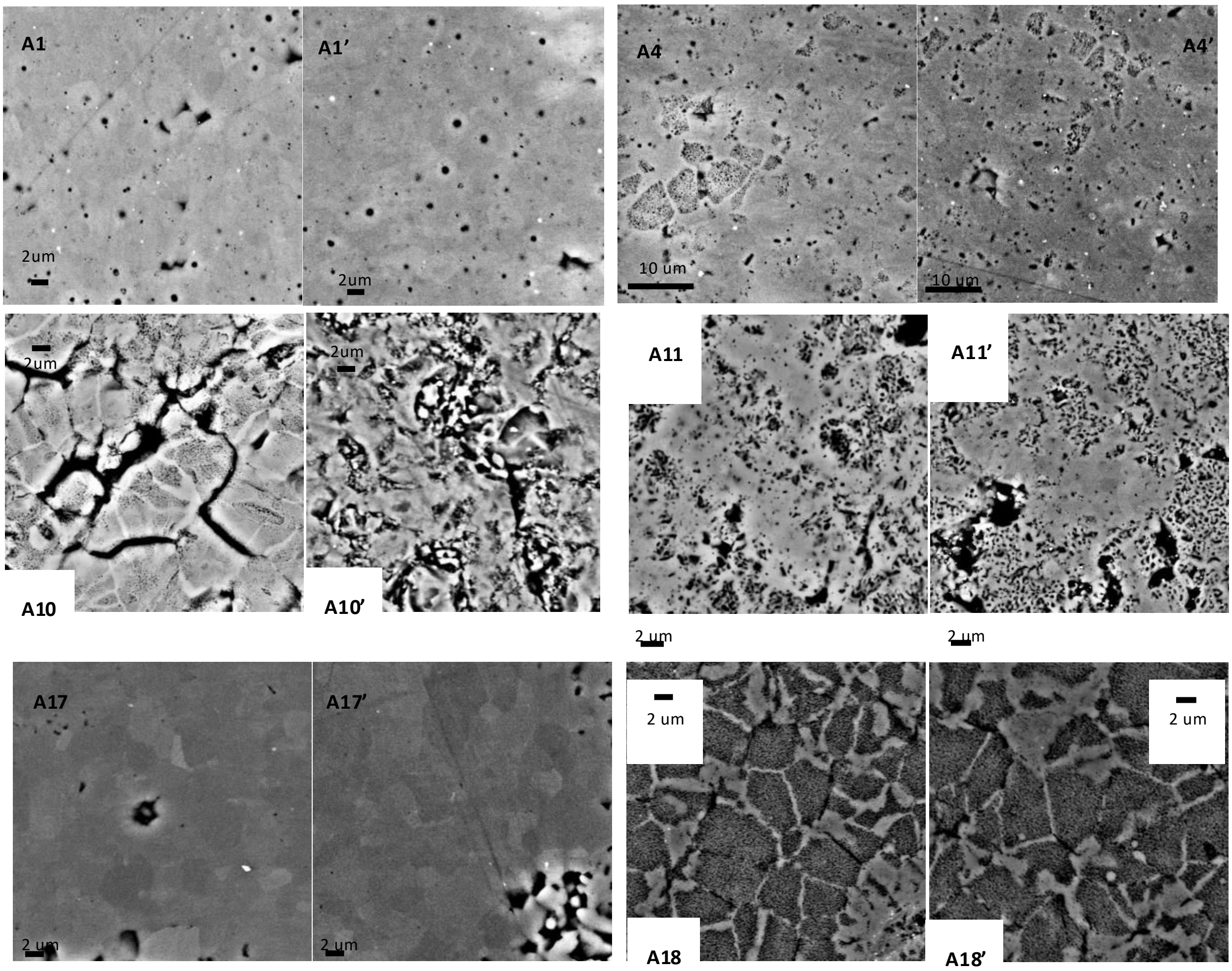

Figure 46. Microstructure of alumina samples before and after HIP post-densification.

4.6 Absorption

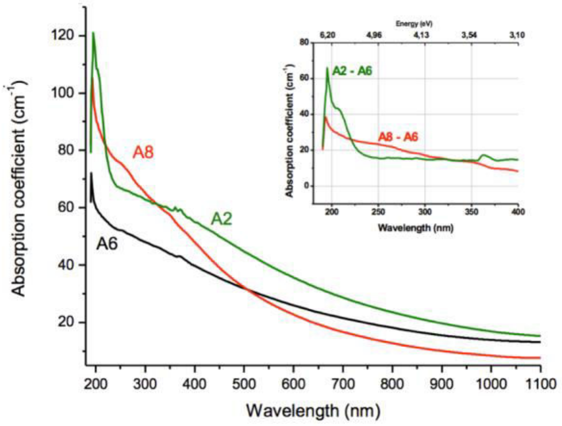

Figure 47. Absorption coefficient for samples A2 (0.8 mm), A6 (1.1 mm) and A8 (0.8 mm).

Absorption coefficients were calculated for translucent samples from the transmission data because this physical parameter takes into account the sample thickness and peaks in absorption spectra can be linked to defects in the material. Thus, absorption coefficient, for our work, is physically more meaningful than mere transmission spectra.

The calculated absorption coefficients of translucent samples A2, A6 and A8 are shown in Figure 47. Additionally, the inset of Figure 47 shows the absorption coefficients of A2 – A6 and A8 – A6 in the range of 190 – 400 nm to better demonstrate the present absorption bands. As mentioned before, A2 is sintered from pure γ-Al_2O_3 and A6, A8 from α-Al_2O_3 (UPA). Thus the similar overall shape of the spectra is to be expected. At 500 nm, our samples had following transmission values: A2 and A6 ~3%, A8 ~10%, compared to maximal theoretical value of ~40% in the case of 0.8 mm thickness and 0.5 μm grain size[204]. Observing the absorption coefficient, the most translucent sample in the 200 – 500 nm range is A6, while from thereon A8 becomes more transparent. To effectively take into account different sample thicknesses, we will here mostly focus on the analysis of the absorption coefficient.

It has been shown for Al_2O_3 single crystals that absorption bands in the range of 200 – 255 nm are related to single defects, more specifically, absorption at ~205 nm corresponds to F centers and absorption at ~255 nm to F^+ centers [205,206]. Slight increase in absorption coefficient of A8 at about 250 nm is known to be brought up by Fe impurities[207], but this is unlikely because of the high purity of UPA powders[121], leading us to attribute it to the ~255 nm absorption of F^+ centers. Absorption at ~357 nm has been related to F_2^+ centers[205], two oxygen vacancies trapping three electrons, known to form in alumina from F⁺ centers when heated at T>350°C. The origin of small bands between 360 and 375 nm has not been identified.

4.7 Luminescence

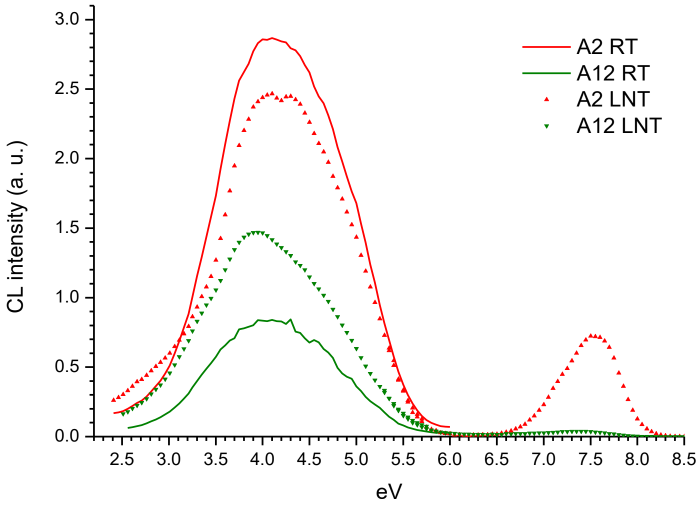

Figure 48. CL spectra of A2 and A12 at room temperature (RT) and liquid nitrogen temperature (LNT).

The cathodoluminescence spectra of A2 and A12 are shown in Figure 48. Interestingly, the luminescence intensity is higher at room temperature (RT, 293 K) in the case of A2 and at liquid nitrogen temperature (LNT, 77K) in the case of A12. A2 was chosen due to its high transparency and A12 was measured to confirm the absence of LiF additive in the final sample, as luminescence can arise from a few ppm impurity content.

Compared to the work of Boumaza *et al*[170,208], our measured CL spectra are less defined, so it is difficult to estimate the exact underlying emissions included in two broad bands in the ranges from 2.5 eV to 5.8 eV and 6.5 eV to 8.5 eV. According to them, there are 4 somewhat distinct peaks in the first range, at about 2.42, 3.91, 4.42 and 5.03 eV. The first of these emissions is not present in our samples. However, an emission at about 3.2 eV, linked to F centers[209] is present in our samples as well as Boumaza *et al*[170] boehmite-sourced sample. This emission is more clearly distinguishable in the spectra measured at LNT. The band at 3.91 eV connected to F⁺ centers is one of the two most intense emission present in our samples. The second intense band is at about 4.4 eV, in line with the emission of disputable origin mentioned by Boumaza *et al*[170]. It is believed that this emission only arises if the excitation density is high. The low-intensity emission at about 5 eV is known to be accompanying to interband transitions.

The vacuum ultraviolet (VUV) emissions are less researched but a similar band as the A2 LNT 6.5 – 8.5 eV has been observed by Lushchik *et al*[171] by CL in corundum single crystal, covering the same range but being more symmetrical. Interestingly, in their case the wide lower-energy band is of much lower intensity than the VUV band. The VUV band is very weak in A12.

4.8 Summary of alumina ceramics

In conclusion, the investigation of sintering various alumina precursors via different SPS cycles resulted in a total of 4 translucent samples (A2, A6, A8, A9). Three out of these four samples were sintered from UPA-derived α-Al_2O_3 (P6). Thus, for following spinel reactive sintering investigations, we will utilize this precursor powder.

We found that the best way to avoid excessive grain growth while still obtaining a translucent sample is to use higher (285 MPa) sintering pressure combined with a short, 3-minute dwell at 1450°C. However, for optimization purposes and analyzing the resulting microstructure of all ceramics obtained via this cycle, an optimization of the sintering temperature should be carried out through a dilatometric study.

The carried out two texturation studies via EBSD and XRD showed no significant texturation, thus allowing us to conclude that the uniaxial pressing via SPS does not induce significant texturation. However, we recognized that EBSD analysis is an advantageous tool for characterizing the grain size distribution of fine-grained ceramics or ceramics with bimodal grain size distribution.

HIP post-densification was shown to be a powerful process to help with densification while conserving previous microstructure, at least in the case of relative sample densities greater than 92%.

The absorption and luminescence analysis revealed the presence of various color centers, with their relative concentrations in line with the optical properties of the ceramics.

5 Spinel ceramics

The goal of the second part of this PhD project is to determine the best precursor production method for the reactive sintering of Al_2O_3 and MgO mixture into monophasic pure spinel. The short and long cycle at 1450°C previously used to sinter alumina are once again carried out here with spinels for comparison reasons. To optimize the sintering conditions of each powder, dilatometric studies were carried out to determine the ideal sintering temperature. Additionally, Ta_2O_5 doping is investigated as a possible tool for reducing the grain size of the sintered ceramics.

In this chapter, three different routes to obtain fully dense transparent spinel ceramics were tested. Firstly, a commercial spinel powder was directly sintered without any pretreatment as a reference. Secondly, stoichiometric amount of MgO was synthesized by the polyol method in the presence of the previously determined as most promising alumina precursor, UPA-derived α-Al_2O_3. Lastly, MgO impregnation of the same alumina precursor was carried out via cycles of doping with $Mg(NO_3)_2$ water solution.

In the beginning of each section, the precursor powders and obtained samples are characterized by SEM and XRD, providing information on their morphology and crystalline structure. The sintering cycles are described and collected SPS data is presented to describe the sintering process. The optical quality of the samples is described and the transmittance measured where possible. Additionally, most promising samples are characterized by luminescence to characterize the defects present in the materials before and after proton irradiation.

5.1 Sintering commercial spinel

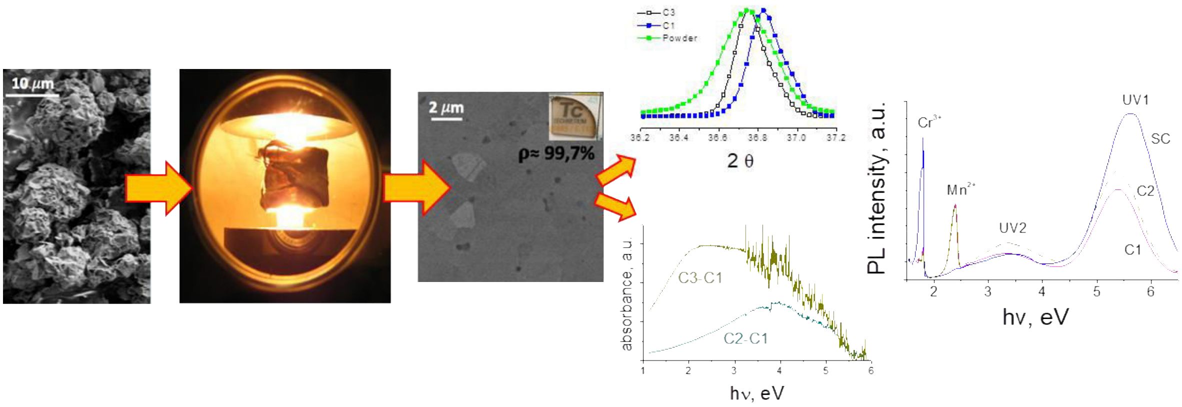

Spinel powder (Sasol GmbH) with average particle size of about 20 µm was directly used for sintering without any pretreatment. The powder particles are assembled from thin platelets (see Figure 49 A). The producer estimates the content of impurities to be in the range of 1 to 5 ppm. The spinel (~98.8 wt%, a=8.0875(1) Å) crystallite size of the powder was determined to be ~115 nm by analyzing the XRD pattern (see Figure 49 B) with Maud[182]. The XRD analysis also revealed the presence of MgO phase (~0.73 wt%, *a*=4.3532(2) Å, crystallite size ~130 nm) and α-Mn impurity (~0.47 wt%, *a*=8.9479(2) Å, crystallite size ~40 nm).

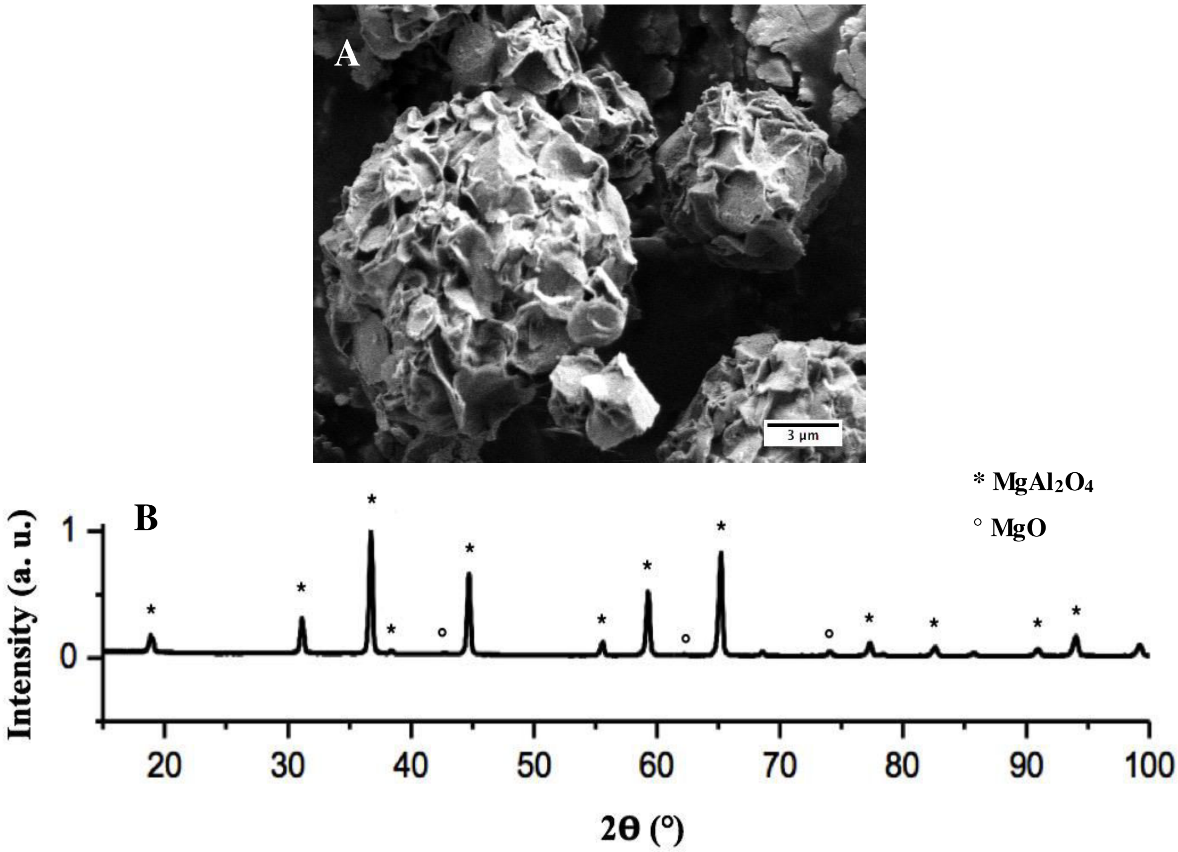

Figure 49. A: SEM micrograph and B: XRD pattern of commercial spinel powder.

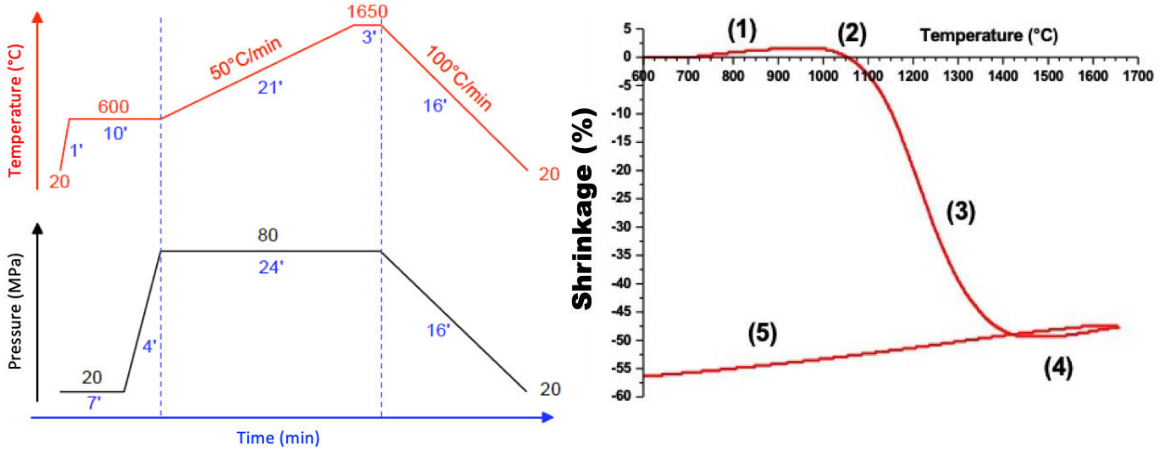

Figure 50. Scheme of the dilatometric cycle (left) and the dilatometric curve of the commercial precursor.

Firstly, a dilatometric study (see cycle scheme in Figure 50 left) of the precursor powder was carried out, using heating rate of 50°C/min from 600°C to 1650°C, holding for 3 minutes and cooling the sample at the rate of 100°C/min. The pressure was applied upon heating up from 600°C and kept constant until the end of the dwell, then released alongside sample cooling. The resulting dilatometric curve can be seen in Figure 50 (right).

Step (1) on the dilatometric curve represents water evaporation and thermal expansion along with recrystallization. Next, step (2) of sintering is characterized by rearrangement of precursor powder grains and the formation of sintered necks at particle contact points, sintering begins. During step (3), adjacent necks trespass each other, bringing about densification and grain growth, closing off porosity. The contact point between points (3) and (4) defines the optimal sintering temperature, any further heating leads to rapid grain growth and thermal expansion. Finally, during cooling (5), the sample retracts.

In the case of the commercial spinel powder, the optimal sintering temperature was determined to be 1430°C from Figure 50 (right), very close to the 1450°C used to sinter alumina in the last chapter, thus the latter temperature was used. Additionally, 1300°C was chosen to avoid the end of densification and rapid grain growth.

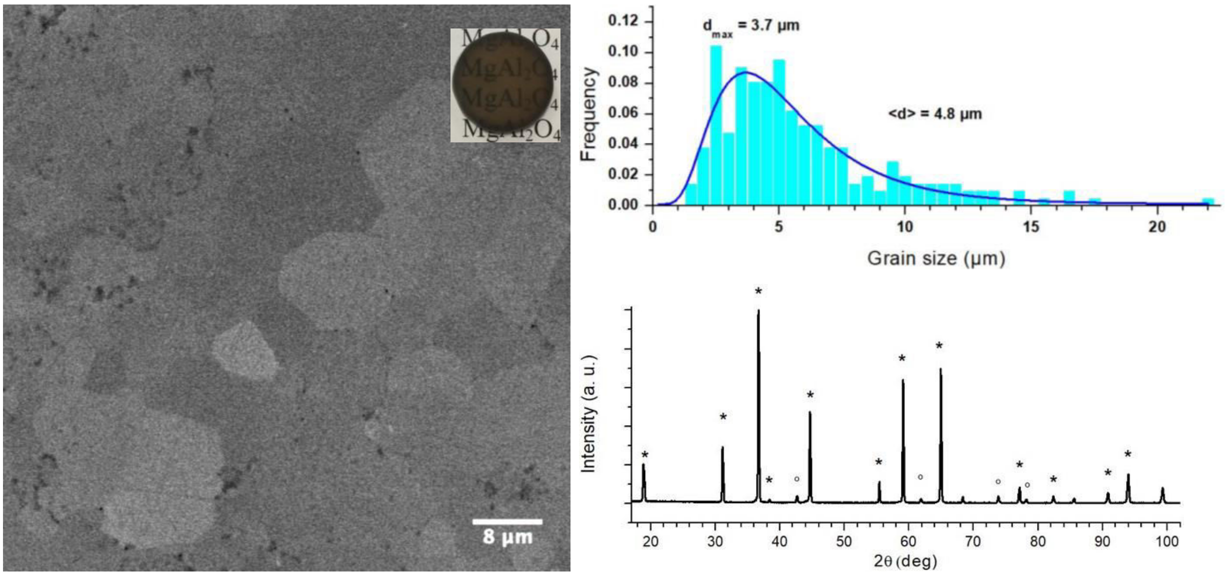

Figure 51. Results of the dilatometric study: SEM micrograph, grain size distribution and XRD profile (denotes spinel and ° MgO (periclase)).*

Figure 51 shows the microstructure, grain size distribution and XRD profile of the ceramic obtained via the dilatometric cycle along with the optical image. It can be seen that while the sample is translucent (transmittance about 45% at 650 nm), the grain size distribution is multi-modal, with maximums at 3.7 and 9.0 µm. The long tail of larger grains in the grain size distribution can be explained by the high sintering temperature and thus started exaggerated grain growth.

Following the dilatometric study, two types of sintering cycles were again used to obtain consolidated ceramics, the long and short cycle (see Figure 52), where T_f was modified according to the optimal temperature retrieved from the dilatometric study. Firstly, samples C1 and C2 were sintered (see Figure 53 A) via the long cycle scheme where the only varied parameter was the temperature of the first 20’ dwell, thus comparing samples C1 and C2 gives

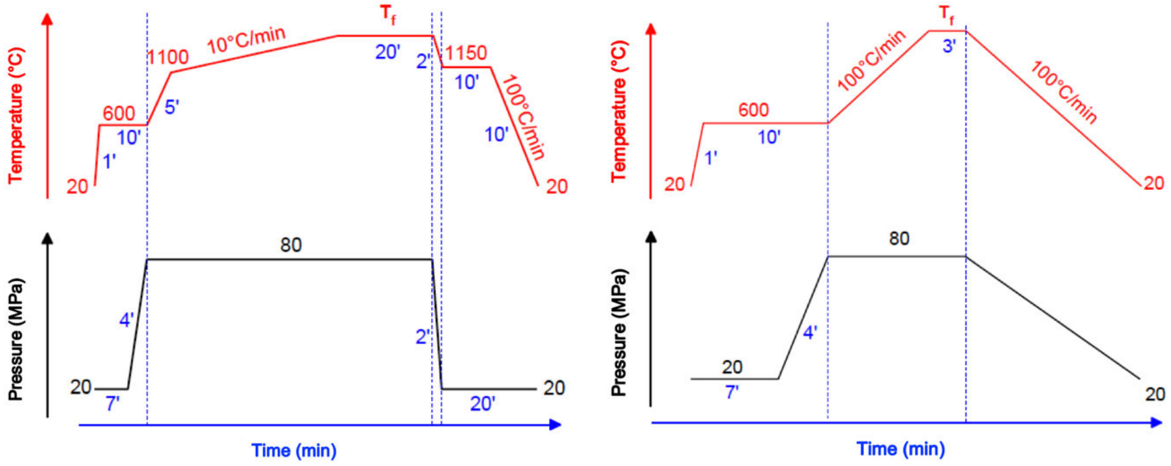

Figure 52. Schemes of the long (left) and short (right) sintering cycle. T_f denotes dwell temperature.

us an idea about the effect of sintering temperature. Samples C3-C5 investigate (see Figure 53 B) the best pressure application point for the short cycle with a constant heating rate of 100°C/min and a 3-minute temperature dwell at 1300°C. Additionally, C6 (see Figure 53 C) was sintered via the short cycle at 1450°C to compare the difference with the long cycle at 1450°C.

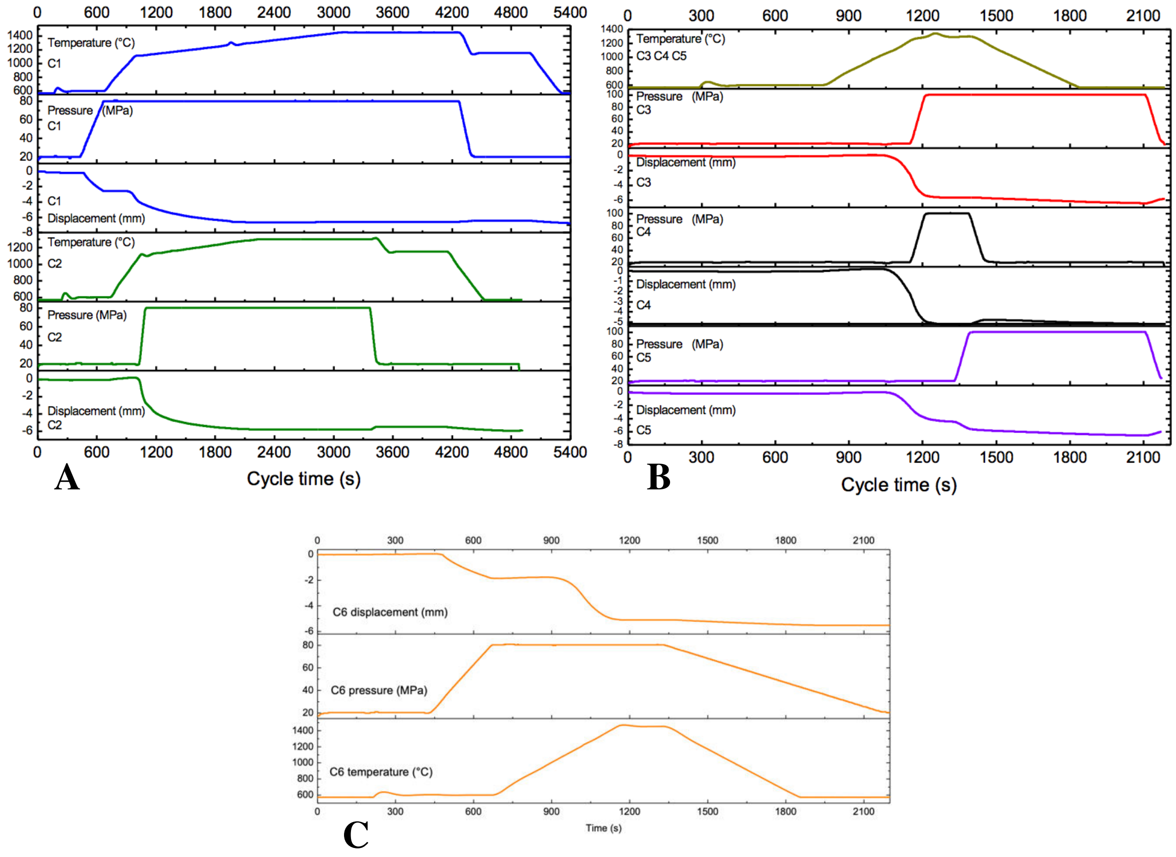

Figure 53. Sintering temperature and pressure with sample displacement for A: C1 and C2; B: C3, C4 and C5, C: C6.

From the displacement profile of C1 in Figure 53 A we can notice densification in two steps, first while the pressure is raised to 80 MPa and second as the sample is heated up from 1100°C, connected by a plateau during heating up to 1100°C. The re-expansion of the sample after releasing the pressure is insignificant. In the case of C2, the densification starts with the pressure application and continues uniformly until about 1250°C is reached, after which the densification is plateaued. Comparing the different pressure application points of C3 – C5 in Figure 53 B shows a distinguishable difference between densification by temperature and pressure only in the case of C5, where the pressure was applied after the dwell. In the case of C6 (Figure 53 C), this distinction can also be made, as the pressure is raised to the dwell value before the temperature is raised above 600°C. The densification plateaus for the duration of heating until about 1100°C and then restarts until the dwell temperature is reached.

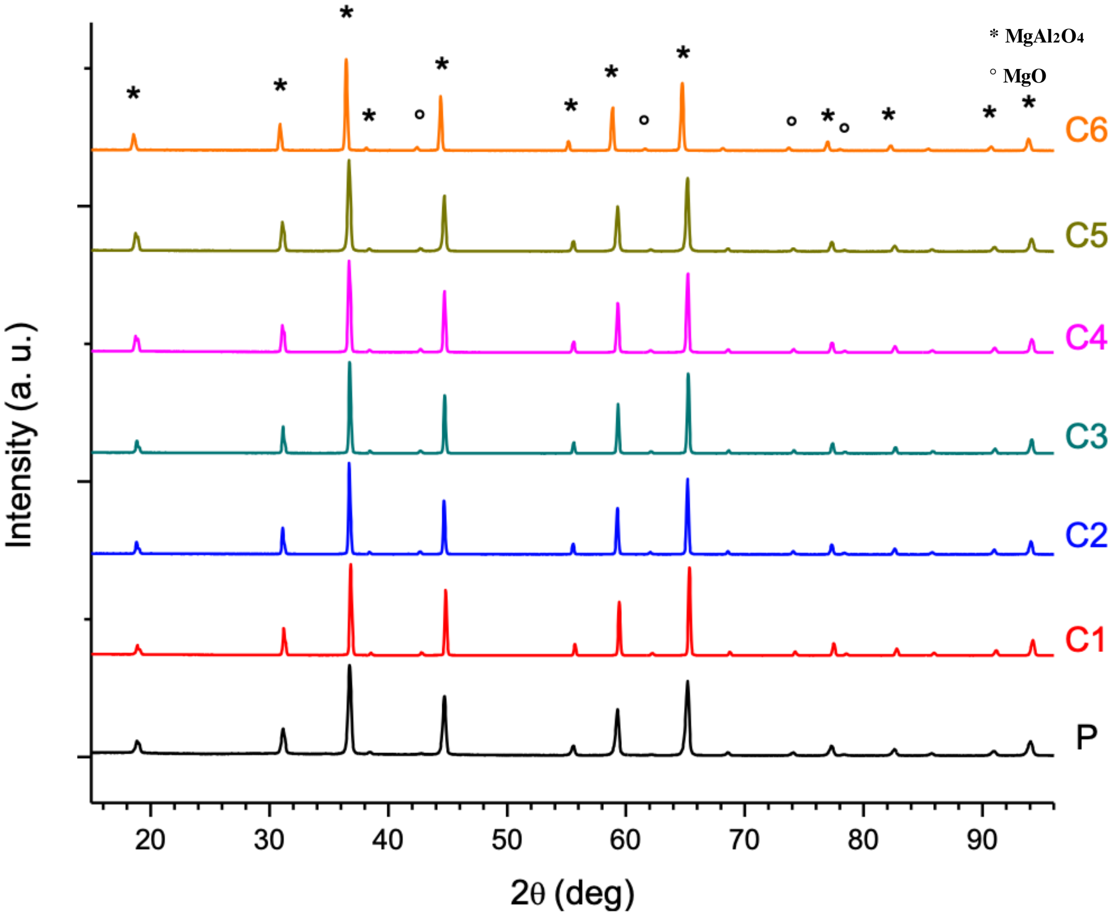

Figure 54. XRD patterns of C1 – C6 and the precursor powder.

The XRD patterns of sintered ceramics are presented in Figure 54. Even though the differences between the diffractograms are small, one can notice slight shifts in peak positions, especially for the 311 reflection plotted out separately in Figure 55 A. The difference of the peak position of C6 and other is most likely due to the change in the machine setup, as this sample was produced and measured 2 years after C1 – C5. The Maud analysis of sintered ceramics (see Table 4) resulted in the cell parameters *a*(C1)=8.0716(1) Å, *a*(C2)=8.0846(1) Å

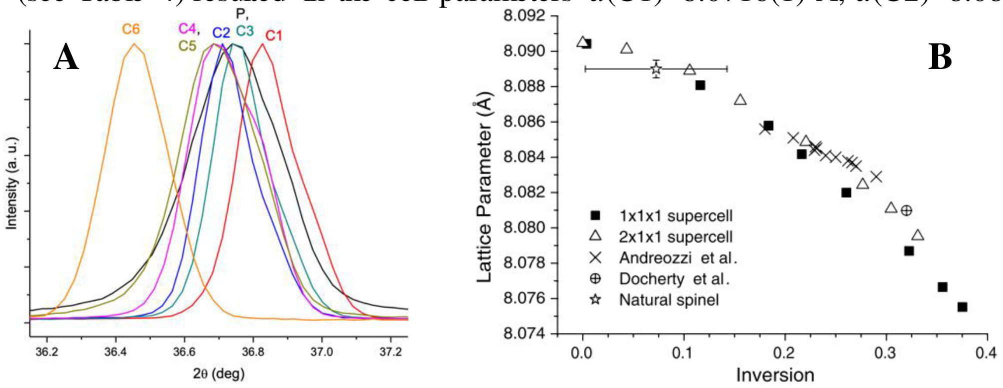

Figure 55. A: The 311 reflections of the precursor powder and the sintered ceramics, B: The dependance of lattice parameter on the crystal lattice inversion[210].

and a(C3)= 8.0781(1). Even though this variation in the lattice parameters is quite small, according to calculations by Ball *et al.*[210] it shows a considerable modification of the inversion degree. That is, the exchange of positions of the Al^{3+} cations normally occupying the octahedral sites and the Mg^{2+} cations normally occupying the tetrahedral sites, resulting in antisite defects characterizable by the inversion degree, usually ranging from 0.1 to 0.6. It has been shown that a change as small as 0.0025 Å in the lattice parameter means an inversion degree of 0.1. The inversion degree changes depending on the thermal history of the sample and is known to be close to zero in natural spinels. According to the model provided by Ball *et al.*[210], the inversion degrees of our ceramics based on their calculated lattice parameters are the following: I_{C1}=0.4 and I_{C3}=0.35 vs I_{C2}=0.2 (also see Table 4).

Table 4. Overview of spinels sintered from the commercial powder.

Sample, SPS conditions	*a* (Å)	***I*** (1)	X (2)	ρ (%)	D (μm)	External observation
Powder	8.0875(1)	0.13	0.96	-	0.115 (3)	White
C1 20' at 1450°C, 10' at 1150°C, 80 MPa during first dwell	8.0716(1)	≥0.40	1.09	99.7(2)	4.3(2)	translucent yellow-black
C2 20' at 1300°C, 10' at 1150°C, 80 MPa during first dwell	8.0846(1)	0.20	0.98	98.1(3)	1.1(1)	translucent gray
C3 3' at 1300°C, 100 MPa from dwell until the end	8.0781(1)	0.35	1.03	97.2(2)	1.2(1)	gray-white
C4 3' at 1300°C, 100 MPa during dwell	8.0811(1)	0.30	1.01	97.6(2)	1.5(1)	opaque gray
C5 3' at 1300°C, 100 MPa during cooling	8.0836(1)	0.23	0.99	91.5(1)	-	White
C6 3' at 1450°C, 80 MPa during heating and dwell				96.0(2)	0.5(1)	Translucent Gray

(1) *Inversion degree obtained from the 1x1x1 supercell model in ref.* [210]
(2) *Alumina and magnesia ratio (stoichiometry) calculated according to an empirical formula from ref.* [35]
(3) *denotes crystallite size*

Figure 56 presents morphology of the starting powder and grain structure of C1 – C5, and inserts in SEM micrographs show their optical quality (transmission). The volume densities and

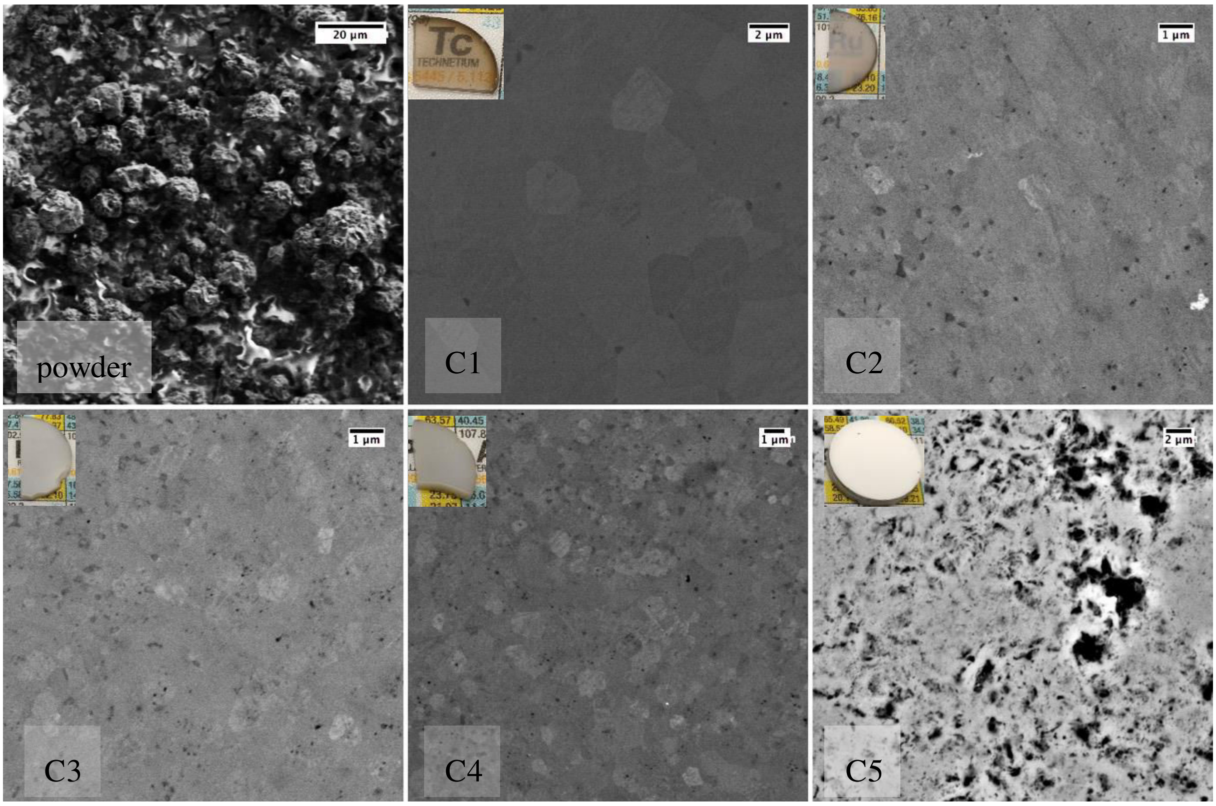

Figure 56. SEM micrographs and optical images of C1 - C5 with a more general view of the starting powder morphology.

grain sizes are listed in Table 4. For C1, we distinguish multiple non-uniformly shaped crystallite grains measuring, on average, about 4 µm in diameter. C2, C3 and C4 samples show visibly finer grain structure, featuring crystallite grains with the mean size between 1.1 and 1.5 µm and a comparable volume density. For the less dense C5 sample, no crystallite grains were

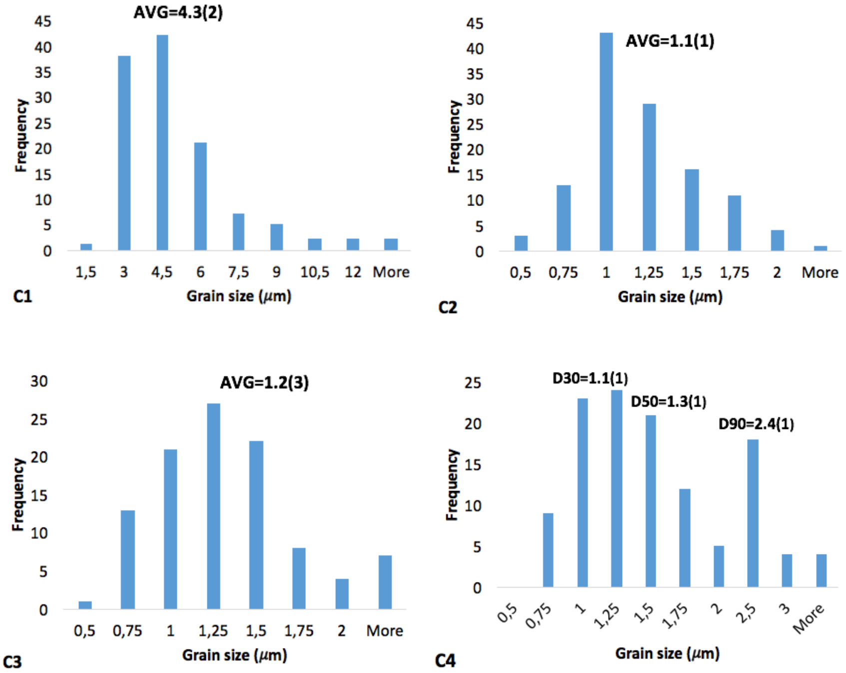

Figure 57. Grain size distributions of C1 - C4 measured from the SEM images.

visible, confirming that higher pressure during dwell is essential to sinter the powder into a dense ceramic. The grain size distributions measured on more than 100 grains for samples C1 – C4 are shown in Figure 57. The SEM micrograph and measured grain size distribution for C6 are shown in Figure 58. The grain size of C6 is 2 times smaller than those of C2 – C4, showing the importance of pressure application during heating and dwell for minimizing grain growth. Additionally, C6 is slightly translucent (about 5% in-line transmission at 550 nm), demonstrating that by raising the short cycle temperature by 150°C, the optical qualities improve.

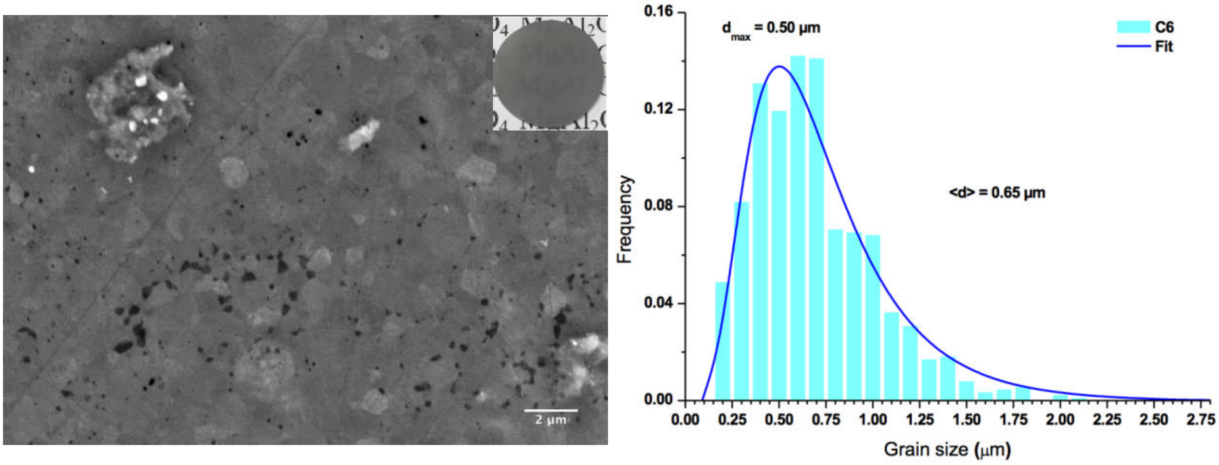

Figure 58. Morphology and grain size of C6.

Comparing optical quality of the samples after sintering, one can notice almost direct correlation with density but not with the grain size. For example, C1 with larger grains possesses a stronger transparency compared to smaller grain ceramics C2, C3 and C4. In the same time, C2 is partially transparent compare to C3 and C4, while it has the smallest grain size of 1.08 μm, between all our sintered MAS ceramics. A weaker transparency of C2 compared to C1 is most natural to attribute to its larger residual porosity. For further investigation on optical transparency, see section 3.2. We also notice 50% larger grain size of C2 compared to ~650 nm reported by Wang and Zhao[125] for a sample sintered via the same cycle, which can be explained by the smaller crystalline size (60 nm, Baikalox S30CR, Baikowski Chimie, Annecy, France) of those starting powders compared to the 115 nm used in this study (Table 4).

By visual comparison of C1 and C2, one can notice a mild black-yellow coloration of C1 (absent in C2), seemingly relating to chemical composition of the interface between grains. The slightly milky appearance of C2 hints to the existence of highly scattering submicronic pores. The darkest coloration aroused under the shortest pressure application condition of C4.

The 80 MPa pressure used in our experiments allowed to obtain ceramics without any additional discoloration of the ceramic, contrary to [125]. This might be due to quite slow pressure application rate (~16 MPa/min during 600°C dwell), which is not generally discussed. Additionally, the dark tint of spinel samples can be related to high concentration of oxygen vacancies, which could be partially filled after post-annealing in air/oxygen environment.

5.1.1 EBSD texture study of C1

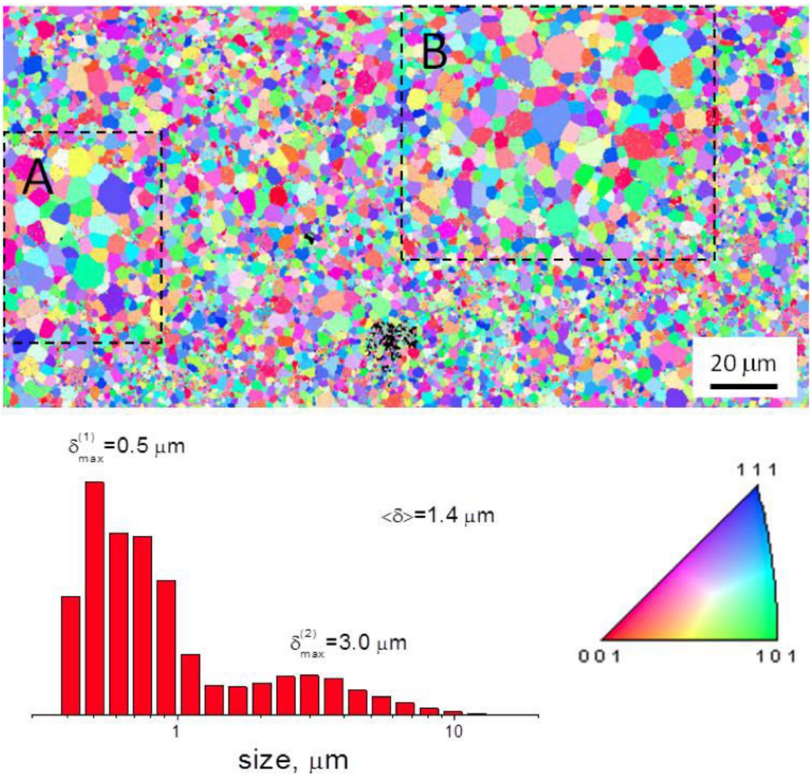

Figure 59. EBSD map and crystallite size distribution of C1.

Figure 59 shows an EBSD scan of sample C1 together with the crystallite size distribution. Like in the texturation study presented previously on an alumina sample, the EBSD map shows no preferential orientation in the prepared ceramics. The presented crystallite size distribution *Number=f(size)* shows a bimodal character with sizes peaked at 0.5 and 3.0 µm. In the same time, the mean normalized on respective area fractions size 4.2 µm calculated from the EBSD map corresponds to the apparent grain size in SEM images. Thus, while EBSD mapping provides detailed information on the exact orientation of grains, the results only confirm the XRD and SEM characterizations. The observed bimodal size distribution may be ultimately connected to the shoulder of 311 XRD peak (Figure 55 A) indicating variation of the cell parameter with the crystallite size. Moreover, the bimodal distribution of grain size can be seen as a spatial heterogeneity of the EBSD map.

Indeed, two areas A and B in Figure 59 are composed of the bigger grains while the rest of the area consists of grains sized well below the average. This picture appears to be related to the heterogeneity of the starting powder and/or sintering conditions. The less frequent large grains may be considered as an accident related to possible hot spots spawned during SPS [92]. Alternatively, the bigger grains might be due to particle size heterogeneity, needing different amount of energy for new crystallite grain formation. In the first case, further optimization of the sintering procedure will permit to overcome the excessive grain growth, in the second case, further filtering of the starting powder particle size is necessary.

5.1.2 Absorption and transmission of C1, C2 and C3

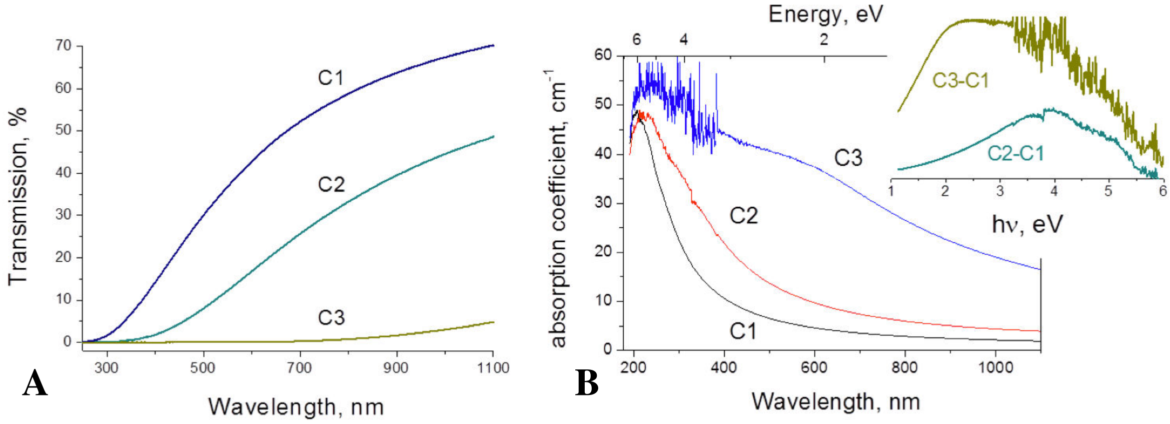

Figure 60. A: Transmission of C1, C2 and C3; B: Absorption coefficients calculated for the same samples.

The transmission spectra of samples C1, C2 and C3 are shown in Figure 60 A and the calculated absorption coefficients for the same samples are presented in Figure 60 B.

The transmission of the samples decreases in the order C1>C2>C3 in agreement with density decrease. However, transmission is wavelength dependent, which can be seen in the difference absorption spectra presented in the inset of Figure 60 B. The absorption spectra clearly show a UV band at ~5.3 eV previously assigned to F centers (two electrons trapped at an oxide-ion vacancy)[39,211], which is the most intense in sample C3. At the same time, the red shift of the band maximum by almost 0.7 eV can be noticed in the least transparent sample C3 compared to C1. The F center absorption is of similar strength in both C1 and C2 despite their different transparencies.

An additional absorption was observed in C2 at ~4.0 eV in the difference spectrum of C2-C1 in the inset of Figure 60 B. This feature has not been identified previously, however, a shoulder of the F center band that appeared at 4.75 eV (260 nm) has been assigned to F^+ centers (one electron trapped at an oxide-ion vacancy) in many papers[39,211]. We noticed that the 4.0 eV band appears in the C2 spectrum despite the similar C2 and C1 absorptions at 5.3 eV, which indicates its different origins compared to F center. We assume that the related absorption strongly depends on the F^+ center environment that may be an additional opportunity to compare the spinel samples.

Another vacancy-type absorption centered at 3.2 eV and associated with holes trapped at some sites deficient in positive charge already present in the crystal [211] did not appear in the spectra of our study. Instead, we observed the absorption extension to 2.0 eV in C3, not visible in C1 and C2, which can be attributed to small clusters of oxygen vacancies (with a maximum at ~2.4 eV) [39] at the grain boundaries. This does not contradict our observations since the relevant spectral feature of C3 also showed the strongest absorption band of F centers. Alternatively, a contribution of the residual submicronic porosity may be considered, which diminishes after a critical wavelength, signifying the onset of Rayleigh-type light scattering.

5.1.3 Cathodoluminescence study

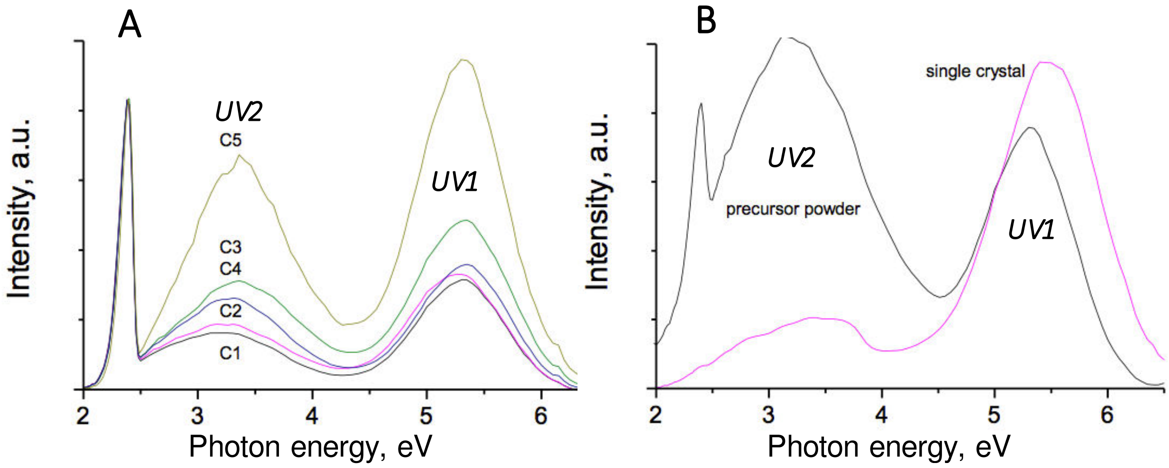

Figure 61. Cathodoluminescence spectra measured at 5K, A: C1 - C5 and B: precursor powder and single crystal.

The low-temperature (5 K) CL spectra of the sintered ceramics, precursor powder, and reference single crystal (SC) are shown in Figure 61. The measured peaks are in agreement with the results published earlier[171,172]. The most long-wavelength emission peaking at ≈1.8

eV (not shown in the figure) corresponds to the well-known R-lines of Cr^{3+} impurity. This impurity inevitably occurs in a wide range of oxides and is easily recognizable in the luminescence spectrum. The emission band at 2.4 eV belongs to transitions in the tetrahedrally coordinated Mn^{2+} impurity. These Cr^{3+} and Mn^{2+} impurities in the prepared ceramics arise from the precursor powder and cannot be modified during the sintering process. Their equal content enables us to normalize the CL spectral intensities and compare the broad intrinsic short-wave spectra. We realize that such normalization is not possible in the case of SC sample whose preparation process and precursor chemistry were different. In contrast to the sintered samples, SC demonstrates an almost negligible luminescence of Mn^{2+} impurity.

Between 2.5 and 4 eV (UV2), the spectra are a sum of F/F^+ centers and complex intrinsic defect emissions. Earlier studies [35] have indicated the F^+ color centers' formation of oxygen vacancies (V_O) induced by the motion of dislocations, which is specific to sintering conditions. In particular, it was shown that the concentration of F^+ centers decreases with the sintering temperature and increases with the heating rate[171].

The heating and cooling rates were kept constant during the preparation of our ceramics C1 and C2 and C3–C5, as explained in section 5.1. Thus, the collectively higher luminescence intensity for C3–C5 in the F^+ center region at 2.7 eV is confirmed. The dependence on the sintering temperature is in perfect agreement with our results, as C1, sintered at the highest temperature, shows the lowest F^+ intensity, even though it is slightly different from C2. The position of the UV luminescence band depends on the stoichiometry X=Al_2O_3/MgO, and it has been empirically established that it shifts to higher energies when this ratio decreases[35]. Our experiments indicated no substantial shift in the UV2 spectra in agreement with the similar stoichiometry of the prepared ceramics (Table 4 in section 5.1). This contrasts with their band intensities related to the number density of the defect centers. One can conclude that the UV2 peak energy in Figure 61 corresponds to the stoichiometric spinel composition ($x\approx1$) (Table 1).

The strongest observed emission band (UV1) has been previously assigned to the recombination of conduction-band electrons with holes captured at the nearby oxygen ions by Gritsyna *et al*[172]. It has been shown that the absorption of F centers (5.3 eV) in spinels occurs at a higher energy compared to that of F^+ centers (4.75 eV), both covering the UV spectral region[39,211]. In luminescence, there is an agreement about F^+ band position, while the assignment of F band in the spinel remains an issue. The analysis of the parent species MgO and Al_2O_3 has shown that the position of F band is at lower energies[212,213]. An intense emission of F^+ centers has been previously reported at 2.7 eV in spinel samples with an excess of Al^{3+} cations[35]. In contrast, in almost stoichiometric samples ($x \approx 1$), this photoluminescence is of low intensity and significantly flatter in the blue range of the spectrum above 3 eV. Thus, our observed UV2 band can be decomposed into two poorly resolved luminescence bands at ~2.7 (F^+) and ~3.4 eV, the higher energy of which we tentatively assign to F centers.

The visible transparency of the prepared ceramics decreases in the order C1, C2 > C4, C3 > C5 in agreement with the increase in the 3.4 eV band intensity. Thus, a conclusion can be drawn about the accumulation of F centers at the grain boundaries. Indeed, the UV2 band is the most intense in the precursor powder, whose specific surface area is the highest among the analyzed materials. On the other hand, the lowest–intensity band at 3.4 eV was found in the case of C1 having the highest optical transparency. We noticed that when the 3.4 eV band weakens, the contribution of the 2.7 eV band (F^+ centers) becomes stronger, which appears as a red shift of the UV2 emission in C1 and C2 compared with C3, C4, and C5 (Figure 61 A). Additionally, the visible absorption of transition-metal impurity ions can be amplified over three orders of magnitude by the neighboring F centers[213], which shows a direct relation between the F center number density and the spinel's transparency. Because the elemental composition of the prepared ceramics is similar to that of the precursor powder, we assume that the difference in the CL spectra is related to the sintering process, and F centers are preferentially formed at the grain boundaries.

We noticed that the peak shape of SC is similar to that of the sintered samples. However, both UV1 and UV2 bands of SC are blue shifted by ~0.25 eV. This may be related to the lower energetic position of V_0 on the surface compared to the bulk of the spinel crystals[214].

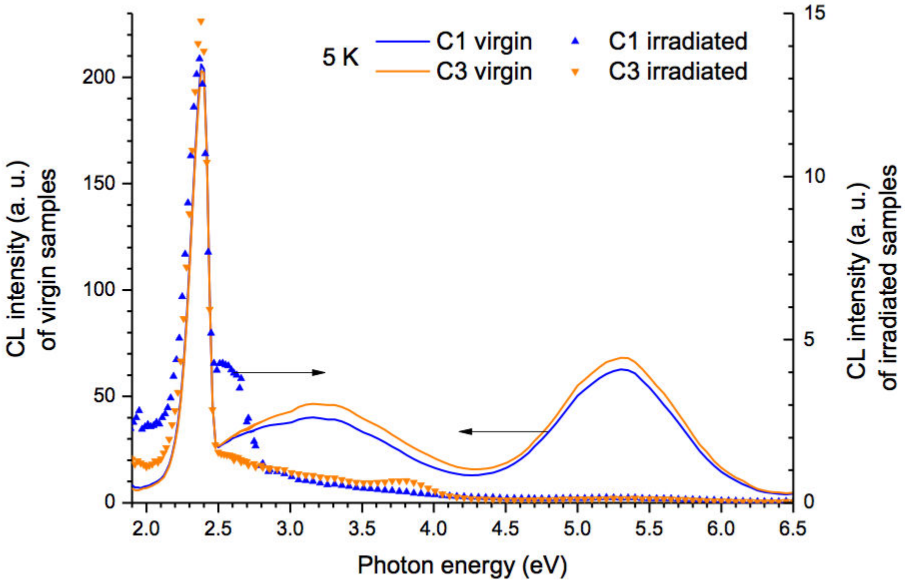

Figure 62. Cathodoluminescence comparison of virgin and irradiated C1 and C3.

Figure 62 compares the CL spectra of virgin C1 and C3 to C1 and C3 irradiated by protons with a dose of 10^{17} cm^{-2}. We notice that essentially the whole CL is quenched after irradiation, even the highest intensity impurity band has only 1/15 of its initial intensity. The exceptions are the band related to Mn^{2+} impurities at ~2.4 eV and a low-intensity band at ~3.8 eV in the case of C3, which has been connected to F and F^+ centers in Al_2O_3 and MgO [211,215]. An additional narrow band appears in the CL spectrum of C1 at ~2.6 eV. This band has previously been assigned to F centers in Al_2O_3[216], but this value is also close to the 2.7 eV emission of F^+ centers in spinel, as explained previously. Thus, as it is known that proton irradiation causes a great amount of Frenkel defect pairs[217], these new appearing bands are most likely caused by F and F+ centers, analogically to Al_2O_3 and MgO.

5.2 *$MgAl_2O_4$ via impregnation and reactive sintering*

From here onward, the pressure application of the short cycle was modified to reflect the best results obtained in the case of commercial spinel powder (Figure 52), the long cycle will be used as described previously (see Figure 52) and dilatometric studies will be carried out to define ideal dwell temperatures (see Figure 50).

The synthesis of $MgAl_2O_4$ via doping in cycles with $Mg(NO_3)_2$ water solution was first mentioned in the PhD thesis of T. di Costanzo in 2001[54]. In this work we used the maximum water solubility concentration of $Mg(NO_3)_2 \cdot 6\ H_2O$, 1.5 mol/l. To achieve stoichiometric 1:1 ratio of Al_2O_3 and MgO inherent to $MgAl_2O_4$ spinel, 9 doping cycles were necessary. However, for comparison purposes, powders were synthesized and sintered with 2, 5, 9 and 12 doping cycles (see XRD results in Figure 63). Instead of classical sintering used in[54], the received powders were subjected to a SPS sintering cycle with a dwell of 20 minutes at 1450°C and 10 minutes at 1150°C (same as ‘long cycle’ used previously) at 80 MPa.

Maud analysis was carried out on powders received after 5 and 9 doping cycles to get an idea about the phase concentrations of alumina and magnesia (periclase). These results along with the cell parameters of sintered spinels are presented in Table 5. Since exact fitting of patterns containing 3 phases was complicated, we present the evolution of the two most intense peaks for each phase in Figure 63 B and D. It becomes clear from Figure 63 C-D that ceramics sintered from powders after 5 and 9 cycles of MgO doping are both monophasic spinels.

The stoichiometric weight percentages of alumina and magnesia in spinel are 71.67 wt% and 28.33 wt%. Thus, according to the Rietveld refinement results presented in Table 5, our 9-cycle powder has a slightly lower content of MgO. This is not a big issue since spinel can have different stoichiometries, the ratio Al_2O_3:MgO (X) can vary between 0.8 and 3.5[24,25]. Viertel and Siefert[36] have developed an empirical formula to calculate this ratio that we used to estimate the stoichiometry of the spinels produced after 5 and 9 MgO doping cycles (see Table 5). The closest value to exact 1:1 Al_2O_3:MgO stoichiometry, 1.12, was achieved after 9 doping cycles. However, sintering the oxide mixture after 5 doping cycles also lead to monophasic spinel with stoichiometry of 1.79.

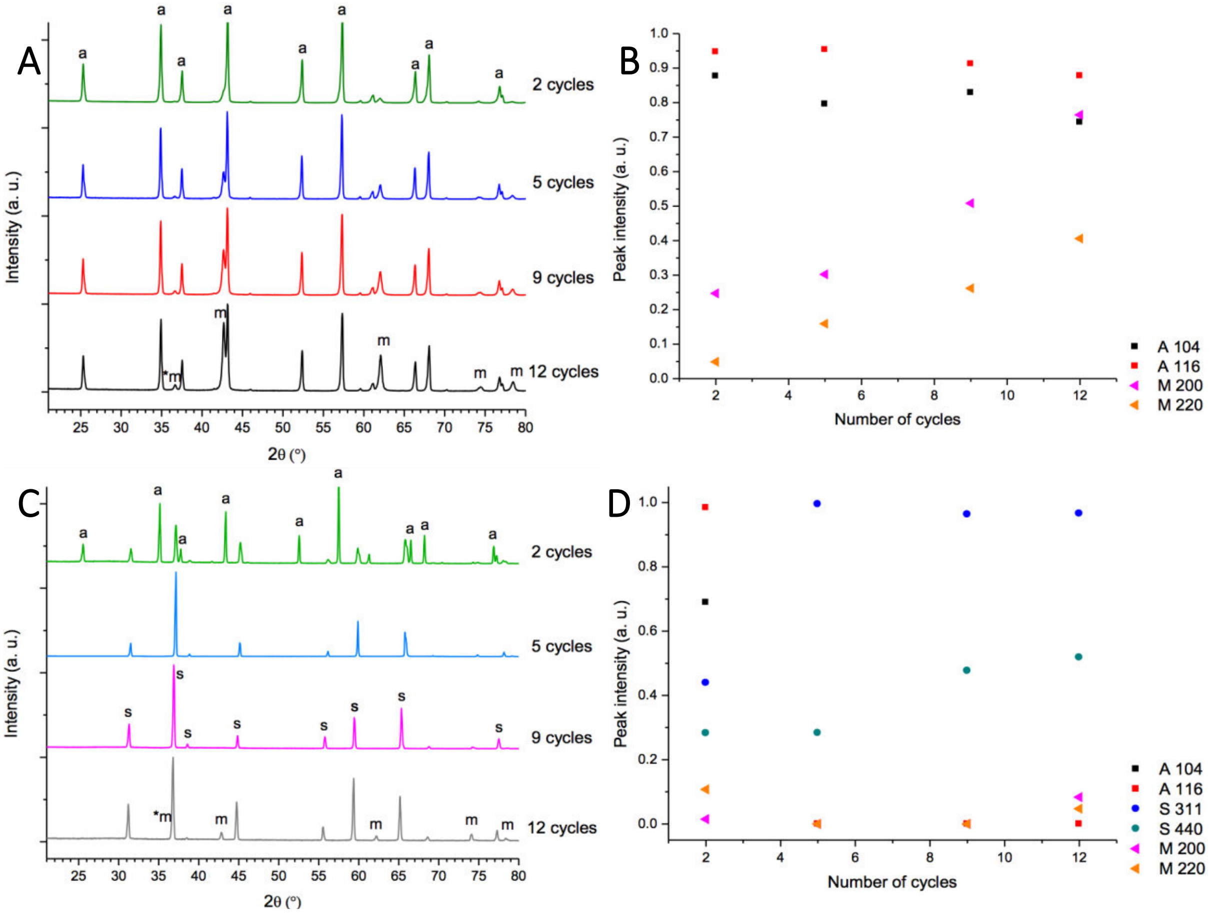

Figure 63. XRD patterns of A: Al_2O_3 powders after a number of impregnation cycles and C: ceramics sintered from these powders. Intensities of the most intense XRD peaks for B: powders after a number of impregnation cycles and D: ceramics sintered from these powders. The letter a denotes diffraction peaks characteristic to alpha-alumina (corundum), m denotes magnesia (periclase) and s denotes spinel.

Table 5. XRD analysis of powders before and after sintering.

Sample	wt% corundum; cell parameters (Å)	wt% periclase; cell parameter (Å)	wt% spinel; cell parameter (Å)	Calculated spinel stoichiometry*, X
5 cycles powder	88.5 a=4.7669(1) c=13.0104(5)	11.5 a=4,2212(2)	-	-
9 cycles powder	75.3 a=4,7662(1); c=13.0091(4)	24.7 a=4.2210(1)	-	-
5 cycles sintered	-	-	100% a=8.0171(1)	1.79
9 cycles sintered	-	-	100% a=8.0681(4)	1.12

*calculated based on the empirical formula developed by Viertel and Siefert [36]

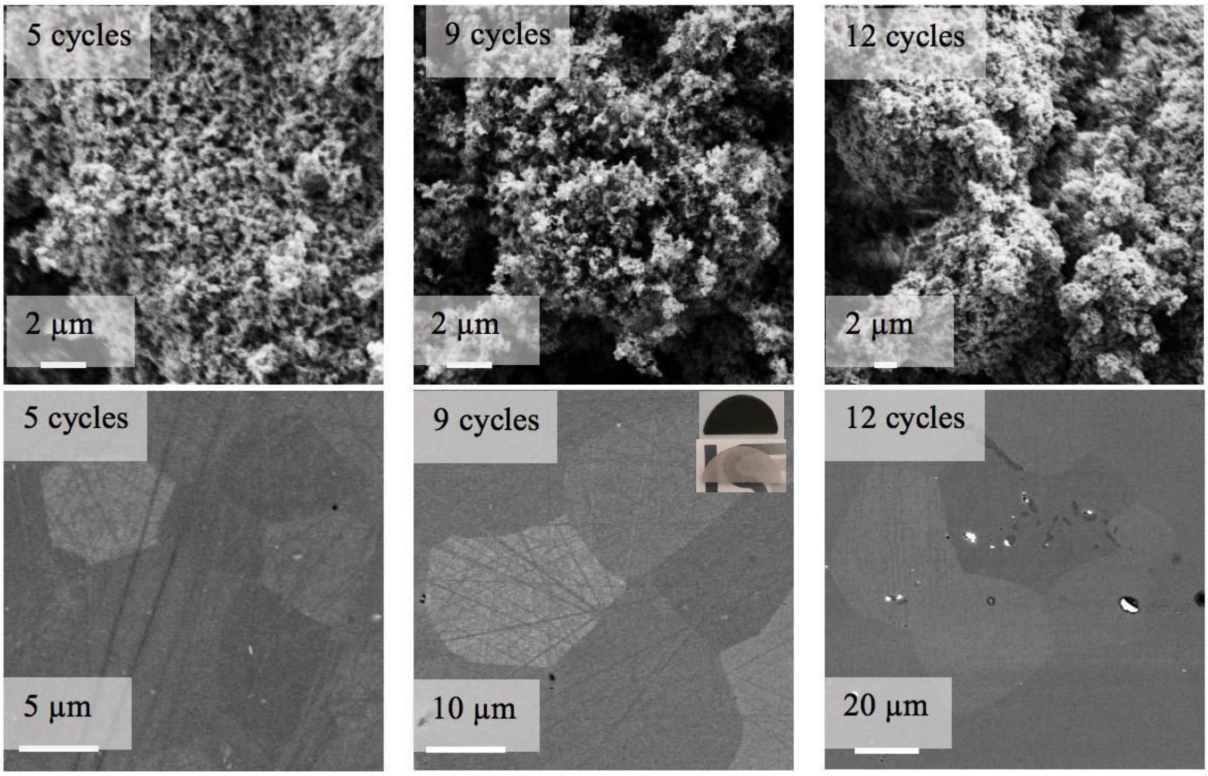

Figure 64. Top row: Al_2O_3 powder after a number of impregnation cycles, bottom row: same powders sintered at 1450°C for 20 minutes.

Produced powders and ceramics morphologies are characterized by SEM imaging seen in Figure 64. It can be observed that as the MgO concentration rises in the sintered composition, the resulting grain size of the sintered compact also increases. This is most likely due to the much smaller magnesia crystallite size (about 60 nm) compared to that of corundum (about 250 nm). This also explains why MgO is a popular sintering additive for Al_2O_3[219,220]. The inset of the optical photos of the 9 cycle sample in Figure 64 shows the optical photos of the sample before and after annealing in air at 1300°C for 30 minutes. Since the initial dark color of the sample transformed into full translucency, we can be sure that the initial color was mostly due to oxygen vacancies that were filled during annealing. This heat treatment was equally carried out on all of the samples and an additional annealing under oxygen flow was executed. The results of these treatments can be observed in Figure 65, no other samples revealed any translucency.

Figure 65. A: 2c, 5c, 9c and 12c samples after 30-minute 1300°C annealing in air; B: Samples after additional 4-hour annealing under oxygen flow at 1350°C.

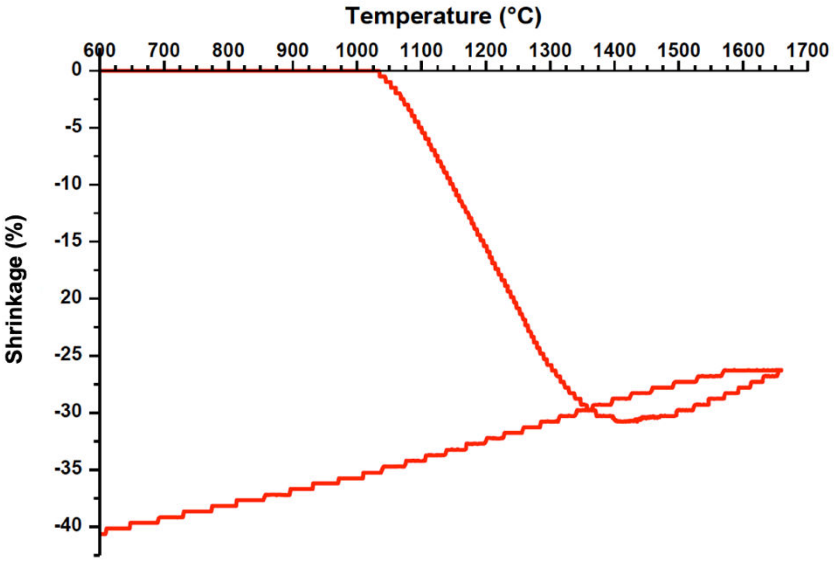

Figure 66. Dilatometric curve of the 9 cycle impregnation powder.

Since all of the ceramics obtained from Al_2O_3 impregnation by MgO had average grain sizes bigger than 7 µm, we next chose to use the short sintering cycle (3’ at 1450°C, 80 MPa) on the stoichiometric powder, as well as to lower the temperature for the long cycle to the optimal 1370°C obtained from the dilatometric curve (see Figure 66).

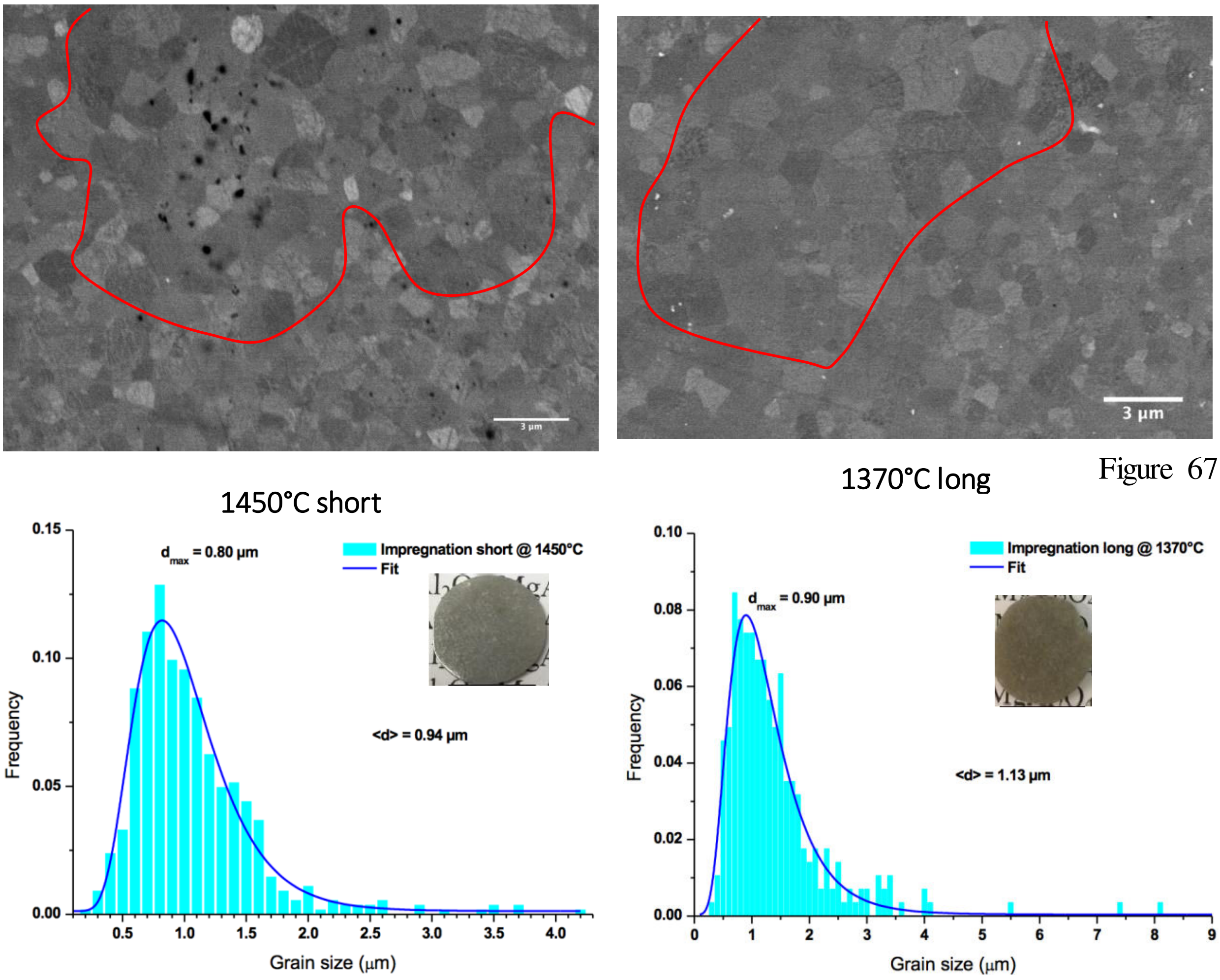

Figure 67. SEM micrographs of the ceramics from the stoichiometric impregnation powder sintered via the short cycle at 1450°C and 1370°C with their grain size distributions. The grains inside the red lines have a much larger average grain size.

Figure 67 showcases the morphology and grain size distributions of spinels sintered from impregnation powder under softer conditions. On the SEM micrographs one can notice two distinct areas, islands with grain sizes bigger than average (see areas surrounded by red lines in Figure 67) and average or smaller sized grains around them. Even though the grain sizes of both samples can be fit with one-peaked spline, we can notice the start of a bimodal grain size distribution, at about 2 µm for the short cycle sample and at about 3.2 µm for the long cycle sample. We also note that the longer sintering duration results in the bigger second order grain size mode. Thus, to keep the grain size low, shorter, higher-temperature cycles should be preferred. This effect was also observed by the EBSD analysis of C1 in chapter 5.1.1. As it has been hypothesized, the less frequent large grains may be considered as an accident related to possible hot spots spawned during SPS[201,202].

Table 6 summarizes the sintering cycles and properties of monophasic spinels obtained from the impregnation precursor. The XRD patterns of the ceramics sintered via the short cycle at 1450°C and the long cycle at 1370°C are shown in Figure 68. While the diffractograms show some low-intensity corundum and periclase peaks, the phases are not concentrated enough to carry out Rietveld refinement, thus leading us to conclude their weight percentage to be under a couple of percent.

Table 6. Overview of spinel ceramics obtained from impregnation precursor powder.

Impregnations	Sintering cycle	Density (%)	Grain size (µm)	Cell parameter	Calculated stoichiometry
5c	1450°C long	100.3(5)	4.0(2)	a=8.0171(1)	1.79
9c	1450°C long	97.2(5)	25(3)	a=8.0681(4)	1.12
9c	1450°C short	98.3(2)	0.9		
9c	1370°C long	97.9(2)	1.1		

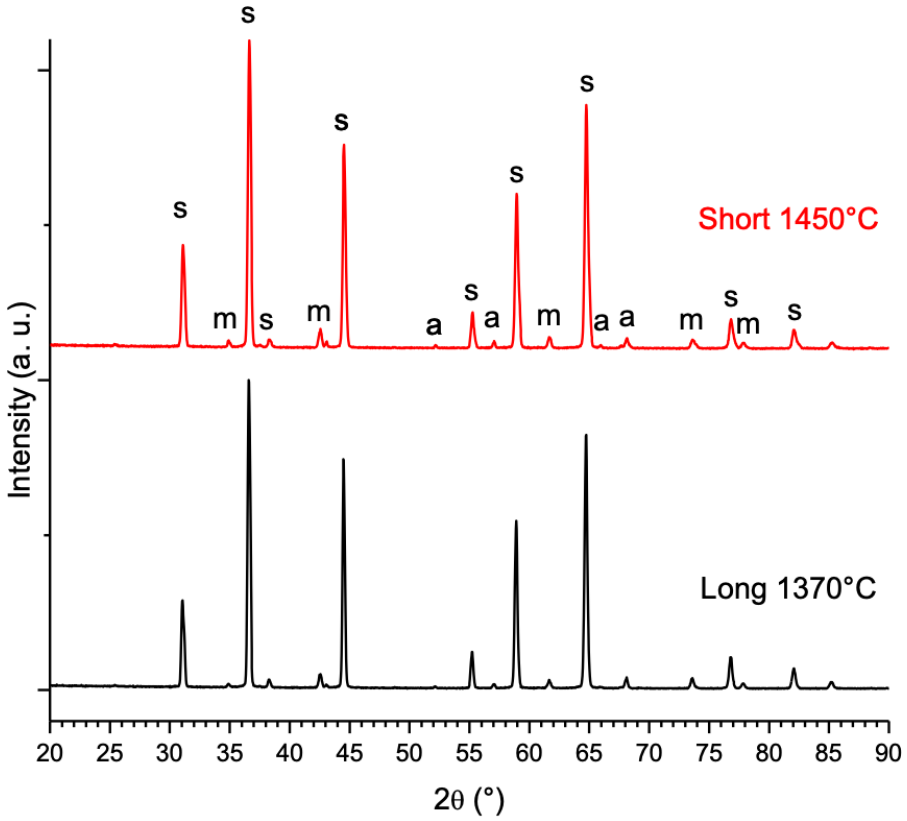

Figure 68. XRD patterns of the 9 cycle impregnation precursor sintered via the short cycle at 1450°C and the long cycle at 1370°C.

5.2.1 Transmittance and absorption

The only sample produced by reactive sintering having a transmission >1% at 550 nm was the 9 cycle impregnation sample sintered via the long cycle at 1450°C and calcined in air at 1300°C for 30 minutes (see Figure 69). Though one can easily read the text below the sample, the transmittance at 650 nm is < 2.5% and comparable to that of C3 discussed earlier (see chapter 5.1.2). This is most likely due to high concentration of pores with sizes around the incident wavelength, making the result of the measurement highly dependent on sample positioning. Some bigger pores are even visible to the naked eye in the inset of Figure 69. The small bands in the range of 320 – 400 nm are most likely brought about due to machine noise.

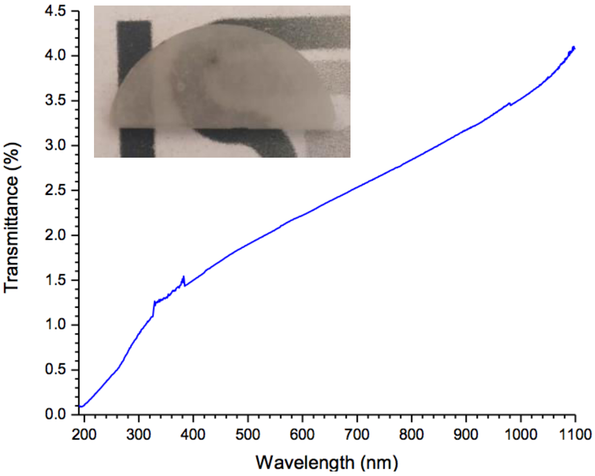

Figure 69. Transmittance of impregnation sample sintered at 1450°C via the long cycle.

5.3 Influence of Ta_2O_5 doping on the grain size

5.3.1 Ta_2O_5 additive in commercial spinel powder

Even though lowering sintering temperature and time resulted in grain size decrease, they also resulted in somewhat lower transparency. Thus, we first carried out dilatometric cycles on the commercial spinel powder doped with 0.5, 1, 2 and 4 wt% of Ta_2O_5 to determine the most suitable doping concentration. This cycle was chosen due to the high sintering temperature, as with expected grain growth inhibition the full densification will take place at a higher temperature. We chose to carry put the optimization for the commercial powder since it is already monophasic, lessening the risk of secondary phase creation.

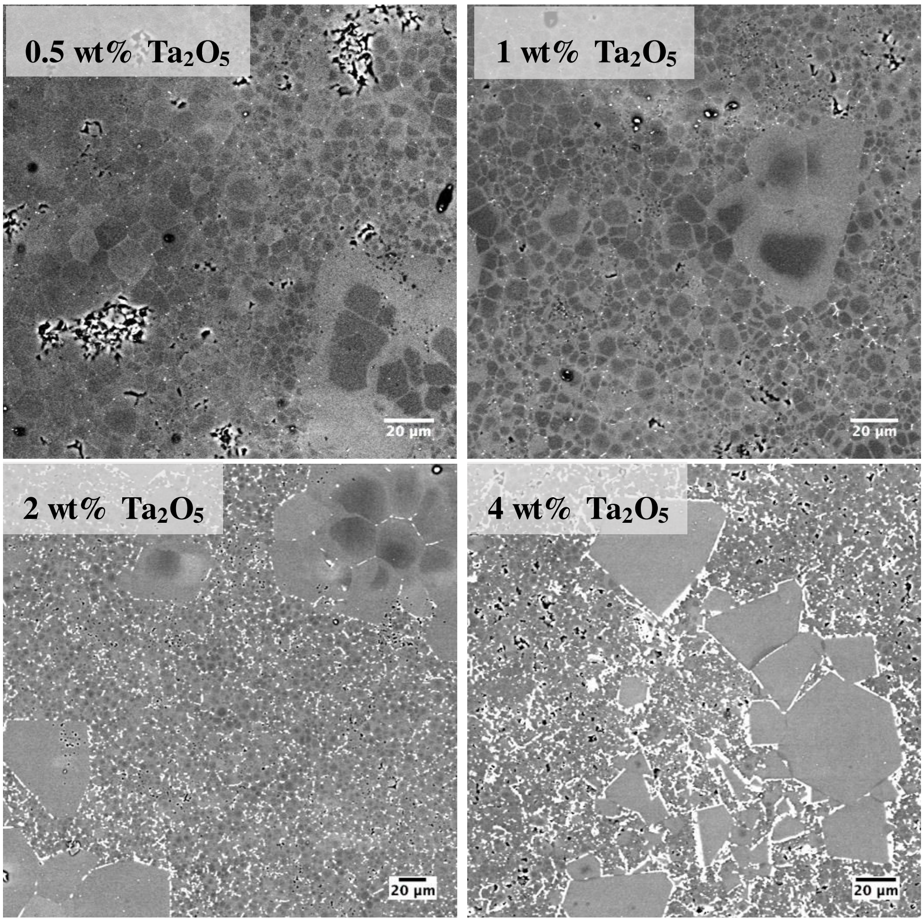

Figure 70. Microstructures of the commercial spinel doped with 0.5, 1, 2 and 4 wt% of Ta_2O_5.

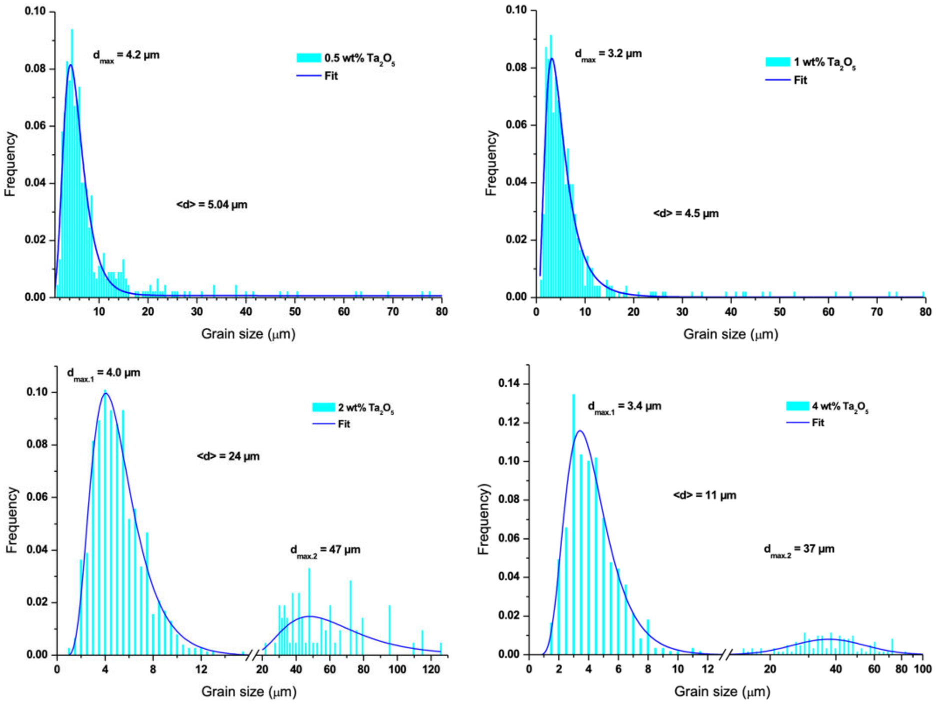

Figure 71. Grain size distributions of the commercial spinel doped with 0.5, 1, 2 and 4 wt% of Ta_2O_5.

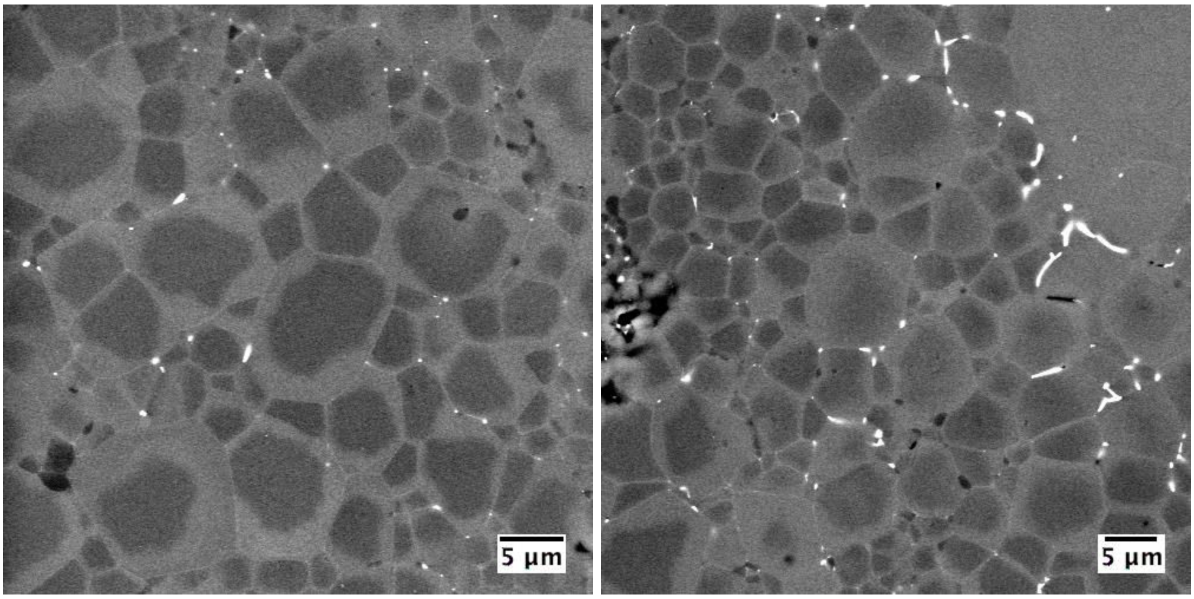

Figure 72. SEM micrographs of spinel doped by 0.5 wt% (left) and 1 wt% (right) Ta_2O_5.

Characteristic low-magnification SEM micrographs of Ta_2O_5 doped spinels are shown in Figure 70 along with the grain size distributions in Figure 71 and a closer look at the microstructure of 0.5 and 1 wt% doped spinels in Figure 72. While the low-magnification micrographs of 0.5 and 1 wt% doped spinels show no significant impurities, a collection of additives along grain boundaries can be observed in Figure 72. A great difference in the clarity of grain boundaries on the micrographs can be noted for all the doped samples, hinting to a change in grain boundary chemistry compared to undoped samples. Grain size analysis revealed that the distribution of grain sizes is extremely bimodal (see Figure 71), with the first mode being 4.2 and 3.2 µm, for 0.5 wt% and 1 wt% doping compared to that of pure spinel (3.7 µm) and the second mode for both ceramics ~ 40 µm. Spinel sintered via the same cycle with no additives also had a second grain size mode at ~ 9 µm. Thus, the higher doping concentration is slightly preferential for grain growth inhibition. However, the high difference between the grain sizes modes remains a problem. In the case of doping concentrations of 2 and 4 wt%, the sample contamination by Ta-derived impurity is even greater, completely packing the grain boundaries with the secondary phase appearing white on the SEM micrographs. Additionally, the size difference between the two grain size modes grows greater with higher level of doping. In addition to the influence of the dopant, the exaggerated grain growth is also brought on by the higher-than-normal sintering temperature.

Figure 73. Optical images of spinels sintered from the commercial powder with various levels of Ta_2O_5 doping.

The optical images of spinels sintered from the commercial precursor with various doping levels are shown in Figure 73. One can notice that for the optical quality of the samples reaches a completely milky state at 2 wt%. Thus, taking into account the accumulation of Ta-derived impurity in the grain boundaries and the optical quality of the samples, 0.5 and 1 wt% seem like the reasonable doping levels.

To further understand the distribution of Ta in the grains, EDX imaging was carried out on samples sintered from commercial spinel with added 0.5 wt% and 1 wt% Ta_2O_5. The EDX results for 0.5 and 1 wt% Ta_2O_5 doping are presented in Figure 74 A and B. Unfortunately, this Ta_2O_5 concentration is too low to be detected by the elemental analysis (see the Ta M α maps). However, by increasing the brightness of the map by 70%, we can notice, especially in the case of 1 wt% doping, that the distribution of Ta is quite uniform, seemingly collecting in the grain boundaries. Correspondingly, the centers of the grains look dark on the SE image, suggesting a local increased atomic mass.

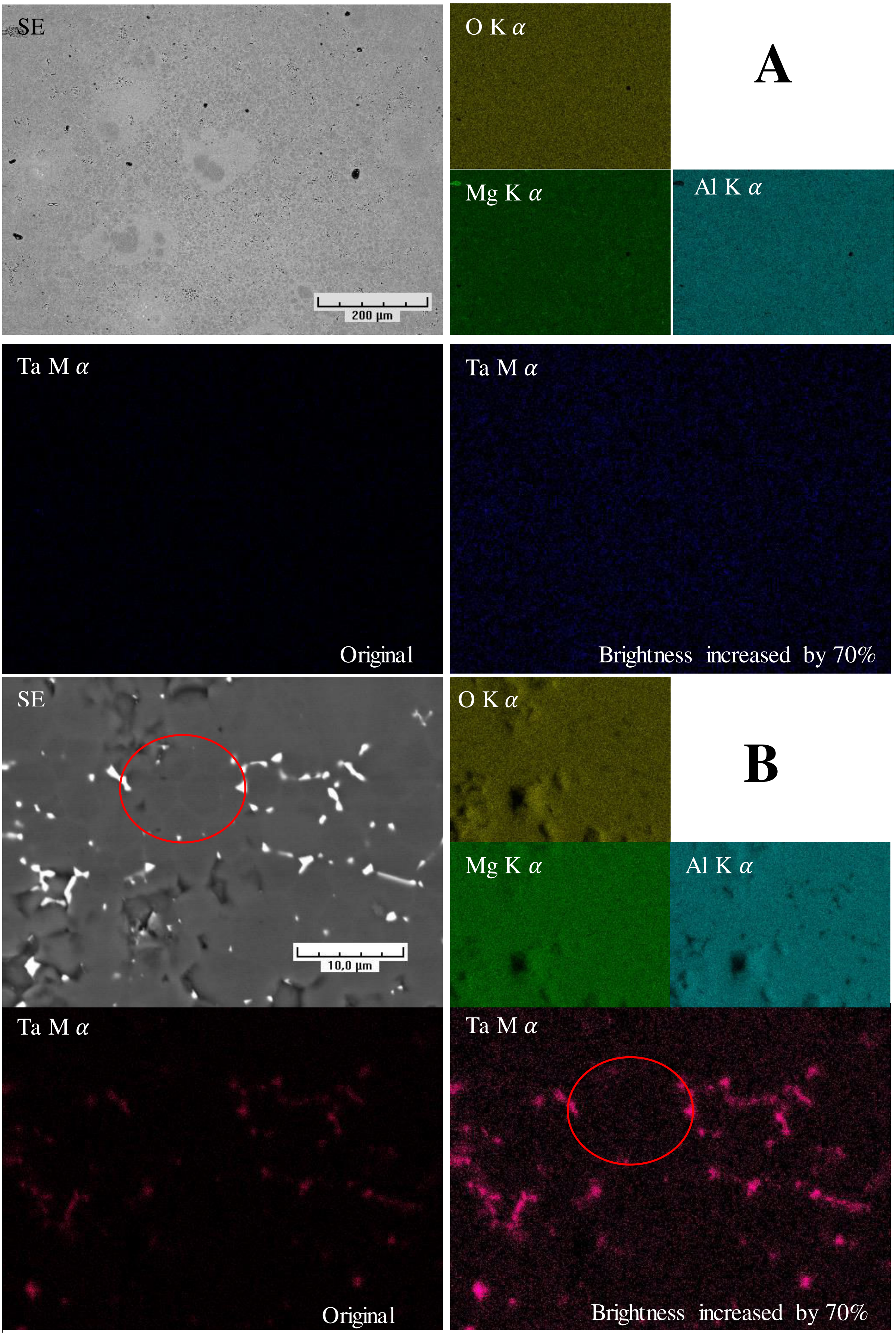

Figure 74. EDX analysis of spinel doped by 0.5 wt % (A) and 1 wt% (B) Ta_2O_5*.*

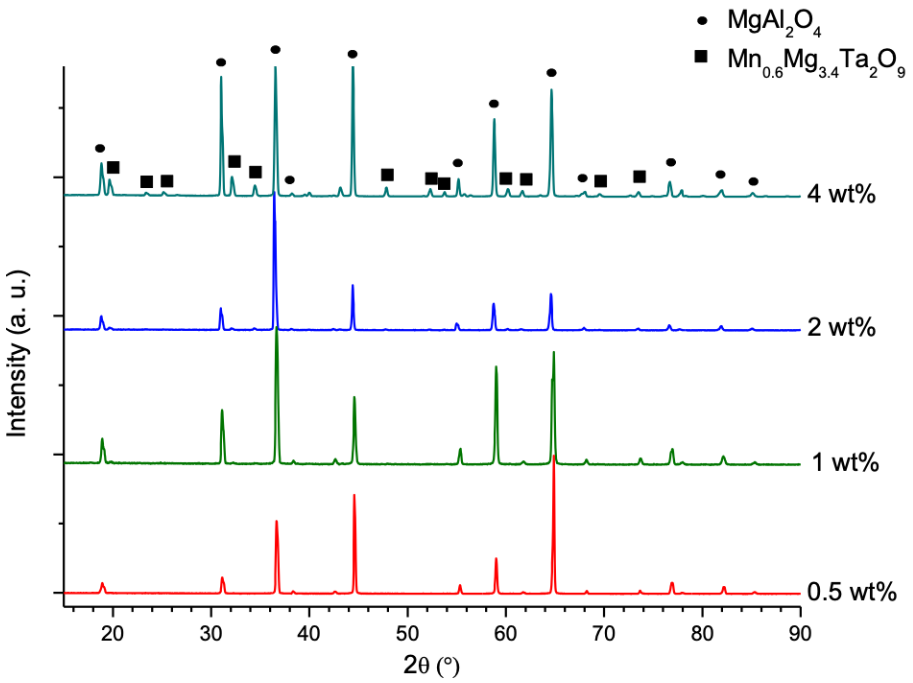

Figure 75. XRD patterns of commercial spinels sintered with 0.5, 1, 2 and 4 wt% of Ta_2O_5.

Table 7. Maud analysis of spinels sintered from commercial powder with various levels of doping.

	Spinel	$Mn_{0.6}Mg_{3.4}Ta_2O_9$	MgO	Maud fit sigma
0.5 wt% Ta_2O_5	98.20 wt% a=8.1291(2) Å	**α-Mn** 0.14 wt% a=8.71(2) Å	1.66 wt% a=4.245(1) Å	4.7
1 wt% Ta_2O_5	97.64 wt% a=8.1314(2) Å	0.26 wt% a=5.196(6) Å c=14.11(3)	2.10 wt% a=4.2438(8) Å	2.4
2 wt% Ta_2O_5	97.64 wt% a=8.1575(3) Å	1.08 wt% a=5.211(3) Å c=14.16(1)	1.28 wt% a=4.258(3) Å	5.6
4 wt% Ta_2O_5	95.03 wt% a=8.1501(3) Å	4.41 wt% a=5.2049(6) c=14.148(3)	0.56 wt% a=4.255(4)	19.0
C1	97.8 wt% a=8.0716(1) Å	**α-Mn** 0.02 wt% a=8.93(6) Å	2.10 wt% a=4.2158(5)	7.6

To understand the chemical and crystallographic nature of the Ta-derived impurity, XRD analysis was carried out at all 4 doping levels. The XRD patterns are presented in Figure 75 and the results of Maud analysis are summarized in Table 7. The Ta-derived impurity was identified as a complex oxide $Mn_{0.6}Mg_{3.4}Ta_2O_9$ from the COD and Match databases. It can be seen that while 0.5 and 1 wt% Ta_2O_5 doping leads to no or very small amount of secondary phase, the doping level of 4 wt% brings about 4.4 wt% of $Mn_{0.6}Mg_{3.4}Ta_2O_9$ phase.

The CL study of commercial spinel powder sintered with 1 wt% addition of Ta_2O_5 via the dilatometric cycle is presented in Figure 76 shows that luminescence present in pure spinels in the region of 4 – 6 eV seems to be extinct due to Ta addition.

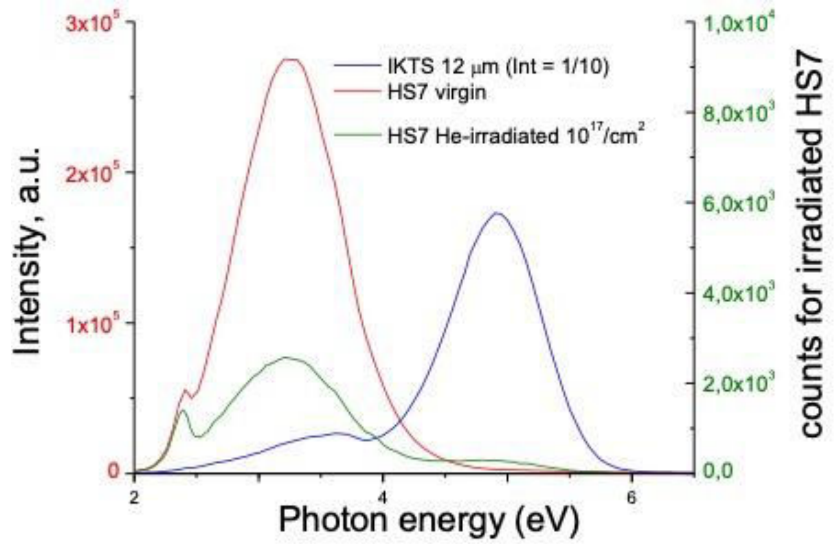

Figure 76. CL spectra of virgin and irradiated commercial spinel sintered with added 1 wt% Ta_2O_5.

5.3.2 Ta_2O_5 additive in the impregnation precursor

As 0.5 and 1 wt% doping was successful in the commercial spinel, these concentrations were also used in the 9 cycle impregnation precursor. Since the chosen sintering temperature seemed to bring about exaggerated grain growth, we tested Ta_2O_5 as a grain growth inhibitor at the selected optimal sintering temperature of 1370°C during the long sintering cycle.

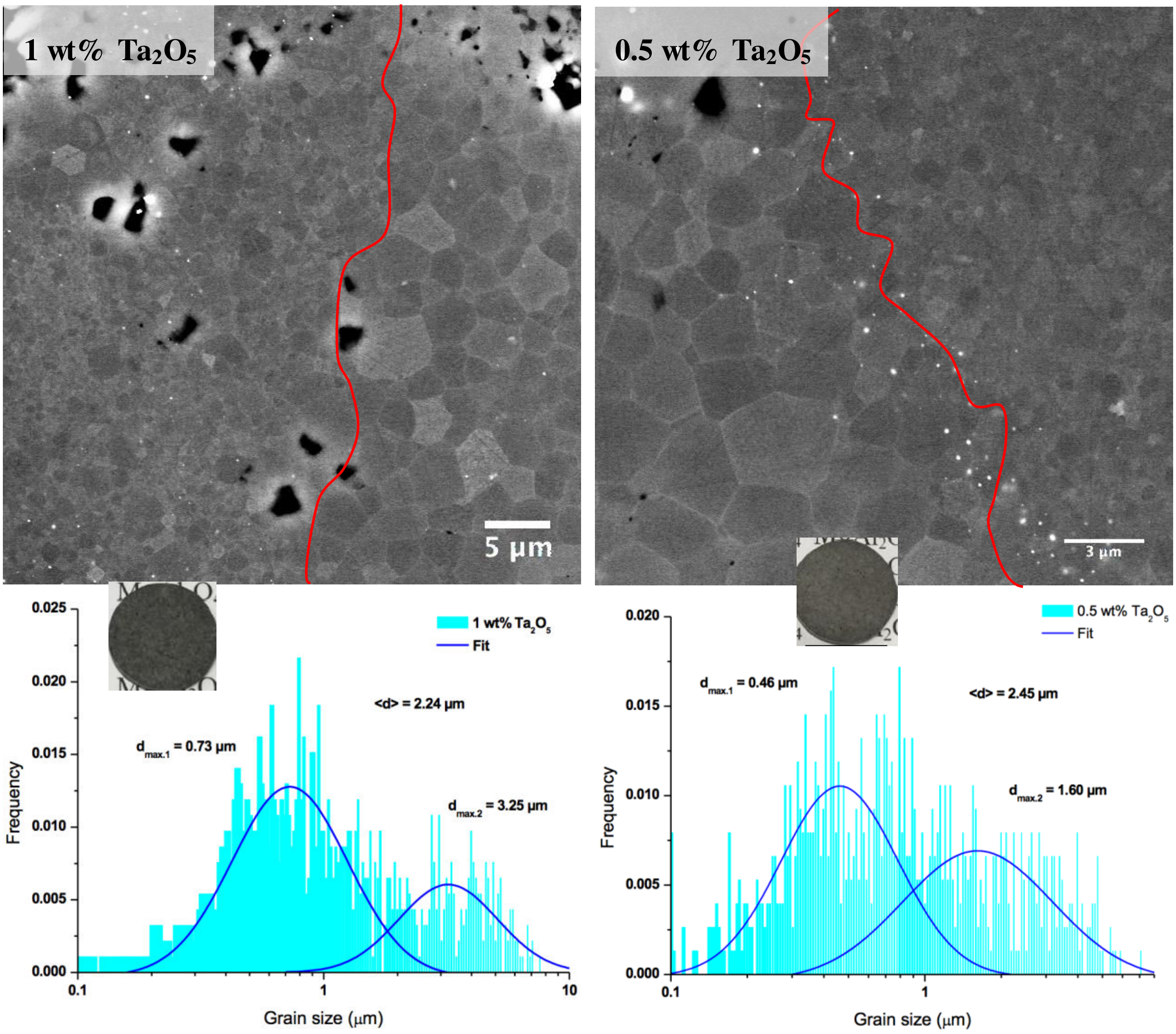

Figure 77. Ceramics sintered from stoichiometric powder at 1370°C by the long cycle with 1 wt% and 0.5 wt% added Ta_2O_5 and their grain size distributions. The red lines separate smaller and bigger grains.

Although the presence of Ta_2O_5 at 0.5 wt% significantly decreased the first mode of the grain size distribution (0.5 vs 0.9 µm of undoped ceramic sintered via the same cycle, see Figure 77 and Figure 67), it greatly emphasized the bimodality of the grain size distribution. The second order grain size mode was once again smaller, but it can be seen from the SEM micrographs that the grain size distribution over the area was not uniform, but split into two types of grain size areas (see Figure 77). This type of inhomogeneity is not preferential for isotropic optical properties. As can be seen from the inset of Figure 77, the ceramics are spotty white-gray upon optical observation. It is also evident that the grain boundaries of doped samples are more contrasted on the SEM micrographs than those of pure ceramics.

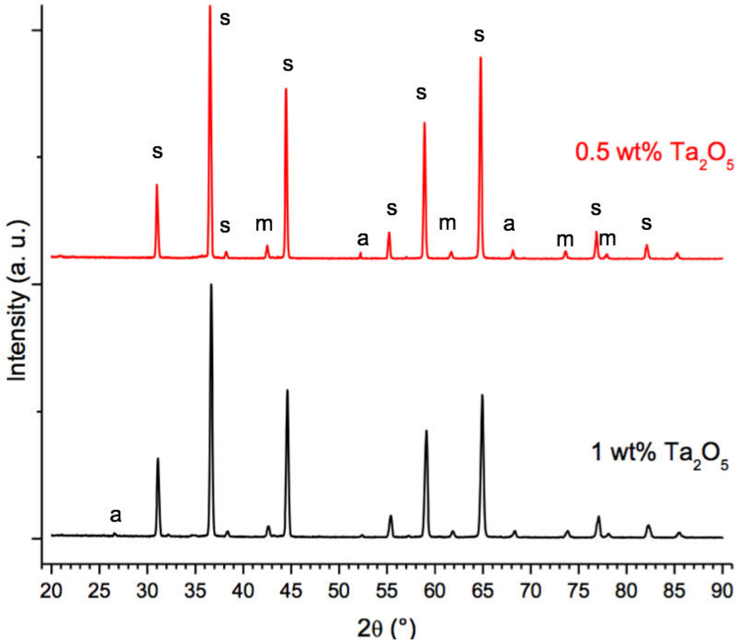

Figure 78. Comparison of XRD patterns of impregnation powder sintered via the long cycle at 1450°C with the addition of 0.5 wt% and 1 wt% Ta_2O_5.

The XRD analysis of the samples (see Figure 78) revealed that the spinel phase is dominant at both doping levels. However, in both cases the presence of corundum and periclase phases is evidenced by some low-intensity peaks that increase as the doping level increases. This means that Ta_2O_5 reacts with a part of the oxide mixture, leaving the stoichiometry unbalanced and possibly creating a concentration of metallic Ta in the sample.

In conclusion, while Ta_2O_5 doping seems to have a slight grain growth inhibiting effect, when the doping concentration is low (0.5 wt%, 0.5 µm via the long cycle at 1370°C), but it also brings up a second mode of grains three times bigger in size. This might be due to a local higher metal concentration in the developing grains, raising the electrical conduction and thus allowing more current to pass through these points.

5.4 $MgAl_2O_4$ via polyol method and reactive sintering

The synthesis of MgO in the presence of alpha-Al_2O_3 (UPA) was carried out by a polyol route to obtain stoichiometric spinel ceramics after reactive sintering by SPS and to compare the results to the impregnation method.

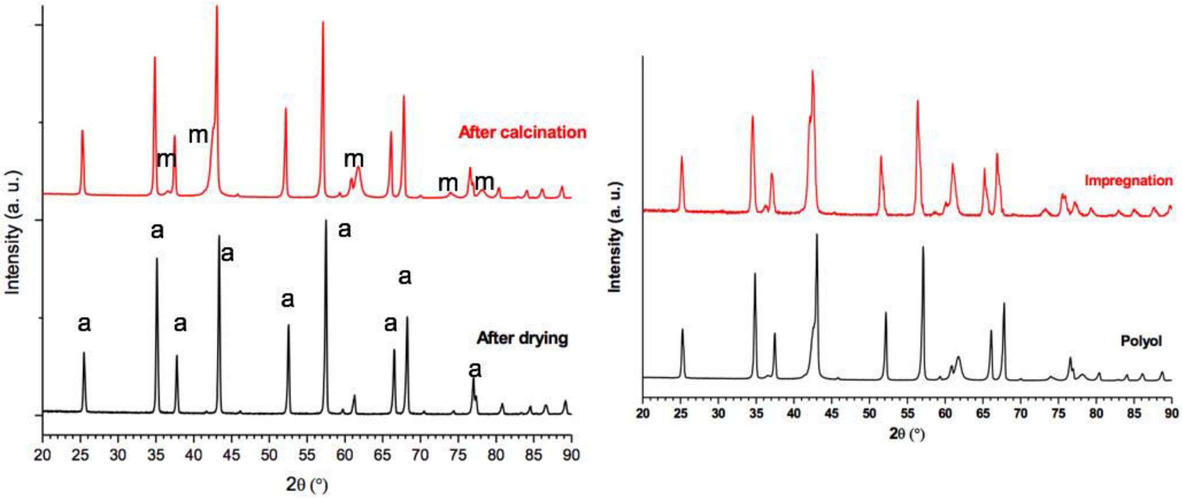

Figure 79. XRD analysis of (left) the polyol powder after drying and after calcination; (right) comparison of the powders obtained by impregnation and polyol methods.

The XRD analysis (see Figure 79 and Table 8) shows the content of MgO synthesized by the polyol method in the presence of corundum to be 25.5%. This value is quite similar to the weight percentage obtained from the impregnation method (24.7%). The crystallite size of the MgO obtained from the polyol method is slightly smaller than that of MgO obtained via impregnation (30 nm-polyol vs 45 nm-impregnation).

Table 8. Comparison of alumina-magnesia powders received from impregnation and polyol process.

Powder	Corundum	Periclase
9 cycles MgO impregnation + A-UPA	75.3 wt% a=4.7662(1); c=13.0091(4) CS~300 nm	24.7 wt% a=4.2210(1) CS~45 nm
Polyol MgO + A-UPA	74.5% a=4.7833(2); c=13.0595(8) CS~300 nm	25.5% a=4.2385(5) CS~30 nm

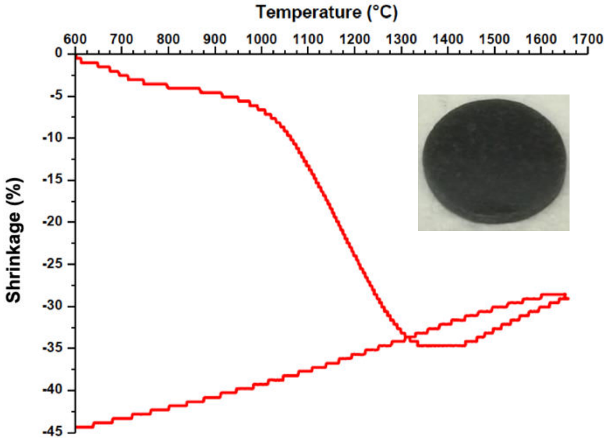

Figure 80. The dilatometric curve of the polyol precursor powder and a photo of the sample.

As before, firstly the dilatometric cycle was applied to the polyol precursor powder (see Figure 80) to optimize the sintering temperature and obtain a reference sample for grain size, density and crystallographic phase. From the dilatometric curve, the optimal sintering temperature for this precursor was determined to be 1315°C.

The SEM microstructure, grain size distribution and XRD pattern of the sintered dilatometric sample are given in Figure 81. From the SEM micrograph and the measured grain size statistics, we can once again note a bimodal distribution of the grain size, with the first mode at 6.5 and the second mode at 44 μm. The XRD analysis shows a nearly monophasic spinel, with some remnant low-intensity corundum and periclase peaks.

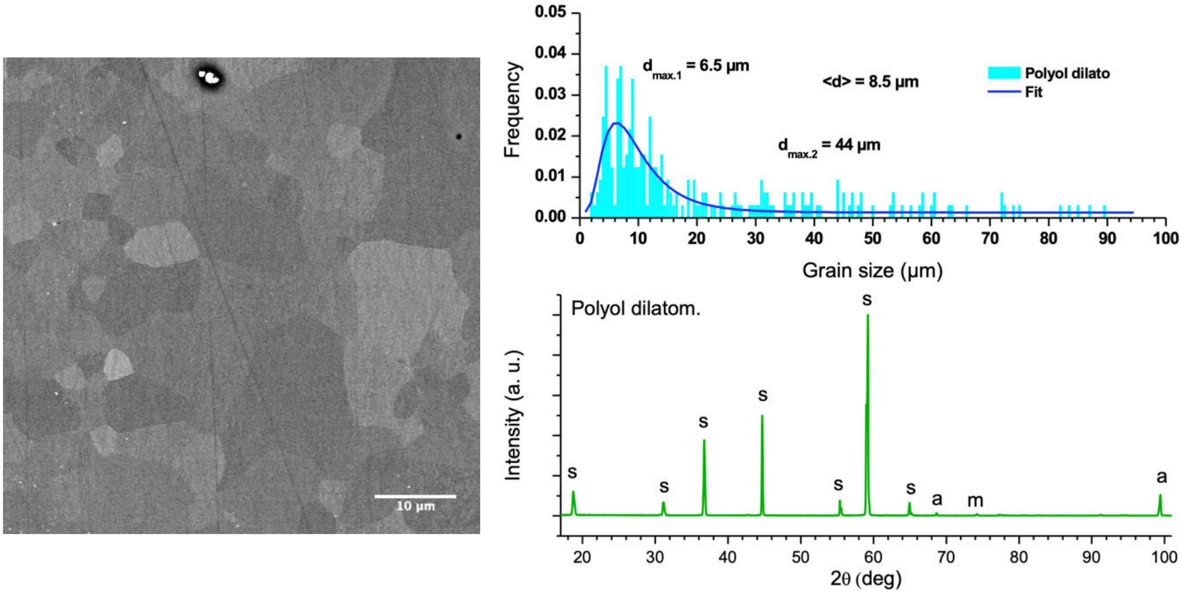

Figure 81. Microstructure, grain size distribution and XRD pattern of the polyol precursor sintered via the dilatometric cycle.

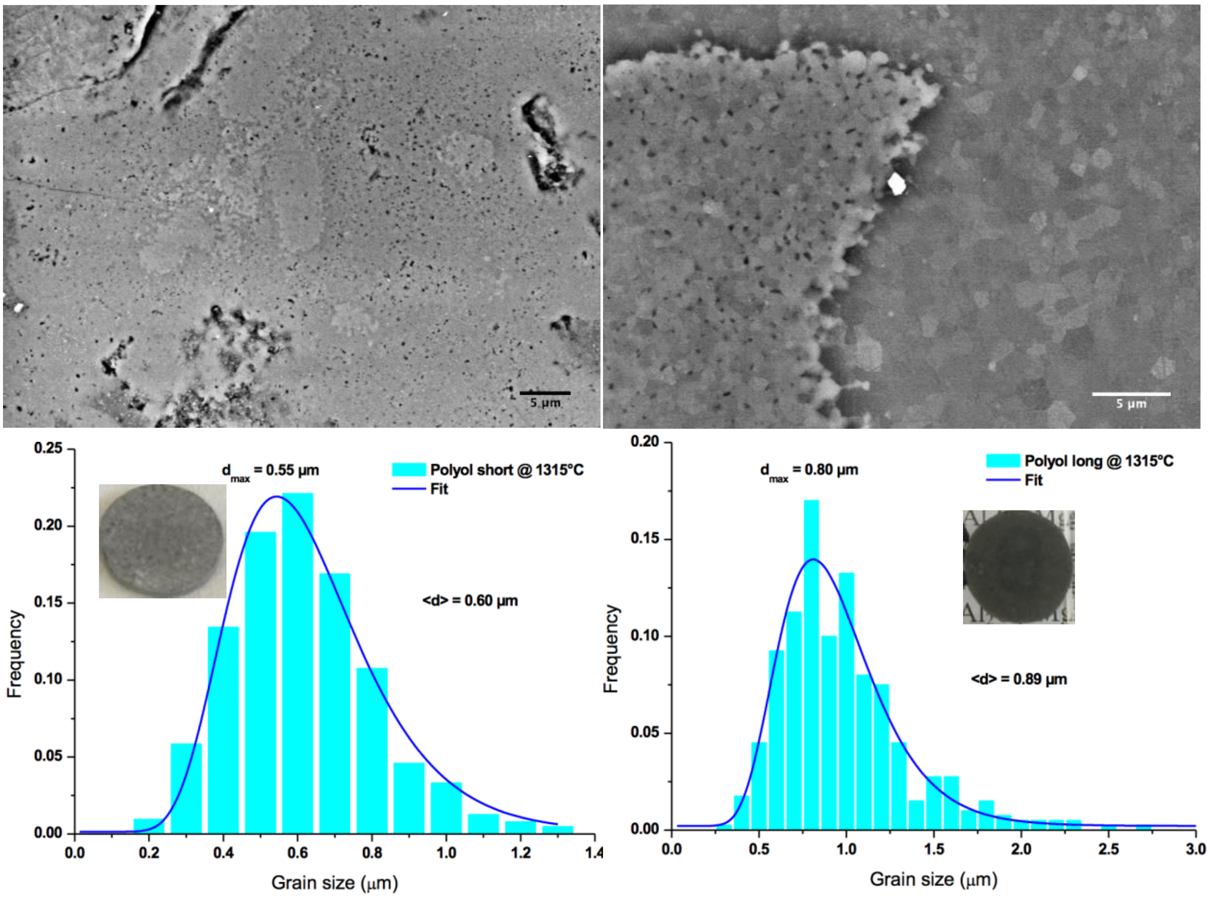

Figure 82. Morphology and grain size distribution of alumina-magnesia mixture sintered by the short (left) and long (right) cycle at 1315°C.

As for the impregnation powder, a dilatometric study was also carried out for the polyol powder, resulting in an optimal sintering temperature of 1315°C. Thus, previously described long and short cycle were carried out at this temperature. The resulting microstructures and grain size distributions are presented in Figure 82. The density of the samples is 3.583(4) and 3.59(1) g/cm^3, respectively for the short and long cycle, leaning again very close to the theoretical density of spinel. However, since we observe high porosity in the SEM micrographs, as well as islands of smaller-sized grains, one can suspect the presence of alumina phase.

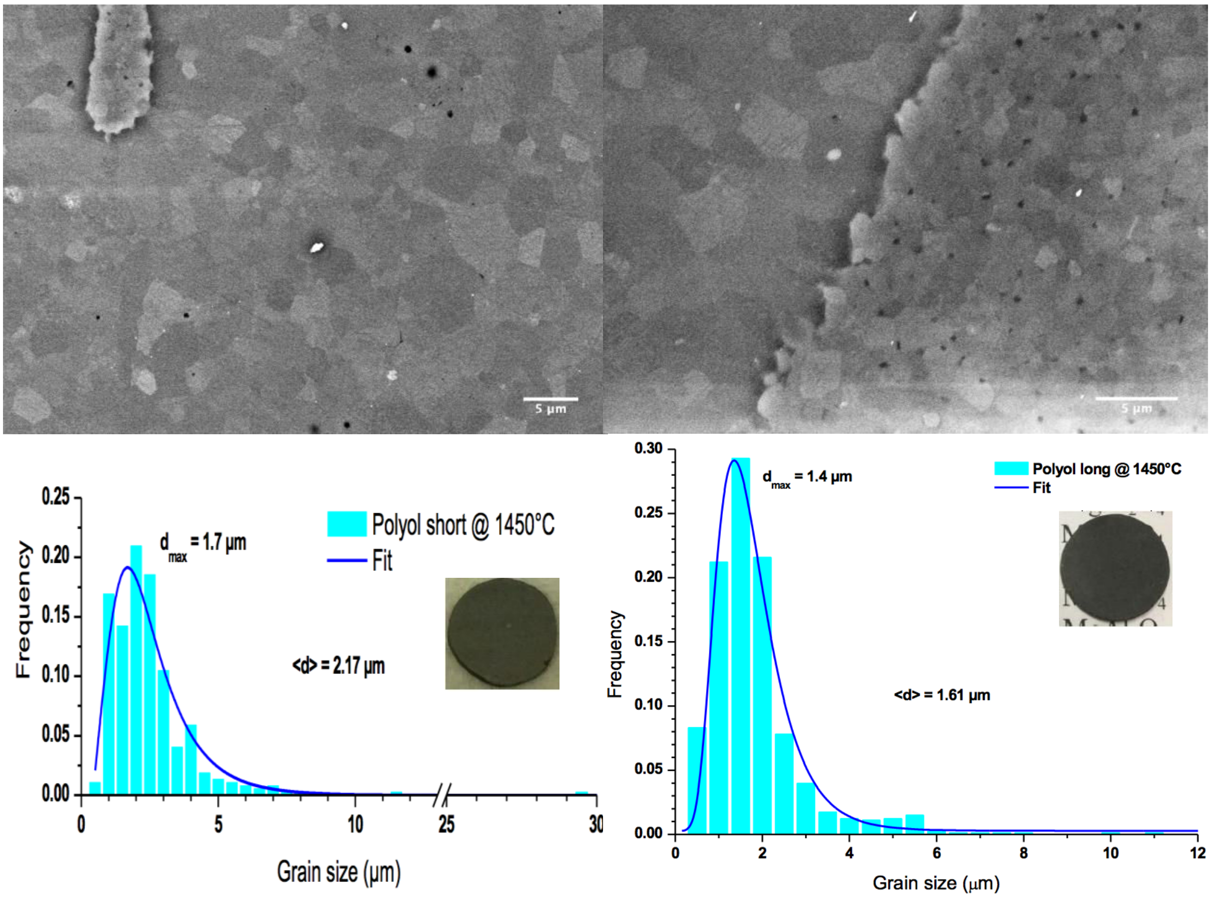

Figure 83. Morphology and grain size distribution of alumina-magnesia mixture sintered by the short (left) and long (right) cycle at 1450°C.

The alumina mixture with magnesia obtained by the polyol process was sintered, as the impregnation powder, by the short and long cycle at 1450°C. Figure 83 shows the microstructure and grain size distribution of both samples. In both cases, we can notice 'islands' of grains sized smaller than the rest of the grains. In the statistical grain size distributions, we can notice a developing bimodal grain size distribution, with first modes quite close for the short and long cycle, at 1.7 and 1.4 µm, respectively. The second modes are starting to develop at 4 µm for the short cycle and at 5.5 µm for the long cycle. While the densities of these ceramics are quite close or even over the theoretical density of spinel (3.550(6) and 3.606(7) g/cm^3), the samples are opaque. This leads us to believe that in addition to spinel, denser alumina phase is also present in these samples.

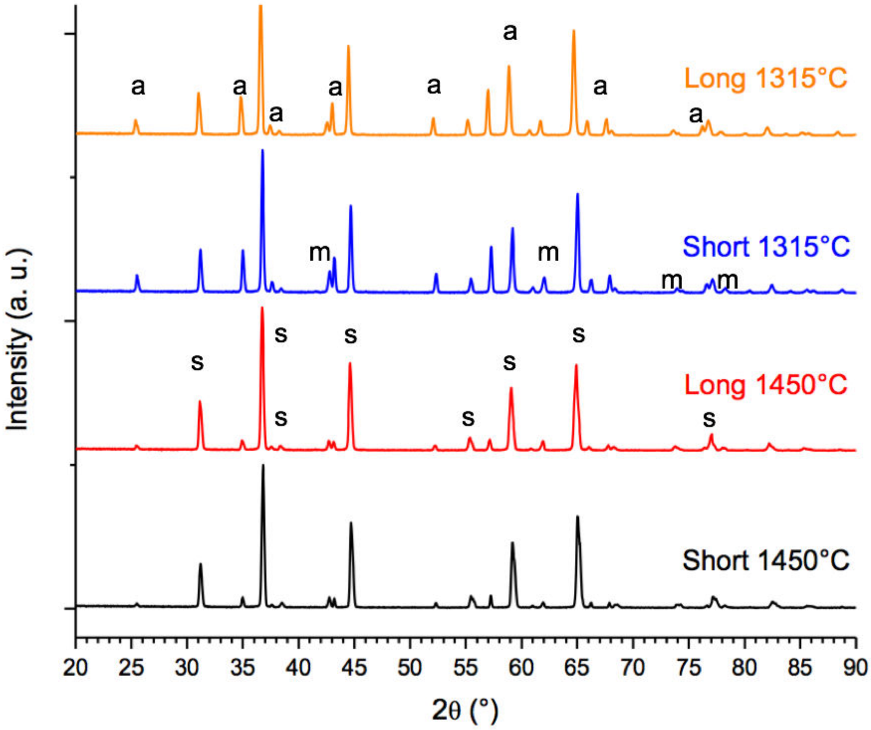

Figure 84. Comparison of XRD patterns of samples sintered from polyol powder.

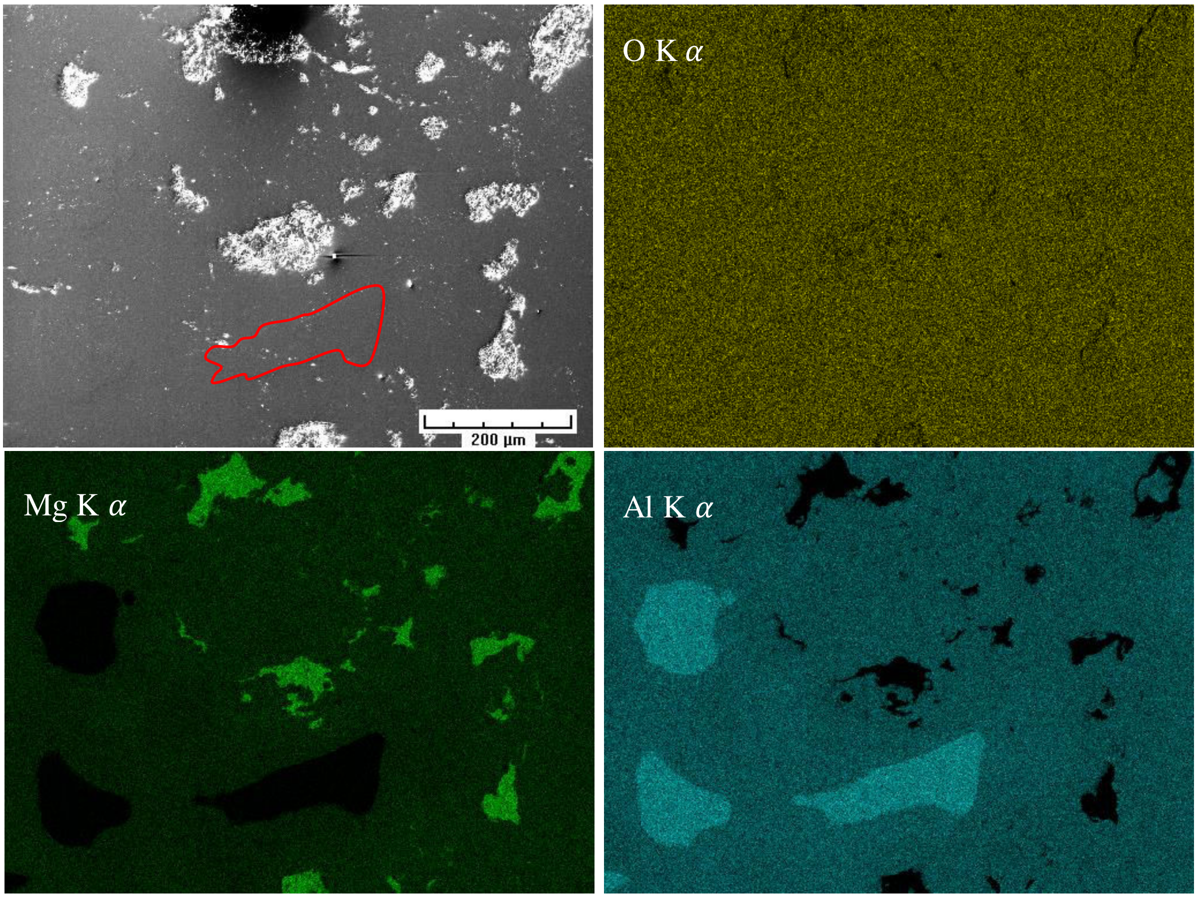

Figure 85. EDX analysis of polyol powder sintered via the long cycle at 1450°C.

To more clearly understand the general and local phase composition, XRD and EDX analysis were carried out. The XRD patterns of all four polyol samples are presented in Figure 84. It is evident that all the sintered samples result in a combination of alumina, magnesia and spinel phases. However, samples sintered at 1450°C show less excess alumina and magnesia than samples sintered at 1315°C. This leads us to conclude that the chosen sintering temperature was in fact not high enough to fully transform the alumina-magnesia mixture into spinel.

Since the polyol sample sintered via the long cycle at 1450°C showed less excess alumina and had the highest density, this sample was chosen for EDX investigation (see Figure 85). As it turns out, the sample consists of ‘islands’ of alumina and ‘ditches’ magnesia, with the spinel phase in between. This means that the mixture of the powder was not homogeneous enough to spark the creation of the spinel phase evenly all over the sample and thus further precursor powder mixing should be considered for future experiments.

5.5 Summary of spinel ceramics

An overview of the sintering cycles, final density and grain size of discussed spinel ceramics received via three different routes is presented in Table 9.

We started our spinel journey by sintering reference samples from a commercially available big-particle spinel powder. The dilatometric study showed the optimal sintering temperature to be 1430°C, which was rounded up to 1450°C to allow comparisons to alumina samples examined in Chapter 4. Unarguably best transparency was obtained when sintering via the long cycle at 1450°C, however, the average grain size of this sample was 4.3 μm, far bigger than desired for radiation resistance applications. Thus, we lowered the sintering temperature to 1300°C and obtained a sample with transmittance of 21% at 650 nm and grain size of 1.1 μm. Various pressure applications were tested during the short cycles; the best results were obtained when applying the pressure from the dwell until the end of the cycle or from the heating to the end of the dwell. The sample sintered via the short cycle at 1450°C showed more promising optical properties and smaller grain size than those sintered at 1300°C. We believe that slightly elongating the 3-minute dwell or applying higher pressure could be sufficient to improve the transparency of this sample even further.

The second and third route to receiving spinel ceramics involve reactive sintering of a stoichiometric mixture of alumina and magnesia. The first doping method, the impregnation method, proved the possibility of obtaining monophasic spinel with various stoichiometries.

After 5 doping cycles we obtained a spinel with Al_2O_3:MgO ratio 1.79 and after 9 doping cycles ratio 1.12, which we consider to be an acceptable approach to the standard 1:1 stoichiometry. The dilatometric study of this precursor showed the optimal sintering temperature to be 1370°C. Sintering via the long cycle at 1370°C allowed us to obtain relative density of about 98% with the grain size of 0.9 μm. This sample was not translucent, thus using longer dwell time or applying higher pressure are topics of interest for further research. While sintering the polyol precursor via the dilatometric cycle at 1650°C resulted in monophasic spinel, the determined optimal sintering temperature of 1315°C was not sufficient to form spinel throughout the whole volume of the sample, thus exhibiting all three phases. Raising sintering temperature to 1450°C increased the spinel mass percentage in the sintered ceramic, but all three phases were still present. Additionally, the EDX analysis of the sample showed islands of alumina and magnesia, hinting to powder inhomogeneity.

Finally, we turned to the investigation of Ta_2O_5 as a possible grain growth inhibitor during reactive sintering. The dopant concentration was first optimized for the commercial powder to lessen the possibility of secondary phase creation. We found that while doping with 1 wt% Ta_2O_5 lessened the grain size from 3.7 μm to 3.2 μm, it also gave rise to a secondary grain size mode of about 40 μm. To avoid exaggerated grain growth, for tests with impregnation precursor, we chose to use its optimal sintering temperature of 1370°C. Doping with 1 wt% Ta_2O_5 lessened the grain size from 0.9 to 0.5 μm, while raising a secondary grain size mode of 1.6 μm. Thus, it seems that bimodal grain size distribution in the case of doping with Ta_2O_5 cannot be avoided, but the size of the secondary mode can be controlled. Combined SEM and EDX analysis confirmed that the secondary Ta-based phase collects in the grain boundaries.

Table 9. Summary of sintered spinel ceramics.

Powder	Sintering cycle	Density (% g/cm^3)	Grain size (µm)	T @ 650 nm (%)	Stoichiometry, X	Comments
Commercial spinel	1650°C dilat, 80 MPa	98.9(3)	3.7	-		C_{dil}
	1450°C long, 80 MPa	99.7(2)	4.30(2)	47	1.09	C1
	1300°C long, 80 MPa	98.1(3)	1.08(2)	21	0.98	C2
	1300°C short, 80 MPa (dwell – end)	97.2(2)	1.20(3)	<1	1.03	C3
	1300°C short, 80 MPa (dwell)	97.6(2)	1.47(4)	-	1.01	C4
	1300°C short, 80 MPa (cooling)	91.5(1)	-	-	0.99	C5
	1450°C short, 80 MPa (heating – end of dwell)	96.0(2)	0.5	<1		C6
	1650°C dilat, 80 MPa	3.563(8)	4.2 // 40	-		0.5 wt% Ta_2O_5
	1650°C dilat, 80 MPa	3.542(11)	3.2 // 40	-		1 wt% Ta_2O_5
	1650°C dilat, 80 MPa	3.573(15)	4.0 // 47	<1		2 wt% Ta_2O_5
	1650°C dilat, 80 MPa	3.593(8)	3.4 // 37	<1		4 wt% Ta_2O_5
A-UPA + MgO impregnation	1650°C dilat, 80 MPa	97.8(2)	22	<1		
	1450°C long, 80 MPa	97.2(2)	25(3)	2	1.12	9 cycles
	1450°C long, 80 MPa	100.3(5)	4.0(2)	-	1.79	5 cycles instead of 9
	1450°C short, 80 MPa	98.3(2)	0.8	-		
	1370°C long, 80 MPa	97.9(2)	0.9	-		
	1370°C long, 80 MPa	3.493(6)	0.7 // 3.3	-		0.5 wt% Ta_2O_5
	1370°C long, 80 MPa	3.446(6)	0.5 // 1.6	-		1 wt% Ta_2O_5
A-UPA + polyol MgO	1650°C dilat, 80 MPa	98.3(3)	6.5 // 44	-		Pure spinel
	1450°C short, 100 MPa	3.550(6)	1.7	-		All three phases present
	1450°C long, 80 MPa	3.606(7)	1.4	-		
	1315°C short, 80 MPa	3.583(4)	-	-		
	1315°C long, 80 MPa	3.595(13)	0.8	-		

Previously, reactive sintering of alumina and magnesia to form spinel has mostly been studied for the hot pressing method or pressureless sintering followed by HIP. Since the phase transformation is accompanied by significant volume expansion, the green body microstructure may be disrupted and thus normally temperatures $\geq$ 1700°C are needed to obtain monophasic spinels with full transparency[1]. Krell *et al*[221] have shown that to effectively erase nanoporosities causing low transparency, it is better to start the reactive sintering from calcined 100 – 200 nm oxide powders than from truly nanometric pre-calcined precursors. In addition, inhomogeneous precursor powders have been shown[222] to lead to microcracked grain boundaries that lower the transparency even further. Thus we believe that one of the ways to improve the transparency and microstructural homogeneity of our reactive sintering spinels is to find and alternative source of alumina with a slightly smaller particle size.

A study[25] on the transparency of non-stoichiometric spinels (n=1…3) has shown that the UV-Vis range is not affected on the alumina concentration, but the IR-limit is. Thus, it would be interesting to study which stoichiometries we are capable to sinter via SPS.

An interesting approach to reactive sintering of spinel via hot pressing is taken in a study[223] investigating sintering a mixture of MgO, Al_2O_3 and LiF. It is presumed that at about 900°C, LiF, MgO and Al_2O_3 will react, forming liquid MgF_2 and solid $LiAlO_2$, the latter of which will then react with the MgF_2 gas formed as the temperature is raised and finally form LiF gas and $MgAl_2O_4$. The resulting samples reach near theoretical transparency, however, the grain sizes are in the range of 100 µm, since the process was carried out at 1600°C. With SPS, we should be able to significantly lower this temperature.

6 Conclusions and perspectives

This PhD thesis investigated the suitability of various alumina and spinel precursor powders for obtaining transparent fine-grained consolidated polycrystalline ceramics via spark plasma sintering. The first part of the work focused on optimizing the precursor and sintering cycles for alumina, to be used as a base material for spinel production in the second part. The challenge of the work is to find an optimal position between using very harsh sintering conditions resulting in fully dense and transparent but huge-grained ceramics and using too soft conditions and not achieving full density but obtaining fine microstructure.

Two types of sintering cycles were used on all precursor powders, the “short” and “long” cycle, and modifications were made according to the characteristics of obtained ceramics. In both cycles, a preliminary 10-minute dwell at 600°C was carried out to stabilize the temperature and evaporate any water from the precursor powders. The cooling rate was kept constant at 100°C/min.

The short cycle was designed to benefit most from the great heating power of SPS, using a constant heating rate of 100°C/min and a short 3-minute dwell at a higher temperature to still allow diffusion. The pressure was generally applied during the 5 minutes leading up to reaching the dwell temperature and lowered also during 5 minutes after the dwell.

The long cycle was designed to obtain maximum densification without exaggerated grain growth due to high heating rate at high temperatures. Thus, 100°C/min heating rate was used to reach 1100°C and from there on the heating rate was lowered to 10°C/min. The sample was held at the dwell temperature for 20 minutes, then cooled down to 1150°C and held for another 10 minutes for further densification without exaggerated grain growth. The pressure was applied as heating up from 600°C started, during 4 minutes and held for 60 minutes, until the end of the 20-minute dwell. The pressure was released during the temperature decrease for the secondary dwell to relax any constraints.

Firstly, six different alumina powders were sintered via the long cycle at 1450°C and 80 MPa. The best transparencies were obtained from the commercial pure γ-Al_2O_3 powder (sample A2) and UPA calcined to α-Al_2O_3 (sample A6), thus proving that dense transparent alumina ceramics can be obtained from both phases. However, the grain size of A2 was 4.9 μm, while A6's reached 16 μm. Previous experience[121] of obtaining fully dense translucent alumina from UPA γ-Al_2O_3 showed that it is possible only after sintering via the long cycle at 1550°C, characterized by the grain size of about 8 μm and in-line transmittance of about 5%. Thus, the importance of precursor powder morphology is revealed. We suppose that the much finer crystallite size of the UPA-obtained γ-Al_2O_3 (~10 nm) compared to the commercial γ-Al_2O_3 (~50 nm) makes the powder much more reactive and thus the grain size during sintering more rapid. Alternatively, finer nanoparticles are more prone to agglomeration, leading to more heterogeneous powder packing which in turn brings up exaggerated and inhomogeneous grain growth.

To minimize the grain size, one has multiple options: 1) using lower dwell temperature, 2) using shorter dwell time, 3) using higher pressure, 4) using sintering additives. The first of these options was dismissed due to previous[121] negative results on sintering UPA-obtained γ-Al_2O_3, where transparency was only reached at 1550°C. Investigation of grain growth inhibiting sintering additions was carried out on spinel ceramics, instead, LiF as a sintering aid was tested on boehmite and boehmite-obtained α-Al_2O_3 precursor powder.

Raising the pressure of the long cycle using α-Al_2O_3 (UPA) to 200 MPa (sample A7) did lead to a slight decrease in grain size, 12.3 μm compared to the 16 μm obtained at 80 MPa. However, it also lead to decrease in density and transparency, confirming that pore growth was brought on by high pressure leading to Ostwald ripening[98], thus eliminating small pores but growing trapped bigger pores. To confirm this hypothesis, the commercial boehmite powder was also sintered by the same long cycle at 200 MPa (sample A14). Even though the sample exhibited nearly full density, the SEM micrographs showed the presence of pores sized under 1 μm, explaining the complete opacity.

The short sintering cycles at 1350 – 1450°C and 100 MPa were not sufficient to obtain translucent ceramics. Nonetheless, short cycles at 1450°C and 285 MPa resulted in translucent ceramics for both precursor powders tested. Especially satisfying results were obtained from α-Al_2O_3 (UPA) powder, which lead to a translucent ceramic (sample A8, 21.3% at 650 nm) with an average grain size of 1.3 μm. Since the density was 96.6%, we decided to pre-press this powder with 4 t before SPS, in efforts to facilitate the densification even further. Unfortunately, the resulting density increase was only 2%, the bigger effect was shown in the grain size, which increased from 1.3 µm to about 24 µm. Thus, keeping in mind our goal of fine microstructure, we do not recommend pre-pressing at the chosen sintering conditions. Alternatively, the sintering conditions to be lowered to avoid exaggerated grain growth.

Addition of 1 wt% LiF to boehmite precursor powder to aid sintering via the short cycle at 1450°C resulted in almost full density and 11.7 µm grain size, however, the sample was opaque due to the presence micrometric pores. This also hints to exaggerated grain growth due to Ostwald ripening.

In conclusion, the most transparent alumina in combination with the finest microstructure was obtained by sintering the α-Al_2O_3 (UPA) via the short cycle at 1450°C and 285 MPa. In contrast, sintering boehmite or a mixture of δ- and γ-Al_2O_3 resulted only in low-density opaque ceramics. Thus, we recommend starting from at least γ-phase when aiming to obtain full-density α-Al_2O_3 ceramics, as it seems that the lower-temperature alumina polymorphs demand harsher sintering conditions to obtain full density.

Absorption studies of the translucent aluminas (samples A2, A6 and A8) showed the presence of single defects, more specifically F, F^+ and F_2^+ centers. The highest concentration of F centers was observed in A2, followed by A8 and A6, while A8 showed the highest concentration of F^+ centers. Cathodoluminescence study of A2 confirmed the existence of F and F^+ centers, additionally, an emission related to interband transitions was observed.

In the second part of the work, spinel ceramics were attained by three different routes. Firstly, a commercial spinel powder was directly sintered without any pretreatment. Secondly, stoichiometric amount of MgO was synthesized by the polyol method in the presence of α-Al_2O_3 (UPA). Lastly, MgO impregnation of α-Al_2O_3 (UPA) was carried out via cycles of doping with $Mg(NO_3)_2$ water solution. The last two methods allowed us to obtain a stoichiometric 1:1 mixture of α-Al_2O_3 and MgO that was directly sintered into spinel via reactive SPS.

Commercial spinel powder resulted in translucent ceramics when sintered via the long cycle at either 1450°C (C1) or 1300°C (C2). C1 sintered at higher temperature showed high density (99.7%) and transparency (47% at 650 nm), as well as relatively big grain size (4.3 µm). Lowering the sintering temperature to 1300°C in the case of C2 allowed us to lower the grain size to 1.1 µm, which unfortunately also resulted in 2.2 times lower transmission at 650 nm (21%). The investigation of pressure application point during the short cycle, we found that for the best density and least amount of discoloration, it is best to apply the pressure in the beginning of the dwell and release it after cooling.

The absorption study showed the highest concentration of F centers in the case of the least translucent sample measured (C3), along with the band maximum red shift of 0.7 eV, while the F center absorption remained similar in the case of C1 and C2, despite their different transparencies. Additionally, C3 shows an absorption at 2 eV, connected to small clusters of oxygen vacancies. Luminescence analysis confirmed the presence of F and F^+ centers along with common Mn^{2+} and Cr^{3+} impurities, in addition showing, as absorption analysis, a higher concentration of color centers for less transparent ceramics. The visible transparency of the prepared ceramics decreases in the order C1, C2 > C4, C3 > C5 in agreement with the increase in the F band intensity. Thus, we conclude that the higher F center concentration is directly linked to the smaller grain size, leading us to believe that the F centers accumulate at grain boundaries.

The sintering of the mixture of α-Al_2O_3 and polyol-obtained MgO resulted in ceramics consisting of areas with all three different phases, thus not satisfying our need for a pure phase. The cause for this remains unclear, but might be related to inhomogeneity in mixing the two oxide phases.

Impregnation of α-Al_2O_3 with MgO allowed us to obtain pure monophasic spinel ceramics with two different stoichiometries, about 1.1 and 1.8, obtaining the stoichiometry of exactly 1 thus remains a topic for further research. Only the precursor powder with 1.1 stoichiometry resulted in a translucent (2%) ceramic after sintering via the long cycle at 1450°C, unfortunately characterized by a grain size of 25 μm. Efforts to lower the sintering temperature to the optimal obtained from the dilatometric study and using Ta_2O_5 as a grain growth inhibitor resulted in non-translucent ceramics. Addition of Ta_2O_5 to the ceramics can be clearly seen on the SEM images, making the grain boundaries draw out much clearer, thus hinting to a presence of conductive metal (Ta) in the grain boundaries. The exact mechanism of Ta_2O_5 reaction with spinel during sintering remains a topic for further research along with the optimization of sintering parameters.

Another option to diminish the grain size of impregnation-obtained spinel would be to sinter the precursor powder via the short cycle at higher pressure (285 MPa). However, precautions should be taken as the reactive sintering is accompanied by a volume change that can be dangerous at high pressures.

To homogenize the reactive sintering precursors obtained via impregnation and polyol method, it might be interesting to use an aluminum salt similar to $Mg(NO_3)_2$ to lessen the heterogeneity of the precursor. We know of only two instances where Al_2O_3 and $MgAl_2O_4$ spinel synthesis by the polyol method were mentioned[224,225], making it quite novel. However, the details of the process are not disclosed. Hence, we see a great benefit in a future parametric study using acetates and chlorides as precursor materials.

In general, homogenizing the precursor powders for sintering remains a future challenge to hopefully minimize observed bimodal grain size distributions. In addition, the impregnation and polyol methods also allow future investigations on the influence of spinel stoichiometry on the mechanical properties and radiation effects as well as fabrication of various spinels based on alumina ($ZnAl_2O_4$, $FeAl_2O_4$ and $MnAl_2O_4$ for example).

Even though HIP of opaque 89 – 97% dense aluminas showed no benefit to transparency, it would be interesting to use HIP to enhance the transparency of ceramics already translucent after SPS. It would be equally interesting to see the resulting grain sizes of what is by some authors considered the most economical and effective way of combining SPS with HIP, carrying out short SPS at slightly lower temperature than the second step HIP (10 min at 1200°C SPS + 3h at 1230°C HIP[155]).

7 PhD candidate's contributions and scientific production

During the thesis work, I carried out the synthesis of ultraporous alumina and alumina doping via the impregnation and polyol methods, as well as spark plasma sintering, polishing, SEM measurements, XRD analysis and density measurements. I co-supervised two Master's interns, the results of their work are included in this thesis. I attended 3 international and 2 national conferences, where I gave oral and poster presentations, detailed here with two journal articles submitted for publication:

- **Oral talk** at ECerS 2017, Budapest, Hungary - The 15th Conference & Exhibition of the European Ceramic Society – *"From wet sponges to optoceramics" 15 min*
- **Poster presentation** at SPS 2017 – Journées Nationales sur le Frittage par Courant Pulsé – *"Influence of starting powder on the properties of ceramics"*
- **Poster presentation** at JNTE 2017, Orléans, France – Journées Nationales sur les Technologies Emergentes en micronanofabrication – *"Spark Plasma Sintering (SPS) of pure and doped alumina ceramics"*
- **Oral talk** at the 4th International Workshop on Spark Plasma Sintering 2018, Cagliari, Italy – *"Spark Plasma Sintering of transparent spinel ceramics" 20 min*
- **Oral talk** at CIMTEC 2018 14th Ceramics Congress, Perugia, Italy – "Spark plasma sintering of alumina-based transparent ceramics" 20 min
- Published **Article**: (Article in Press) Annika Pille, Mohamed Amamra, Andrei Kanaev, Frédéric Schoenstein, Microstructure and optical properties of alumina sintered from various phases, Ceramics International, 2018, 10.1016/j.ceramint.2018.10.209.
- **Article** submitted for publishing: (in review) Annika Pille, Hugo Spiridigliozzi, Mohamed Amamra, Thierry Billeton, Mustapha Zaghrioui, Eduard Feldbach, Andrei Kanaev, Frédéric Schoenstein, Microstructure and luminescence of $MgAl_2O_4$ ceramics obtained via spark plasma sintering.

I am the main author of the two article manuscripts submitted (and in the first case accepted) for publication.

8 References

[1] A. Goldstein, A. Krell, Transparent Ceramics at 50: Progress Made and Further Prospects, J. Am. Ceram. Soc. 99 (2016) 3173–3197. doi:10.1111/jace.14553.

[2] Allied Market Research: Transparent Ceramics Market, (2017). https://www.alliedmarketresearch.com/transparent-ceramics-market (accessed October 10, 2018).

[3] Grand View Research: Transparent ceramics Market 2018-2024, (2018). https://www.grandviewresearch.com/industry-analysis/transparent-ceramics-market (accessed October 10, 2018).

[4] EUROfusion, (n.d.). https://www.euro-fusion.org/programme/ (accessed November 7, 2018).

[5] G. Ackland, Controlling Radiation Damage, Science (80-.). 327 (2010) 1587–1588. doi:10.1126/science.1188088.

[6] X.-M. Bai, A.F. Voter, R.G. Hoagland, M. Nastasi, B.P. Uberuaga, Efficient Annealing of Radiation Damage Near Grain Boundaries via Interstitial Emission, Science (80-.). 327 (2010) 1631–1635. www.sciencemag.org.

[7] P. Kulis, Z. Rachko, M. Springis, I. Tale, J. Jansons, Defect assisted intrinsic luminescence in Al2O3 crystals, Radiat. Eff. Defects Solids. 119–121 (1991) 963–968. doi:10.1080/10420159108220850.

[8] C.J. Ting, H.Y. Lu, Defect reactions and the controlling mechanism in the sintering of magnesium aluminate spinel, J. Am. Ceram. Soc. 82 (1999) 841–848. doi:10.1111/j.1151-2916.1999.tb01844.x.

[9] V.N. Krasil'nikov, I.V. Baklanova, V.P. Zhukov, N.I. Medvedeva, A.P. Tyutyunnik, R.F. Samigullina, O.I. Gyrdasova, M.A. Melkozerova, The luminescence properties of γ-Al2O3:C produced by precursor method, J. Alloys Compd. 698 (2017) 1102–1110. doi:10.1016/j.jallcom.2016.12.243.

[10] I. V. Afanasyev-Charkin, D.W. Cooke, M. Ishimaru, B.L. Bennett, V.T. Gritsyna, J.R. Williams, K.E. Sickafus, Refractive indices of metastable and amorphous phases in Ne+-ion irradiated magnesium-aluminate spinel, Opt. Mater. (Amst). 16 (2001) 397–402. doi:10.1016/S0925-3467(00)00048-3.

[11] M. Beauvy, J.-L. Vignes, D. Michel, L. Mazerolles, C. Frappart, T. Di Costanzo, Method of preparation of monolithic hydrated aluminas, amorphous or crystalline aluminas, aluminates and composite materials by oxidation of aluminum or of an

aluminum alloy, US7799385B2, 2010.

[12] J.-L. Vignes, L. Mazerolles, D. Michel, A novel method for preparing porous alumina objects, Key Eng. Mater. 132–136 (1997) 432–435. doi:10.4028/www.scientific.net/KEM.132-136.432.

[13] F. Maglia, I.G. Tredici, U. Anselmi-Tamburini, Densification and properties of bulk nanocrystalline functional ceramics with grain size below 50nm, J. Eur. Ceram. Soc. 33 (2013) 1045–1066. doi:10.1016/j.jeurceramsoc.2012.12.004.

[14] K. Wefers, C. Misra, Oxides and Hydroxides of Aluminum, Alcoa Tech. Pap. 19 (1987) 1–100.

[15] C. Misra, Industrial alumina chemicals, American Chemical Society, Washington D.C., 1986.

[16] H.C. Stumpf, a. S. Russel, J.W. Newsome, C.M. Tucker, Thermal Transfomations of Aluminas and Alumina Hydrates, Ind. Eng. Chem. 42 (1950) 1398–1403. doi:10.1021/ie50487a039.

[17] Corundum mineral data, (n.d.). http://webmineral.com/data/Corundum.shtml#.W5oQvdh_K_U (accessed September 12, 2018).

[18] I. Levin, D. Brandon, Metastable Alumina Polymorphs: Crystal Structures and Transition Sequences, J. Am. Ceram. Soc. 81 (2005) 1995–2012. doi:10.1111/j.1151-2916.1998.tb02581.x.

[19] Corundum unit cell, (n.d.). https://fr.m.wikipedia.org/wiki/Fichier:Corundum-unit-cell-3D-balls.png (accessed September 12, 2018).

[20] Corundum XRD data NIMS, (n.d.). https://crystdb.nims.go.jp/crystdb/search-details?substance_id=6917&tabDetail=pageD&need_more_value=&pageD=1&reference_id=4295037654&pageA=1&pageSubP=1&errorCode=0&pageSubD=1&pageSubA=1&isVisiblePeriodicTable=false&tab=pageD&tabSub=pageD&isNeedMoreValueEr (accessed November 10, 2018).

[21] H. Sawada, Residual electron density study of chromium sesquioxide by crystal structure and scattering factor refinement, Mater. Res. Bull. 29 (1994) 239–245. doi:10.1016/0025-5408(94)90019-1.

[22] J.H. Crawford Jr, L.M. Slifkin, Point Defects in Solids, Plenum Press, New York, 1972.

[23] H. Mao, M. Selleby, B. Sundman, A re-evaluation of the liquid phases in the CaO-Al2O3and MgO-Al2O3systems, Calphad Comput. Coupling Phase Diagrams

Thermochem. 28 (2004) 307–312. doi:10.1016/j.calphad.2004.09.001.

[24] D. Han, J. Zhang, P. Liu, G. Li, S. Wang, Densification and microstructure evolution of reactively sintered transparent spinel ceramics, Ceram. Int. 44 (2018) 11101–11108. doi:10.1016/j.ceramint.2018.03.109.

[25] A. Krell, K. Waetzig, J. Klimke, Influence of the structure of MgO·nAl2O3 spinel lattices on transparent ceramics processing and properties, J. Eur. Ceram. Soc. 32 (2012) 2887–2898. doi:10.1016/j.jeurceramsoc.2012.02.054.

[26] J.A. Ball, Computer Simulation of Disorder in Ceramic Materials - CHAPTER 3: Cation Disorder in MgAl2O4 Spinel, Imperial College of Science, Technology and Medicine, 2006. doi:10.1080/14786430903341402.

[27] J.A. Ball, M. Pirzada, R.W. Grimes, M.O. Zacate, D.W. Price, B.P. Uberuaga, Predicting lattice parameter as a function of cation disorder in $MgAl_2O_4$ spinel, J. Phys. Condens. Matter. 17 (2005) 7621–7631. doi:10.1088/0953-8984/17/48/014.

[28] D. Dwibedi, From cation flexibility to multifaceted industrial adoptability: a voyage to the resourceful spinel, Adv. Appl. Ceram. 0 (2017) 1–15. doi:10.1080/17436753.2017.1371946.

[29] S.S. Balabanov, A.V. Belyaev, E.M. Gavrishchuk, I.B. Mukhin, A.V. Novikova, O.V. Palashov, D.A. Permin, I.L. Snetkov, Fabrication and measurement of optical and spectral properties of the transparent Yb:MgAl2O4 ceramics, Opt. Mater. (Amst). 71 (2017) 17–22. doi:10.1016/j.optmat.2016.10.033.

[30] W. Luo, P. Ma, T. Xie, J. Dai, Y. Pan, H. Kou, J. Li, Fabrication and spectroscopic properties of Co:MgAl2O4 transparent ceramics by the HIP post-treatment, Opt. Mater. (Amst). 69 (2017) 152–157. doi:10.1016/j.optmat.2017.03.036.

[31] A.A. Kachaev, D. V. Grashchenkov, Y.E. Lebedeva, S. St. Solntsev, O.L. Khasanov, Optically Transparent Ceramic (Review), Glas. Ceram. 73 (2016) 117–123. doi:10.1007/s10717-016-9838-3.

[32] R. Basso, S. Carbonin, A. Dell Giusta, Cation and vacancy distribution in a synthetic defect spinel, Zeitschrift Fur Krist. - New Cryst. Struct. 194 (1991) 111–119. doi:10.1524/zkri.1991.194.1-2.111.

[33] Spinel XRD, (n.d.). https://crystdb.nims.go.jp/crystdb/search-details?substance_id=970&tabDetail=pageD&need_more_value=&pageD=1&reference_id=4295085878&pageA=1&pageSubP=0&errorCode=0&pageSubD=1&pageSubA=1&isVisiblePeriodicTable=false&tab=pageD&tabSub=pageD&isNeedMoreValueErr (accessed November 11, 2018).

[34] H.U. Viertel, F. Seifert, Physical properties of defect spinels in the system MgAl2O4-Al2O3, Neues Jahrb. Für Mineral. Abhandlungen. (1979).

[35] S. Sawai, T. Uchino, Visible photoluminescence from MgAl2O4 spinel with cation disorder and oxygen vacancy, J. Appl. Phys. 112 (2012) 103523. doi:10.1063/1.4767228.

[36] C.-J. Ting, H.-Y. Lu, Deterioration in the Final-Stage Sintering of Magnesium Aluminate Spinel, J. Am. Ceram. Soc. 83 (2000) 1592–1598. doi:10.1111/j.1151-2916.2000.tb01436.x.

[37] R. Sarkar, H.S. Tripathi, A. Ghosh, Reaction sintering of different spinel compositions in the presence of Y2O3, Mater. Lett. 58 (2004) 2186–2191. doi:10.1016/j.matlet.2004.01.015.

[38] S. Imine, F. Schoenstein, S. Mercone, M. Zaghrioui, N. Bettahar, N. Jouini, Bottom-up and new compaction processes: A way to tunable properties of nanostructured cobalt ferrite ceramics, J. Eur. Ceram. Soc. 31 (2011) 2943–2955. doi:10.1016/j.jeurceramsoc.2011.06.004.

[39] A. Ibarra, D. Bravo, F.J. Lopez, F.A. Garner, High-dose neutron irradiation of MgAl2O4 spinel: Effects of post-irradiation thermal annealing on EPR and optical absorption, J. Nucl. Mater. 336 (2005) 156–162. doi:10.1016/j.jnucmat.2004.09.003.

[40] I. Ganesh, A review on magnesium aluminate ($MgAl_2O_4$) spinel: synthesis, processing and applications, Int. Mater. Rev. 58 (2012) 63–112. doi:10.1179/1743280412Y.0000000001.

[41] E.J.W. Verwey, The Structure of the electrolytical oxide Layer on Aluminium, Zeitschrift Für Krist. - Cryst. Mater. 91 (1935) 319–323. doi:10.1524/zkri.1935.91.1.317.

[42] B.E. Yoldas, Transparent activated nanoparticulate alumina and method of preparing same, 3941719, 1973. https://patents.justia.com/patent/3941719.

[43] B.E. Yoldas, Alumina gels that form porous transparent Al2O3, J. Mater. Sci. 10 (1975) 1856–1860. doi:10.1007/BF00754473.

[44] B.E. Yoldas, Hydrolysis of aluminium alkoxides and bayerite conversion, J. Appl. Chem. Biotechnol. 23 (1973) 803–809. doi:10.1002/jctb.5020231103.

[45] D. Levy, M. Zayat, eds., The Sol-Gel Handbook: Synthesis, Characterization, and Applications, John Wiley & Sons, 2015. https://www.wiley.com/en-fr/The+Sol+Gel+Handbook%3A+Synthesis%2C+Characterization%2C+and+Applications%2C+3+Volume+Set-p-9783527670833.

[46] H. Dong, Y.-C. Chen, C. Feldmann, Polyol synthesis of nanoparticles: status and options regarding metals, oxides, chalcogenides, and non-metal elements, Green Chem. 17 (2015) 4107–4132. doi:10.1039/C5GC00943J.

[47] F. Fievet, J.P. Lagier, M. Figlarz, Preparing Monodisperse Metal Powders in Micrometer and Submicrometer Sizes by the Polyol Process, MRS Bull. 14 (1989) 29–34.

[48] D. Jezequel, J. Guenot, N. Jouini, F. Fievet, Preparation and Morphological Characterization of Fine, Spherical, Monodisperse Particles of ZnO, Mater. Sci. Forum. 152–153 (1994) 339–342. doi:10.4028/www.scientific.net/MSF.152-153.339.

[49] D. Jézéquel, J. Guenot, N. Jouini, F. Fiévet, Submicrometer zinc oxide particles: Elaboration in polyol medium and morphological characteristics, J. Mater. Res. 10 (1995) 77–83. doi:10.1557/JMR.1995.0077.

[50] A. Subramania, G.V. Kumar, A.R.S. Priya, T. Vasudevan, Polyol-mediated thermolysis process for the synthesis of MgO nanoparticles and nanowires, Nanotechnology. 18 (2007) 225601. doi:10.1088/0957-4484/18/22/225601.

[51] T. Itoh, T. Uchida, I. Matsubara, N. Izu, W. Shin, H. Miyazaki, H. Tanjo, K. Kanda, Preparation of??-alumina large grain particles with large specific surface area via polyol synthesis, Ceram. Int. 41 (2015) 3631–3638. doi:10.1016/j.ceramint.2014.11.028.

[52] J.L. Vignes, C. Frappart, T. Di Costanzo, J.C. Rouchaud, L. Mazerolles, D. Michel, Ultraporous monoliths of alumina prepared at room temperature by aluminium oxidation, J. Mater. Sci. 43 (2008) 1234–1240. doi:10.1007/s10853-007-2260-z.

[53] T. Costanzo, A.A. Fomkin, C. Frappart, A.N. Khodan, D.G. Kuznetsov, L. Mazerolles, D. Michel, A.A. Minaev, V.A. Sinitsin, J. Vignes, New method of porous oxide synthesis: alumina and alumina based compounds, Mater. Sci. Forum. 453–454 (2004) 315–322. doi:10.4028/www.scientific.net/MSF.453-454.315.

[54] T. di Costanzo, Réactivité d'une alumine monolithique poreuse. Stabilisation de diverses phases d'alumine de transition. Élaboration de matériaux monolithiques poreux., Université Paris V, 2001.

[55] A. Khodan, T.H.N. Nguyen, M. Esaulkov, M.R. Kiselev, M. Amamra, J.-L. Vignes, A. Kanaev, Porous monoliths consisting of aluminum oxyhydroxide nanofibrils : 3D structure , chemical composition , and phase transformations in the temperature range 25 – 1700 ° C, J Nanopart Res 20 194. 20 (2018). doi:10.1007/s11051-018-4285-4.

[56] M. Bouslama, M.C. Amamra, Z. Jia, M. Ben Amar, K. Chhor, O. Brinza, M.

Abderrabba, J.L. Vignes, A. Kanaev, Nanoparticulate TiO2-Al2O3photocatalytic media: Effect of particle size and polymorphism on photocatalytic activity, ACS Catal. 2 (2012) 1884–1892. doi:10.1021/cs300033y.

[57] M. Bouslama, M.C. Amamra, O. Brinza, S. Tieng, K. Chhor, M. Abderrabba, J.L. Vignes, a Kanaev, Isolation of titania nanoparticles in monolithic ultraporous alumina: Effect of nanoparticle aggregation on anatase phase stability and photocatalytic activity, Appl. Catal. AGeneral. 402 (2011) 156–161. doi:10.1016/j.apcata.2011.05.042.

[58] V.K. Singh, R.K. Sinha, Low temperature synthesis of spinel (MgAl2O4), Mater. Lett. 31 (1997) 281–285.

[59] M. Suarez, V. Rocha, A. Fernandez, J.L. Menendez, R. Torrecillas, Synthesis and processing of spinel powders for transparent ceramics, Ceram. Int. 40 (2014) 4065–4069. doi:10.1016/j.ceramint.2013.08.060.

[60] A. Krell, J. Klimke, T. Hutzler, Transparent compact ceramics: Inherent physical issues, Opt. Mater. (Amst). 31 (2009) 1144–1150. doi:10.1016/j.optmat.2008.12.009.

[61] J.-J. Choi, J. Ryu, H.-E. Kim, Microstructural Evolution of Transparent PLZT Ceramics Sintered in Air and Oxygen Atmospheres, J. Am. Ceram. Soc. 84 (2001) 1465–1469.

[62] H. Schneider, M. Schmücker, K. Ikeda, W.A. Kaysser, Optically Translucent Mullite Ceramics, J. Am. Ceram. Soc. 76 (1993) 2912–2914. doi:10.1111/j.1151-2916.1993.tb04037.x.

[63] J.G.J. Peelen, Transparent hot-pressed alumina. I: Hot pressing of alumina, Ceramurg. Int. 5 (1979) 70–75. doi:10.1016/0390-5519(79)90032-2.

[64] S.-M. Ho, B.E. Yoldas, D.M. Mattox, Economic preparation of alumina suitabe for isostatic pressing and sintering, 4357427, 1982.

[65] R.J. BRATTON, Sintering and Grain-Growth Kinetics of MgAl2O4, J. Am. Ceram. Soc. 54 (1971) 141–143. doi:10.1111/j.1151-2916.1971.tb12241.x.

[66] D.C. Harris, History of development of polycrystalline optical spinel in the U.S., Proc. SPIE. 5786 (2005) 1. doi:10.1117/12.609708.

[67] CeramTec history, (n.d.). https://www.ceramtec.com/history/ (accessed October 10, 2018).

[68] Fraunhofer IKTS, (n.d.). doi:https://www.ikts.fraunhofer.de/en/aboutus/history.html.

[69] F.W. Clinard, Ceramics for fusion applications, Ceram. Int. 13 (1987) 69–75. doi:10.1016/0272-8842(87)90041-1.

[70] T. Watanabe, Grain boundary engineering: Historical perspective and future prospects, J. Mater. Sci. 46 (2011) 4095–4115. doi:10.1007/s10853-011-5393-z.

[71] L. Tan, T.R. Allen, J.T. Busby, Grain boundary engineering for structure materials of nuclear reactors, J. Nucl. Mater. 441 (2013) 661–666. doi:10.1016/j.jnucmat.2013.03.050.

[72] A.M. Stoneham, J.R. Matthews, I.J. Ford, Innovative materials for fusion power plant structures: Separating functions, J. Phys. Condens. Matter. 16 (2004). doi:10.1088/0953-8984/16/27/001.

[73] M.J. Demkowicz, R.G. Hoagland, J.P. Hirth, Interface structure and radiation damage resistance in Cu-Nb multilayer nanocomposites, Phys. Rev. Lett. 100 (2008) 2–5. doi:10.1103/PhysRevLett.100.136102.

[74] M. Rose, A.G. Balogh, H. Hahn, Instability of irradiation induced defects in nanostructured materials, Nucl. Instruments Methods Phys. Res. Sect. B Beam Interact. with Mater. Atoms. 127–128 (1997) 119–122. doi:10.1016/S0168-583X(96)00863-4.

[75] S. Boninelli, A. Claverie, G. Impellizzeri, S. Mirabella, F. Priolo, E. Napolitani, F. Cristiano, Evidences of F-induced nanobubbles as sink for self-interstitials in Si, Appl. Phys. Lett. 89 (2006) 2–5. doi:10.1063/1.2364271.

[76] T.D. Shen, S. Feng, M. Tang, J.A. Valdez, Y. Wang, K.E. Sickafus, Enhanced radiation tolerance in nanocrystalline Mg Ga2 O4, Appl. Phys. Lett. 90 (2007) 2–5. doi:10.1063/1.2753098.

[77] K. Trachenko, Understanding resistance to amorphization by radiation damage, J. Phys. Condens. Matter. 16 (2004). doi:10.1088/0953-8984/16/49/R03.

[78] V.M. Koshkin, L.P. Gal'chinetskii, V.N. Kulik, U.A. Ulmanis, Radiation stability of AIII 2 BVI 3semiconductors, Radiat. Eff. 29 (1976) 1–6. doi:10.1080/00337577208231184.

[79] A. Krell, P. Blank, H. Ma, Processing of High-Density Submicrometer Al2O3 for New Applications, J. Am. Ceram. Soc. 86 (2003) 546–553. doi:10.1111/j.1151-2916.2003.tb03339.x.

[80] T.G. Nieh, J. Wadsworth, F. Wakai, Recent advances in superplastic ceramics and ceramic composites, Int. Mater. Rev. 36 (1991) 146–161. doi:10.1179/imr.1991.36.1.146.

[81] I. Chen, X. Wang, Sintering dense nanocrystalline ceramics without final-stage grain growth, Nature. 404 (2000) 168–71. doi:10.1038/35004548.

[82] C. Wang, Z. Zhao, Transparent polycrystalline ruby ceramic by spark plasma sintering,

Mater. Res. Bull. 45 (2010) 1127–1131. doi:10.1016/j.materresbull.2010.05.034.

[83] S. Ghanizadeh, S. Grasso, P. Ramanujam, B. Vaidhyanathan, J. Binner, P. Brown, J. Goldwasser, Improved transparency and hardness in ??-alumina ceramics fabricated by high-pressure SPS of nanopowders, Ceram. Int. 43 (2017) 275–281. doi:10.1016/j.ceramint.2016.09.150.

[84] M. Tang, J.A. Valdez, Y. Wang, J. Zhang, B.P. Uberuaga, K.E. Sickafus, Ion irradiation-induced crystal structure changes in inverse spinel MgIn2O4, Scr. Mater. 125 (2016) 10–14. doi:10.1016/j.scriptamat.2016.07.009.

[85] N. Ouar, M.A. Bousnina, F. Schoenstein, S. Mercone, O. Brinza, S. Farhat, N. Jouini, Spark Plasma Sintering of Co80Ni20nanopowders synthesized by polyol process and their magnetic and mechanical properties, J. Alloys Compd. 615 (2015) S269–S275. doi:10.1016/j.jallcom.2014.01.058.

[86] G.F. Taylor, Apparatus for making hard metal compositions, US1896854A, 1933. https://patents.google.com/patent/US1896854.

[87] K. Inoue, Electric-discharge sintering, US3241956A, 1966. https://patents.google.com/patent/US3241956A/en.

[88] K. Inoue, Apparatus for electrically sintering discrete bodies, US3250892A, 1966.

[89] O. Yanagisawa, T. Hatayama, K. Matsugi, Recent research on spark sintering, Mateira Japan. 33 (1994) 1489–1496.

[90] Z. Shen, H. Peng, J. Liu, M. Nygren, Conversion from nano- to micron-sized structures: Experimental observations, J. Eur. Ceram. Soc. 24 (2004) 3447–3452. doi:10.1016/j.jeurceramsoc.2003.10.033.

[91] F. Meng, Z. Fu, J. Zhang, H. Wang, W. Wang, Y. Wang, Q. Zhang, Rapid densification of nano-grained alumina by high temperature and pressure with a very high heating rate, J. Am. Ceram. Soc. 90 (2007) 1262–1264. doi:10.1111/j.1551-2916.2007.01599.x.

[92] O. Guillon, J. Gonzalez-Julian, B. Dargatz, T. Kessel, G. Schierning, J. Räthel, M. Herrmann, Field-assisted sintering technology/spark plasma sintering: Mechanisms, materials, and technology developments, Adv. Eng. Mater. 16 (2014) 830–849. doi:10.1002/adem.201300409.

[93] U. Anselmi-Tamburini, S. Gennari, J.E. Garay, Z.A. Munir, Fundamental investigations on the spark plasma sintering/synthesis process II. Modeling of current and temperature distributions, Mater. Sci. Eng. A. 394 (2005) 139–148. doi:10.1016/j.msea.2004.11.019.

[94] C. Estournès, Mise en forme de matériaux par frittage flash, Tech. l'ingénieur. 33 (2006) IN 56.

[95] J.-M. Haussonne, J.L. Barton, P. Bowen, C.P. Carry, Céramiques et verres - TM vol 16, Presses polytechniques et universitaires Romandes, 2005.

[96] L. Stanciu, D. Quach, C. Faconti, J.R. Groza, F. Raether, Initial stages of sintering of alumina by thermo-optical measurements, J. Am. Ceram. Soc. 90 (2007) 2716–2722. doi:10.1111/j.1551-2916.2007.01778.x.

[97] R. Chaim, M. Levin, A. Shlayer, C. Estournes, Sintering and densification of nanocrystalline ceramic oxide powders: a review, Adv. Appl. Ceram. 107 (2008) 159–169. doi:10.1179/174367508X297812.

[98] C.S. Yuan, Z.J. Wang, Q. Zhi, Y.M. Zhang, X.D. Wang, J.F. Yang, The Preparation and Properties of Alumina Ceramics through a Two-Step Pressureless Sintering Process, Mater. Sci. Forum. 922 (2018) 47–54. doi:10.4028/www.scientific.net/MSF.922.47.

[99] A. Rothman, S. Kalabukhov, N. Sverdlov, M.P. Dariel, N. Frage, The Effect of Grain Size on the Mechanical and Optical Properties of Spark Plasma Sintering-Processed Magnesium Aluminate Spinel MgAl\n 2\n O\n 4, Int. J. Appl. Ceram. Technol. 11 (2014) 146–153. doi:10.1111/j.1744-7402.2012.02849.x.

[100] K.A. Padmanabhan, H. Gleiter, On the structure of grain/interphase boundaries and interfaces, Beilstein J. Nanotechnol. 5 (2014) 1603–1615. doi:10.3762/bjnano.5.172.

[101] F.J. Humphreys, M. Hatherly, Recrystallization and related annealing phenomena, Elsevier Ltd, 2004. doi:10.1016/B978-0-08-044164-1.X5000-2.

[102] C. Scott, M. Kaliszewski, C. Greskovich, L. Levinson, Conversion of Polycrystalline Al 2 O 3 into Single-Crystal Sapphire by, J. Am. Ceram. Soc. 85 (2002) 1275–1280.

[103] P.A. Badkar, J.E. Bailey, H.A. Barker, Sintering and related phenomena, 1973.

[104] R. Chaim, G. Chevallier, A. Weibel, C. Estournès, Grain growth during spark plasma and flash sintering of ceramic nanoparticles : a review, J Mater Sci. (2017). doi:https://doi.org/10.1007/s10853-017-1761-7.

[105] G.R. Villalobos, J.S. Sanghera, I.D. Aggarwal, Degradation of magnesium aluminum spinel by lithium fluoride sintering aid, J. Am. Ceram. Soc. 88 (2005) 1321–1322. doi:10.1111/j.1551-2916.2005.00209.x.

[106] R. Marder, C. Estournès, G. Chevallier, S. Kalabukhov, R. Chaim, Spark plasma sintering of ductile ceramic particles: Study of LiF, J. Mater. Sci. 49 (2014) 5237–5245. doi:10.1007/s10853-013-7786-7.

[107] A.C. Sutorik, G. Gilde, C. Cooper, J. Wright, C. Hilton, The effect of varied amounts of LiF sintering aid on the transparency of alumina rich spinel ceramic with the composition MgO ??1.5 Al 2 O 3, J. Am. Ceram. Soc. 95 (2012) 1807–1810. doi:10.1111/j.1551-2916.2012.05217.x.

[108] M. Sokol, S. Kalabukhov, M.P. Dariel, N. Frage, High-pressure spark plasma sintering (SPS) of transparent polycrystalline magnesium aluminate spinel (PMAS), J. Eur. Ceram. Soc. 34 (2014) 4305–4310. doi:10.1016/j.jeurceramsoc.2014.07.022.

[109] R.R. Suchomel, R.S. Cook, M.F. Berard, O.J. Hunter, HfO2 and Ta2O5 as grain growth inhibitors in Eu2O3, J. Nucl. Mater. 61 (1976) 99–104.

[110] C. Wanqiu, Z. Yujuan, Z. Yun, Effects of Ta2O5 and MgO additives on microstructure and mechanical properties of ultra-pure alumina ceramics, Ceram. Int. 14 (1988) 133–140. doi:10.1016/0272-8842(88)90001-6.

[111] R. Apetz, M.P.B. van Bruggen, Transparent Alumina: A Light-Scattering Model, J. Am. Ceram. Soc. 86 (2003) 480–486. doi:10.1111/j.1151-2916.2003.tb03325.x.

[112] S.H. Risbud, C.H. Shan, A.K. Mukherjee, M.J. Kim, J.S. Bow, R.A. Holl, Retention of Nanostructure in Aluminum-Oxide by very Rapid Sintering at 1150-Degrees-C, J. Mater. Res. 10 (1995) 237–239. doi:10.1557/JMR.1995.0237.

[113] K. Hayashi, O. Kobayashi, S. Toyoda, K. Morinaga, Transmission Optical Properties of Polycrystalline Alunina with Submicron Grains, Mater. Trans. JIM. 32 (1991) 1024–1029.

[114] B.N. Kim, K. Hiraga, K. Morita, H. Yoshida, Spark plasma sintering of transparent alumina, Scr. Mater. 57 (2007) 607–610. doi:10.1016/j.scriptamat.2007.06.009.

[115] D. Jiang, D.M. Hulbert, U. Anselmi-Tamburini, T. Ng, D. Land, A.K. Mukherjee, Optically transparent polycrystalline Al2O3 produced by spark plasma sintering, J. Am. Ceram. Soc. 91 (2008) 151–154. doi:10.1111/j.1551-2916.2007.02086.x.

[116] K. Morita, B.N. Kim, K. Hiraga, H. Yoshida, Fabrication of transparent MgAl2O4 spinel polycrystal by spark plasma sintering processing, Scr. Mater. 58 (2008) 1114–1117. doi:10.1016/j.scriptamat.2008.02.008.

[117] A. V. Bersh, A. V. Belyakov, D.Y. Mazalov, S.A. Solov'ev, L. V. Sudnik, A. V. Fedotov, Formation and Sintering of Boehmite and Aluminum Oxide Nanopowders, Refract. Ind. Ceram. 57 (2017) 655–660. doi:10.1007/s11148-017-0040-0.

[118] Z. Zhao, V. Buscaglia, P. Bowen, M. Nygren, Spark Plasma Sintering of Nano-crystalline Ceramics, Key Eng. Mater. 264–268 (2004) 2297–2300. doi:10.4028/www.scientific.net/KEM.264-268.2297.

[119] S. Kwon, G.L. Messing, Sintering of Mixtures of Seeded Boehmite and Ultrafine -Alumina, J. Am. Ceram. Soc. 83 (2000) 82–88. doi:10.1111/j.1151-2916.2000.tb01152.x.

[120] C.S. Nordahl, G.L. Messing, Sintering of a-Al2O3 seeded nanocrystalline g-Al2O3 powders, J. Eur. Ceram. Soc. 22 (2002) 415–422.

[121] E. Tõldsepp, F. Schoenstein, M. Amamra, R. Saar, E. Feldbach, A. Kanaev, M. Kirm, Spark plasma sintering of ultra-porous γ-Al2O3, Ceram. Int. 42 (2016) 11709–11715. doi:10.1016/j.ceramint.2016.04.089.

[122] M. Prakasam, D. Michau, O. Viraphong, A. Largeteau, Optimal sintering parameters for Al_2O_3 optoceramics with high transparency by spark plasma sintering, Adv. Appl. Ceram. 115 (2016) 333–341. doi:10.1080/17436753.2016.1149909.

[123] K. Bodišová, D. Galusek, P. Švančárek, V. Pouchlý, K. Maca, Grain growth suppression in alumina via doping and two-step sintering, Ceram. Int. 41 (2015) 11975–11983. doi:10.1016/j.ceramint.2015.05.162.

[124] Z. Shen, Z. Zhe, M. Johansson, M. Nygren, Production of transparent ceramic articles with grain size in the nano-to-submicrometer range by sintering with pulsed direct current, SE0303403A, 2006. https://was.prv.se/spd/patent?p1=uwT5yjfL-Dt7eM42P9NdVA&p2=arWrqItMeOQ&hits=true&tab=1&content=SE0303403&lang=en&hitsstart=0&start=0.

[125] C. Wang, Z. Zhao, Transparent MgAl2O4 ceramic produced by spark plasma sintering, Scr. Mater. 61 (2009) 193–196. doi:10.1016/j.scriptamat.2009.03.039.

[126] A. Krell, T. Hutzler, J. Klimke, A. Potthoff, Fine-grained transparent spinel windows by the processing of different nanopowders, J. Am. Ceram. Soc. 93 (2010) 2656–2666. doi:10.1111/j.1551-2916.2010.03814.x.

[127] N. Frage, S. Cohen, S. Meir, S. Kalabukhov, M.P. Dariel, Spark plasma sintering (SPS) of transparent magnesium-aluminate spinel, J. Mater. Sci. 42 (2007) 3273–3275. doi:10.1007/s10853-007-1672-0.

[128] E.A. Olevsky, S. Kandukuri, L. Froyen, Consolidation enhancement in spark-plasma sintering: Impact of high heating rates, J. Appl. Phys. 102 (2007). doi:10.1063/1.2822189.

[129] K. Morita, B.N. Kim, H. Yoshida, K. Hiraga, Spark-plasma-sintering condition optimization for producing transparent MgAl2O4spinel polycrystal, J. Am. Ceram. Soc. 92 (2009) 1208–1216. doi:10.1111/j.1551-2916.2009.03074.x.

[130] J. Zhang, T. Lu, X. Chang, N. Wei, W. Xu, Related mechanism of transparency in

$MgAl_2O_4$ nano-ceramics prepared by sintering under high pressure and low temperature, J. Phys. D. Appl. Phys. 42 (2009) 052002. doi:10.1088/0022-3727/42/5/052002.

[131] M. Michálek, M. Michálková, G. Blugan, J. Kuebler, Effect of carbon contamination on the sintering of alumina ceramics, J. Eur. Ceram. Soc. 38 (2018) 193–199. doi:10.1016/j.jeurceramsoc.2017.08.011.

[132] K. Morita, B.-N. Kim, H. Yoshida, K. Hiraga, Y. Sakka, Distribution of carbon contamination in MgAl 2 O 4 spinel occurring during spark-plasma-sintering (SPS) processing: I – Effect of heating rate and post-annealing, J. Eur. Ceram. Soc. (2017) 0–1. doi:10.1016/j.jeurceramsoc.2017.09.038.

[133] K. Morita, B.-N. Kim, H. Yoshida, K. Hiraga, Y. Sakka, Spectroscopic study of the discoloration of transparent MgAl2O4 spinel fabricated by spark-plasma-sintering (SPS) processing, Acta Mater. 84 (2015) 9–19. doi:10.1016/j.actamat.2014.10.030.

[134] K. Morita, B. Kim, H. Yoshida, K. Hiraga, Y. Sakka, Assessment of carbon contamination in MgAl2O4 spinel during spark-plasma-sintering (SPS) processing, J. Ceram. Soc. Japan. 123 (2015) 983–988. doi:10.1016/j.scriptamat.2010.06.012.

[135] P. Wang, M. Yang, S. Zhang, R. Tu, T. Goto, L. Zhang, Suppression of carbon contamination in SPSed CaF2transparent ceramics by Mo foil, J. Eur. Ceram. Soc. 37 (2017) 4103–4107. doi:10.1016/j.jeurceramsoc.2017.04.070.

[136] J.P. Winterstein, M. Sezen, A. Rečnik, C. Barry Carter, Electron microscopy observations of the spinel-forming reaction using MgO nanocubes on Al2O3 substrates, J. Mater. Sci. 51 (2016) 144–157. doi:10.1007/s10853-015-9366-5.

[137] R. Marder, R. Chaim, G. Chevallier, C. Estournès, Effect of 1wt% LiF additive on the densification of nanocrystalline Y2O3 ceramics by spark plasma sintering, J. Eur. Ceram. Soc. 31 (2011) 1057–1066. doi:10.1016/j.jeurceramsoc.2010.12.032.

[138] A. Katz, E. Barraud, S. Lemonnier, E. Sorrel, M. Eichhorn, S. d'Astorg, A. Leriche, Role of LiF additive on spark plasma sintered transparent YAG ceramics, Ceram. Int. (2017) 1–9. doi:10.1016/j.ceramint.2017.08.119.

[139] M. Sokol, B. Ratzker, S. Kalabukhov, M. Peter Dariel, E. Galun, N. Frage, M. Sokol, B. Ratzker, S. Kalabukhov, M.P. Dariel, N. Frage, E. Galun, Transparent Polycrystalline Magnesium Aluminate Spinel Fabricated by Spark Plasma Sintering, Adv. Mater. 1706283 (2018) 1–11. doi:10.1002/adma.201706283.

[140] S. Meir, Fabrication of Transparent Magnesium Aluminate Spinel by the Spark Plasma Sintering Technique, Ben-Gurion University of the Negev, 2008.

http://aranne5.lib.ad.bgu.ac.il/others/MeirShay.pdf.

[141] N. Frage, S. Kalabukhov, N. Sverdlov, V. Ezersky, M.P. Dariel, Densification of transparent yttrium aluminum garnet (YAG) by SPS processing, J. Eur. Ceram. Soc. 30 (2010) 3331–3337. doi:10.1016/j.jeurceramsoc.2010.08.006.

[142] S. Meir, S. Kalabukhov, N. Froumin, M.P. Dariel, N. Frage, Synthesis and densification of transparent magnesium aluminate spinel by SPS processing, J. Am. Ceram. Soc. 92 (2009) 358–364. doi:10.1111/j.1551-2916.2008.02893.x.

[143] S. Grasso, B.-N. Kim, C. Hu, G. Maizza, Y. Sakka, Highly Transparent Pure Alumina Fabricated by High-Pressure Spark Plasma Sintering, J. Am. Ceram. Soc. 93 (2010) 2460–2462. doi:10.1111/j.1551-2916.2010.03811.x.

[144] C. Manière, L. Durand, E. Brisson, H. Desplats, P. Carré, P. Rogeon, C. Estournès, Contact resistances in spark plasma sintering: From in-situ and ex-situ determinations to an extended model for the scale up of the process, J. Eur. Ceram. Soc. 37 (2017) 1593–1605. doi:10.1016/j.jeurceramsoc.2016.12.010.

[145] D. Galusek, J. Sedláček, J. Chovanec, M. Michálková, The influence of MgO, Y2O3 and ZrO2 additions on densification and grain growth of submicrometre alumina sintered by SPS and HIP, Ceram. Int. 41 (2015) 9692–9700. doi:10.1016/j.ceramint.2015.04.038.

[146] B.-N. Kim, K. Hiraga, K. Morita, H. Yoshida, T. Miyazaki, Y. Kagawa, Microstructure and optical properties of transparent alumina, Acta Mater. 57 (2009) 1319–1326. doi:10.1016/j.actamat.2008.11.010.

[147] J. Diatta, G. Antou, F. Courreges, M. Georges, N. Pradeilles, A. Ma??tre, Effect of the current pulse pattern during heating in a spark plasma sintering device: Experimental and numerical modeling approaches, J. Mater. Process. Technol. 246 (2017) 93–101. doi:10.1016/j.jmatprotec.2017.03.004.

[148] M. Trunec, K. Maca, R. Chmelik, Polycrystalline alumina ceramics doped with nanoparticles for increased transparency, J. Eur. Ceram. Soc. 35 (2015) 1001–1009. doi:10.1016/j.jeurceramsoc.2014.09.041.

[149] N. Nishiyama, T. Taniguchi, H. Ohfuji, K. Yoshida, F. Wakai, B.-N. Kim, H. Yoshida, Y. Higo, A. Holzheid, O. Beermann, T. Irifune, Y. Sakka, K. Funakoshi, Transparent nanocrystalline bulk alumina obtained at 7.7GPa and 800°C, Scr. Mater. 69 (2013) 362–365. doi:10.1016/j.scriptamat.2013.05.017.

[150] J.G. Santanach, A. Weibel, C. Estournès, Q. Yang, C. Laurent, A. Peigney, Spark plasma sintering of alumina: Study of parameters, formal sintering analysis and

hypotheses on the mechanism(s) involved in densification and grain growth, Acta Mater. 59 (2011) 1400–1408. doi:10.1016/j.actamat.2010.11.002.

[151] J. Echeberria, J. Tarazona, J.. Y. He, T. Butler, F. Castro, Sinter-HIP of alumina powders with sub micron grain sizes, J. Eur. Ceram. Soc. 22 (2002) 1801–1809. doi:10.1016/S0955-2219(01)00510-6.

[152] X. Zhang, S. Liang, H. Li, J. Yang, Mechanical and optical properties of transparent alumina obtained by rapid vacuum sintering, Ceram. Int. 43 (2017) 420–426. doi:10.1016/j.ceramint.2016.09.175.

[153] S. Grasso, C. Hu, G. Maizza, B.N. Kim, Y. Sakka, Effects of pressure application method on transparency of spark plasma sintered alumina, J. Am. Ceram. Soc. 94 (2011) 1405–1409. doi:10.1111/j.1551-2916.2010.04274.x.

[154] V. Pouchly, J. Hruby, K. Maca, A practical approach for the calculation of the activation energy of the sintering, Sci. Sinter. 48 (2016) 317–324. doi:10.2298/SOS1603317P.

[155] M. Trunec, J. Klimke, Z.J. Shen, Transparent alumina ceramics densified by a combinational approach of spark plasma sintering and hot isostatic pressing, J. Eur. Ceram. Soc. 36 (2016) 4333–4337. doi:10.1016/j.jeurceramsoc.2016.06.004.

[156] S. Grasso, H. Yoshida, H. Porwal, Y. Sakka, M. Reece, Highly transparent α-alumina obtained by low cost high pressure SPS, Ceram. Int. 39 (2013) 3243–3248. doi:10.1016/j.ceramint.2012.10.012.

[157] C. Gajdowski, J. Böhmler, Y. Lorgouilloux, S. Lemonnier, S. d'Astorg, E. Barraud, A. Leriche, Influence of post-HIP temperature on microstructural and optical properties of pure MgAl2O4spinel: From opaque to transparent ceramics, J. Eur. Ceram. Soc. 37 (2017) 5347–5351. doi:10.1016/j.jeurceramsoc.2017.07.031.

[158] A. Krell, P. Blank, H. Ma, T. Hutzler, M.P.B. Van Bruggen, R. Apetz, Transparent Sintered Corundum with High Hardness and Strength, J. Am. Ceram. Soc. 86 (2003) 12–18.

[159] K. TSUKUMA, Transparent MgAl2O4 Spinel Ceramics Produced by HIP Post-Sintering, J. Ceram. Soc. Japan. 114 (2006) 802–806. doi:10.2109/jcersj.114.802.

[160] Y. Tamura, E. Zapata-Solvas, B.M. Moshtaghioun, D. Gómez-García, A. Domínguez-Rodríguez, Grain-boundary diffusion coefficient in α-Al2O3from spark plasma sintering tests: Evidence of collective motion of charge disconnections, Ceram. Int. (2018). doi:10.1016/j.ceramint.2018.07.073.

[161] B. Kim, K. Hiraga, A. Jeong, C. Hu, T.S. Suzuki, J. Yun, Y. Sakka, Transparent

ZnAl2O4 ceramics fabricated by spark plasma sintering, J. Ceram. Soc. Japan. 122 (2014) 784–787. doi:0.2109/jcersj2.122.784.

[162] J.G.J. Peelen, R. Metselaar, Light scattering by pores in polycrystalline materials: Transmission properties of alumina, J. Appl. Phys. 45 (1974) 216–220. doi:10.1063/1.1662961.

[163] A.A. Kachaev, D. V Grashchenkov, Y.E. Lebedeva, S. St. Solntsev, O.L. Khasanov, Optically Transparent Ceramic (Review), Glas. Ceram. 73 (2016) 117–123. doi:10.1007/s10717-016-9838-3.

[164] S.F. Wang, J. Zhang, D.W. Luo, F. Gu, D.Y. Tang, Z.L. Dong, G.E.B. Tan, W.X. Que, T.S. Zhang, S. Li, L.B. Kong, Transparent ceramics: Processing, materials and applications, Prog. Solid State Chem. 41 (2013) 20–54. doi:10.1016/j.progsolidstchem.2012.12.002.

[165] Transparent Ceramics: Enabling Large, Durable, Multifunctional Optics, (n.d.). https://www.photonics.com/Article.aspx?AID=57166 (accessed October 10, 2018).

[166] M. Izerrouken, Y. Djouadi, H. Zirour, Annealing process of F- and F+-centers in Al2O 3 single crystal induced by fast neutrons irradiation, Nucl. Instruments Methods Phys. Res. Sect. B Beam Interact. with Mater. Atoms. 319 (2014) 29–33. doi:10.1016/j.nimb.2013.11.009.

[167] L.S. Welch, A.E. Hughes, G.P. Pells, Polarised luminescence in neutron- and proton-irradiated α-Al 2O3, J. Phys. C Solid State Phys. 13 (1980) 1805–1816. doi:10.1088/0022-3719/13/9/025.

[168] J. Valbis, N. Itoh, Electronic excitations, luminescence and lattice defect formation in α-Al2O3 crystals, Radiat. Eff. Defects Solids. 116 (1991) 171–189. doi:10.1080/10420159108221357.

[169] P. Jonnard, C. Bonnelle, G. Blaise, G. Rémond, C. Roques-Carmes, F+ and F centers in α-Al2O3 by electron-induced x-ray emission spectroscopy and cathodoluminescence, J. Appl. Phys. 88 (2000) 6413–6417. doi:10.1063/1.1324697.

[170] A. Boumaza, A. Djelloul, F. Guerrab, Specific signatures of α-alumina powders prepared by calcination of boehmite or gibbsite, Powder Technol. 201 (2010) 177–180. doi:10.1016/j.powtec.2010.03.036.

[171] A. Lushchik, M. Kirm, A. Kotlov, P. Liblik, C. Lushchik, A. Maaroos, V. Nagirnyi, T. Savikhina, G. Zimmerer, Intrinsic and impurity luminescence and multiplication of excitations in complex oxides, J. Lumin. 102–103 (2003) 38–43. doi:10.1016/S0022-2313(02)00540-9.

[172] V.T. Gritsyna, Y.G. Kazarinov, V.A. Kobyakov, I.E. Reimanis, Radiation-induced luminescence in magnesium aluminate spinel crystals and ceramics, Nucl. Instruments Methods Phys. Res. Sect. B Beam Interact. with Mater. Atoms. 250 (2006) 342–348. doi:10.1016/j.nimb.2006.04.135.

[173] L. Museur, M. Bouslama, M. Amamra, A. Kanaev, Electronic transitions in α, θ and γ polymorphs of ultraporous monolithic alumina, Phys. Status Solidi - Rapid Res. Lett. 7 (2013) 1026–1029. doi:10.1002/pssr.201308040.

[174] C.-K. Lee, E. Cho, H.-S. Lee, K. Seol, S. Han, Comparative study of electronic structures and dielectric properties of alumina polymorphs by first-principles methods, Phys. Rev. B. 76 (2007) 245110. doi:10.1103/PhysRevB.76.245110.

[175] V.Y. Chekhovskoi, V.A. Petrov, Melting point of corundum, Meas. Tech. 6 (1963) 751–753. doi:10.1007/BF01419351.

[176] NIST Al2O3 thermochemical data, (n.d.). https://webbook.nist.gov/cgi/cbook.cgi?Formula=Al2O3&NoIon=on&Units=SI&cTC=on#Thermo-Condensed.

[177] NIST spinel thermochemical data, (n.d.). https://webbook.nist.gov/cgi/cbook.cgi?Formula=MgAl2O4&NoIon=on&Units=SI&cTC=on.

[178] Al2O3 properties - Accuratus, (n.d.). https://accuratus.com/alumox.html (accessed November 10, 2018).

[179] M. Suárez, A. Fernández, Sintering to Transparency of Polycrystalline Ceramic Materials, Sinter. Ceram. - New Emerg. Tech. (2012) 610.

[180] Refractive index of Al2O3, (n.d.). https://refractiveindex.info/?shelf=main&book=Al2O3&page=Malitson-o (accessed November 10, 2018).

[181] H.M. Rietveld, A profile refinement method for nuclear and magnetic structures, J. Appl. Crystallogr. 2 (1969) 65–71. doi:10.1107/S0021889869006558.

[182] L. Lutterotti, D. Chateigner, S. Ferrari, J. Ricote, Texture, residual stress and structural analysis of thin films using a combined X-ray analysis, Thin Solid Films. 450 (2004) 34–41. doi:10.1016/j.tsf.2003.10.150.

[183] XRD full profile search match, (n.d.). http://nanoair.dii.unitn.it:8080/sfpm/.

[184] S. Graulis, D. Chateigner, R.T. Downs, A.F.T. Yokochi, M. Quirós, L. Lutterotti, E. Manakova, J. Butkus, P. Moeck, A. Le Bail, Crystallography Open Database - An open-access collection of crystal structures, J. Appl. Crystallogr. 42 (2009) 726–729.

doi:10.1107/S0021889809016690.

[185] INEL EQUINOX 1000, (n.d.). https://www.inel.us/index.php/xrd-products/equinox-family/equinox-1000 (accessed October 15, 2018).

[186] M. Morales, D. Chateigner, L. Lutterotti, J. Ricote, X-Ray Combined QTA Using a CPS Applied to a Ferroelectric Ultrastructure, Mater. Sci. Forum. 408–412 (2002) 113–118. doi:10.4028/www.scientific.net/MSF.408-412.113.

[187] D. Chateigner, Combined Analysis, ISTE Ltd, John Wiley & Sons Inc, 2010.

[188] L. Lutterotti, Total pattern fitting for the combined size-strain-stress-texture determination in thin film diffraction, Nucl. Instruments Methods Phys. Res. Sect. B Beam Interact. with Mater. Atoms. 268 (2010) 334–340. doi:10.1016/j.nimb.2009.09.053.

[189] N.C. Popa, The (hkl) Dependence of Diffraction-Line Broadening Caused by Strain and Size for all Laue Groups in Rietveld Refinement, J. Appl. Crystallogr. 31 (1998) 176–180. doi:10.1107/S0021889897009795.

[190] Zeiss Supra brochure, (n.d.). http://www.fis.unipr.it/dokuwiki/lib/exe/fetch.php?media=lmn:brochure.pdf (accessed November 10, 2018).

[191] J. Ruste, Microscopie électronique à balayage: Images, applications et développements, Tech. l'ingénieur. 33 (2013) 24.

[192] S. Canovic, T. Jonsson, M. Halvarsson, Grain contrast imaging in FIB and SEM, J. Phys. Conf. Ser. 126 (2008) 1–4. doi:10.1088/1742-6596/126/1/012054.

[193] T. Baudin, Analyse EBSD - Principe et cartographies d ' orientations, Tech. L'Ingénieur. 33 (2010).

[194] Pycnometer, (n.d.). http://www.micromeritics.com/Product-Showcase/AccuPyc-II-1340.aspx (accessed November 10, 2018).

[195] E. Feldbach, E. Tõldsepp, M. Kirm, A. Lushchik, K. Mizohata, J. Räisänen, Radiation resistance diagnostics of wide-gap optical materials, Opt. Mater. (Amst). 55 (2016) 164–167. doi:10.1016/j.optmat.2016.03.008.

[196] H. Bialas, H.J. Stolz, Lattice dynamics of sapphire (Corundum), Z. Phys. B. 21 (1975) 319–324.

[197] H. V. Hart, H.G. Drickamer, Effect of high pressure on the lattice parameters of Al2O3, J. Chem. Phys. 43 (1965) 2265–2266. doi:10.1063/1.1697121.

[198] O. Khatim, T.H.N. Nguyen, M. Amamra, L. Museur, A. Khodan, A. Kanaev, Synthesis and photoluminescence properties of nanostructured mullite/alpha-Al2O3, Acta Mater.

71 (2014) 108–116. doi:10.1016/j.actamat.2014.03.006 1359-6454/?

[199] A. Krell, P. Blank, The Influence of Shaping Method on the Grain Size Dependence of Strength in Dense Submicrometre Alumina, J. Eur. Ceram. Soc. 16 (1996) 1189–1200. doi:10.1016/0955-2219(96)00044-1.

[200] D. Wang, L. Shen, S. Ran, Q. Huang, Transparent alumina fabricated by SPS sintering with AlF3doping, Scr. Mater. 92 (2014) 31–34. doi:10.1016/j.scriptamat.2014.08.007.

[201] M. Suárez, A. Fernández, J.L. Menéndez, R. Torrecillas, H.U. Kessel, J. Hennicke, R. Kirchner, T. Kessel, Challenges and Opportunities for Spark Plasma Sintering : A Key Technology for a New Generation of Materials, Sinter. Appl. (2013) 319–342. doi:10.5772/53706.

[202] C. Collard, Z. Trzaska, L. Durand, J.-M. Chaix, J.-P. Monchoux, Theoretical and experimental investigations of local overheating at particle contacts in spark plasma sintering, Powder Technol. 321 (2017) 458–470. doi:10.1016/j.powtec.2017.08.033.

[203] E. Guilmeau, C. Henrist, T.S. Suzuki, Y. Sakka, D. Chateigner, D. Grossin, B. Ouladdiaf, Texture of Alumina by Neutron Diffraction and SEM-EBSD, Mater. Sci. Forum. 495–497 (2005) 1395–1400. doi:10.4028/www.scientific.net/MSF.495-497.1395.

[204] R. Apetz, M.P.B. Van Bruggen, Transparent Alumina: A light - Scattering Model, J. Am. Ceram. Soc. 86 (2003) 480–486. doi:10.1016/j.infsof.2008.09.005.

[205] M. Izerrouken, T. Benyahia, Absorption and photoluminescence study of Al2O3 single crystal irradiated with fast neutrons, Nucl. Instruments Methods Phys. Res. Sect. B Beam Interact. with Mater. Atoms. 268 (2010) 2987–2990. doi:10.1016/j.nimb.2010.05.024.

[206] A. Stashans, E. Kotomin, J.L. Calais, Calculations of the ground and excited states of F-type centers in corundum crystals, Phys. Rev. B. 49 (1994) 14854–14858. doi:10.1103/PhysRevB.49.14854.

[207] M.E. Innocenzi, R.T. Swimm, M. Bass, R.H. French, A.B. Villaverde, M.R. Kokta, Room-temperature optical absorption in undoped α-Al2O3, J. Appl. Phys. 67 (1990) 7542–7546. doi:10.1063/1.345817.

[208] A. Boumaza, A. Djelloul, Estimation of the intrinsic stresses in ??-alumina in relation with its elaboration mode, J. Solid State Chem. 183 (2010) 1063–1070. doi:10.1016/j.jssc.2010.03.012.

[209] V.N. Makhov, A. Lushchik, C.B. Lushchik, M. Kirm, E. Vasil'chenko, S. Vielhauer, V. V. Harutunyan, E. Aleksanyan, Luminescence and radiation defects in electron-

irradiated Al2O3and Al2O3:Cr, Nucl. Instruments Methods Phys. Res. Sect. B Beam Interact. with Mater. Atoms. 266 (2008) 2949–2952. doi:10.1016/j.nimb.2008.03.145.

[210] J.A. Ball, M. Pirzada, R.W. Grimes, M.O. Zacate, D.W. Price, B.P. Uberuaga, Predicting lattice parameter as a function of cation disorder in $MgAl_2O_4$ spinel, J. Phys. Condens. Matter. 17 (2005) 7621–7631. doi:10.1088/0953-8984/17/48/014.

[211] G.P. Summers, G.S. White, K.H. Lee, J.H. Crawford Jr, Radiation damage in MgAl204, Phys. Rev. B. 21 (1980) 2578–2584.

[212] Y. Williams, G.P., Rosenblatt, G.H., Ferry, M.J., Williams, R.T., Chen, Time resolved luminescence and absorption spectroscopy of defects in MgO and Al2O3, J. Lu. 40–41 (1988) 339–340.

[213] Y. Cain, L. S., Pogatshnik, G. J., Chen, Optical transitions in neutron-irradiated MgAl2O4 spinel crystals, Phys. Rev. B. 37 (1988) 2645–2652.

[214] V.E. Alexandrov, E.A. Kotomin, J. Maier, R.A. Evarestov, First-principles study of bulk and surface oxygen vacancies in SrTiO 3 crystal, Eur. Phys. J. B. 72 (2009) 53–57. doi:10.1140/epjb/e2009-00339-4.

[215] M. Kirm, A. Lushchik, C. Lushchik, S. Vielhauer, G. Zimmerer, Luminescence of pure and doped Al2O3 and MgO single crystals under inner-shell excitation, J. Lumin. 102–103 (2003) 307–312. doi:10.1016/S0022-2313(02)00521-5.

[216] M. Kirm, E. Feldbach, A. Kotlov, P. Liblik, A. Lushchik, M. Oja, E. Palcevskis, VUV spectroscopy and electronic excitations in nano-size alumina, Radiat. Meas. 45 (2010) 618–620. doi:10.1016/j.radmeas.2009.12.006.

[217] C. Jardin, B. Canut, S.M.M. Ramos, The luminescence of sapphire subjected to the irradiation of energetic hydrogen and helium ions, J. Phys. D. Appl. Phys. 29 (1996) 2066–2070. doi:10.1088/0022-3727/29/8/002.

[218] NIST MgO thermochemical data, (n.d.).

[219] H. Xu-Guo, C. Zi-Shang, L. Xiao-Ping, B. Sheng, Effect of sintering additives size on the microstructure and wear properties of Al_2O_3 ceramics, Ferroelectrics. 521 (2017) 101–107. doi:10.1080/00150193.2017.1390973.

[220] H. Zhang, Y. Xu, B. Wang, X. Zhang, J. Yang, K. Niihara, Effects of heating rate on the microstructure and mechanical properties of rapid vacuum sintered translucent alumina, Ceram. Int. 41 (2015) 12499–12503. doi:10.1016/j.ceramint.2015.05.136.

[221] A. Krell, K. Waetzig, J. Klimke, Effects and elimination of nanoporosity in transparent sintered spinel, Proc. SPIE. 8016 (2011) 1–10. doi:10.1117/12.883958.

[222] A.F. Dericioglu, Y. Kagawa, Effect of grain boundary microcracking on the light

transmittance of sintered transparent MgAl 2 O 4, J. Eur. Ceram. Soc. 23 (2003) 951–959.

[223] L. Esposito, A. Piancastelli, S. Martelli, Production and characterization of transparent MgAl2O4prepared by hot pressing, J. Eur. Ceram. Soc. 33 (2013) 737–747. doi:10.1016/j.jeurceramsoc.2012.10.013.

[224] C. Feldmann, Polyol mediated synthesis of oxide particle suspensions and their application, Scr. Mater. 44 (2001) 2193–2196. doi:10.1016/S1359-6462(01)00902-2.

[225] C. Feldmann, H.O. Jungk, Polyol-mediated preparation of nanoscale oxide particles, Angew. Chemie - Int. Ed. 40 (2001) 359–362. doi:10.1002/1521-3773(20010119)40:2<359::AID-ANIE359>3.0.CO;2-B.

9 Annexes

9.1 Article published in Ceramics International

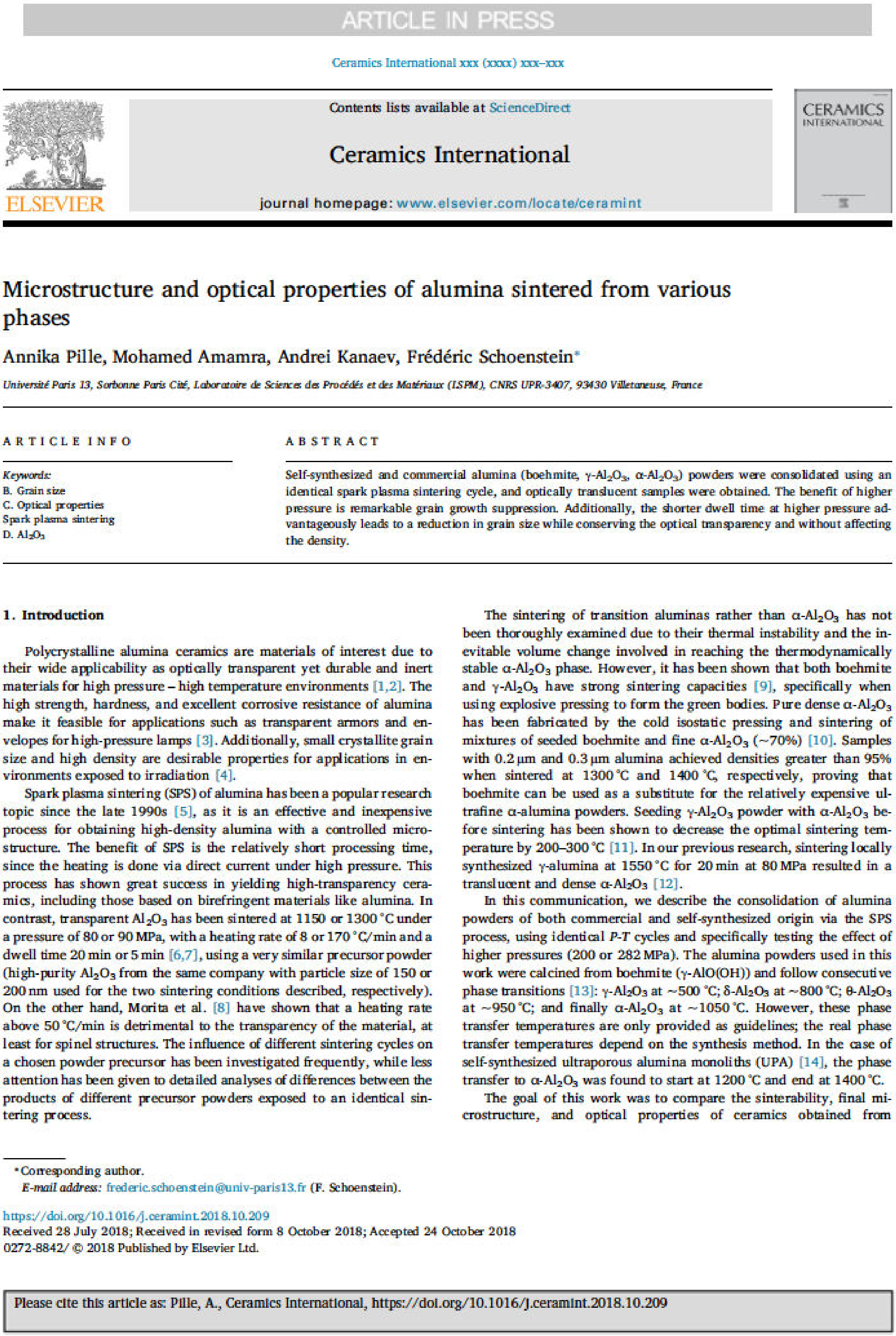

ARTICLE IN PRESS

Ceramics International xxx (xxxx) xxx–xxx

Contents lists available at ScienceDirect

Ceramics International

journal homepage: www.elsevier.com/locate/ceramint

Microstructure and optical properties of alumina sintered from various phases

Annika Pille, Mohamed Amamra, Andrei Kanaev, Frédéric Schoenstein*

Université Paris 13, Sorbonne Paris Cité, Laboratoire de Sciences des Procédés et des Matériaux (LSPM), CNRS UPR-3407, 93430 Villetaneuse, France

ARTICLE INFO

Keywords:
B. Grain size
C. Optical properties
Spark plasma sintering
D. Al_2O_3

ABSTRACT

Self-synthesized and commercial alumina (boehmite, γ-Al_2O_3, α-Al_2O_3) powders were consolidated using an identical spark plasma sintering cycle, and optically translucent samples were obtained. The benefit of higher pressure is remarkable grain growth suppression. Additionally, the shorter dwell time at higher pressure advantageously leads to a reduction in grain size while conserving the optical transparency and without affecting the density.

1. Introduction

Polycrystalline alumina ceramics are materials of interest due to their wide applicability as optically transparent yet durable and inert materials for high pressure – high temperature environments [1,2]. The high strength, hardness, and excellent corrosive resistance of alumina make it feasible for applications such as transparent armors and envelopes for high-pressure lamps [3]. Additionally, small crystallite grain size and high density are desirable properties for applications in environments exposed to irradiation [4].

Spark plasma sintering (SPS) of alumina has been a popular research topic since the late 1990s [5], as it is an effective and inexpensive process for obtaining high-density alumina with a controlled microstructure. The benefit of SPS is the relatively short processing time, since the heating is done via direct current under high pressure. This process has shown great success in yielding high-transparency ceramics, including those based on birefringent materials like alumina. In contrast, transparent Al_2O_3 has been sintered at 1150 or 1300 °C under a pressure of 80 or 90 MPa, with a heating rate of 8 or 170 °C/min and a dwell time 20 min or 5 min [6,7], using a very similar precursor powder (high-purity Al_2O_3 from the same company with particle size of 150 or 200 nm used for the two sintering conditions described, respectively). On the other hand, Morita et al. [8] have shown that a heating rate above 50 °C/min is detrimental to the transparency of the material, at least for spinel structures. The influence of different sintering cycles on a chosen powder precursor has been investigated frequently, while less attention has been given to detailed analyses of differences between the products of different precursor powders exposed to an identical sintering process.

The sintering of transition aluminas rather than α-Al_2O_3 has not been thoroughly examined due to their thermal instability and the inevitable volume change involved in reaching the thermodynamically stable α-Al_2O_3 phase. However, it has been shown that both boehmite and γ-Al_2O_3 have strong sintering capacities [9], specifically when using explosive pressing to form the green bodies. Pure dense α-Al_2O_3 has been fabricated by the cold isostatic pressing and sintering of mixtures of seeded boehmite and fine α-Al_2O_3 (~70%) [10]. Samples with 0.2 µm and 0.3 µm alumina achieved densities greater than 95% when sintered at 1300 °C and 1400 °C, respectively, proving that boehmite can be used as a substitute for the relatively expensive ultrafine α-alumina powders. Seeding γ-Al_2O_3 powder with α-Al_2O_3 before sintering has been shown to decrease the optimal sintering temperature by 200–300 °C [11]. In our previous research, sintering locally synthesized γ-alumina at 1550 °C for 20 min at 80 MPa resulted in a translucent and dense α-Al_2O_3 [12].

In this communication, we describe the consolidation of alumina powders of both commercial and self-synthesized origin via the SPS process, using identical *P-T* cycles and specifically testing the effect of higher pressures (200 or 282 MPa). The alumina powders used in this work were calcined from boehmite (γ-AlO(OH)) and follow consecutive phase transitions [13]: γ-Al_2O_3 at ~500 °C; δ-Al_2O_3 at ~800 °C; θ-Al_2O_3 at ~950 °C; and finally α-Al_2O_3 at ~1050 °C. However, these phase transfer temperatures are only provided as guidelines; the real phase transfer temperatures depend on the synthesis method. In the case of self-synthesized ultraporous alumina monoliths (UPA) [14], the phase transfer to α-Al_2O_3 was found to start at 1200 °C and end at 1400 °C.

The goal of this work was to compare the sinterability, final microstructure, and optical properties of ceramics obtained from

---

* Corresponding author.
E-mail address: frederic.schoenstein@univ-paris13.fr (F. Schoenstein).

https://doi.org/10.1016/j.ceramint.2018.10.209
Received 28 July 2018; Received in revised form 8 October 2018; Accepted 24 October 2018

Please cite this article as: Pille, A., Ceramics International, https://doi.org/10.1016/j.ceramint.2018.10.209

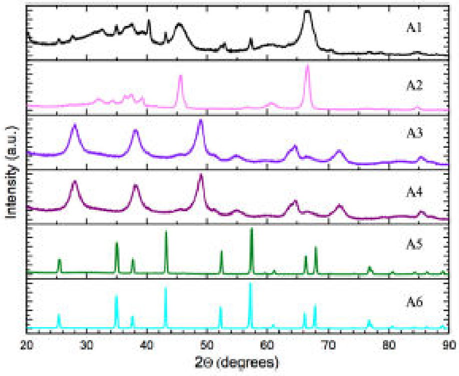

Fig. 1. XRD of powders used for sintering.

commercial boehmite, γ-Al_2O_3, and δ:γ-Al_2O_3 powders with those obtained them to locally synthesized ultrapure α-Al_2O_3 from UPA.

2. Material and methods

2.1. Powders

Fig. 1 shows XRD patterns of the different powders used for sintering: A1, 70% δ-Al_2O_3/30% γ-Al_2O_3 (δ:γ-Al_2O_3), crystallite size 40–50 nm (Alfa Aesar); A2, γ-Al_2O_3, TEM crystallite size 50 nm (Sigma Aldrich); A3, boehmite (Sasol GmbH) exposed to 30-min ultrasonic (US) deagglomeration in acetone at 40% amplitude; A4, boehmite (Sasol GmbH); A5, boehmite (Sasol GmbH) calcined to α-Al_2O_3 via 4-h heat treatment at 1400 °C. Powders A6-A9 were ultra-porous alumina (UPA) elaborated via an original patented process [14,15] at our laboratory (LSPM-CNRS) and calcined to α-Al_2O_3 via a 4-h treatment at 1400 °C. UPA powders were elaborated at room temperature under a humid atmosphere via oxidation of aluminum plates through a liquid mercury-silver layer. This process produces amorphous monoliths with high porosity (> 99%). The microstructure consists of tangled hydrated alumina fibers with diameter of approximately 5 nm. The crystallization of UPA begins at 870 °C after being dehydrated, and transfer to the γ-alumina phase is completed around 1000 °C. To obtain pure α-alumina, further heat treatment at 1400 °C is necessary [14], which results in a microstructure with grain size of 200–300 nm.

No visible differences were seen between the XRD patterns of the two α-Al_2O_3 powders, nor the boehmite powders with and without ultrasonic treatment.

2.2. Sintering setup and cycles

Due to the combined effect of temperature and pressure, spark plasma sintering (SPS) was chosen for this work as it is a particularly fitting technique for obtaining materials with controlled density and grain size. Imine et al. [16] and Jean et al. [17] reported nano- and microstructured oxide ceramics obtained by SPS which had interesting and tunable properties due to their controlled structures, similarly to a report by Teber et al. [18] regarding cermet. In addition, Dakhlaoui-Omrani et al. [19] and Ouar et al. also successfully used SPS to sinter metals (Ni- and Co-based) which presented organized [20] and controlled-sized [21] grains.

The powders described in Section 2.1 were consolidated without any additional pretreatment or sintering additives, using SPS (Dr. Sinter LAB Series SPS-515S, Japan) under a vacuum of 20 Pa. A standard pulse pattern of 12:2 (on:off) with a pulse duration of 3.4 ms was used. About 2 g of alumina powder (1.2 g when 280 MPa pressure was employed) was poured into a graphite paper-insulated graphite die (or a carbon-carbon composite quality CX31V Toyo Tanso die in the case of 200 or 280 MPa pressures) with an inner diameter of 15 mm. The die was then covered by carbon felt to suppress heat escape from the surface, leaving a small area uncovered to measure the temperature via an optical pyrometer (CHINO IR-AH). Samples were held under vacuum at 600 °C for 10 min to remove adsorbed water before starting the sintering process at higher temperatures.

Powders A1–A6 were sintered using a previously established [12] long sintering scheme: 10 min dwell at 600 °C to remove excess water, heating from 600 °C to 1100 °C over 5 min, further heating to 1450 °C over 35 min, holding for 20 min, cooling to 1150 °C, and holding for an additional 10 min to diminish internal stresses. In this process, 80 MPa pressure was applied at the end of the 600 °C dwell and held until the end of the 1450 °C dwell. For A7, the pressure was raised to 200 MPa instead of 80 MPa, but the rest of the parameters were kept identical. A8 was sintered via a shorter, high-pressure (282 MPa) cycle, still beginning with the 10 min dwell at 600 °C, heating directly at 100 °C/min to 1450 °C and holding for 3 min, and then cooling. The pressure was applied over 5 min, reaching 282 MPa by the 1450 °C dwell, and was then released after the dwell over 5 min.

2.3. Sample preparation and characterization

After sintering, the pellets were ground to remove graphite paper and polished using diamond liquids and pastes down to 0.25 µm. Translucent samples were ground to thicknesses of 0.8–1.1 mm and mirror-polished.

The mass density of the pellets was measured by a helium pycnometer (Micromeritics AccuPyc II 1340), and the relative density was calculated assuming the full density of Al_2O_3 to be 3.987 g/cm^3 [22]. The cell parameters of the sintered pellets were determined from X-ray diffraction (XRD; Cu Kα, INEL EQUINOX 1000) patterns using Maud software [23]. The apparent grain sizes of the resultant ceramics were measured from backscattered electron images from a scanning electron microscope (SEM; ZEISS Gemini SUPRA 40VP FEG-SEM) operated at 20 Pa with accelerating voltage of 10–20 kV. To obtain average grain sizes, the measured values were multiplied by 1.56 [24] (except for A6, due to the elongated shape of the grains). The crystalline orientations of sample A2 were mapped via electron backscattered diffraction (EBSD) carried out on the same SEM. The EBSD mapping was generated and average grain size was estimated using the imaging software OIM (version 4, TexSem Laboratories).

The transmittance of the samples was measured using a SAFAS UVmc1 spectrophotometer (SAFAS, Monaco) by placing a 5 mm pinhole before the sample and positioning the sample about 1 cm from the detector.

3. Results and discussion

All sintered ceramics, independent of the crystalline phase of the starting powder, were in α-Al_2O_3 phase, as expected from the high sintering temperature. The morphology, density, and grain size of the resultant ceramics are discussed in Section 3.1, and the optical properties are discussed in Section 3.2.

3.1. Morphology, density and grain size

Fig. 2 summarizes the microstructures of the ceramics sintered from the various starting phases, and Fig. 3 shows the results of sintering α-Al_2O_3 with the same long cycle at 1450 °C (A5–A6), as well as samples sintered at higher pressures (A7–A8). The densities of the sintered ceramics as well as their lattice parameters are presented in Table 1.

For sample A1, the ceramic resulting from the long SPS cycle at 1450 °C had relatively low density (95.8%) and rather small grain size (3.3 µm). A2 had a higher density and was translucent (see Section 3.2),

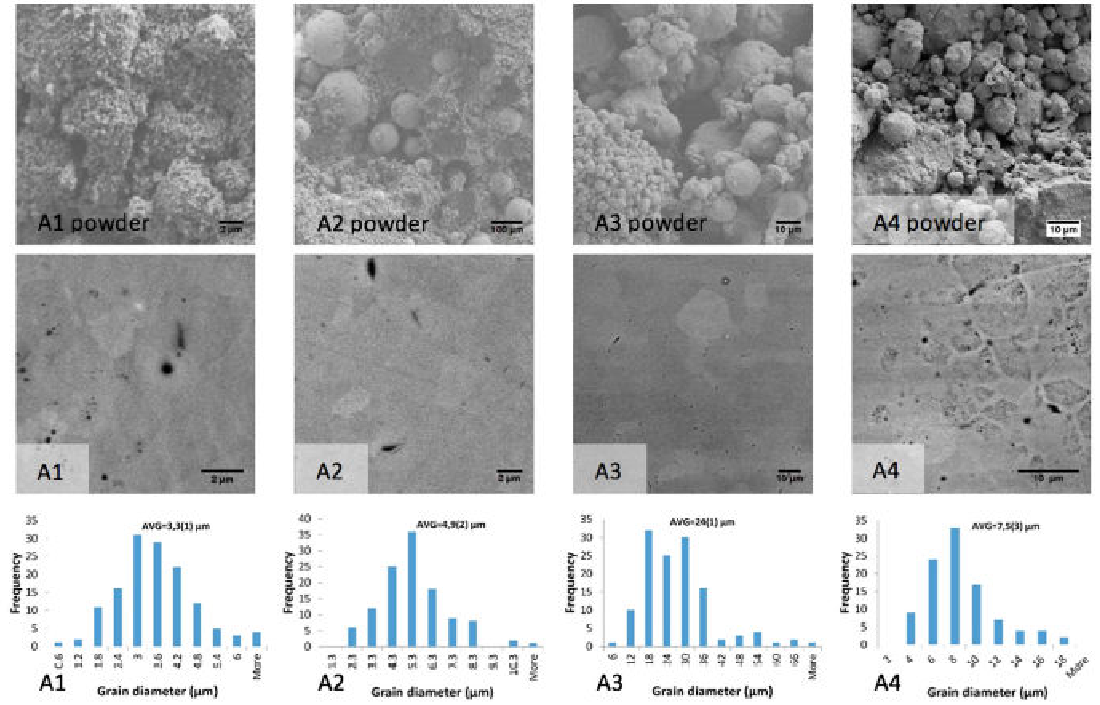

Fig. 2. SEM micrographs of A1–A4 powders and sintered pellets with the grain size distribution of the latter.

even though the only difference between the starting powders was the 70% δ-Al_2O_3 content in A1 compared to the pure γ-Al_2O_3 phase of the A2 powder. The average grain size of A2 was 4.9 µm, which is much larger than the 2 µm average grain size obtained via sintering 10 nm γ-Al_2O_3 (UPA), as reported in our previous work [12]. The full density of the previously reported sample was also in the same range as the density observed here for A2. The previously obtained ceramic from 10 nm γ-Al_2O_3 via the same sintering cycle was not optically transparent, whereas A2 was translucent (see Section 3.2). Boehmite powders for samples A3 and A4 are distinguished only by the 30-min US treatment in acetone. Although this treatment did not result in any obvious morphological differences in the SEM images, A3 had an average grain size 3 times bigger (24 µm) than that of A4, as well as a slightly higher final density, indicating that US treatment is a useful tool for increasing the sinterability of powders. Compared to the 30% boehmite which was cold isostatically pressed and sintered by Kwon and Messing [10], the grain size of our samples was much larger (~7 µm vs < 1 µm), while the density remained the same at around 95%.

A5–A8 were all sintered from α-Al_2O_3 powders; A5 from calcined boehmite and the rest from calcined UPA. A5 was chosen as a comparison, since the α-Al_2O_3 crystallites from UPA have an elongated rectangular shape (crystallite length 250–300 nm, see [25]) remaining from the initial nanofibrous monolith. In addition to the specific morphology, compared to the commonly used TM-DAR powder [6,26], the crystallite size of our precursor powder was slightly bigger (0.15–0.2 µm vs 0.2–0.3 µm), leading undoubtedly to the larger final condensed grain size in the ceramics. Unfortunately, the density of the α-Al_2O_3 received as boehmite was only 94.1% after sintering, which is most likely due to large agglomerates in boehmite before calcination which result in hard sintered particles during calcination and thus demands more extreme sintering conditions for final densification via SPS. A6, on the other hand, had high density (98.4%) and transparency (see Section 3.2), which was interestingly accompanied by a morphology consisting of long crystallite grains (average length 16 µm). In an attempt to suppress the lengthening of the crystallites, A7 and A8 were sintered under higher pressures, which is known to aid in suppressing grain growth [27].

In the case of A7, the temperature cycle was identical and only the applied pressure was increased, from 80 MPa to 200 MPa. To further investigate the capabilities of high pressure sintering, a short 3-min dwell sintering cycle at 282 MPa (the maximum attainable with our setup) was applied to A8. Interestingly, while the density of A7 was higher than that of A8, multiple elongated pores are notable in the SEM image of A7, hinting to different pore size distributions in the two samples. This is in line with the optical opacity of A7 and translucency of A8, since optical absorption arises primarily from pores of the same size range as the wavelength of the light. Holding the sample at high pressure for a long time (60 min) is thus counterproductive. Furthermore, the grain morphology of A8 was not elongated, proving the ability of higher pressure to suppress grain growth.

Thus, the best resultant ceramic with high density but fine microstructure (1.3 µm) was obtained using UPA α-Al_2O_3 powder with a short sintering cycle at 282 MPa (A8). Similarly, raising the pressure to 500 MPa allowed Grasso et al. [27] to lower the sintering temperature to 950–1000 °C and nearly suppress grain growth entirely.

Since all sintered ceramics were in the α-Al_2O_3 phase as expected, only the lattice parameters *a* and *c* are presented in Table 1. The maximal differences between the *a* values and the *c* values were 0.01 Å and 0.03 Å, respectively. The cell parameters of the α-Al_2O_3 ceramic examined herein were slightly smaller than those of the standard hexagonal unit cell (a_H= 4.759 Å, c_H =12.991 Å [28]), which is most likely

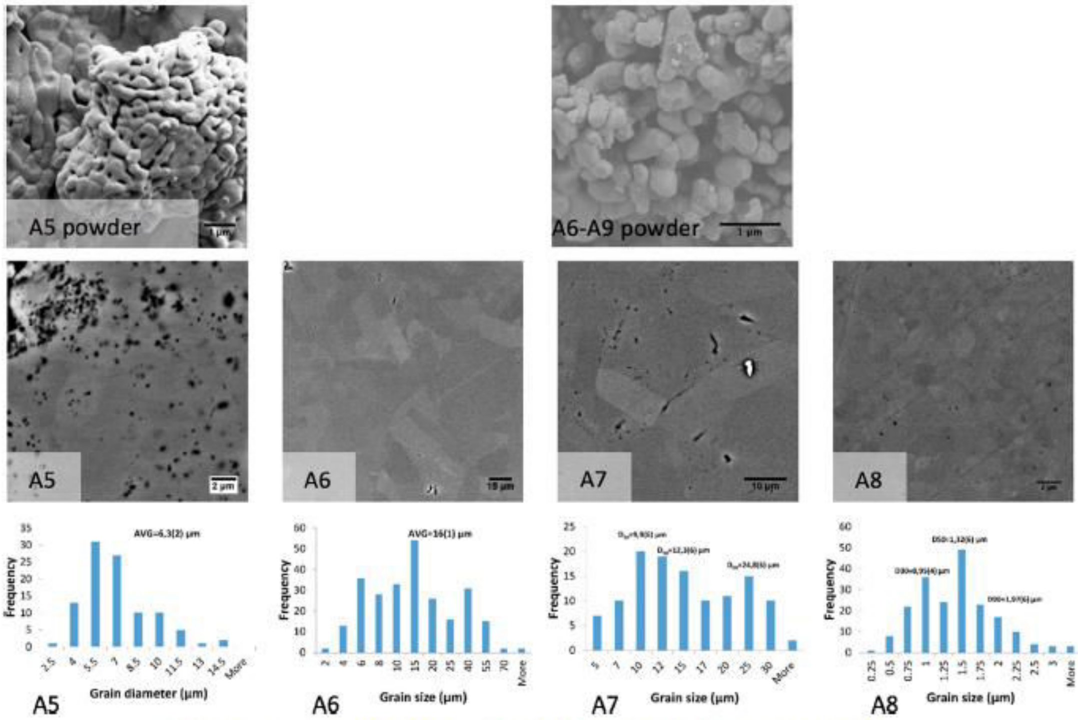

Fig. 3. SEM micrographs of A5–A8 powders and sintered pellets with the grain size distribution of the latter.

due to the pressures used during sintering, even though α-Al_2O_3 is known to be only 9% compressible at 300 kbar [29].

Fig. 4 shows the results of EBSD mapping of A2, which was carried out to confirm the validity of the measurements of the grain sizes of the ceramics from SEM images and investigate the potential preferential orientation of the grains. EBSD analysis did not indicate any preferential orientation of crystallites, meaning that no strong texturation was created during the SPS process. The average grain size obtained from SEM micrographs (4.9(2) µm) is in agreement with the average grain size of ~6 µm obtained from EBSD analysis, taking into account the presence of grains with size > 10 µm that were not visible in the SEM micrographs. Similarly, grains smaller than 0.5 µm are difficult to measure due to low contrast (the right side of Fig. 4 shows the grain boundaries overlapped on an SEM image). The somewhat scattered larger grains were most likely due to the formation of so-called 'hot spots' during SPS, wherein the current distribution localizes into a small area, increasing local temperatures and even causing melting [30,31].

3.2. Optical properties

The measured transmission spectra (left) and calculated absorption coefficients (right) of translucent samples A2, A6, and A8 are shown in Fig. 5. Additionally, the inset in the right side of Fig. 5 shows the absorption coefficients of A2–A6 and A8–A6 to better demonstrate the absorption bands. As previously mentioned before, A2 is sintered from pure γ-Al_2O_3 while A6 and A8 are sintered from α-Al_2O_3 (UPA). Thus, it was expected that the spectra would have an overall similar shape. At 500 nm, our samples had transmission values of ~3% for A2 and A6, and ~10% for A8, which can be compared to the maximum theoretical value of ~40% in the case of 0.8 mm thickness and 0.5 µm grain size [32]. Considering the absorption coefficient, the sample with the highest translucency in the 200–500 nm range was A6, while A8 was more transparent above 500 nm. To effectively consider the influence of the different sample thicknesses, the analysis herein focuses primarily on the absorption coefficient.

It has been shown that for single crystals of Al_2O_3, absorption bands

Table 1
Samples, their sintering conditions and characteristics.

Sample	Sintering	a (Å)	c (Å)	Grain size (µm)	Density (%)	Visual appearance
A1	20 min at 1450 °C, 80 MPa	4.7583(3)	12.9960(20)	3.3(1)	95.8(1)	Gray
A2		4.7548(1)	12.9859(5)	4.9(2)	98.0(3)	Translucent
A3		4.7515(1)	12.9806(4)	24(1)	94.7(1)	White
A4		4.7575(1)	12.9936(5)	7.5(3)	94.2(7)	Gray-White
A5		4.7509(1)	12.9774(4)	6.3(2)	94.1(3)	White
A6		4.7613(7)	13.0090(30)	16.0(10)	98.4(7)	Translucent
A7	20 min at 1450 °C, 200 MPa	4.7546(1)	12.9877(6)	12.3(6)	97.4(2)	Foggy white
A8	3 min at 1450 °C, 282 MPa	4.7535(2)	12.9870(8)	1.3(1)	96.6(1)	Translucent

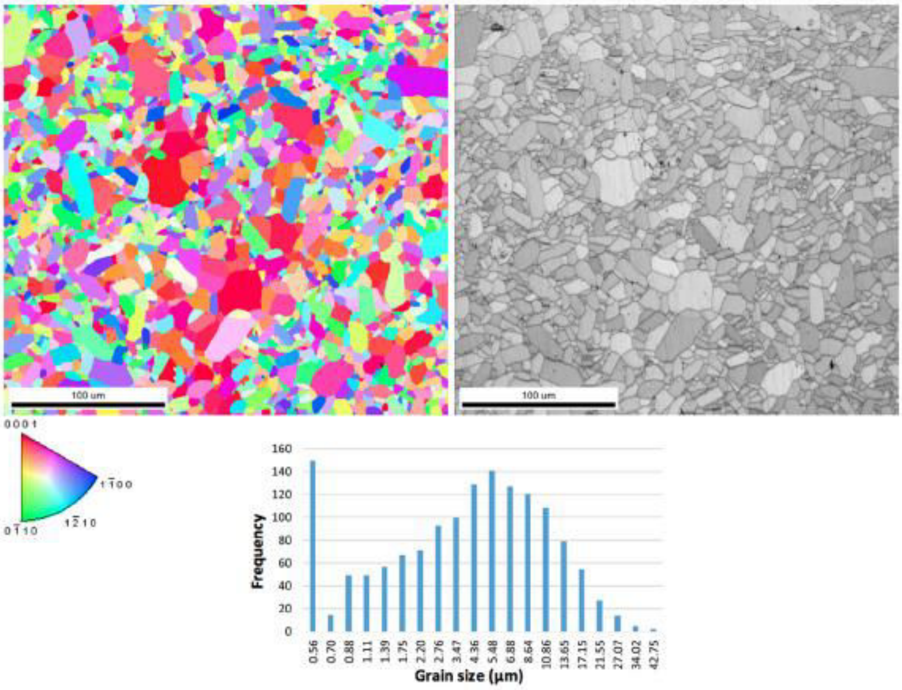

Fig. 4. EBSD mapping of A2 and surface-averaged grain size from EBSD.

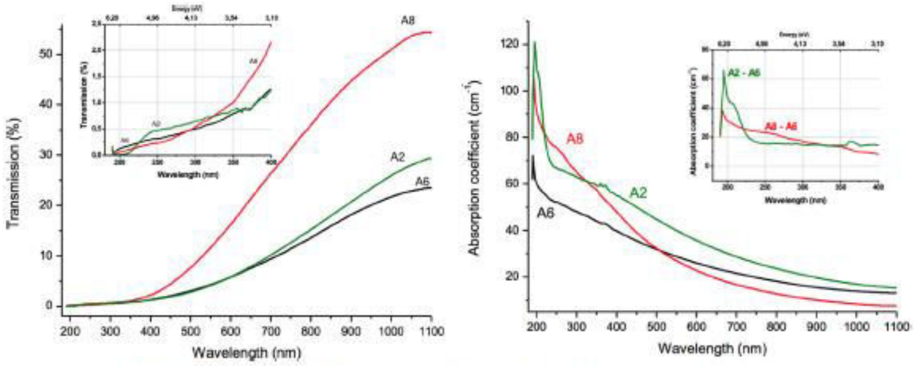

Fig. 5. Transmission and absorption coefficient of A2 (0.8 mm), A6 (1.1 mm) and A8 (0.8 mm).

in the range of 200–255 nm are related to single defects. More specifically, absorption at ~205 nm corresponds to F centers and absorption at ~255 nm corresponds to F$^+$ centers [33,34]. Slight increases in absorption coefficient of A8 at about 250 nm are known to be the result of Fe impurities [35], but this is unlikely in this experiment because of the high purity of the UPA powders used [12]. Thus, the increase was attributed to the ~255 nm absorption by F$^+$ centers. Absorption at ~357 nm has been attributed to F$_2$$^+$ centers [33], which occur when two oxygen vacancies trap three electrons, and are known to form in alumina from F$^+$ centers when heated beyond 350 °C. The origin of the small bands between 360 and 375 nm has not yet been identified.

4. Conclusions

In conclusion, to obtain dense α-Al_2O_3 ceramics under the chosen sintering conditions, the γ-Al_2O_3 phase should be used as a starting material, since sintering a mixture of γ- and δ-Al_2O_3 leads to a decreased final density. Optically translucent samples were sintered at 1450 °C using a 20-min dwell time, starting from 50 nm γ-Al_2O_3 (A2) or 300 nm α-Al_2O_3 powders (A6, A8). The benefit of sintering small-grained γ-Al_2O_3 powder (A2) was that the final ceramic grain size was smaller, with the drawback of high absorption in the visible range due to the increased number of grain boundaries. Using 300 nm α-Al_2O_3 powder instead removed the requirement for phase transfer during sintering (thus there was no sudden volume change at temperatures < 1400 °C, resulting in a more stable process), the final density was slightly higher, and the lowest absorption in the visible range was achieved (A6). Using 300 nm α-Al_2O_3 powder in conjunction with higher-pressure sintering (282 MPa; A8) resulted in a ceramic with high density and acceptable transparency in the visible range after a dwell time of only 3 min at 1450 °C.

Absorption bands related to single defects (F, F^+, and F_2^+ centers) were observed for all translucent samples.

Acknowledgements

The authors are grateful to FR-FCM, France for financial support for this work. The authors would like to thank O. Brinza (LSPM-CNRS, France) for carrying out the EBSD analysis and H. Spiridigliozzi (University Paris 13, France) for carrying out the transparency measurements. The authors are grateful to take part in the SPS platform of Ile-de-France (ICMPE-CNRS, France) and would like to thank B. Villeroy (ICMPE-CNRS, France) for his technical expertise. Annika Pille thanks the Université Paris 13 for financial support for her PhD studies.

References

[1] S.F. Wang, J. Zhang, D.W. Luo, F. Gu, D.Y. Tang, Z.L. Dong, G.E.B. Tan, W.X. Que, T.S. Zhang, S. Li, L.B. Kong, Transparent ceramics: processing, materials and applications, Prog. Solid State Chem. 41 (2013) 20–54, https://doi.org/10.1016/j.progsolidstchem.2012.12.002.

[2] A.A. Kachaev, D.V. Grashchenkov, Y.E. Lebedeva, S. St. Solntsev, O.L. Khasanov, Optically transparent ceramic (Review), Glass Ceram. 73 (2016) 117–123, https://doi.org/10.1007/s10717-016-9838-3.

[3] X. Jin, L. Gao, J. Sun, Highly transparent alumina spark plasma sintered from common-grade commercial powder: the effect of powder treatment, J. Am. Ceram. Soc. 93 (2010) 1232–1236, https://doi.org/10.1111/j.1551-2916.2009.03544.x.

[4] G. Ackland, Controlling radiation damage, Science (80-.) 327 (2010) 1587–1588, https://doi.org/10.1126/science.1188088.

[5] S.H. Risbud, C.H. Shan, A.K. Mukherjee, M.J. Kim, J.S. Bow, R.A. Holl, Retention of nanostructure in aluminum-oxide by very rapid sintering at 1150-degrees-C, J. Mater. Res. 10 (1995) 237–239, https://doi.org/10.1557/JMR.1995.0237.

[6] B.N. Kim, K. Hiraga, K. Morita, H. Yoshida, Spark plasma sintering of transparent alumina, Scr. Mater. 57 (2007) 607–610, https://doi.org/10.1016/j.scriptamat.2007.06.009.

[7] D. Jiang, D.M. Hulbert, U. Anselmi-Tamburini, T. Ng, D. Land, A.K. Mukherjee, Optically transparent polycrystalline Al_2O_3 produced by spark plasma sintering, J. Am. Ceram. Soc. 91 (2008) 151–154, https://doi.org/10.1111/j.1551-2916.2007.02086.x.

[8] K. Morita, B.N. Kim, K. Hiraga, H. Yoshida, Fabrication of transparent $MgAl_2O_4$ spinel polycrystal by spark plasma sintering processing, Scr. Mater. 58 (2008) 1114–1117, https://doi.org/10.1016/j.scriptamat.2008.02.008.

[9] A.V. Bersh, A.V. Belyakov, D.Y. Mazalov, S.A. Solov'ev, L.V. Sudnik, A.V. Fedotov, Formation and sintering of boehmite and aluminum oxide nanopowders, Refract. Ind. Ceram. 57 (2017) 655–660, https://doi.org/10.1007/s11148-017-0040-0.

[10] S. Kwon, G.L. Messing, Sintering of mixtures of seeded boehmite and ultrafine-alumina, J. Am. Ceram. Soc. 83 (2000) 82–88, https://doi.org/10.1111/j.1151-2916.2000.tb01152.x.

[11] C.S. Nordahl, G.L. Messing, Sintering of α-Al_2O_3 seeded nanocrystalline γ-Al_2O_3 powders, J. Eur. Ceram. Soc. 22 (2002) 415–422.

[12] E. Töldsepp, F. Schoenstein, M. Amamra, R. Saar, E. Feldbach, A. Kanaev, M. Kirm, Spark plasma sintering of ultra-porous γ-Al_2O_3, Ceram. Int. 42 (2016) 11709–11715, https://doi.org/10.1016/j.ceramint.2016.04.089.

[13] K. Wefers, C. Misra, Oxides and hydroxides of aluminum, Alcoa Tech. Pap. 19 (1987) 1–100.

[14] J.L. Vignes, C. Frappart, T. Di Costanzo, J.C. Rouchaud, L. Mazerolles, D. Michel, Ultraporous monoliths of alumina prepared at room temperature by aluminium oxidation, J. Mater. Sci. 43 (2008) 1234–1240, https://doi.org/10.1007/s10853-007-2260-z.

[15] M. Beauvy, J.-L. Vignes, D. Michel, L. Mazerolles, C. Frappart, T.Di. Costanzo, Method of Preparation of Monolithic Hydrated Aluminas, Amorphous or Crystalline Aluminas, Aluminates and Composite Materials by Oxidation of Aluminum or of An Aluminum Alloy, US7799385B2, 2010.

[16] S. Imine, F. Schoenstein, S. Mercone, M. Zaghrioui, N. Bettahar, N. Jouini, Bottom-up and new compaction processes: a way to tunable properties of nanostructured cobalt ferrite ceramics, J. Eur. Ceram. Soc. 31 (2011) 2943–2955, https://doi.org/10.1016/j.jeurceramsoc.2011.06.004.

[17] F. Jean, F. Schoenstein, M. Zaghrioui, M. Bah, P. Marchet, J. Bustillo, F. Giovannelli, I. Monot-Laffez, Composite microstructures and piezoelectric properties in tantalum substituted lead-free $K_{0.5}Na_{0.5}Nb_{1-x}Ta_xO_3$ ceramics, Ceram. Int. 44 (2018) 9463–9471, https://doi.org/10.1016/j.ceramint.2018.02.163.

[18] A. Teber, F. Schoenstein, F. Têtard, M. Abdellaoui, N. Jouini, The effect of Ti substitution by Zr on the microstructure and mechanical properties of the cermet $Ti_{1-x}Zr_xC$ sintered by SPS, Int. J. Refract. Met. Hard Mater. 31 (2012) 132–137, https://doi.org/10.1016/j.ijrmhm.2011.10.002.

[19] A.D. Omrani, M.A. Bousnina, L.S. Smiri, M. Taibi, P. Leone, F. Schoenstein, N. Jouini, Elaboration of nickel nanoparticles by modified polyol process and their spark plasma sintering, characterization and magnetic properties of the nanoparticles and the dense nano-structured material, Mater. Chem. Phys. 123 (2010) 821–828, https://doi.org/10.1016/j.matchemphys.2010.05.068.

[20] N. Ouar, F. Schoenstein, S. Mercone, S. Farhat, B. Villeroy, B. Leridon, N. Jouini, Spark-plasma-sintering magnetic field assisted compaction of Co80Ni20 nanowires for anisotropic ferromagnetic bulk materials, J. Appl. Phys. 114 (2013) 3–8, https://doi.org/10.1063/1.4827199.

[21] N. Ouar, M.A. Bousnina, F. Schoenstein, S. Mercone, O. Brinza, S. Farhat, N. Jouini, Spark Plasma Sintering of Co80Ni20 nanopowders synthesized by polyol process and their magnetic and mechanical properties, J. Alloy. Compd. 615 (2015) S269–S275, https://doi.org/10.1016/j.jallcom.2014.01.058.

[22] Y. Aman, V. Garnier, E. Djurado, Influence of green state processes on the sintering behaviour and the subsequent optical properties of spark plasma sintered alumina, J. Eur. Ceram. Soc. 29 (2009) 3363–3370, https://doi.org/10.1016/j.jeurceramsoc.2009.07.014.

[23] L. Lutterotti, D. Chateigner, S. Ferrari, J. Ricote, Texture, residual stress and structural analysis of thin films using a combined X-ray analysis, Thin Solid Films 450 (2004) 34–41, https://doi.org/10.1016/j.tsf.2003.10.150.

[24] M.I. Mendelson, Average grain size in polycrystalline ceramics, J. Am. Ceram. Soc. 52 (1969) 443–446, https://doi.org/10.1111/j.1151-2916.1969.tb11975.x.

[25] O. Khatim, T.H.N. Nguyen, M. Amamra, L. Museur, A. Khodan, A. Kanaev, Synthesis and photoluminescence properties of nanostructured mullite/alpha-Al_2O_3, Acta Mater. 71 (2014) 108–116, https://doi.org/10.1016/j.actamat.2014.03.006 1359-6454/?.

[26] J.G. Santanach, A. Weibel, C. Estournès, Q. Yang, C. Laurent, A. Peigney, Spark plasma sintering of alumina: study of parameters, formal sintering analysis and hypotheses on the mechanism(s) involved in densification and grain growth, Acta Mater. 59 (2011) 1400–1408, https://doi.org/10.1016/j.actamat.2010.11.002.

[27] S. Grasso, B.-N. Kim, C. Hu, G. Maizza, Y. Sakka, Highly transparent pure alumina fabricated by high-pressure spark plasma sintering, J. Am. Ceram. Soc. 93 (2010) 2460–2462, https://doi.org/10.1111/j.1551-2916.2010.03811.x.

[28] H. Bialas, H.J. Stolz, Lattice dynamics of sapphire (Corundum), Z. Phys. B. 21 (1975) 319–324.

[29] H.V. Hart, H.G. Drickamer, Effect of high pressure on the lattice parameters of Al_2O_3, J. Chem. Phys. 43 (1965) 2265–2266, https://doi.org/10.1063/1.1697121.

[30] M. Suárez, A. Fernández, J.L. Menéndez, R. Torrecillas, H.U. Kessel, J. Hennicke, R. Kirchner, T. Kessel, Challenges and opportunities for spark plasma sintering: a key technology for a new generation of materials, Sinter. Appl. (2013) 319–342, https://doi.org/10.5772/53706.

[31] C. Collard, Z. Trzaska, L. Durand, J.-M. Chaix, J.-P. Monchoux, Theoretical and experimental investigations of local overheating at particle contacts in spark plasma sintering, Powder Technol. 321 (2017) 458–470, https://doi.org/10.1016/j.powtec.2017.08.033.

[32] R. Apetz, M.P.B. Van Bruggen, Transparent alumina: a light – scattering model, J. Am. Ceram. Soc. 86 (2003) 480–486, https://doi.org/10.1016/j.infsof.2008.09.005.

[33] M. Izerrouken, T. Benyahia, Absorption and photoluminescence study of Al_2O_3 single crystal irradiated with fast neutrons, Nucl. Instrum. Methods Phys. Res. Sect. B Beam Interact. Mater. At. 268 (2010) 2987–2990, https://doi.org/10.1016/j.nimb.2010.05.024.

[34] A. Stashans, E. Kotomin, J.L. Calais, Calculations of the ground and excited states of F-type centers in corundum crystals, Phys. Rev. B 49 (1994) 14854–14858, https://doi.org/10.1103/PhysRevB.49.14854.

[35] M.E. Innocenzi, R.T. Swimm, M. Bass, R.H. French, A.B. Villaverde, M.R. Kokta, Room-temperature optical absorption in undoped α-Al_2O_3, J. Appl. Phys. 67 (1990) 7542–7546, https://doi.org/10.1063/1.345817.

Abstract

This thesis deals with the elaboration and study of the physical properties of optically transparent and luminescent alumina-based ceramics for which applications are foreseen in the field of ionizing radiation resistant materials. The challenge of this work was to obtain a material that simultaneously has a high density and grain size at the nanoscale in order to give the ceramic transparency properties and resistance to ionizing radiation by capturing and recombination of induced charges at the grain boundaries.

Ceramics of composition Al_2O_3 and $MgAl_2O_4$ were consolidated by Spark Plasma Sintering (SPS) from ultra-porous aluminas (UPA) on the one hand, and by reactive sintering of a mixture of Al_2O_3: MgO precursor in a ratio of 1 : 1 on the other hand. The UPAs were developed using an original process implemented at the LSPM. They were then impregnated with a solution of magnesium nitrate and then calcined at low temperature to obtain the "Nanostructured Precursor" (NP) for the spinel phase $MgAl_2O_4$. The synthesized NPs, like the UPAs, were then consolidated by SPS. The sintering parameters have been optimized to obtain ceramics with the desired microstructural and physical properties. The effect of Ta_2O_5 as a grain growth inhibitor has been tested on the microstructure of elaborated ceramics. The transmittance and luminescence properties, before and after irradiation, of the most promising materials were measured and correlated with their structural characteristics.

Keywords: *nanopowder synthesis, spark plasma sintering, reactive sintering, final microstructure, optical transparency, luminescence, alumina, spinel*

Résumé

Ce travail de thèse porte sur l'élaboration et l'étude des propriétés physiques de céramiques à base d'alumine optiquement transparentes et luminescentes pour lesquelles des applications sont envisagées dans le domaine des matériaux résistants aux rayonnements ionisants. L'enjeu de ce travail a consisté à obtenir un matériau qui présente simultanément une densité élevée et des tailles de grains à l'échelle nanométrique afin de conférer respectivement à la céramique des propriétés de transparence et une résistance aux radiations ionisantes par la capture et la recombinaison des charges induites au niveau des joints de grains.

Des céramiques de composition Al_2O_3 et $MgAl_2O_4$ ont été consolidées par Spark Plasma Sintering (SPS) à partir d'alumines ultra-poreuses (UPA) d'une part, et par frittage réactif d'un mélange de précurseur Al_2O_3 : MgO dans un ratio 1 : 1 d'autre part. Les UPA ont été élaborés par un procédé original mis en place au LSPM. Elles ont ensuite été imprégnées par une solution de nitrate de magnésium puis calcinée à basse température afin d'obtenir le « Précurseur Nanostructuré » (PN) pour la phase spinelle $MgAl_2O_4$. Les PNs synthétisés, tout comme les UPA, ont ensuite été consolidées par SPS. Les paramètres de frittage ont été optimisés de manière à obtenir des céramiques possédant les propriétés microstructurales et physiques visées. L'effet de Ta_2O_5 comme inhibiteur de croissance des grains a été éprouvé sur la microstructure des céramiques élaborées. Les propriétés de transmittance ainsi que de luminescence, avant et après irradiation, des matériaux les plus prometteurs ont été mesurées et corrélées à leurs caractéristiques structurales.

Mots-clés : *synthèse de poudres nanométriques, frittage par courant pulsé, frittage réactif, microstructure finale, transparence optique, luminescence, alumine, spinelle*